New Generation Finite Element Methods For Forward Seismic Modelling

Charlotta Jasmine Howarth

January 2014

This thesis is submitted to the Department of Mathematics and Statistics in partial fulfilment of the requirement for the degree of Doctorate of Philosophy.

Abstract

The Ultra Weak Variational Formulation (UWVF) is a powerful numerical method for the simulation of acoustic, elastic, and electromagnetic waves. Key to its strength is the superior approximation properties of the Trefftz basis of local solutions of the homogeneous form of the equation to be solved. In this thesis we consider time harmonic acoustic wave propagation in two dimensions, as modelled by the Helmholtz equation. We investigate enrichment of the UWVF basis for wave scattering and propagation problems, with applications in geophysics.

A new Hankel basis is implemented in the UWVF, allowing greater flexibility than the traditional plane wave basis. We use ray tracing techniques to provide a good a priori choice of direction of propagation for the UWVF basis. A reduction in the number of degrees of freedom required for a given level of accuracy is achieved for the case of scattering by a smooth convex obstacle.

The use of the UWVF for forward seismic modelling is considered, simulating wave propagation through a synthetic sound speed profile of the subsurface of the Earth. The practicalities of implementation in a domain of highly varying sound speed are discussed, and a ray enhanced basis is trialled. Wave propagation from a source on the interior of the domain is simulated, representative of an explosive sound source positioned at depth. The UWVF typically has difficulties representing the inhomogenous Helmholtz equation. An augmentation to the UWVF called the Source Extraction UWVF is presented which allows the superior approximation properties of the Trefftz basis to be maintained.

Declaration

I confirm that this is my own work and the use of all material from other sources has been properly and fully acknowledged.

Signed .....

Charlotta Jasmine Howarth

Acknowledgements

I would like to thank my three supervisors, Dr Steve Langdon, Dr Paul Childs, and Professor Simon Chandler-Wilde. Over the last three years Steve has always made time to answer any of my questions and always made sure that I was clear in my understanding. He has also been an absolute star when it came to providing corrections! I am grateful to Paul for the many hours of interesting discussions we had in my summer placements. His guidance ensured I learnt a great deal, not just of the mathematics, but of the wider seismic industry. Paul has also provided the Marmousi data set and the finite difference comparison solution used in this thesis. Simon has provided very thorough explanations, and could always point me in the right direction literature wise. I would also like to thank Andrea Moiola for being an ever helpful resource, I very much appreciated his attention to detail, and his funny Italian sense of humour.

I thank the Natural Environment Research Council for their financial support, which has made my studies possible. I would like to thank Schlumberger Gould Research (formerly Schlumberger Cambridge Research) not just for their financial support, but for providing some of the most interesting and enjoyable topics of my studies. The three summers I spent interning there were both wonderful and fascinating, and I am very grateful to have had the opportunity to work among such supportive and brilliant scientists. I would also like to thank the Society for Industrial and Applied Mathematics, for providing the funding for the summer school in Vancouver.

I would like to thank my close family and friends for their love, support, and encouragement throughout my studies. Thanks also go to my fellow PhD students and the staff of the mathematics department, for aiding an enjoyable PhD experience. Thank

you to Colin Singleton, for being a loyal lunch buddy and friend. I would also like to thank Alistair Hall, for his continuous encouragement helping me towards the finish, and for the workspace and excellent computing facillities he provided me. Finally, I would like to extend my deepest thanks to Atahl Nathanson. Over the last few years she has been my voice of reason for all of the worst times, and my laughing companion for all of the best. I honestly don't think I would have gotten this far without her.

Contents

List of Figures

List of Tables

Notation

Symbol	Definition/Use
α	Vector in MFS system
α_j	Amplitude coefficient in MFS
$\beta(\cdot)$	Antilinear functional for $\hat{b}$ vector of UWVF
$\hat{\beta}(\cdot)$	Antilinear functional for $\hat{b}$ vector of Source Extraction UWVF
$\delta(\mathbf{x})$	Dirac delta function at a point $\mathbf{x}$
Δx	Spatial step in x direction
Δz	Spatial step in z direction
$\frac{\partial}{\partial n}$	Normal derivative
$\frac{\partial}{\partial x}$	Derivative in x direction
$\frac{\partial}{\partial z}$	Derivative in z direction
$\partial\Omega$	Boundary of domain
$\partial\Omega_k$	Boundary of element Ω_k
ϵ	A small parameter
ε_m	The Neumann symbol
Γ	Boundary of domain
Γ_1	Boundary of scatterer
Γ_{FMM}	Fast Marching Method initial wavefront boundary
Γ_{lit}	Illuminated boundary
Γ_{shadow}	Boundary in shadow
Γ_{SB}	Shadow boundary

Γ_k	Edge of element Ω_k on exterior boundary Γ
Γ^E	Closed curve exterior to $\bar{\Omega}$
Γ^S	Boundary of source domain Ω^S
$\Gamma_{surface}$	Upper boundary of domain corresponding to sea surface
κ	Wavenumber
κ_k	Wavenumber in element Ω_k
κ^S	Wavenumber in region Ω^S
κ_{sea}	Wavenumber in region corresponding to sea
λ	Wavelength
$\tilde{\lambda}$	Distance parameter of an extended ray
λ^*	Limiting value of $\tilde{\lambda}$
ν	Flow parameter
ω	Angular wave frequency
Ω	Domain
Ω_k	Element number k
Ω^S	Inner domain containing source
Ω^E	Exterior Domain
Ω^+	Domain of scattering object
Ω_{lit}	Illuminated region
Ω_{shadow}	Shadow region
ϕ	Angular coordinate of a point in the domain
ϕ^*	Set of basis functions
ϕ_k	Basis function on element k
$\phi_{k,l}$	Basis function l of element k
$\Phi(\mathbf{x}, \mathbf{y})$	Fundamental solution of the Helmholtz equation, at $\mathbf{x}$, centred at $\mathbf{y}$
ψ	Angular coordinate of boundary interaction point
$\psi(\cdot)$	Phase function
ρ	Density
ρ_k	Density in element Ω_k
ρ^S	Density in region Ω^S

σ	Impedance parameter
$\Sigma_{k,j}$	Interelement edge between Ω_k and Ω_j
θ	Angle in $(-\pi, \pi]$
θ_i	Angle of incidence
θ_r	Angle of reflection
θ_t	Angle of refraction
τ	The eikonal
$\tau_{i,j}$	The eikonal at a point indexed by i, j
τ	Test function for first order system variable
$\boldsymbol{\tau}_k$	Test function for first order system variable in Ω_k
χ_k^a	Approximation of impedance trace on the edges of element k
χ_k	Impedance trace on the edges of element k
$\chi_{k,l}$	Amplitude coefficient of basis function $\phi_{k,l}$
ξ_N	Best approximation basis
$\boldsymbol{\zeta}$	First order system variable
$\boldsymbol{\zeta}_k$	First order system variable on element Ω_k
$\hat{\boldsymbol{\zeta}}$	Numerical flux of first order system variable
A	Matrix in MFS system
$A(\cdot)$	Wave amplitude
$A_{m,j}$	Coefficient in MFS system
a	Major axis of ellipse
b	Minor axis of ellipse
$\hat{b}$	Vector $\hat{b}$ of UWVF
$B_\epsilon(\mathbf{x})$	Circle centred at $\mathbf{x}$ of radius ϵ
BEM	Boundary Element Method
c	Sound speed
$c_{i,j}$	Sound speed at point indexed by i, j
$\frac{1}{c}$	Slowness, reciprocal of speed
$c(\cdot,\cdot)$	Billinear/sesquilinear form for C matrix
$\hat{c}$	Constant

C	C Matrix of UWVF
$\mathbb{C}$	Set of complex numbers
$C_{k,j}$	Submatrix of C Matrix corresponding to Ω_k and adjacent Ω_j
$C_{k,j}^{l,m}$	Entry of submatrix of $C_{k,j}$ corresponding to basis functions $\phi_{j,m}$ and $\phi_{k,l}$
$C_R(0,0)$	Circle of radius R centred at the origin
$d(\cdot,\cdot)$	Billinear/sesquilinear form for D matrix
$\mathbf{d}_{k,l}$	Unit direction vector of plane wave basis l on element k
$\mathbf{d}$	Unit direction vector
$\mathbf{d}_i$	Unit incident direction vector
$\mathbf{d}_r$	Unit reflected direction vector
$\mathbf{d}_{ray}$	Unit ray traced direction vector
D	D Matrix of UWVF
D_k	Submatrix of D Matrix corresponding to Ω_k
$D_k^{l,m}$	Entry of submatrix of D_k Matrix corresponding to basis functions $\phi_{k,l}$ and $\phi_{k,m}$
DEM	Discontinuous Enrichment Method
DG	Discontinuous Galerkin
e	Exponential constant, Euler's number
exp	Exponential function
E	Dimensionless best approximation constant
f	Interior source term
$f(\cdot)$	Function of a single angle
$f(\cdot,\cdot)$	Function of two angles
f_r	Frequency
F	Adjoint impedance trace operator
$F(\mathbf{X})$	Functional of variables in Hamilton Jacobi system
FD	Finite Difference
FEM	Finite Element Method
FMM	Fast Marching Method
g	Source term on the boundary of the domain
g_{FMM}	Fast Marching Method initial boundary data

h	Mesh size parameter
H	Space of Treftz functions
H^1	Sobolev space
$\tilde{H}$	Space of functions in H^1 with normal derivative in L^2
$H(\cdot,\cdot)$	Hamilton-Jacobi equation
H_k	Discrete subspace of Treftz functions
$\tilde{H}_k$	Discrete subspace of $\tilde{H}$
$H_\nu^l(\mathbf{z})$	Hankel function of the lth kind of order ν centred at $\mathbf{z}$
Hz	Hertz: one cycle per second
i	Imaginary unit
$\mathcal{I}$	Impedance trace operator
$Im(\cdot)$	Imaginary part
J_ν	Bessel function of the first kind of order ν
k	Element index
K	Total number of elements
$L^2(\Omega)$	Space of square integrable functions in Ω
$L^2(\partial\Omega)$	Space of square integrable functions on boundary $\partial\Omega$
M	Number of collocation points in MFS approximation
MFS	Method of Fundamental Solutions
$\mathbf{n}$	Exterior normal direction vector
$\mathbf{n}_k$	Exterior normal vector from element Ω_k
$\mathbf{n}_E$	Exterior normal vector from region Ω_E
$\mathbf{n}_S$	Exterior normal vector from region Ω_S
N	Number of fundamental solutions in MFS approximation
N_P	Number of evaluation points
N_T	Total number of degrees of freedom
N_λ	Number of degrees of freedom per wavelength
p	Maximum number of basis functions per element
p_k	Number of basis functions on element Ω_k
PDE	Partial differential equation

PUFEM	Partition of Unity Finite Element Method
PWDG	Plane Wave Discontinuous Galerkin
Q	Boundary condition parameter
r	Radial distance of point
R	Radial distance
$R(\cdot)$	Radial distance of scatterer boundary
$\mathrm{Re}(\cdot)$	Real part
$\mathbb{R}^d$	The set of real numbers, in d dimensions
$\mathbb{R}^2$	The set of real numbers, in 2 dimensions
RSME	Root Mean Square Error
RRSME	Relative Root Mean Square Error
$\mathbf{s}$	Slowness vector
s_i	Slowness in each direction
t	Time
$\mathcal{T}$	Partitioning of mesh
$\mathcal{T}^E$	Partitioning of mesh in Ω^E
$\mathcal{T}^S$	Partitioning of mesh in Ω^S
u	Acoustic pressure in the frequency domain
u_k	Approximation of acoustic pressure on element Ω_k
u_h	Discrete acoustic pressure approximation
u_h^*	Discrete acoustic pressure approximation either with $* = S$ in Ω^S or with $* = E$ in Ω^E
u^i	Incident field
u^E	Unknown field in Ω^E
u^I	Known field in Ω^S
u^s	Scattered field
u^S	Unknown backscattered field in Ω^S
$\hat{u}$	Numerical flux of acoustic pressure approximation
U	Acoustic pressure in the time domain
UWVF	Ultra Weak Variational Formulation

v	Variational form test function
v_k	Variational form test function on element k
$\mathbf{v}$	Unit direction vector perpendicular to normal $\mathbf{n}$
V	Trace space of L^2 functions
w	Variational form test function
w_k	Variational form test function on element k
w_h	Discrete variational form test function
x	Single horizontal spatial direction
x_i	Single spatial direction
x_k^C	First coordinate of centroid of an element Ω_k
$\mathbf{x}$	Spatial variable
$\mathbf{x}_0$	Position of interior point source
$\mathbf{x}_s$	Position of exterior point source
$\mathbf{x}_C$	Ray traced centre of curvature
$\mathbf{x}_k^C$	Centroid of an element Ω_k
X	Vector of amplitude coefficients in UWVF
$\mathbf{X}$	Vector of variables in Hamilton Jacobi system
y	Vertical spatial direction
y_k^C	Second coordinate of centroid of an element Ω_k
$\mathbf{y}_j$	Point source of fundamental solution in the MFS
$\mathbf{y}_{k,l}$	Point source of basis function l of element k
Y_ν	Bessel function of the second kind of order ν
z	Vertical spatial direction, depth
$\hat{\mathbf{z}}$	Centre of curvature
$\hat{\mathbf{z}}_{opt}$	Optimal centre of curvature
$\|\cdot\|_{L^2(\partial\Omega)}$	L^2 norm on boundary $\partial\Omega$
$\|\cdot\|_{L^2(\Omega)}$	L^2 norm on domain Ω
$\{\{\cdot\}\}$	Average
$[[\cdot]]$	Jump

Chapter 1

Introduction

1.1 Motivation

Time harmonic wave theory for elliptic partial differential equation (PDE) problems encompasses acoustic waves (on the scalar field) [19], elastic waves (over scalar and vector fields) [43], and electromagnetic waves (over two coupled vector fields) [24, 57]. The wave propagation problems associated with these wave types are numerous, and are areas of intensive study in mathematics, physics, and engineering. The widespread interest in the accurate simulation of wave propagation is due to the broad range of applications, such as those in defense, seismology, and medical physics. Wave scattering techniques are commonly used in imaging processes, for example in radar, sonar, seismic imaging, and non invasive medical imaging [18, 43, 70].

Commonly used numerical methods for the approximation of wave propagation, including Finite Difference (FD) and Finite Element Methods (FEM), often require a fixed number of degrees of freedom per wavelength in order to resolve the oscillatory nature of the solution [20]. This means that to obtain an accurate approximation, the number of degrees of freedom required grows linearly in each dimension with the wave frequency, i.e., of the order of the wavenumber to the power of the number of dimensions. High frequency problems are those where the wavelength is very small compared to the domain of definition, thus the solution is highly oscillatory. At high

frequencies, the number of degrees of freedom per wavelength has to be even larger, in comparison to cases of relatively low frequencies where a rule of thumb of ten degrees of freedom per wavelength are required to achieve enginering accuracy [18, 44, 47]. Due to the linear requirement on the number of degrees of freedom in each direction, the numerical approximation of high frequency solutions can lead to linear systems of a large number of unknowns, which can be highly computationally expensive to solve. This computational expense can be reduced through the use of enhanced approximation spaces, such as polynomials of a high degree [4, 56] or those which incorporate the known oscillatory behaviour [9, 21, 44].

This thesis is on the subject of new generation FEM, motivated by applications in geophysics. Current iterative and FEM for the simulation of seismic wave propagation and reflection in the Earth's subsurface are hugely expensive in computational resources [26]. Due to the large scale of the domain of interest, accurate simulations come with large storage requirements and long computation times. We consider a class of numerical methods called Trefftz methods, the Ultra Weak Variational Formulation (UWVF) [16, 17] in particular. Those in the seismic industry have an interest in methods of this type, as it is hoped that they will be more efficient for imaging the Earth's subsurface in order to locate hydrocarbon bearing rocks. The concept that is key to this improved efficiency is the assumption of wave like behaviour on each element, incorporating the known physical behaviour of the solution.

1.2 Aims and Key Results

The overall aim of this thesis is to increase the stock of knowledge about the UWVF, and to give greater insight into the potential for its increased widespread use. Specifically we aim to:

- Investigate and assess the impact of enrichment of the UWVF basis.
- Find ways of reducing the computational cost of approximating solutions whilst maintaining high levels of accuracy.

- Investigate the applicability of the UWVF as a method for forward seismic modeling.

To do this we consider several areas:

1. The use of a Hankel basis in the UWVF.
2. The use of ray tracing techniques, for both constant and non constant media, to give a good a priori choice of basis.
3. The use of the UWVF to approximate wave propagation in a domain of highly variable parameters typical of those seen in the subsurface of the Earth.
4. The UWVF approximation of point sources on the interior of the domain, representative of a likely real world set up of a sound source down a well.

Key results of this thesis are

1. We present an alternative method for solving inhomogeneous equations in the UWVF, called the Source Extraction UWVF [38]. Numerical results are presented that are of higher accuracy than the standard UWVF.
2. We use the UWVF to approximate wave propagation in a synthetic seismic domain, the Marmousi model [54], where the sound speed profile is complex and highly varying.
3. We present an algorithm for finding the local ray traced centre of curvature of the scattered field produced by wave interaction with a smooth convex obstacle.
4. We augment the UWVF basis with these ray traced centres of curvature, resulting in a reduction in the number of degrees of freedom required for a given level of accuracy.
5. In the case of a domain of varying wavespeed, we use Fast Marching Methods [13,63] to provide ray directions for use in the basis in the UWVF approximation.

6. We use a new Hankel basis in the UWVF, which allows greater flexibility in the level of curvature and variability of wavefronts than the standard plane wave basis.

7. We present a comparative study of the Hankel and traditional plane wave basis, focusing on the accuracy achieved and the conditioning of the linear system of equations.

8. We derive what is to the author's knowledge the first Discontinuous Galerkin (DG) formulation of the UWVF for the inhomogeneous Helmholtz equation in a domain where the wavenumber and density are non-constant.

1.3 Outline

The thesis structure is as follows.

In Chapter 2 we provide the context for the research in the subsequent chapters. We introduce some background of acoustic wave propagation, and the equation governing wave motion: the Helmholtz equation. Factors that need to be taken into consideration for the accurate numerical simulation of time harmonic acoustic wave propagation are explained, such as the truncation of an infinite domain, the imposition of boundary conditions, and computational time and storage costs. Details of two very different methods for understanding wave propagation are given. The first, the Method of Fundamental Solutions (MFS) [9], approximates the solution of the Helmholtz equation throughout the domain by a linear combination of fundamental solutions, by forcing conditions to hold on the boundary of the domain. The second method, Ray Tracing, is a method widely used in the seismic industry [2, 12, 32]. It provides a high frequency approximation to the direction of propagation of wavefronts and the travel time taken. This thesis is concerned with forward modelling, that is the simulation of wave propagation given a domain and set parameters that hold. Details of the related inverse problem are explained, where the structures within or parameters that hold in the domain are predicted often based upon the results of multiple trials of the

forward problem, either at varying frequencies or differing parameter set-ups [70]. The motivation for this research comes from the seismic imaging industry. We give background as to the numerical methods currently used in the seismic industry, and detail the practicalities of real world data acquisition.

In Chapter 3, we introduce the UWVF [16,17,44]. The UWVF is a powerful numerical method for the approximation of acoustic, elastic, and electromagnetic waves in two and three dimensions. The UWVF belongs to a category called Trefftz methods: the solution of the equation governing wave motion is approximated by a basis of functions that also satisfy the homogeneous form of the governing equation in each polygonal element of a discretised domain. The specific problem set up for the Helmholtz equation and the UWVF approximation form is given, as well as the derivation of the UWVF in the original variational and the more recently shown DG framework [15, 29, 31]. To the author's knowledge, the DG formulation of the Helmholtz equation presented is the first such derivation for a domain of non-constant wavenumber and density. Key theoretical results from the literature are explained. Computational aspects of the UWVF are then detailed, including the derivation of the linear system of equations, conditioning issues that arise. A plane wave basis has been used in most UWVF literature to date [16, 17, 40, 41, 44], however there has been some experimentation with a Bessel basis in [52, 53]. Here, we introduce a Hankel basis, of circular wavefronts propagating outwards from a point source. This basis allows flexibility in the set, as varying levels of curvature of the wavefronts may be included, with zero curvature returning the classical plane waves. We present a comparison study of wave propagation using either a plane wave or Hankel basis, considering both the convergence to the exact solution, the conditioning of the linear system of equations, and the point at which ill-conditioning causes the solution to break down.

In Chapter 5 we consider the case of wave scattering by a smooth convex obstacle, in a domain of constant wavespeed. We use ray tracing techniques in order to find a good a priori choice of basis function. We do this by finding the ray trajectory of a wavefront that propagates through a domain and interacts with a scatterer, causing a

reflected wave. An algorithm is developed that gives the centre of curvature for the reflected wavefronts, that can then be used in the UWVF Hankel basis. The algorithm is presented for a general smooth convex obstacle, with the specific examples of a circular and an elliptical scatterer further expanded upon. An initial study of the best approximation in an individual element for scattering by a circle is presented, as well as an investigation into the question of in which regions of the domain the ray traced basis is most accurate.

Chapter 5 is the first in which we investigate the enrichment of the UWVF basis for specific problem types. Similar strategies have been investigated in [9, 11]. We present the UWVF approximations to wave scattering by a circle, and then by an ellipse. We use first of all the traditional equi-spaced plane wave basis, and then compare with the results of using a basis augmented by the ray traced centres of curvature. Numerical results show there is a significant reduction in the number of degrees of freedom required for a given level of accuracy when using the ray traced augmented basis.

In Chapter 6 we extend the use of ray tracing techniques for enriching the UWVF basis to a domain where the wavespeed profile varies. This case is more relevant to the seismic community, as the sound speed profile of the subsurface of the Earth is one which varies with depth, usually in horizontal layers with seismic faults. For our numerical experiments we use the Marmousi model, a two-dimensional synthetic sound speed profile often used as a test case in the seismic industry [2, 54]. To the author's knowledge this is the first time the UWVF has been used to approximate wave propagation in a complicated domain of highly varying wavenumbers. Ray tracing techniques are widely used in the seismic community [2, 12, 22]. Two methods for ray tracing are presented: the first uses the Method of Characteristics to provide multiple ray paths of wavefronts based upon an initial starting trajectory; the second uses Fast Marching Methods (FMM) to find the direction of the ray path of the fastest propagating wavefront, at any point in the domain. Ray directions from the latter method are implemented into the UWVF basis, and compared with results of the standard equi-spaced plane wave basis. In this case numerical results suggest that alternative methods of

incorporating ray directions on the UWVF basis may prove more effective. With the FMM ray directions used in the UWVF basis, although there are some initial gains in accuracy by using the ray traced basis, these gains are lost as the number of degrees of freedom used increases and the solution converges to a steady state.

In Chapter 7 we consider another problem highly relevant to seismic imaging, that of wave propagation from a source on the interior of the domain. This set-up is commonplace in the seismic industry, as real world data collection often uses an explosive sound source positioned at a significant depth below ground level [28, 68]. To approximate a sound source on the interior domain requires solving the inhomogeneous form of the Helmholtz equation. Due to the Trefftz basis, the UWVF is not well disposed to solving the inhomogeneous Helmholtz equation (as explained in [16, §I.2.1.5]): we present example results demonstrating this for the case of wave propagation from an interior sound source in a domain of constant wavenumber. We then present an augmentation to the UWVF which we call the Source Extraction UWVF. In this new method we effectively remove the inhomogeneity of the equation, splitting the domain into a small region containing the source where only the back scattered field is approximated, and the remainder of the domain where the total field is approximated. The two fields are matched on the inter-region boundaries through the use of augmented impedance traces. Similar techniques have been used in [6, 29, 59]. Accurate results of the Source Extraction UWVF are presented for a domain of constant wavenumber. Results for differing discretisations and frequencies are presented for wave propagation in a section of a smoothed Marmousi velocity profile, which concur with those using a high order FD approximation. This work has been published seperately in [38].

Finally in Chapter 8 the findings of this thesis are summarised and conclusions drawn. Ideas for further work are also presented.

Chapter 2

Background

In this chapter we provide some background for the research of this thesis. In §2.1 we explain key concepts in acoustic wave propagation, such as the Helmholtz equation, boundary conditions, and scattering problems. Numerical techniques used in acoustic wave simulation are discussed in §2.2, including the MFS and ray tracing. Finally, in §2.3, we explain aspects of the use of acoustic wave propagation in seismic imaging, such as the forward and inverse problems, and real world data acquisition.

2.1 Acoustic Wave Scattering

Time harmonic wave propagation can take the form of acoustic, elastic, or electromagnetic waves. There are many applications in which they arise, providing areas for intensive research in mathematics, physics, and engineering. Here we focus on two dimensional (2D) time harmonic acoustic wave propagation, and its applications in seismic imaging. As well as seismic imaging however, there are many more applications of acoustic wave propagation, for example to communicate with or detect vessels using sonar, or medical imaging via ultrasound.

2.1.1 The Wave Equation and Helmholtz Equation.

Acoustic waves are small oscillations in pressure in an acoustic medium (a compressible ideal fluid), which interact in such a way that energy is transferred through the medium [45]. We consider the 2D spatial variable $\mathbf{x} = (x, y)$ and denote time by t. For acoustic waves, the velocity potential or pressure fluctuation $U = U(\mathbf{x}, t)$ satisfies the wave equation

$$\frac{1}{c^2}U_{tt} = \Delta U = \frac{\partial^2 U}{\partial x^2} + \frac{\partial^2 U}{\partial y^2}, \qquad \mathbf{x} \in \Omega,\ t > 0, \tag{2.1}$$

(in two dimensions), where the domain $\Omega \subset \mathbb{R}^2$, $\Delta = \nabla^2$ is the Laplacian, and c is the speed of sound. The time harmonic case assumes that all waves are steady state, and so the time variable can be separated from a stationary function of the space variable, resulting in the form

$$U(\mathbf{x}, t) = \mathrm{Re}\{\mathrm{e}^{-\mathrm{i}\omega t}u(\mathbf{x})\}.$$

Here i is the imaginary unit, $\omega = 2\pi f_r$ is the angular wave frequency, f_r is the frequency, and the complex valued u is the acoustic pressure. The parameter $\kappa = \omega/c$ is known as the wavenumber. It is the spatial frequency of the wave, and depends upon the wave frequency $\omega > 0$ and the speed of sound c. It follows that

$$\frac{\partial^2 U}{\partial t^2} = -\omega^2 \mathrm{Re}\{\mathrm{e}^{-\mathrm{i}\omega t}u(\mathbf{x})\} = -\kappa^2 c^2 \mathrm{Re}\{\mathrm{e}^{-\mathrm{i}\omega t}u(\mathbf{x})\}, \qquad \mathbf{x} \in \Omega,\ t > 0,$$

and substituting this into (2.1) we have

$$-\kappa^2 \mathrm{Re}\{\mathrm{e}^{-\mathrm{i}\omega t}u(\mathbf{x})\} = \mathrm{Re}\{\mathrm{e}^{-\mathrm{i}\omega t}\Delta u(\mathbf{x})\} \qquad \mathbf{x} \in \Omega,\ t > 0.$$

By rearranging, we see that u satisfies the Helmholtz equation

$$\Delta u + \kappa^2 u = 0 \qquad \mathbf{x} \in \Omega. \tag{2.2}$$

The simplest plane wave solutions of the Helmholtz equation, $\mathrm{e}^{\mathrm{i}\kappa \mathbf{x}\cdot\mathbf{d}}$, where $\mathbf{d}$ is a constant unit vector, are spatially periodic, the length of the period given by the wavelength

$$\lambda = \frac{2\pi}{\kappa}. \tag{2.3}$$

The Helmholtz equation is elliptic, and the use of Green's functions is particularly appropriate for solving this type of PDE [66]. The standard fundamental solution $\Phi(\mathbf{x}, \mathbf{y})$ of the Helmholtz equation is the solution that satisfies

$$\Delta u(\mathbf{x}) + \kappa^2 u(\mathbf{x}) = -\delta(\mathbf{x} - \mathbf{y}), \tag{2.4}$$

for $\mathbf{x} \in \Omega := \mathrm{R}^2$, where δ is the Dirac delta function, and $\mathbf{y} \in \Omega$ is the source point. The solution of (2.4) gives the acoustic pressure field from a time-harmonic point sound source in free space. In 2D the standard fundamental solution of the Helmholtz equation is the Green's function [18, Equation 1.2]

$$\Phi(\mathbf{x}, \mathbf{y}) = \frac{\mathrm{i}}{4} H_0^{(1)}(\kappa|\mathbf{x} - \mathbf{y}|), \tag{2.5}$$

where $H_0^{(1)}$ denotes the Hankel function of the first kind of order zero. In three dimensions (3D) it is given by (also [18, Equation 1.2])

$$\Phi(\mathbf{x}, \mathbf{y}) = \frac{\mathrm{e}^{\mathrm{i}\kappa|\mathbf{x}-\mathbf{y}|}}{4\pi|\mathbf{x} - \mathbf{y}|}. \tag{2.6}$$

In both the 2D and 3D case, $\Phi(\mathbf{x}, \mathbf{y})$ is singular at $\mathbf{x} = \mathbf{y}$, i.e. $|\Phi(\mathbf{x}, \mathbf{y})| \to \infty$ as $\mathbf{x} \to \mathbf{y}$, as explained for (2.5) by [3, Equation 9.1.8]. The behaviour of the singularity for the 2D case is given by

$$\Phi(\mathbf{x}, \mathbf{y}) \sim \frac{1}{2\pi} \ln|\mathbf{x} - \mathbf{y}| \qquad \text{as } |\mathbf{x} - \mathbf{y}| \to 0. \tag{2.7}$$

The Hankel function is also known as a Bessel function of the third kind, so called as it is a complex linear combination of Bessel's functions of the first kind $J_\nu(x)$, and second kind $Y_\nu(x)$, both of order ν, given by

$$H_\nu^{(1)}(x) = J_\nu(x) + \mathrm{i}Y_\nu(x).$$

Bessel functions are so called as they are linearly independent solutions of Bessel's equation

$$x^2 y'' + xy' + (x^2 - \nu^2)y = 0.$$

In free space ($\Omega = \mathbb{R}^n$, where $n = 2, 3$ is the dimension), the physical solutions we seek are outgoing, thus we require for our approximations that there are no wave

reflections at infinity. The Sommerfeld radiation condition [12, §6.4] is a far field condition which ensures waves are absorbed at infinity and not reflected back. It is derived through integration of the Helmholtz equation with the Green's function fundamental solution [45, §1.1.3]. The Sommerfeld radiation condition in 2D is that waves are absorbed at infinity provided

$$u = O(r^{-1/2}), \qquad \mathrm{i}\kappa u - \frac{\partial u}{\partial r} = o(r^{-1/2}), \qquad \text{as } r \to \infty. \tag{2.8}$$

The notation $f(\mathbf{x}) = O(g(\mathbf{x}))$ as $r \to \infty$, uniformly in $\hat{\mathbf{x}} = \mathbf{x}/r$, means that, for some $\hat{c} > 0$ and $R > 0$, $|f(\mathbf{x})/g(\mathbf{x})| \leq \hat{c}$ for $|\mathbf{x}| \geq R$, whilst $f(\mathbf{x}) = o(g(\mathbf{x}))$ means $f(\mathbf{x})/g(\mathbf{x}) \to 0$ uniformly in $\hat{\mathbf{x}}/|\mathbf{x}|$ as $r \to \infty$. The first equation in (2.8) characterises the decay of the solution, whilst the second ensures the direction of the far field behaviour is outgoing.

2.1.2 Acoustic wave scattering typical problem set-up.

There are many different problem set-ups often considered in the study of acoustic wave propagation. In this thesis we consider two types of problem:

1. the Helmholtz equation (2.2) with constant wavenumber holds in $\Omega = \mathbb{R}^2 \backslash \overline{\Omega^+}$, where Ω^+ is a bounded Lipschitz domain - this represents scattering by an obstacle in a homogeneous medium;

2. the Helmholtz equation with spatially varying wavenumber holds in $\Omega \subset \mathbb{R}^2$, i.e. (2.2) holds in Ω where $\kappa = \kappa(\mathbf{x})$ - this represents propogation and scattering in an inhomogeneous medium with varying wavespeed.

Problem 1 is known as a scattering problem, in which there are one or more obstacles on the interior of the domain, as per Figure 2.1. The field generated by a source is known as the incident field. An incident wave field propagating in Ω will interact with the boundary of the obstacle Γ_1, causing a scattered field to be produced. Thus the total wave field u can be expressed as the sum of the known incident field u^i, and the scattered field u^s produced:

$$u = u^i + u^s.$$

Both of u^i and u^s are separately solutions of the Helmholtz equation (2.2). Incident fields commonly used, for example, are a plane wave as shown in Figure 2.2, a circular wave propagating outwards from a point source as shown in Figure 2.3, or a linear combination of these wave types, such as a dipole source (two point sources positioned proportionally to the wavelength, that are of opposite phase).

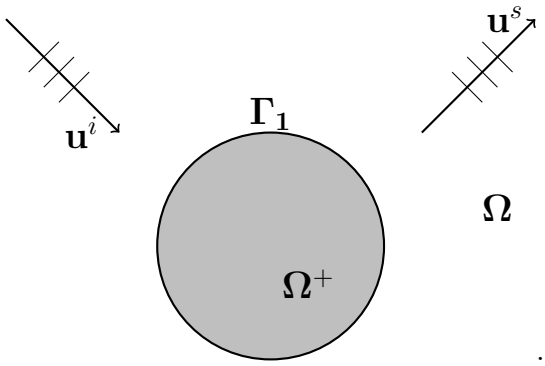

Figure 2.1: Total wave field $u = u^i + u^s$, where u^i is the incident wave and u^s is the scattered wave.

Problem 2 is known as an interior problem, in which we solve for the wave field propagating through the interior of a bounded domain $\Omega \subset \mathbb{R}^2$. The incident field is generated from an interior or exterior source. The scattered field is created by reflection and diffraction effects caused at the boundary, or by variations in the physical parameters of the medium, such as the density or sound speed.

When we take Ω as a bounded domain, boundary conditions are applied to match the physical set up required. Dirichlet boundary conditions, or the *boundary condition of the first kind* [12, §6.1], are those where data is provided on boundary Γ as a restriction of the solution u, referred to as being sound-soft in the case of acoustic scattering. Neumann boundary conditions, or the *boundary condition of the second kind*, are referred to as being sound-hard; here $\partial u/\partial n$ is specified on Γ, that is the rate of change of the solution in the direction normal to the boundary. Note that here and throughout, $\partial/\partial n$ denotes the outward normal derivative. The case of boundary data being provided as a linear combination $\partial u/\partial n - \alpha u$ for some $\alpha \in \mathrm{C}$ is known as mixed, impedance, or Robin boundary conditions. When the mixed condition is of the form $\partial u/\partial n - \mathrm{i}\kappa\hat{\beta}u =$

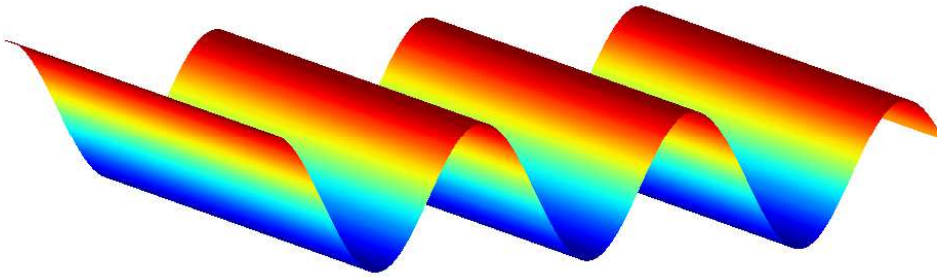

Figure 2.2: A plane wave

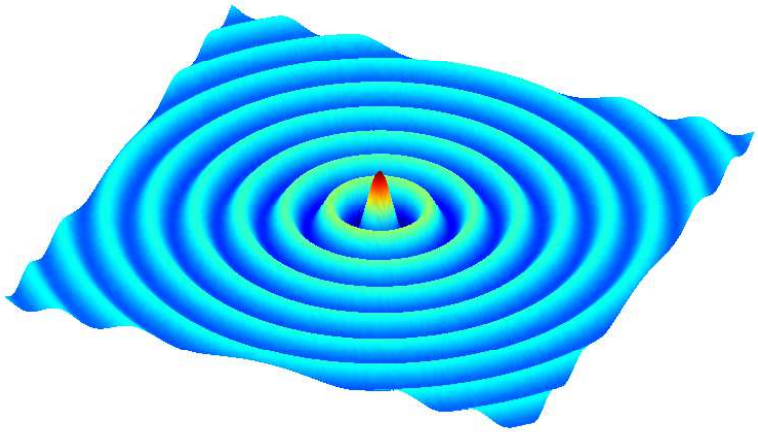

Figure 2.3: A Hankel circular wave from a point source

g, the function $\hat{\beta}$ is the relative surface admittance, which governs the level of flow permitted through the boundary [19]. The impedance boundary condition with $\hat{\beta} = 1$ is often used as a crude approximation to the Sommerfeld radiation condition, as it forces the wave field to be out-going in the normal direction.

For the case of scattering by an obstacle, the obstacle will cause the total reflection of waves that interact with it. In this case we can apply Dirichlet or Neumann boundary conditions on Γ_1. In the case of a concave obstacle or multiple scatterers, it is possible to get multiple reflections, and even trapped modes where the oscillations are confined to a region, and the wave energy dissipates only exponentially slowly. Alternatively, one could simulate an obstacle which is penetrable, allowing some wave energy to flow into and out of the obstacle. In this case we would solve the Helmholtz equation in $\Omega \cup \Omega^+$, and set transmission boundary conditions on Γ_1 to replicate the comparative properties of the two media [34].

2.1.3 Forward and inverse problem.

A major reason for the extensive interest in wave theory and simulation is due to imaging applications, where properties inside a domain that is not easily accessible can be discovered non-invasively [12]. These applications include medical imaging, such as x-ray and MRI, where details of bone fractures or tumors can be imaged without the need for surgery. Non-Destructive Testing is another wide ranging application in engineering, construction and aerospace, where wave scattering techniques are used to find cracks and faults in structures and engine parts. Wave based imaging techniques are widely used in the defence industry, including radar and sonar, where they can be used to identify unknown vessels or concealed weapons. Details of the use of acoustics in seismic imaging are given in §2.3.

For many applications there are two stages required in the imaging process: the solving of the direct or forward problem on multiple levels, and then solving the inverse problem. The direct scattering problem is that which aims to find the scattered field produced by the interaction of a known incident wavefield with structures in the

domain or variations in the medium, based upon knowledge of the differential equation governing the wave motion. The inverse scattering problem is that of trying to determine the nature of the object or domain of definition, based upon the behaviour of the scattered field. There exist inverse methods which do not require the forward problem to be solved, such as the sampling method [23] and the point source method [65]. However in situations where information is limited, for example if the wavefield is only available on the boundary of the domain, iterative techniques are more widely used. In this type of inverse method the forward problem would be solved several times for a given domain structure, either for different source types or positions, or over a range of frequencies. Through comparison of the actual received signals and travel times with those generated by the numerical simulations, the wave trajectories from the source can be reconstructed, and an image of the domain created based upon a structure that would cause the said trajectories.

2.2 Numerical Methods for Acoustic Wave Modelling

When solving acoustic wave propagation problems, it is impossible to find an analytical solution unless the geometry of the domain is particularly simple. Consequently, numerical schemes are required. The accurate simulation of acoustic wave propagation is an area that has been extensively studied, and in which many different methods have been proposed. When choosing the appropriate method to use, there are many factors to consider. These include: whether the discrete solution is unique or not; the level of accuracy of solutions required; the stability of the method; the rate of convergence of solutions; factors that might make a scheme particularly suited to the problem type; and the computational cost of producing the solutions, both in terms of time and storage.

The FEM is in numerical technique for approximating solutions to boundary value problems of PDEs, through the use of a variational formulation. The domain of approximation is discretised into a finite number of elements, in which solutions are approx-

imated by a linear combination of basis functions. When approximating solutions of time-harmonic equations, it can be beneficial to adopt a strategy of incorporating information of the equation into the scheme, in order to save on computational expense. To this end many different wave-based numerical methods have been proposed, which incorporate the wavenumber into the approximation space. Trefftz methods are so named after Erich Trefftz [64]. The title includes all finite element schemes in which the test and trial spaces are spanned by solutions of the governing equation, for example, a solution of the Helmholtz equation is approximated by a linear combination of basis functions which are also solutions of the Helmholtz equation. Knowledge of the oscillatory character of solutions and their intrinsic wavelengths are thus incorporated into the discretisation of the problem through the use of oscillatory basis functions. These type of methods include Plane Wave Discontinuous Galerkin (PWDG) methods [29,31], the UWVF [16, 17, 44], and the Discontinuous Enrichment Method (DEM) [69]. More extensive detail of the two former methods are given in Chapter 3. An alternative technique commonly used for incorporating the wavenumber into the numerical scheme is through the use of the modulated basis: oscillatory shape functions that are the product of local solutions of the equation and non-oscillatory functions, usually low-degree polynomials. This has been done both for FEM [11, 48] and Boundary Element Methods (BEM) [18, 34], usually using plane wave local solutions (although Bessel solutions have also been used in [48]). Polynomial modulated methods include the Partition of Unity FEM (PUFEM) and wave interpolation finite element schemes [47]. A comparison of these wave based methods with the UWVF can be found in [30, 39]. For further discussion of the pollution effect in FEM for approximating the Helmholtz equation, see [7].

High order FEM schemes, where the oscillatory behaviour is instead captured by polynomials of a high degree, have also proved to be highly effective [4, 56]. However, as the wave frequency increases, a higher number of degrees of freedom are required to obtain a given level of accuracy. When improving the approximation through the use of mesh refinement, known as $h-$version FEM, the approximation suffers from numerical dispersion, also known as the pollution effect: solutions show an accumulation

of phase error. A very fine mesh is required in order to overcome these pollution errors when approximating high frequency solutions, rendering $h-$version FEM too computationally expensive to implement in some cases [57]. By instead improving the solution through increased polynomial degree, pollution errors can be avoided, at the cost of the locality of the approximation. Similarly, $h-$version PWDG methods also suffer from the pollution effect [31], and so improving the solution through an increased number of wave basis functions is recommended [31, 36].

Another type of method where the oscillatory behaviour and wavelength of the solution is incorporated is the Method of Fundamental Solutions (MFS) [9]. The MFS is a collocation method, which approximates the Helmholtz solution by a linear combination of its fundamental solutions (2.5). More detail of this method is given in the following section §2.2.1. We then detail in §2.2.2 a very different type of method widely used in the study of acoustic wave propagation, not for finding an approximate solution, but for approximating the direction of wave propagation and travel time taken: that of ray tracing.

2.2.1 The Method of Fundamental Solutions

The MFS is a collocation method for solving Helmholtz boundary value problems, as detailed in [9]. In this section we detail this numerical method so that it can be used later in §4.2.3 to provide a comparison solution with which to compare our UWVF results. We solve the Helmholtz equation (2.2) where Ω is a bounded domain in $\mathbb{R}^2$, with boundary Γ, and the wave number $\kappa > 0$ is constant throughout (the medium is homogenous). On Γ, a source term $g \in L^2(\Gamma)$ is applied through boundary conditions, enforced as discussed below. The solution of (2.2) is approximated by $u^{(N)}$, a solution which takes the form of a linear combination of N fundamental solutions

$$u(\mathbf{x}) \approx u^{(N)}(\mathbf{x}) = \frac{\mathrm{i}}{4} \sum_{j=1}^{N} \alpha_j H_0^{(1)}(\kappa|\mathbf{x} - \mathbf{y}_j|) \qquad \mathbf{y}_j \in \mathbb{R}^2 \backslash \overline{\Omega}, \tag{2.9}$$

where α_j are amplitude coefficients to be found. The $\mathbf{y}_j$ are the source or charge points of the fundamental solutions: cylindrical waves propagate outwards from these points.

They are all chosen to lie outside of the domain, thus avoiding the singularity of the Hankel function at zero. They are commonly chosen to be equally spaced along a smooth curve: this allows the interpretation of the method as a discretisation of an external single layer representation of u [9]. Consider a closed curve Γ^E enclosing the closure of the domain of approximation $\overline{\Omega}$ such that Γ and Γ^E are distinct, $\text{dist}(\Gamma, \Gamma^E) > 0$, as illustrated in Figure 2.4. For a given density function $\tilde{g}(\mathbf{s}) = \sum_{j=1}^{N} \alpha_j \delta(\mathbf{s} - \mathbf{y}_j)$ with a point set $\{\mathbf{y}_j\} \subset \Gamma^E$, the MFS formulation (2.9) is equivalent to

$$u(\mathbf{x}) \approx u^{(N)}(\mathbf{x}) = \frac{\mathrm{i}}{4} \int_{\Gamma^E} \tilde{g}(\mathbf{s}) H_0^{(1)}(\kappa|\mathbf{x} - \mathbf{s}|) d\mathbf{s}, \qquad \mathbf{x} \in \Omega. \tag{2.10}$$

The MFS is different from BEM (see [18,19]), which also use single and double layer representations, in that the boundary of the domain and the curve of sources are distinct, avoiding singularities of the kernel and allowing ease and accuracy of evaluation.

A linear system $A\alpha = \mathbf{g}$ is created by forcing (2.9) to hold at $M \geq N$ collocation points $\mathbf{x}_m$, $m = 1, \ldots, M$ on the boundary Γ. Using a standard matrix solver, this system is then solved to find the vector α of coefficients α_j. For numerical results in this thesis we use an appropriate solver as chosen by Matlab's backslash operator. For the case that $M = N$ (A is square), the backslash operator uses Gaussian elimination with partial pivoting to find the solution α to $A\alpha = \mathbf{g}$. If $M > N$, the system is overdetermined, and so the backslash operator finds the least squares solution which minimises $||A\alpha - \mathbf{g}||_2^2$. The coefficients in α can then be used in (2.9) to approximate the solution over the whole domain.

For example, if we wish to solve (2.2) with the Dirichlet boundary condition

$$u = g \qquad \text{on } \Gamma, \tag{2.11}$$

assuming a form (2.9) and forcing (2.11) to hold at the collocation points on $\partial\Omega$ results in entries of matrix A being given by

$$A_{m,j} = \frac{\mathrm{i}}{4} H_0^{(1)}(\kappa|\mathbf{x}_m - \mathbf{y}_j|). \tag{2.12}$$

If instead we had the mixed boundary condition given by

$$\frac{\partial u}{\partial n} - \mathrm{i}\kappa u = g \qquad \text{on } \Gamma, \tag{2.13}$$

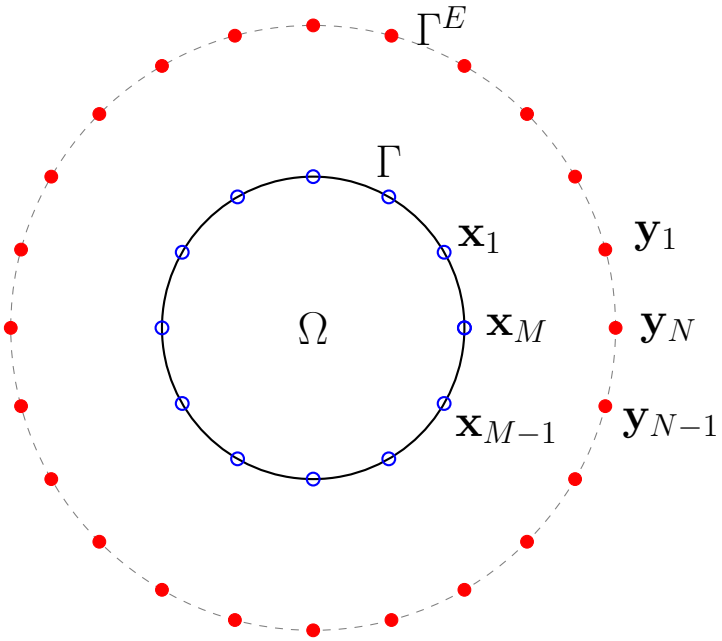

Figure 2.4: The MFS set-up for wave propagation in a unit circle. The source points are represented by red dots, and the collocation points are represented by blue circles.

the matrix A would have entries

$$A_{m,j} = \frac{\kappa}{4}\left(H_0^{(1)}(\kappa|\mathbf{x}_m - \mathbf{y}_j|) - \mathrm{i}\mathbf{n}_m \cdot \frac{\mathbf{x}_m - \mathbf{y}_j}{|\mathbf{x}_m - \mathbf{y}_j|} H_1^1(\kappa|\mathbf{x}_m - \mathbf{y}_j|)\right). \tag{2.14}$$

In this equation $\mathbf{n}_m$ represents the outward normal vector at $\mathbf{x}_m$.

As explained in [9], for the interior Dirichlet problem, the boundary error norm

$$\left\|u^{(N)} - g\right\|_{L^2(\Gamma)} \tag{2.15}$$

controls the error on the interior as

$$\left\|u^{(N)} - u\right\|_{L^2(\Omega)} \leq \frac{C_\Omega}{d}\left\|u^{(N)} - g\right\|_{L^2(\Gamma)}. \tag{2.16}$$

Here $d := \min_j[|\kappa^2 - E_j|/E_j]$, with $E_j > 0$ the domain's Dirichlet eigenvalues (the values of κ^2 for which there exists a non-zero solution of (2.2) satisfying the homogeneous Dirichlet condition $u = 0$ on Γ), and C_Ω is a domain dependant constant. This means that we may use the boundary norm as a bound on the L^2 error on the interior for any fixed non-resonant κ.

2.2.2 Ray Tracing

Ray methods provide a natural combination of mathematical and physical insights into wave propagation. They originate from the basic concepts in geometric optics, and have been extended to other wave phenomena, including acoustic, elastic and electromagnetic wave propagation [12]. Ray methods provide a high frequency asymptotic approximation to the direction of propagation of expanding wave fronts and the travel time taken. Although the formal derivation and rigorous analysis hold for $\kappa \to \infty$, this is by no means the limit to which the method has been demonstrated to be valid. Indeed, the high frequency approximations remain valid even in mid-range frequencies.

Ray tracing techniques use the ansatz that the wave behaves locally as a plane wave [5, 14],

$$u(\mathbf{x}) = A(x)\exp(\mathrm{i}\psi(\mathbf{x})), \qquad \mathbf{x} \in \Omega, \tag{2.17}$$

where $A(\mathbf{x}) \geq 0$ is the amplitude of the wave at the point $\mathbf{x} = (x, y)$, and $\psi(\mathbf{x}) \in \mathbb{R}$ is the phase. The rays are in the direction $\nabla\psi$, travelling perpendicular to the wavefronts (lines of constant phase). A ray model gives good understanding of the direction in which the waves are travelling at high frequencies, due to the high frequency asympotic derivation of the ray tracing equations, as will be explained below. Rays that travel through a medium of varying wavespeed are often turning. This is due to Snell's Law (or the law of refraction): at an interface of two media the ratio of the sines of the angle of incidence θ_i and angle of refraction θ_t when measured from the normal is equal to the ratio of the phase velocities of each of the media [32]. For piecewise smooth media, with velocity c_1 in the initial medium and c_2 in the second medium, Snell's Law states that

$$\frac{\sin(\theta_i)}{\sin(\theta_t)} = \frac{c_1}{c_2}. \tag{2.18}$$

To many in the geophysics industry, ray theory is considered the cornerstone of high frequency wave seismology [22]. It is a vital aid for the description and interpretation of seismic signals in the realistically complex media of the subsurface of the Earth. Asymptotic ray theory for an acoustic medium can be separated into three main strands: kinematic ray theory, dynamic ray theory, and polarisation theory. Kinematic ray

theory gives a description of the geometry and the travel times of rays and wave fronts. Dynamical ray theory describes the geometric spreading of rays and the magnitude of displacement. Finally polarisation theory describes the direction of displacement. Here we concentrate on kinematic ray theory.

The key aspect in acoustic kinematic ray theory is the solving of the acoustic Eikonal equation

$$(\nabla\tau)^2 = \frac{1}{c^2} \tag{2.19}$$

where τ is known as the Eikonal, and $\frac{1}{c}$ is the slowness, determined by the local wavespeed c. As detailed in [5, 12, 22], the acoustic Eikonal equation derives from applying the ray ansatz (2.17) to equations of acoustic wave motion and constitutive relations for an acoustic medium. The ray ansatz assumes that the solution behaves locally as a plane wave, and so the velocity and pressure can be represented as a sum of multiple plane wave ray paths, known as the ray expansion. The path of each ray is itself a function of the source, the receiver, and other parameters along the ray such as reflections and transmissions history. This allows the representation of the solution as a function of frequency-dependent phase factors and frequency-independent travel times combined with a frequency-independent series of amplitude coefficients. After the ray ansatz is applied, coefficients of each power of the angular frequency ω are set to zero [12,22], which must hold for the equations to be true for arbitrary frequencies. By taking the first non-zero terms of the expansion we obtain the Eikonal equation (2.19). For more details on the derivation see [22].

For the isotropic acoustic wave equation, rays travel orthogonal to wave fronts. The wave front surfaces are given by the Eikonal $\tau(\mathbf{x}) = t$ at time t: the different times correspond to the different wave fronts as a wave travels through a medium [14]. The slowness vector $\mathbf{s}$ is equivalent to the travel time gradient, with a magnitude equal to the reciprocal of the velocity, $|\mathbf{s}| = \frac{1}{c}$. It is perpendicular to the wave front, thus rays travel in the direction of the slowness vector $\mathbf{s}$ [12]. As they travel orthogonal to the wavefronts we have

$$\mathbf{s}(\mathbf{x}) = \nabla\tau(\mathbf{x}) \tag{2.20}$$

[14, Equation (2.25)]. Thus we can write the Eikonal equation as

$$\|\mathbf{s}(\mathbf{x})\|_2^2 = \frac{1}{c(\mathbf{x})^2}. \tag{2.21}$$

This represents a non-linear constraint for the slowness vector $\mathbf{s}$, where $c(\mathbf{x})$ is the sound speed at the point $\mathbf{x}$. By solving (2.20) for the Eikonal τ we calculate first arrival travel times along the geometric trajectories.

As explained in [14], there are several different approaches to solving the Eikonal equation. In Chapter 6 we detail two of these methods. The first is that of using the method of characteristics to solve the Eikonal equation in the form of a Hamilton-Jacobi system of equations. This technique provides multi-travel timed ray paths for ray trajectories in chosen directions from a point source. The second approach, the Fast Marching Method, is a grid based direct solver which provides for any point in the domain the direction of the fastest propagating wavefront.

2.3 Seismic Imaging

Geophysical exploration for oil and other minerals is a major world wide industry. Investment in drilling operations may cost millions of dollars per well, and so extensive research is done beforehand into the viability of potential drilling sites [68]. Seismic imaging to determine the interior structure of the Earth is one type of method widely used in these initial investigations, in the search for economically useful deposits. In seismology there are two directions in which this is done: the forward problem and the inverse problem. The former is that of computing seismic wave properties such as wave forms and travel times for a given model of the Earth's sub-structure and given seismic source. The inverse problem is that of comparing this computed data with the real data collected by physical experiments, in order to deduce the actual sub-structure. In reality seismic waves are elastic, however due to their complex nature more often in practice acoustic wave propagation is simulated instead. This can often provide sufficient insight necessary for exploration applications.

For foward modelling, there are many different methods used in the seismic industry.

Wave fields may be modelled in 2 or 3 spatial dimensions as well as in time, on large domains of highly complex media. Thus it is preferable to use numerical methods which minimise computational expense both in terms of memory and processing requirements, and are parallelisable. Explict FD methods are popular in the seismic industry due to the speed at which the solution can be evaluated: many FD methods can be solved more quickly than the linear system of equations resultant from FEM discretisations for a given number of degrees of freedom [26]. However there are also various FEMs used by the seismic modelling community. Although they may be less efficient than FD discretisations, there are advantages in that the discretisation of the domain can be specially designed to replicate the surface topography and the discontinuities in the velocity profile that arise due to the layered structure of the subsurface of the Earth. High order polynomial basis functions can well represent the oscillatory nature of the solution, and so high levels of accuracy can be achieved. The spectral-element method (SEM) is one type of FEM used for seismic imaging, particularly for complex geometries such as boreholes and fractures. It uses polynomials of a high degree in the approximation space, where a low sampling ratio of $4-5$ nodes per wavelength in an eighth order method has been demonstrated to achieve high accuracy [26]. Also widely used are various forms of DG methods. These are well suited to seismic applications, as the discontinuities of the basis functions on element interfaces are suited to discontinities in the velocity profile and other model parameters. Both types of method mentioned here have been used for the simulation of both acoustic and elastic wave propagation [26].

In order to distinguish the physical qualities of the actual substructure of the Earth, the forward modelling solution must be considered with the inverse problem: does the wave signal pattern received at the surface in physical experiments match those predicted by the numerical model? Full waveform inversion (FWI) is one method of inversion, an iterative method where by readjusting various parameters of a model a good level of agreement between the predictive model and the real data can be achieved [70]. This is done in the form of an iterative optimisation problem. The forward modelling of the waveform is performed on an initial starting model, usually

for several sources of a single frequency or frequency group. The starting model may be highly inaccurate, as there may be limited information about the substructure available, either from the real data set or geological knowledge of the region. If there is extra information available however, with this method there is the ability to incorporate a large amount of the geological qualities of the domain. The discretisation of the wave equation results in a linear system of equations which is solved iteratively, each iteration providing an update to the velocity profile which will converge to that of the real data [70]. As the forward modelling process must be repeated for each iteration of the inversion process, it is favourable to use a forward modelling technique that can provide accurate solutions with minimal memory and processing requirements.

There are various other types of inversion process that have been developed for seismics, such as travel time inversion and reflection seismology [12]. In travel time inversion, details of the the domain's background velocity profile is deduced by consideration of the arrival times of a wave packet as a function of the distance between the seismic source and the signal receiver [5]. In the case of reflection seismograms, the seismic velocity profile of the domain is not recovered, but instead the impedance, the product of the velocity and density. This is recovered by considering the echoes received after an impulsive seismic wave is sent downward and reflects off layers in the Earth's interior. These inverse techniques can be a more useful alternative in the case that the direct modelling technique is highly complicated, or there is a large amount of high resolution real data available for the seismic domain.

On the practical side of seismic imaging is the acquisition of real seismic data. A seismic source, or 'shot', is set off either on ground level or down a seismic well, and sent as a wave signal through the sub-surface below. This wave signal interacts with the sub-surface structures, and is reflected, refracted, or scattered back to the surface, where an array of receivers picks up the signal [28]. There are various techniques available for the data acquisition in a seismic survey, dependent upon the amount of data required and the region to be imaged. For land-based data acquisition, the source may be generated by either explosives or vibrators. For explosive sources, a series of shot holes

up to 100 metres deep are drilled, the explosive charges are buried inside, and then detonated by electronic detonators [28]. For vibrator sources (Vibroseis), a specially designed large truck equipped with hydraulic pumps or electromagnetic vibrators can produce an extended signal at a range of frequencies. The signals will then be received by an array of seismometers (detectors) called geophones, which are highly sensitive to seismic motion. This set up is illustrated in Figure 2.5. In sea-based data acquisition, data production may be much higher as a ship can be used to gather data up to 24 hours a day (there are fewer legal restrictions to noise levels at sea). Marine sources are either in the form of explosives or air guns, where pulses of compressed air are released behind the ship. A floating cable of hydrophones (water-based seismometers) trails behind the ship, recording the reflected arrivals, as illustrated in Figure 2.6. In all inversion techniques, there is also the inaccuracy of the geophysical data to bear in mind. In the acquisition of data there may be both measurement error and noise, as well as incompleteness in the data set. Before data can be reliably used, it may need to be corrected for any variation in the positioning of receivers, and processed to remove noise and distortions produced by the instruments [28].

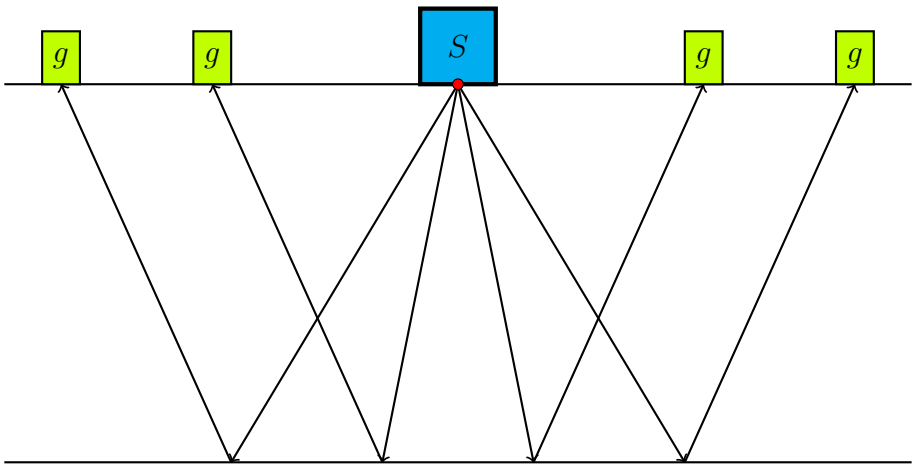

Figure 2.5: Seismic data acquisition on land. A shot is fired at the source S, producing sound waves. These propagate in the direction of the ray paths, reflecting off lower layers. The reflected arrivals are recorded by an array of geophones g.

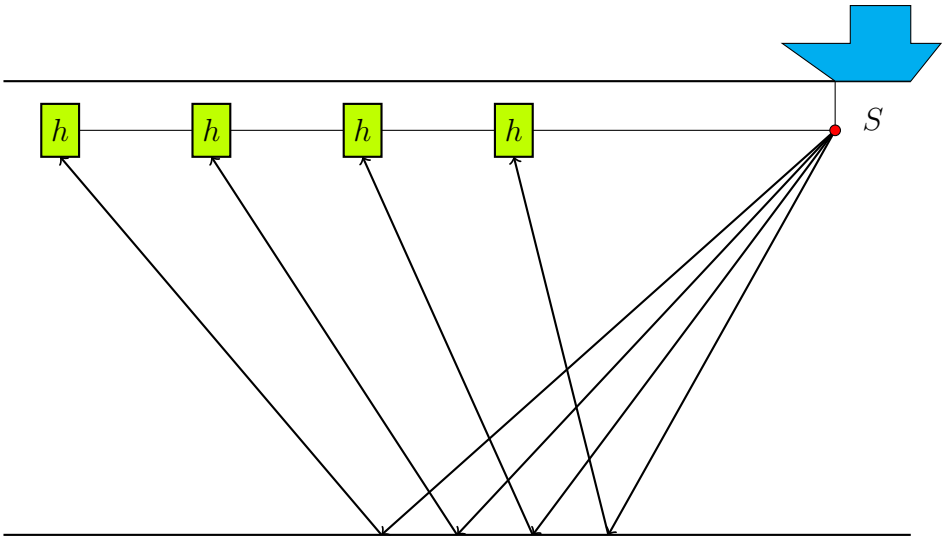

Figure 2.6: Seismic data acquisition at sea. A shot S is fired from the ship, producing sound waves. These propagate in the direction of the ray paths, reflecting off the sea bed and lower layers. The reflected arrivals are recorded by a cable of hydrophones h.

Chapter 3

The Ultra-Weak Variational Formulation

In this chapter we introduce a powerful numerical method for the approximation of accousic wave propagation, the Ultra-Weak Variational Formulation (UWVF). Key to this method is the use of solutions of the homogeneous form of the equation to be solved in the approximation space. In §3.1 we give details of the background of the UWVF, the Helmholtz problem to be solved, the approximation space and the formulation. In §3.2 we present the derivation of the UWVF, in its original variational framework. We then follow in §3.3 with an equivalent derivation in a Plane Wave Discontinuous Galerkin (PWDG) framework. To the author's knowledge this is the first time that the UWVF for the inhomogenoeous Helmholtz problem with non-constant wavenumber κ and density ρ has been derived in the PWDG setting. Due to the equivalence with PWDG, much progress has been made on the convergence analysis of the UWVF; key results are presented in §3.4. Computational aspects are discussed in §3.5, including the linear system of equations that arise in the discretisation of the UWVF, as well as issues relating to the conditioning of the system. A new Hankel basis for the UWVF is introduced in §3.6, and a comparison study of the conditioning of the linear system with the original plane wave and the Hankel basis is presented in §3.7.

3.1 The Ultra-Weak Variational Formulation

The UWVF was originally proposed in the mid 1990s by Cessenat and Després, in [16, 17]. It is a new generation FEM which has been used for the accurate simulation of acoustic waves in 2D [16, 17, 27, 44] and 3D [41], as well as elastic [40, 51] and electromagnetic [16, 24, 25, 42] waves. Applications have included wave propagation, transmission, and scattering [40, 41, 53], road traffic noise simulation [27], and radiation in optoelectronic devices [50]. Here we restrict our attention to time harmonic acoustic wave propagation, modelled in 2D by the following Helmholtz boundary value problem (BVP):

$$\nabla \cdot \left(\frac{1}{\rho}\nabla u\right) + \frac{\kappa^2}{\rho}u = f \qquad \text{in } \Omega, \tag{3.1a}$$

$$\left(\frac{1}{\rho}\frac{\partial u}{\partial n} - \mathrm{i}\sigma u\right) = Q\left(-\frac{1}{\rho}\frac{\partial u}{\partial n} - \mathrm{i}\sigma u\right) + g \qquad \text{on } \Gamma. \tag{3.1b}$$

Here $\Omega \subset \mathbb{R}^2$ is a bounded domain with Lipschitz boundary Γ. The wavenumber $\kappa = \kappa(\mathbf{x})$ is complex with $\mathrm{Im}(\kappa) \geq 0$ and $\mathrm{Re}(\kappa) > 0$. The density $\rho = \rho(\mathbf{x})$ and impedance parameter σ are real and positive; and $f \in L^2(\Omega)$ and $g \in L^2(\Gamma)$ are the volume and boundary source terms respectively. The parameter Q is complex with $|Q| \leq 1$. The choice of Q is important as it gives the type of boundary condition. Taking $Q = -1$ gives the Dirichlet boundary condition,

$$u = \frac{g\mathrm{i}}{2\sigma};$$

taking $Q = 1$ gives the Neumann boundary condition

$$\frac{\partial u}{\partial n} = \frac{\rho g}{2};$$

taking $Q = 0$ gives the impedance boundary condition

$$\frac{1}{\rho}\frac{\partial u}{\partial n} - \mathrm{i}\sigma u = g.$$

The UWVF is a Trefftz-type method: the exact solution of a Helmholtz boundary value problem is approximated by a linear combination of basis functions which, inside each mesh element, are solutions of the homogeneous Helmholtz equation, i.e. equation

(3.1a) with right-hand side $f = 0$. As with standard FEM, the domain Ω is partitioned into a polygonal mesh; however the solution variables are impedance traces on the skeleton of the mesh. These traces are approximated by the corresponding traces of a Trefftz trial space; the approximation is automatically achieved also in the element interiors if the discretised BVP is homogeneous ($f = 0$), see [15, Theorem 4.1], [37, Theorem 4.5]. In [15,31,36] the UWVF has been derived in a DG framework, allowing a more general derivation of the formulation (see e.g. [36, §3.2]), extensive analysis of the method, and the derivation of error estimates. By incorporating the known wavelike behaviour of the solution into the approximation space, the UWVF can produce accurate results requiring significantly fewer degrees of freedom than standard FEMs, in some cases for mesh sizes encompassing several wavelengths λ. This is because the wavelike behaviour is captured directly by the oscillatory basis functions, rather than by high degree piecewise polynomials as in standard FEM. The solution of the Helmholtz equation is often approximated using a plane wave basis [15–17,31,36], however it is also possible to use other solutions of the homogeneous Helmholtz equation, such as a Bessel function basis as used in [52].

We introduce in this section the classic UWVF for the inhomogeneous Helmholtz BVP (3.1), which is slightly more general than that considered in [17] in the fact that varying coefficients are allowed (compare also with [44]). We will mainly follow the notation of [44]. Note that complex wavenumbers κ (i.e. absorbing media) can be considered as in [15, §5].

We partition Ω into a mesh $\mathcal{T} = \{\Omega_k\}_{k=1}^K$ composed of triangular elements Ω_k, in which we find local solutions $u_k \approx u|_{\Omega_k}$. The boundary of each element is denoted by $\partial\Omega_k$. The interelement edge between elements Ω_k and Ω_j, is denoted by $\Sigma_{k,j} = \partial\Omega_k \cap \partial\Omega_j$. Any exterior edges are denoted by $\Gamma_k = \partial\Omega_k \cap \Gamma$. The outward pointing unit normal vector on $\partial\Omega_k$ is denoted $\mathbf{n}_k$. We denote the outward normal derivative from element Ω_k by $\frac{\partial}{\partial n_k}$. This set-up is illustrated in Figure 3.1. For all numerical results in this thesis, the triangulated mesh is provided by Distmesh, a mesh generator in Matlab written by P-O. Persson and G. Strang [61,62]. Inputs required for the mesh

generator are function handles detailing the structure of the domain to be meshed and the refinement levels required. Outputs provided by the mesh generator are two vectors: the first containing the node numbers of the vertices of each element, and the second containing the node positionings in Cartesian co-ordinates.

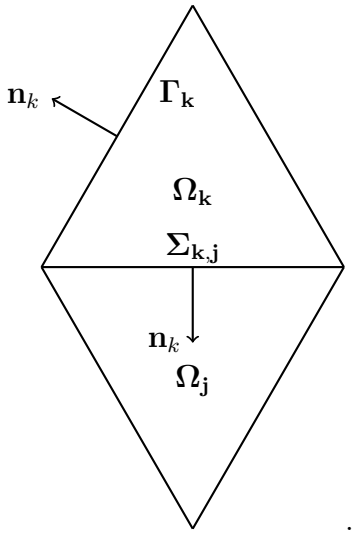

Figure 3.1: Element structure: the edge between elements Ω_k and Ω_j, is denoted by $\Sigma_{k,j}$, exterior edges are denoted by Γ_k, and all normals are exterior.

The method uses a variational formulation that ensures that the solution is weakly continuous across the boundaries of elements. The wavenumber and density are taken to be constant inside each element, so piecewise constant in Ω, with $\kappa_k = \kappa|_{\Omega_k}$ and $\rho_k = \rho|_{\Omega_k}$. The impedance parameter σ is defined as

$$\sigma = \frac{1}{2}\left(\frac{\mathrm{Re}(\kappa_k)}{\rho_k} + \frac{\mathrm{Re}(\kappa_j)}{\rho_j}\right), \qquad \text{on } \Sigma_{k,j} \tag{3.2}$$

and as

$$\sigma = \frac{\mathrm{Re}(\kappa_k)}{\rho_k}, \qquad \text{on } \Gamma_k. \tag{3.3}$$

We introduce the Trefftz space $H := \prod_{k=1}^{K} H_k$, with

$$H_k := \left\{ v_k \in H^1(\Omega_k) \middle| -\nabla\cdot\left(\frac{1}{\rho_k}\nabla v_k\right) - \frac{\kappa_k^2}{\rho_k} v_k = 0 \text{ in } \Omega_k,\ \frac{\partial v_k}{\partial n_k} \in L^2(\partial\Omega_k) \right\}, \tag{3.4}$$

and we represent any $v \in H$ as a vector $\{v_k\}_{k=1}^{K}$ with $v_k := v|_{\Omega_k}$. To avoid technical difficulties with the regularity of f and the solution u of the BVP (3.1), as in [16, Section

I.5.1] we start by assuming that u belongs to

$$\widetilde{H} := \prod_{k=1}^{K} \widetilde{H}_k \qquad \text{with} \qquad \widetilde{H}_k := \left\{ v_k \in H^1(\Omega_k), \frac{\partial v_k}{\partial n_k} \in L^2(\partial\Omega_k) \right\}.$$

If ρ is constant and $f \in L^2(\Omega)$, this is always guaranteed [38]. For piecewise constant ρ, $H^1(\Omega)$ regularity of u was discussed in [10]. However the L^2 regularity of the normal derivatives on the element boundaries is not entirely clear.

We define the sesquilinear forms $d, c : \widetilde{H} \times \widetilde{H} \to \mathbb{C}$ as

$$\begin{aligned} d(v,w) :=& \sum_{k=1}^{K} \int_{\partial\Omega_k} \frac{1}{\sigma} \left(-\frac{1}{\rho_k} \frac{\partial}{\partial n_k} - \mathrm{i}\sigma \right) v_k \overline{\left(-\frac{1}{\rho_k} \frac{\partial}{\partial n_k} - \mathrm{i}\sigma \right) w_k} \, \mathrm{d}S, \\ c(v,w) :=& \sum_{\substack{k,j=1 \\ k \neq j}}^{K} \int_{\Sigma_{k,j}} \frac{1}{\sigma} \left(-\frac{1}{\rho_j} \frac{\partial}{\partial n_j} - \mathrm{i}\sigma \right) v_j \overline{\left(\frac{1}{\rho_k} \frac{\partial}{\partial n_k} - \mathrm{i}\sigma \right) w_k} \, \mathrm{d}S \\ &+ \sum_{k=1}^{K} \int_{\Gamma_k} \frac{Q}{\sigma} \left(-\frac{1}{\rho_k} \frac{\partial}{\partial n_k} - \mathrm{i}\sigma \right) v_k \overline{\left(\frac{1}{\rho_k} \frac{\partial}{\partial n_k} - \mathrm{i}\sigma \right) w_k} \, \mathrm{d}S. \end{aligned} \tag{3.5}$$

We define the antilinear functional $\beta : \widetilde{H} \to \mathbb{C}$ as

$$\beta(w) := -2\mathrm{i} \sum_{k=1}^{K} \int_{\Omega_k} f \overline{w_k} \, \mathrm{d}V + \sum_{k=1}^{K} \int_{\Gamma_k} \frac{g}{\sigma} \overline{\left(\frac{1}{\rho_k} \frac{\partial}{\partial n_k} - \mathrm{i}\sigma \right) w_k} \, \mathrm{d}S. \tag{3.6}$$

In [17, Theorem 1.3] it is proved that, if $|Q| < 1$ (to ensure well-posedness), ρ and κ are constant, $f \in L^2(\Omega)$ and $g \in L^2(\Gamma)$, then the solution $u \in \widetilde{H}$ of the BVP (3.1a) satisfies the variational problem

$$d(u,v) - c(u,v) = \beta(v) \tag{3.7}$$

for all $v \in H$. The same proof (see also [44, Equation (10)]) holds true also for discontinuous coefficients (recall that we assumed $u \in \widetilde{H}$).

Define $\chi \in V := \prod_{k=1}^{K} L^2(\partial\Omega_k)$ as

$$\chi|_{\partial\Omega_k} = \chi_k = \left(-\frac{1}{\rho_k} \frac{\partial u_k}{\partial n_k} - \mathrm{i}\sigma u_k \right) |_{\partial\Omega_k} \qquad 1 \leq k \leq K. \tag{3.8}$$

In order to find the solution u of (3.1a) with (3.1b) using the UWVF, we must find the

union of the unique solutions $u_k \in \widetilde{H}(\Omega_k)$, $k = 1, \ldots, K$, that exist if χ is a solution of

$$\begin{aligned}
&\sum_k \int_{\partial\Omega_k} \frac{1}{\sigma}\chi_k \overline{(-\frac{1}{\rho_k}\frac{\partial\phi_k}{\partial n_k} - \mathrm{i}\sigma\phi_k)}\,\mathrm{d}S \\
&- \sum_k \sum_j \int_{\Sigma_{k,j}} \frac{1}{\sigma}\chi_j \overline{(\frac{1}{\rho_k}\frac{\partial\phi_k}{\partial n_k} - \mathrm{i}\sigma\phi_k)}\,\mathrm{d}S + \sum_k \int_{\Gamma_k} \frac{Q}{\sigma}\chi_k \overline{(\frac{1}{\rho_k}\frac{\partial\phi_k}{\partial n_k} - \mathrm{i}\sigma\phi_k)}\,\mathrm{d}S \\
&= -2\mathrm{i}\sum_k \int_{\Omega_k} f\overline{\phi_k}\,\mathrm{d}V + \sum_k \int_{\Gamma_k} \frac{g}{\sigma}\overline{(\frac{1}{\rho_k}\frac{\partial\phi_k}{\partial n_k} - \mathrm{i}\sigma\phi_k)}\,\mathrm{d}S. \qquad (3.9)
\end{aligned}$$

We explain in §3.2 how the UWVF (3.9) is derived. We require that equation (3.9) must hold for any $\phi^* \in H$, $\phi^* = (\phi_k)_{k=1,\ldots,K}$. The test space of basis functions is spanned by Trefftz functions ϕ_k, with $\mathrm{supp}(\phi_k) = \Omega_k$, that satisfy the homogeneous form of the Helmholtz equation

$$\nabla^2\phi_k + \kappa_k^2\phi_k = 0 \qquad \text{in } \Omega_k. \qquad (3.10)$$

The UWVF discretisation consists of considering the variational problem (3.9) in the discrete space $H_h = \prod_{k=1}^K \mathrm{span}\{\phi_{k,l}\}_{l=1}^{p_k} \subset H$ defined by the basis functions $\phi_{k,l} \in H_k$, $1 \le k \le K$, $1 \le l \le p_k$, of which we give specific examples below. Basis functions ϕ_k are those which have support in Ω_k; we denote by p_k the number of basis functions that have support in element Ω_k. As there can be between one and p_k basis functions per element, these are then indexed by l, so that $\phi_{k,l}$ is the l-th basis function on element Ω_k.

The solution in each element is approximated by a linear combination of basis functions that holds on the respective element,

$$u_k = \sum_{l=1}^{p_k} \chi_{k,l}\phi_{k,l} \qquad k = 1, \ldots, K. \qquad (3.11)$$

We then approximate χ_k, as defined in (3.8), by

$$\chi_k \approx \chi_k^a = \sum_{l=1}^{p_k} \chi_{k,l}\left(-\frac{1}{\rho_k}\frac{\partial}{\partial n_k} - \mathrm{i}\sigma\right)\phi_{k,l} \qquad k = 1, \ldots, K \qquad (3.12)$$

where $\chi_{k,l}$ are the unknown amplitude coefficients to be determined. Once these amplitude coefficients are found, they can be used in (3.11) to approximate the solution in each element, and thus in the entire domain.

Much current literature uses a plane wave basis on each element, in p_k equally spaced directions, but with the number of directions used varying over the different elements. A plane wave basis allows the integrals that arise in the UWVF to be evaluated in closed form. The plane wave basis functions are defined as

$$\phi_{k,l}(x) = \begin{cases} \exp(\mathrm{i}\kappa_k \mathbf{d}_{k,l} \cdot \mathbf{x}) & \text{in } \Omega_k \\ 0 & \text{elsewhere,} \end{cases} \tag{3.13}$$

with κ the wavenumber to be taken as piecewise constant, with $\kappa_k \equiv \kappa|_{\Omega_k}$, and

$$\mathbf{d}_{k,l} = \left(\cos\left(2\pi \frac{(l-1)}{p_k} \right), \sin\left(2\pi \frac{(l-1)}{p_k} \right) \right), \qquad l = 1, ..., p_k. \tag{3.14}$$

There are a variety of alternative options for the basis $\phi_{k,l}$, for example a Bessel or Hankel basis set may also be used. The key requirement in the choice of basis functions is that they must also be solutions of the homogeneous Helmholtz equation (recall (3.10)). This ensures the cancellation of many domain integrals in the UWVF, leaving integrals over the element boundaries only in case of solving the homogeneous form of the Helmholtz equation.

3.2 Derivation of the UWVF: Variational Framework

We now explain the derivation of the UWVF, in the variational setting in which it was originally proposed. As shown in [16,17,44], the UWVF is derived by multiplying (3.1a) by a test function ϕ in each element, and applying the Divergence Theorem twice to find the (ultra) weak form of (3.1a). In standard FEM the Divergence Theorem is applied once to obtain the weak form of the equation; by applying the Divergence Theorem a second time we obtain a very, i.e., ultra weak form. Transmission conditions are applied to match the solutions and its normal derivative on the interelement boundaries, followed by the application of boundary conditions.

The derivation of the UWVF is as follows. As per [16, 17, 53], we can write the

identity

$$\int_{\partial\Omega_k} \frac{1}{\sigma}(-\frac{1}{\rho_k}\frac{\partial}{\partial n_k} - \mathrm{i}\sigma)u_k\overline{(-\frac{1}{\rho_k}\frac{\partial\phi_k}{\partial n_k} - \mathrm{i}\sigma\phi_k)}\,\mathrm{d}S - \int_{\partial\Omega_k} \frac{1}{\sigma}(\frac{1}{\rho_k}\frac{\partial}{\partial n_k} - \mathrm{i}\sigma)u_k\overline{(\frac{1}{\rho_k}\frac{\partial\phi_k}{\partial n_k} - \mathrm{i}\sigma\phi_k)}\,\mathrm{d}S = \int_{\partial\Omega_k} \frac{2\mathrm{i}}{\rho_k}(u_k\overline{\frac{\partial\phi_k}{\partial n_k}} - \frac{\partial u_k}{\partial n_k}\overline{\phi_k})\,\mathrm{d}S. \tag{3.15}$$

We wish to solve equation (3.1a) in each element,

$$\nabla\cdot\left(\frac{1}{\rho_k}\nabla u_k\right) + \frac{\kappa_k^2}{\rho_k}u_k = f, \qquad \text{in } \Omega_k, \tag{3.16}$$

using an approximation by Trefftz basis functions that solve (3.10),

$$\nabla^2\phi_k + \kappa_k^2\phi_k = 0 \qquad \text{in } \Omega_k.$$

We multiply (3.16) by $\overline{\phi_k}$ and multiply the conjugate of (3.10) by u_k. We then integrate over the element and apply the Divergence Theorem to each equation, thus applying the Divergence Theorem twice. This results in

$$\int_{\Omega_k}\left(-\frac{1}{\rho_k}\nabla u_k\overline{\nabla\phi_k} + \frac{\kappa_k^2}{\rho_k}u_k\overline{\phi_k}\right)\mathrm{d}V + \int_{\partial\Omega_k}\frac{\overline{\phi_k}}{\rho_k}\frac{\partial u_k}{\partial n_k}\,\mathrm{d}S = \int_{\Omega_k} f\overline{\phi_k}\,\mathrm{d}V \tag{3.17}$$

and

$$\int_{\Omega_k}\left(-\frac{1}{\rho_k}\nabla u_k\overline{\nabla\phi_k} + \frac{\kappa_k^2}{\rho_k}u_k\overline{\phi_k}\right)\mathrm{d}V + \int_{\partial\Omega_k}\frac{u_k}{\rho_k}\overline{\frac{\partial\phi_k}{\partial n_k}}\,\mathrm{d}S = 0. \tag{3.18}$$

By subtracting (3.17) from (3.18) we are left with

$$\int_{\partial\Omega_k}\left(\frac{u_k}{\rho_k}\overline{\frac{\partial\phi_k}{\partial n_k}} - \frac{\overline{\phi_k}}{\rho_k}\frac{\partial u_k}{\partial n_k}\right)\mathrm{d}S = -\int_{\Omega_k} f\overline{\phi_k}\,\mathrm{d}V. \tag{3.19}$$

Using (3.19) in (3.15) we have

$$\int_{\partial\Omega_k} \frac{1}{\sigma}(-\frac{1}{\rho_k}\frac{\partial}{\partial n_k} - \mathrm{i}\sigma)u_k\overline{(-\frac{1}{\rho_k}\frac{\partial\phi_k}{\partial n_k} - \mathrm{i}\sigma\phi_k)}\,\mathrm{d}S - \int_{\partial\Omega_k} \frac{1}{\sigma}(\frac{1}{\rho_k}\frac{\partial}{\partial n_k} - \mathrm{i}\sigma)u_k\overline{(\frac{1}{\rho_k}\frac{\partial\phi_k}{\partial n_k} - \mathrm{i}\sigma\phi_k)}\,\mathrm{d}S = \int_{\Omega_k} -2\mathrm{i}f\overline{\phi_k}\,\mathrm{d}V. \tag{3.20}$$

We assert transmission conditions in coupled form:

$$\left(\frac{1}{\rho_k}\frac{\partial}{\partial n_k} - \mathrm{i}\sigma\right)u_k|_{\Sigma_{k,j}} = \left(-\frac{1}{\rho_k}\frac{\partial}{\partial n_j} - \mathrm{i}\sigma\right)u_j|_{\Sigma_{j,k}}. \tag{3.21}$$

This ensures that the solution on the boundary of one element matches that on the boundary of an adjacent element, and ensures that the flow going into an element is equal to the flow out of the adjacent element. The boundary conditions (3.1b) are applied on an individual element in the form

$$(\frac{1}{\rho}\frac{\partial u}{\partial n} - \mathrm{i}\sigma u)|_{\Gamma_k} = Q(-\frac{1}{\rho}\frac{\partial u}{\partial n} - \mathrm{i}\sigma u)|_{\Gamma_k} + g. \tag{3.22}$$

Substituting (3.21) and (3.22) into (3.20) results in

$$\int_{\partial\Omega_k} \frac{1}{\sigma}(-\frac{1}{\rho_k}\frac{\partial}{\partial n_k} - \mathrm{i}\sigma)u_k\overline{(-\frac{1}{\rho_k}\frac{\partial \phi_k}{\partial n_k} - \mathrm{i}\sigma\phi_k)}\,\mathrm{d}S \tag{3.23}$$

$$-\left(\int_{\Sigma_{k,j}} \frac{1}{\sigma}(-\frac{1}{\rho_j}\frac{\partial}{\partial n_j} - \mathrm{i}\sigma)u_j\overline{(\frac{1}{\rho_k}\frac{\partial \phi_k}{\partial n_k} - \mathrm{i}\sigma\phi_k)}\,\mathrm{d}S \right. \tag{3.24}$$

$$\left. + \int_{\Gamma_k} \frac{Q}{\sigma}(-\frac{1}{\rho_k}\frac{\partial}{\partial n_k} - \mathrm{i}\sigma)u_k\overline{(\frac{1}{\rho_k}\frac{\partial \phi_k}{\partial n_k} - \mathrm{i}\sigma\phi_k)}\,\mathrm{d}S\right) \tag{3.25}$$

$$= \int_{\Omega_k} -2\mathrm{i}f\overline{\phi_k}\,\mathrm{d}V + \int_{\Gamma_k} \frac{g}{\sigma}\overline{(\frac{1}{\rho_k}\frac{\partial \phi_k}{\partial n_k} - \mathrm{i}\sigma\phi_k)}\,\mathrm{d}S. \tag{3.26}$$

Using χ given by (3.8) and summing over all basis functions and elements, we are left with the formulation (3.9).

For further clarification of the derivation of the formulation see [16, 17, 44].

3.3 Reformulation of the UWVF as a PWDG Method

After its original derivation in a variational setting, the UWVF has been shown to be equivalent to a form of PWDG method, through a certain choice of flux parameters. There are several derivations available, such as those in [15, 29, 31]. This realisation has led to significant advances in error analysis, as techniques for the analysis of DG methods can now also be used for the UWVF. Here for completeness we present the unification of the original derivation of the UWVF and the DG formulation setting, following the approach from [15, 52]. To the author's knowledge this is the first derivation of the UWVF of (3.1) in the DG framework for a medium where the wavenumber κ and density ρ are non-constant. In the following §3.4, we detail some of the theoretical convergence results achieved in the literature.

First our Helmholtz problem (3.1) is reformulated as a coupled first order system

$$\begin{cases} -\mathrm{i}\boldsymbol{\zeta} = \frac{\nabla u}{\rho} & \text{in } \Omega, \\ -\frac{\mathrm{i}\kappa u}{\rho} - \frac{1}{\kappa}\nabla\cdot\boldsymbol{\zeta} = \frac{1}{\mathrm{i}\kappa} f & \text{in } \Omega, \\ (-\mathrm{i}\boldsymbol{\zeta}\cdot\mathbf{n} - \mathrm{i}\sigma u) = Q\,(\mathrm{i}\boldsymbol{\zeta}\cdot\mathbf{n} - \mathrm{i}\sigma u) + g & \text{on } \partial\Omega. \end{cases} \tag{3.27}$$

Here as before, Ω is a bounded Lipshitz domain in $\mathbb{R}^2$ (as we work in here, although the derivation holds for $\mathbb{R}^d$, $d = 2, 3$) with boundary Γ, $\kappa(\mathbf{x}) > 0$ is the wavenumber, and $f \in L^2(\Omega)$ and $g \in L^2(\Gamma)$ are the domain and boundary source terms respectively. Using the finite element mesh $\mathcal{T}$ on Ω, we multiply the first and second equations of (3.27) by smooth test functions $\boldsymbol{\tau}$ and v respectively, integrate over each element, and apply the Divergence Theorem to each equation, resulting in

$$\int_{\Omega_k} -\mathrm{i}\boldsymbol{\zeta}\cdot\overline{\boldsymbol{\tau}} + \frac{u}{\rho}\overline{\nabla\cdot\boldsymbol{\tau}}\,\mathrm{d}V - \int_{\partial\Omega_k}\frac{u}{\rho}\overline{\boldsymbol{\tau}\cdot\mathbf{n}}\,\mathrm{d}S = 0 \tag{3.28}$$

and

$$\int_{\Omega_k} -\frac{\mathrm{i}}{\rho}\kappa u\overline{v} + \frac{1}{\kappa}\boldsymbol{\zeta}\cdot\overline{\nabla v}\,\mathrm{d}V - \int_{\partial\Omega_k}\frac{1}{\kappa}\boldsymbol{\zeta}\cdot\mathbf{n}\overline{v}\,\mathrm{d}S = \int_{\Omega_k}\frac{1}{\mathrm{i}\kappa} f\overline{v}\,\mathrm{d}V. \tag{3.29}$$

Approximating by discrete functions on each element we have

$$\int_{\Omega_k} -\mathrm{i}\boldsymbol{\zeta}_k\cdot\overline{\boldsymbol{\tau}_k} + \frac{u_k}{\rho_k}\overline{\nabla\cdot\boldsymbol{\tau}_k}\,\mathrm{d}V - \int_{\partial\Omega_k}\frac{u_k}{\rho_k}\overline{\boldsymbol{\tau}_k\cdot\mathbf{n}_k}\,\mathrm{d}S = 0 \tag{3.30}$$

and

$$\int_{\Omega_k} -\frac{\mathrm{i}}{\rho_k}\kappa_k u_k\overline{v_k} + \frac{1}{\kappa_k}\boldsymbol{\zeta}_k\cdot\overline{\nabla v_k}\,\mathrm{d}V - \int_{\partial\Omega_k}\frac{1}{\kappa_k}\boldsymbol{\zeta}_k\cdot\mathbf{n}_k\overline{v_k}\,\mathrm{d}S = \int_{\Omega_k}\frac{1}{\mathrm{i}\kappa_k} f\overline{v_k}\,\mathrm{d}V. \tag{3.31}$$

By multiplying (3.30) by ρ_k and (3.31) by κ_k, adding the two, and approximating u_k and $\boldsymbol{\zeta}_k$ across the interelement boundaries by their numerical fluxes $\hat{u}$ and $\hat{\boldsymbol{\zeta}}$, it follows

$$\begin{aligned} &\int_{\Omega_k}\boldsymbol{\zeta}_k\cdot\overline{(\mathrm{i}\rho_k\boldsymbol{\tau}_k + \nabla v_k)} + u_k\overline{\left(\mathrm{i}\frac{\kappa_k^2}{\rho_k}v_k + \nabla\cdot\boldsymbol{\tau}_k\right)}\,\mathrm{d}V \\ = \; &-\int_{\Omega_k}\mathrm{i}f\overline{v}\,\mathrm{d}V + \int_{\partial\Omega_k}\hat{u}\overline{\boldsymbol{\tau}_k\cdot\mathbf{n}_k} + \hat{\boldsymbol{\zeta}}_k\cdot\mathbf{n}_k\overline{v_k}\,\mathrm{d}S. \end{aligned} \tag{3.32}$$

Through the choice of Trefftz-type basis functions v_k and $\boldsymbol{\tau}_k$ that satisfy the adjoint Helmholtz equation

$$\left(\overline{\mathrm{i}\rho_k\boldsymbol{\tau}_k + \nabla v_k}\right) = 0 \text{ and } \left(\overline{\mathrm{i}\frac{\kappa_k^2 v_k}{\rho_k} + \nabla\cdot\boldsymbol{\tau}_k}\right) = 0 \qquad \text{in } \Omega_k, \tag{3.33}$$

we obtain

$$\int_{\partial\Omega_k} \hat{u}\overline{\boldsymbol{\tau}_k \cdot \mathbf{n}_k} + \hat{\boldsymbol{\zeta}} \cdot \mathbf{n}_k \overline{v_k}\, \mathrm{d}S = \int_{\Omega_k} \mathrm{i} f \overline{v_k}\, \mathrm{d}V. \tag{3.34}$$

The DG approach is to use numerical fluxes composed of a linear combination of the averages and jumps. We define the averages by

$$\{\{u\}\} := \frac{u_k + u_j}{2}, \qquad \{\{\boldsymbol{\zeta}\}\} := \frac{\boldsymbol{\zeta}_k + \boldsymbol{\zeta}_j}{2} \tag{3.35}$$

and the jumps by

$$[[u]] := u_k \mathbf{n}_k + u_j \mathbf{n}_j, \qquad [[\boldsymbol{\zeta}]] := \boldsymbol{\zeta}_k \cdot \mathbf{n}_k + \boldsymbol{\zeta}_j \cdot \mathbf{n}_j. \tag{3.36}$$

Using different choices for the flux results in alternative DG methods. Using similar strategies to the formulations in [31,36,52], the DG numerical fluxes on the interelement edges are given by

$$\hat{\boldsymbol{\zeta}} = \{\{\boldsymbol{\zeta}\}\} - \frac{\sigma}{2}[[u]], \tag{3.37}$$

and

$$\hat{u} = \{\{u\}\} - \frac{1}{2\sigma}[[\boldsymbol{\zeta}]]. \tag{3.38}$$

Using the defined fluxes (3.37) and (3.38), and the definitions of the averages (3.35) and jumps (3.36), (3.34) can be rearranged to give

$$\begin{aligned}
&\int_{\Sigma_{k,j}} \hat{u}\overline{\boldsymbol{\tau}_k \cdot \mathbf{n}_k} + \hat{\boldsymbol{\zeta}} \cdot \mathbf{n}_k \overline{v_k}\, \mathrm{d}S \\
= &\int_{\Sigma_{k,j}} \left(\frac{u_k + u_j}{2} - \frac{1}{2\sigma}\left[\boldsymbol{\zeta}_k \cdot \mathbf{n}_k + \boldsymbol{\zeta}_j \cdot \mathbf{n}_j\right] \right) \overline{\boldsymbol{\tau}_k \cdot \mathbf{n}_k} \\
&+ \left(\frac{\boldsymbol{\zeta}_k + \boldsymbol{\zeta}_j}{2} - \frac{\sigma}{2}\left[u_k \mathbf{n}_k + u_j \mathbf{n}_j\right] \right) \cdot \mathbf{n}_k \overline{v_k}\, \mathrm{d}S \\
= &\int_{\Sigma_{k,j}} \frac{1}{2}\left[u_k \overline{\boldsymbol{\tau}_k \cdot \mathbf{n}_k} - \frac{1}{\sigma}\boldsymbol{\zeta}_k \cdot \mathbf{n}_k \overline{\boldsymbol{\tau}_k \cdot \mathbf{n}_k} + \boldsymbol{\zeta}_k \cdot \mathbf{n}_k \overline{v_k} - \sigma u_k \overline{v_k} \right] \mathrm{d}S \\
&+ \int_{\Sigma_{k,j}} \frac{1}{2}\left[u_j \overline{\boldsymbol{\tau}_k \cdot \mathbf{n}_k} - \frac{1}{\sigma}\boldsymbol{\zeta}_j \cdot \mathbf{n}_j \overline{\boldsymbol{\tau}_k \cdot \mathbf{n}_k} + \boldsymbol{\zeta}_j \cdot \mathbf{n}_k \overline{v_k} + \sigma u_j \overline{v_k} \right] \mathrm{d}S \\
= &-\int_{\Sigma_{k,j}} \frac{1}{2\sigma}\left[\left(-\mathrm{i}\sigma u_k + \mathrm{i}\boldsymbol{\zeta}_k \cdot \mathbf{n}_k\right) \left(\overline{-\mathrm{i}\sigma v_k + \mathrm{i}\mathbf{n}_k \cdot \boldsymbol{\tau}_k}\right) \right] \mathrm{d}S \\
&+ \int_{\Sigma_{k,j}} \frac{1}{2\sigma}\left[\left(-\mathrm{i}\sigma u_j + \mathrm{i}\boldsymbol{\zeta}_j \cdot \mathbf{n}_j\right) \left(\overline{-\mathrm{i}\sigma v_k - \mathrm{i}\mathbf{n}_k \cdot \boldsymbol{\tau}_k}\right) \right] \mathrm{d}S \\
= &-\int_{\Sigma_{k,j}} \frac{1}{2\sigma}\mathcal{X}_k \overline{\mathcal{Y}_k}\, \mathrm{d}S + \int_{\Sigma_{k,j}} \frac{1}{2\sigma}\mathcal{X}_j \overline{F_k(\mathcal{Y}_k)}\, \mathrm{d}S
\end{aligned} \tag{3.39}$$

on a single interlement edge. Here $\mathcal{X}_k := (-\mathrm{i}\sigma u_k + \mathrm{i}\boldsymbol{\zeta}_k \cdot \mathbf{n}_k)$, $\mathcal{Y}_k := (-\mathrm{i}\sigma v_k + \mathrm{i}\mathbf{n}_k \cdot \boldsymbol{\tau}_k)$, and $F_k(\mathcal{Y}_k) := (-\mathrm{i}\sigma v_k - \mathrm{i}\mathbf{n}_k \cdot \boldsymbol{\tau}_k)$. On the exterior edges Γ_k we define the fluxes $\hat{u} = u$ and $\hat{\boldsymbol{\zeta}} = \boldsymbol{\zeta}$, thus similarly we have

$$\begin{aligned}
&\int_{\Gamma_k} \hat{u}\overline{\boldsymbol{\tau}_k \cdot \mathbf{n}_k} + \hat{\boldsymbol{\zeta}} \cdot \mathbf{n}_k \overline{v_k}\,\mathrm{d}S \\
= &\int_{\Gamma_k} \frac{1}{2\sigma}\left[(-\mathrm{i}\sigma u_k - \mathrm{i}\boldsymbol{\zeta}_k \cdot \mathbf{n}_k)\left(\overline{-\mathrm{i}\sigma v_k - \mathrm{i}\mathbf{n}_k \cdot \boldsymbol{\tau}_k}\right)\right]\,\mathrm{d}S \\
&- \int_{\Gamma_k} \frac{1}{2\sigma}\left[\left(-\mathrm{i}\sigma u_j + \mathrm{i}\boldsymbol{\zeta}_j \cdot \mathbf{n}_j\right)\left(\overline{-\mathrm{i}\sigma v_k + \mathrm{i}\mathbf{n}_k \cdot \boldsymbol{\tau}_k}\right)\right]\,\mathrm{d}S \\
= &\int_{\Gamma_k} \frac{1}{2\sigma} F_k(\mathcal{X}_k)\overline{F_k\mathcal{Y}_k}\,\mathrm{d}S - \int_{\Gamma_k} \frac{1}{2\sigma}\mathcal{X}_j\overline{(\mathcal{Y}_k)}\,\mathrm{d}S. \qquad (3.40)
\end{aligned}$$

Adding (3.39) and (3.40) and rearanging, (3.34) can then be written as

$$\begin{aligned}
&\int_{\partial\Omega_k} \frac{1}{\sigma}\mathcal{X}_k\overline{\mathcal{Y}_k}\,\mathrm{d}S - \sum_j \int_{\Sigma_{k,j}} \frac{1}{\sigma}\mathcal{X}_j\overline{F_k(\mathcal{Y}_k)}\,\mathrm{d}S \\
= &-\int_{\Omega_k} 2\mathrm{i}f\overline{v_k}\,\mathrm{d}V + \int_{\Gamma_k} \frac{1}{\sigma}F_k(\mathcal{X}_k)\overline{F_k(\mathcal{Y}_k)}\,\mathrm{d}S. \qquad (3.41)
\end{aligned}$$

Now including the boundary conditions given in the third equation of (3.27), and summing over all elements $k = 1, \ldots, K$, we obtain the original UWVF: find $\mathcal{X} \in L^2(\partial\Omega_k)$ such that

$$\begin{aligned}
&\sum_{k=1}^{K}\int_{\partial\Omega_k} \frac{1}{\sigma}\mathcal{X}_k\overline{\mathcal{Y}_k}\,\mathrm{d}S - \sum_{k=1}^{K}\sum_{j=1,j\neq k}^{K}\int_{\Sigma_{k,j}} \frac{1}{\sigma}\mathcal{X}_j\overline{F_k(\mathcal{Y}_k)}\,\mathrm{d}S \\
&- \sum_{k=1}^{K}\int_{\Gamma_k} \frac{Q}{\sigma}\mathcal{X}_k\overline{F_k(\mathcal{Y}_k)}\,\mathrm{d}S \\
= &-\sum_{k=1}^{K}\int_{\Omega_k} 2\mathrm{i}f\overline{v_k}\,\mathrm{d}V + \sum_{k=1}^{K}\int_{\Gamma_k} \frac{1}{\sigma}g\overline{F_k(\mathcal{Y}_k)}\,\mathrm{d}S \qquad (3.42)
\end{aligned}$$

for all $\mathcal{Y}_k \in L^2(\partial\Omega_k)$, $k = 1, \ldots, K$. This is equivalent to the original formulation (3.9).

3.4 Convergence Results

Since the realisation that the UWVF can be reformulated as a class of PWDG methods, there has been extensive progress in the analysis of the method, as DG analysis techniques can now be used. Several equivalent derivations were presented in $2007 - 2009$, available in [15, 29, 31].

The existence and uniqueness of discrete solutions were proved first of all by Cessenat and Després in [16,17], and then separately in the DG setting by Gittelson et al. in [31]. Convergence analysis is presented in [31] for the h-version (improving the solution through refinement of the numerical mesh) of PWDG methods. However the choice of flux parameters considered are not those which fit the UWVF, and although the results presented have given insight and motivation for further work (in [52]), they do not apply to the UWVF. An a-priori convergence analysis of PWDG methods, in which the UWVF is this time included, is presented in [36] for the case of p refinement, where the solution is improved through increasing the number of plane wave basis functions per element. Convergence rates are derived for the homogeneous Helmholtz equation on 2D convex domains with impedance boundary conditions ($Q = 0$), using mesh skeleton based norms. The p-version error estimates require the product κh, where h is the mesh size parameter, to be sufficiently small in order for the wavelength to be resolved in the trial space. However the requirement on κh is less severe than that which is required in standard FEM for the avoidance of pollution errors. A bound for the L^2 norm of the error is presented, as well as best approximation estimates in a norm on the mesh skeleton.

The unification of the UWVF and DG methods is presented by Buffa and Monk in [15], as well as explicit error estimates in a mesh dependant norm. Extensive numerical results suggest however that the UWVF does converge not just on the mesh skeleton, but throughout the entire domain. In the case of a convex domain, the mesh norm estimate can be used as an estimate of the $L^2(\Omega)$ norm of the error. Recent work by Melenk et al. [55] presents theory for the stability and convergence of the UWVF, in the case of a highly indefinite Helmholtz problem in up to three spatial dimensions.

3.5 The Linear System of Equations

The standard formulation (3.9) results in the linear system, given in matrix form by

$$(D - C)X = \hat{b}. \tag{3.43}$$

Entries in the matrix D correspond to the integral (3.23), entries of C to those of (3.24) and (3.25), and the entries of vector $\hat{b}$ to (3.26). The coefficients $\chi_{k,l}$ are determined by solving the linear system (3.43) where

$$X = (\chi_{1,1}, \chi_{1,2}, ..., \chi_{1,p_1}, \chi_{2,1}, ..., \chi_{K,p_K})^T.$$

Here $\chi_{k,l}$ refers to the coefficient corresponding to the lth basis function ($l = 1, \ldots, p_k$) on the kth element ($k = 1, \ldots, K$). The linear system (3.43) is solved for the elements of X, so that they can then be used to approximate u over the whole domain using (3.11) (where $u|_{\Omega_k} = u_k$). The matrix D is block diagonal, made up of blocks $D_k = [D_k^{l,m}]$ corresponding to each element $k = 1, \ldots, K$. Each of these blocks contains integrals combining the impedance traces of each basis function that holds in the element, for $l = 1, \ldots, p_k$, $m = 1, \ldots, p_k$. This results in the form

$$D = \begin{pmatrix} [D_1^{l,m}] & & & \\ & [D_2^{l,m}] & & \\ & & \ddots & \\ & & & [D_K^{l,m}] \end{pmatrix} \tag{3.44}$$

with entries given by

$$D_k^{l,m} = \int_{\partial\Omega_k} \frac{1}{\sigma}(-\frac{1}{\rho_k}\frac{\partial\phi_{k,m}}{\partial n} - \mathrm{i}\sigma\phi_{k,m})\overline{(-\frac{1}{\rho_k}\frac{\partial\phi_{k,l}}{\partial n} - \mathrm{i}\sigma\phi_{k,l})}\,\mathrm{d}S \tag{3.45}$$

for $k = 1, ..., K$, $l = 1, ..., p_k$, $m = 1, ..., p_k$.

Entries of the matrix C are given by

$$\begin{aligned} C_{k,j}^{l,m} &= \int_{\Sigma_{k,j}} \frac{1}{\sigma}(\frac{1}{\rho_j}\frac{\partial\phi_{j,m}}{\partial n_k} - \mathrm{i}\sigma\phi_{j,m})\overline{(\frac{1}{\rho_k}\frac{\partial\phi_{k,l}}{\partial n_k} - \mathrm{i}\sigma\phi_{k,l})}\,\mathrm{d}S \\ &+ \int_{\Gamma_k} \frac{Q}{\sigma}(-\frac{1}{\rho_k}\frac{\partial\phi_{k,m}}{\partial n_k} - \mathrm{i}\sigma\phi_{k,m})\overline{(\frac{1}{\rho_k}\frac{\partial\phi_{k,l}}{\partial n_k} - \mathrm{i}\sigma\phi_{k,l})}\,\mathrm{d}S, \end{aligned} \tag{3.46}$$

resulting in up to three integrals over the internal edges $\Sigma_{k,j}$, and another integral over any exterior edges Γ_k. This results in the matrix C having a sparse block structure, with submatrices $C_{k,j}$ being non-zero only if elements Ω_k and Ω_j are adjacent, or if Ω_k has a side on the exterior boundary Γ.

For the right-hand side vector $\hat{b}$, entries are given by

$$b_k^l = \int_{\Omega_k} -2\mathrm{i}f\overline{\phi_k}\,\mathrm{d}V + \int_{\Gamma_k} \frac{g}{\sigma}\overline{(\frac{1}{\rho_k}\frac{\partial\phi_{k,l}}{\partial n} - \mathrm{i}\sigma\phi_{k,l})}\,\mathrm{d}S, \tag{3.47}$$

for $k = 1, ..., K$, $l = 1, ..., p_k$. When solving the homogeneous Helmholtz equation ($f \equiv 0$), vector $\hat{b}$ has non-zero entries for the kth subvector only when Ω_k has an exterior edge.

It is suggested in [16, 44] that for numerical stability, the matrix system (3.43) is best solved in the preconditioned form

$$(I - D^{-1}C)X = D^{-1}\hat{b}. \tag{3.48}$$

As the matrix D has a sparse, block diagonal structure, inversion of the matrix can be done element wise for each D_k. For numerical results in this thesis, we solve the system (3.48) iteratively using the biconjugate gradient stabilized method (BiCGStab).

A main complication in the practical use of the UWVF is the issue of ill-conditioning. The condition number of the submatrices D_k increases as we increase the number of directions p_k tested on each element, causing the solution to break down. This is because when using basis functions in equally spaced directions in an element Ω_k, as we increase the number of basis functions p_k, the angle between the consecutive wave directions decrease, thus the basis becomes closer to being linearly dependent. For a plane wave basis of waves propagating in directions $\mathbf{d}$ and $\mathbf{d}'$, as the directions get closer together, $\mathbf{d} \to \mathbf{d}'$, and so a single basis function can tend to a multiple of another:

$$\begin{aligned} \exp(\mathrm{i}\kappa\mathbf{d}\cdot\mathbf{x}) &= \exp(\mathrm{i}\kappa(\mathbf{d}-\mathbf{d}')\cdot\mathbf{x})\exp(\mathrm{i}\kappa\mathbf{d}'\cdot\mathbf{x}) \\ &\to \exp(\mathrm{i}\kappa\mathbf{d}'\cdot\mathbf{x}) \qquad \text{as } \mathbf{d}\to\mathbf{d}'. \end{aligned}$$

The conditioning of the matrix D_k depends upon p_k but also upon $\kappa_k\varnothing_k$ where $\varnothing_k$ is the diameter of the element Ω_k. The factor $\kappa_k\varnothing_k$ is larger when the wavelength is small in comparison to the size of the element, and smaller when the wavelength is large in comparison to the size of the element. For a plane wave basis propagating in direction $\mathbf{d}$,

$$\begin{aligned} \exp(\mathrm{i}\kappa\mathbf{d}\cdot\mathbf{x}) &= \exp(\mathrm{i}\kappa\mathbf{d}\cdot\mathbf{x_0})\exp(\mathrm{i}\kappa\mathbf{d}\cdot(\mathbf{x}-\mathbf{x_0})) \\ &= \exp(\mathrm{i}\kappa\mathbf{d}\cdot\mathbf{x_0})[1+\mathrm{i}\kappa\mathbf{d}\cdot(\mathbf{x}-\mathbf{x_0})+O((\kappa\varnothing_k)^2)] \qquad \text{as } \kappa_k\varnothing_k\to 0 \end{aligned}$$

since $|\kappa \mathbf{d} \cdot (\mathbf{x} - \mathbf{x_0})| \leq \kappa \varnothing_k$ for an element with centroid $\mathbf{x_0}$. Thus as $\kappa_k \varnothing_k \to 0$, when the wavelength is very large compared to the element size, the plane waves become approximately linearly dependent. In either case, as the basis set approaches linear dependency, the condition number of the corresponding submatrix D_k grows.

By consulting the existing literature [44] and through running experiments we were able to choose an upper bound of 10^{10} for the maximum condition number of each submatrix $\max(\text{cond}(D_k))$, beneath which the solution did not break down. A varying number of basis functions per element was then implemented based upon this upper bound: an initial maximum number of basis functions per element was chosen, if the condition number of the respective submatrix D_k exceeded the desired upper bound the number of basis functions was reduced and D_k recomputed until the condition number was below the upper bound. This scheme, first introduced in [44], allows for stable inversion of all blocks D_k.

3.6 A Hankel Basis for the UWVF

In the above we have detailed the plane wave basis for the UWVF, which has been studied widely in much literature including [16, 17, 31, 36, 41, 44]. Recently there has been investigation into the use of a Bessel basis, in [52, 53]. As an alternative form of Trefftz basis functions $\phi_{k,l} \in H_k$, from now on in this thesis we instead consider a Hankel basis. A Hankel basis allows greater flexibility than the plane wave basis, providing the possibilty of adapting the basis to the curvature of the solution's wavefronts, and also providing more freedom to reduce the linear dependence of the basis. However a Hankel basis does mean extra computational expense, as the integrals in (3.9) can no longer be solved in closed form, and so a numerical quadrature must be used.

The Hankel basis functions are circular waves in 2D, defined as

$$\phi_{k,l}(\mathbf{x}) = \begin{cases} H_0^1(\kappa_k |\mathbf{x} - \mathbf{y}_{k,l}|) & \text{in } \Omega_k \\ 0 & \text{elsewhere,} \end{cases} \tag{3.49}$$

for $l = 1, ..., p_k$, $k = 1, ..., K$. The wavenumber κ is taken to be piecewise constant with

$\kappa_k \equiv \kappa|_{\Omega_k}$, and the point source locations are given by

$$\mathbf{y}_{k,l} = \left(x_k^C + R_{PS} \cos\left(\frac{2\pi l}{p_k}\right), y_k^C + R_{PS} \sin\left(\frac{2\pi l}{p_k}\right) \right), \qquad l = 1, ..., p_k. \tag{3.50}$$

Here $R_{PS} > d_{max} > 0$ is a positive constant greater than the maximum distance

$$d_{max} = \max_s(|\mathbf{x}_k^C - \mathbf{x}_{k,s}^V|)$$

between the centroid of the element $\mathbf{x}_k^C = (x_k^C, y_k^C)$ and each vertex of the triangular element $\mathbf{x}_{k,s}^V$, $s = 1, .., 3$, ensuring each point source is exterior of its corresponding element.

A Hankel set is a good choice of basis in the UWVF as it allows flexibility in both the direction of propagation and in the level of curvature of the wave fronts that hold over an element, as illustrated in Figure 3.2. By taking the points $\mathbf{y}_{k,l}$ far from the element, we can replicate the conventional plane wave basis. This important property comes from the leading order asymptotic behaviour of the Hankel function [12, 6.3.18]

$$H_\nu^{(1)}(\mathbf{z}) \sim \sqrt{(2/(\pi\mathbf{z}))} \exp(\mathrm{i}(\mathbf{z} - \nu\pi/2 - \pi/4)) \qquad -\pi < \arg \mathbf{z} < 2\pi, \quad |\mathbf{z}| \to \infty. \tag{3.51}$$

By choosing the positioning in the near field to the element, a higher level of curvature of wave fronts can be introduced.

With the use of the Hankel basis, there is extra computational expense when compared to the traditional plane wave basis. As can be seen in Table 3.1, the average computation time in Matlab for the evaluation of a Hankel function at various points is orders of magnitude longer than the same for a plane wave evaluation. Thus it will be preferable to keep the number of basis functions to evaluate at a minimum for our approximations. As well as the Hankel evaluation expense, there is also extra computational expense with this choice of basis set compared with the plane wave basis in that the UWVF integrals in (3.9) cannot be evaluated in closed form, thus we require a numerical integration method. We use a Gauss–Legendre quadrature rule, with forty grid points per wavelength for high accuracy. This high number of Gauss integration points may be excessive, and lead to additional round-off errors.

Table 3.1: Average Evaluation Time of Wave Functions

Function Type	Average Time (seconds)
Hankel	1.12×10^{-4}
Plane Wave	2.12×10^{-6}

3.7 A Comparison Study of Conditioning: The Hankel and Plane Wave Bases

One of the main issues that is a hindrance to the UWVF is that of ill-conditioning. As explained in §3.5, the traditional plane wave basis can become close to linearly dependant when a large number of basis functions are used on each element, resulting in the submatrices D_k becoming badly conditioned and the solution breaking down. By using a Hankel function basis, more variation in the wavefronts can be enforced, so that a large number can be used on an element without the set becoming close to linearly dependent. Here we present a comparison study of the conditioning of the UWVF for differing bases. We consider acoustic wave propagation through a 2D bounded domain. The problem we consider here is identical to that in the thesis of Andrea Moiola [57] using a plane wave basis. Here we repeat using a Hankel basis, comparing three choices of the set:

- point sources equi-spaced around a ring in the far field, simulating a plane wave basis;
- point sources equi-spaced around a ring in the near field to each element;
- point sources equi-spaced around two rings near each element.

We compare the convergence of errors and conditioning of the system using the three Hankel basis sets, as well as the traditional equi-spaced plane wave basis.

In the square domain $\Omega = [0, 1] \times [-0.5, 0.5]$ we approximate the regular solution of the Helmholtz equation

$$u(\mathbf{x}) = J_1(\kappa r)\cos(\theta), \tag{3.52}$$

given in polar coordinates $\mathbf{x} = (r\cos(\theta), r\sin(\theta))$ centred at the origin, where J_1 denotes the Bessel function of the first kind of order one. We use the same wavenumber $\kappa = 10$ as in [57], and the same mesh, with $K = 8$ elements all of the same size. Following the notation of §3.1, we consider the homogeneous problem with $f = 0$, use a constant density $\rho = 1$, the impedance condition with $Q = 0$, and

$$g = \frac{\partial u}{\partial n} - \mathrm{i}\kappa u$$

is given on the boundary of the domain. The domain and mesh are shown on the left hand side of Figure 3.3, whilst the exact solution is shown on the right.

In the numerical experiments we do not impose a bound on the condition numbers of the submatrices D_k that arise in the system of equations, instead we maintain a constant number of basis functions on each element. For the first set of basis functions, the point sources are equally spaced around a circle of radius $R_{PS} = 600$ taken from the centroid of each element, so that wavefronts over the element are close to parallel, similar to those of a plane wave basis. For the second set, the point sources are taken equally spaced around a circle of radius $R_{PS} = 1.1 \times \mathbf{d}_{max}$ where $\mathbf{d}_{max}$ is the maximum distance between the centroid of the element and its vertices. For the third set, the point sources are taken equally spaced around two circles, as per Figure 3.4, where the inner circle is of radius $R^I_{PS} = 0.5$ and the outer radius is $R^O_{PS} = 2$ (so $R^I_{PS} = 1.34 \times \mathbf{d}_{max}$ and $R^O_{PS} = 5.37 \times \mathbf{d}_{max}$). The basis functions are angularly equi-spaced and split equally between the two rings: only even total numbers of basis functions are tested.

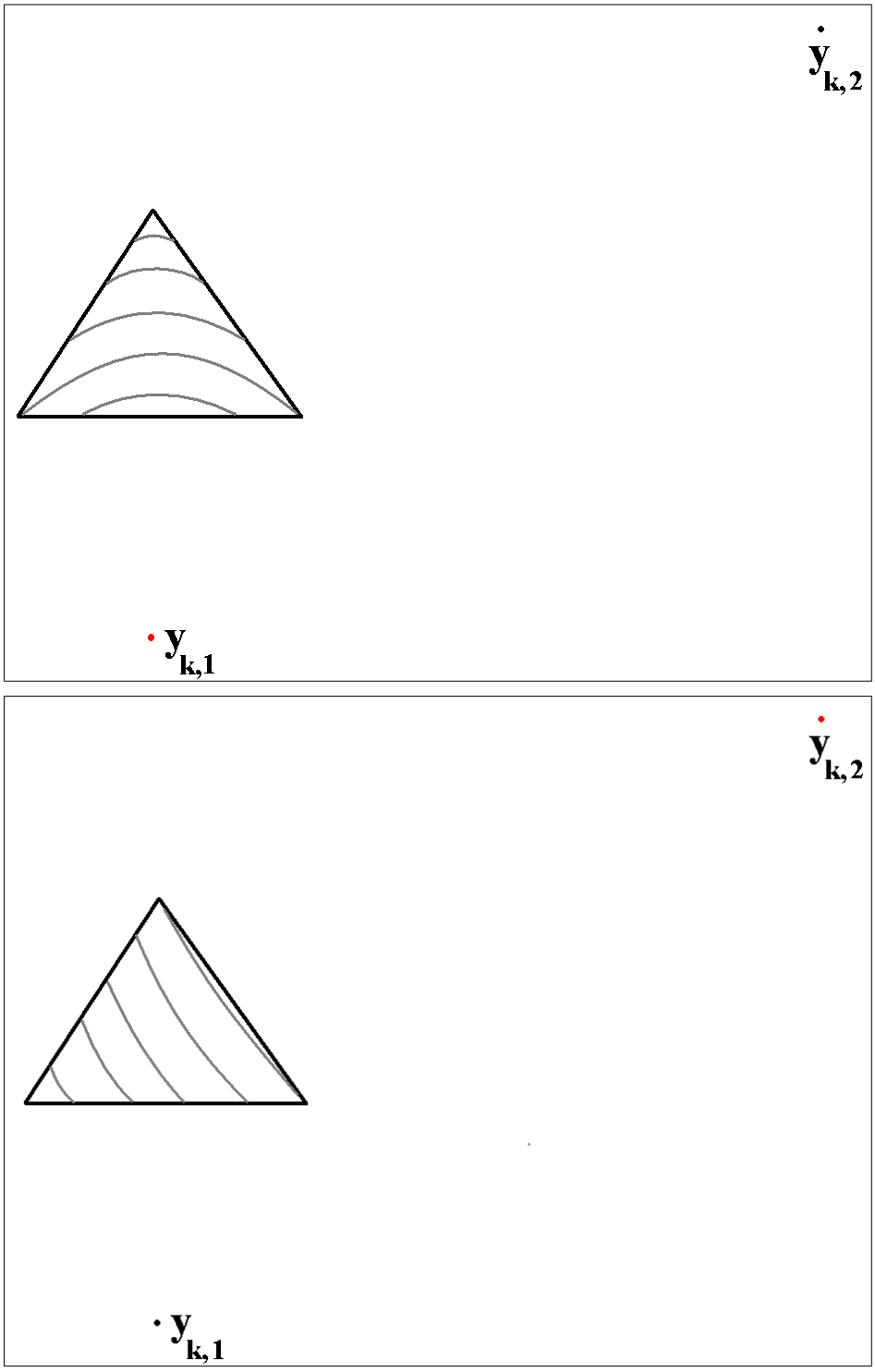

Figure 3.2: Orientation of the point source basis affects both the direction and level of curvature of wave fronts over an element. In the upper plot: wavefronts in an element for $H_0^1(\kappa|\mathbf{x}-\mathbf{y}_{k,1}|)$. By taking a point source in the near field to the element, a high level of curvature of the wavefronts can be obtained. In the lower plot: wavefronts in an element for $H_0^1(\kappa|\mathbf{x}-\mathbf{y}_{k,2}|)$. By taking a point source further in the field from the element we obtain wavefronts that are less curved.

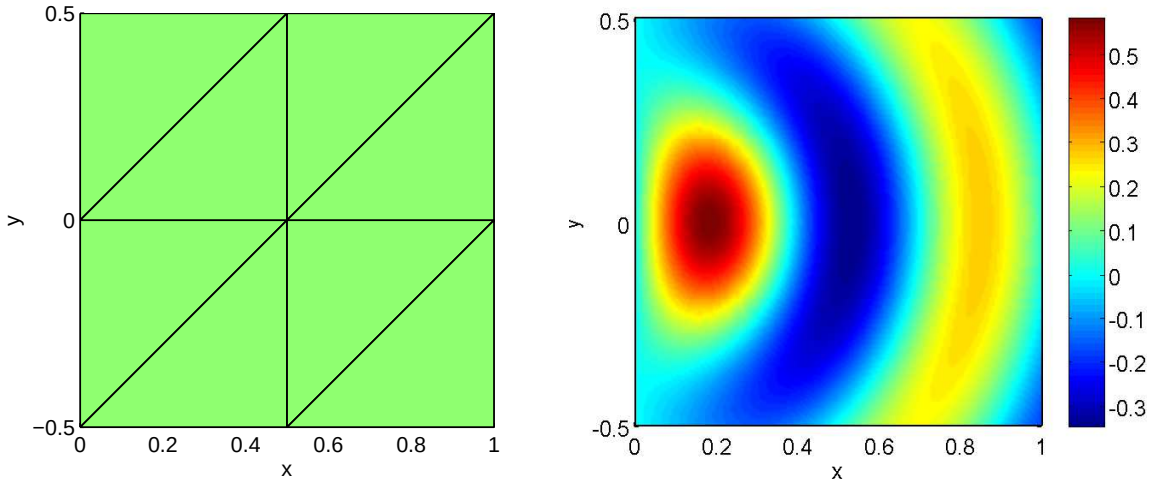

Figure 3.3: The mesh of $K = 8$ elements used (left) and the exact solution for $\kappa = 10$ (right).

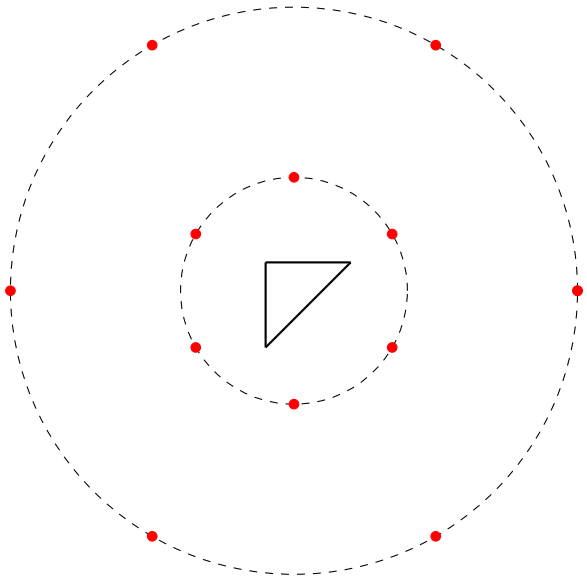

Figure 3.4: Diagrammatic of point source positions in two ring case.

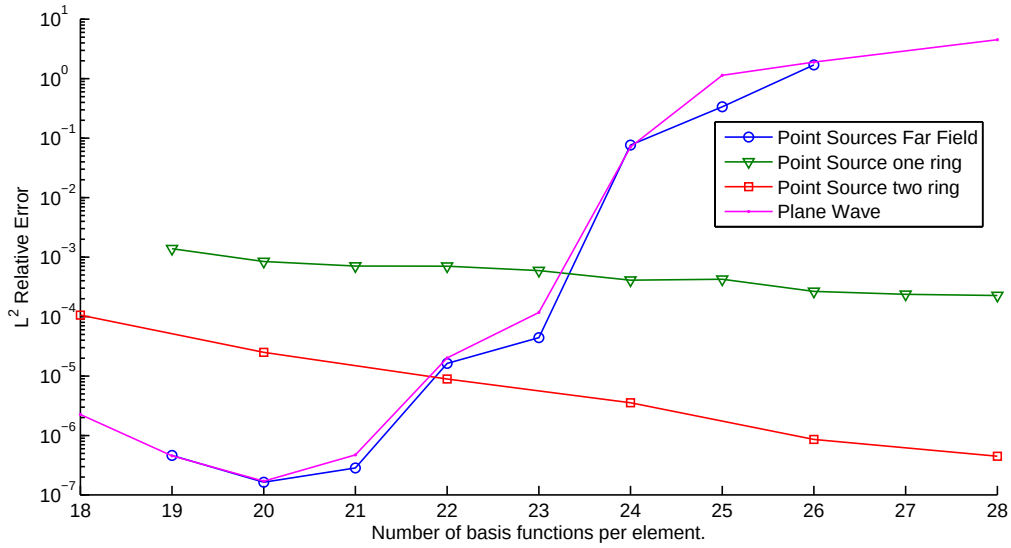

Figure 3.5: L^2 relative errors against number of basis functions per element.

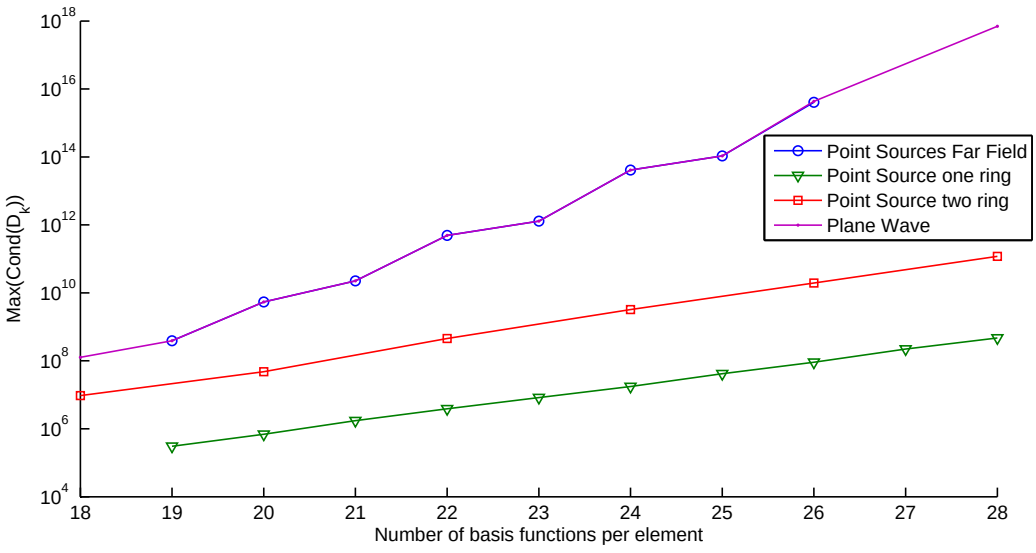

Figure 3.6: Maximum condition number of D_k against number of basis functions per element.

The $L^2(\Omega)$ relative errors against number of point source basis functions per element is plotted in Figure 3.5, and the estimated maximum condition number of the submatrices D_k again against number of point source basis functions per element is plotted in Figure 3.6. The condition number of each submatrix is estimated by a lower bound for the 1 norm condition number. The far field point source and plane wave bases give similar levels of errors and achieve the same estimates on the condition number, as the far field sources are set to replicate plane waves. Their results are by far the most accurate for the fewest number of degrees of freedom. However, the solution breaks down and errors grow as the system becomes more ill-conditioned. The near field point sources on a single ring are much less accurate even when a much higher number of degrees of freedom is used in the approximation. This could be due to many factors, such as the basis wave field having an incorrect level of curvature across the element, or the peak close to the singularity of the Hankel function not well representing the exact solution. This basis does however maintain relatively low condition numbers throughout. For the sources on the two rings around each element, high accuracy is achieved, but at a much greater cost than with the far field sources. It is also worth noting that the ill-conditioning increases as functions in the basis become more similar to plane waves. In this case it appears that a plane wave basis is preferable if there is little consideration given to the placing of the point sources relative to the expected solution. In the following chapter, we will consider how to choose the point source positions of the Hankel basis more appropriately.

Chapter 4

Ray Tracing for High Frequency Scattering by Convex Obstacles

Ray tracing techniques are widely used in the geophysics community [5, 12, 22]. As detailed in Chapter 2, rays are a high frequency asymptotic approximation of the direction of wave propagation. Thus at high frequencies, a ray model gives a good understanding of the direction of propagation of a wave and its reflections.

To further progress the UWVF, we use ray tracing techniques in order to find a good a-priori choice of basis function. Similar techniques have been trialled in [11]. We consider the case of two dimensional wave scattering by a smooth convex obstacle, in a domain where the wave speed, and thus the wavenumber, is constant. In this chapter we detail a method for finding a ray traced centre of curvature for wavefronts at points in the domain. In the following Chapter 5 we then use these ray traced centres of curvature to augment the UWVF basis. We will consider how similar ideas can be applied to more general domains of non-constant wavespeed in Chapter 6. A smooth convex obstacle is a good choice of scatterer to study with regards to ray tracing, as without corners there will be no strong diffraction effects, and due to the convexity there can be no multiple reflections. There will still however be creeping waves generated at the shadow boundary [18].

As we consider in this chapter a domain where the wave speed is constant, wavefronts

will propagate without turning. Rays travel perpendicular to the wavefronts, so ray directions will be straight lines. When these rays interact with a surface, the Law of Reflection from geometric optics states that the direction of the reflected ray is determined by the angle the incident ray makes with the surface normal [22]. The incident and reflected rays lie in a single plane, and the angle of reflection between the reflected ray and the surface normal, θ_r, is the same as that between the incident ray and the normal, known as the angle of incidence θ_i. That is, $\theta_i = \theta_r$, as illustrated in Figure 4.1.

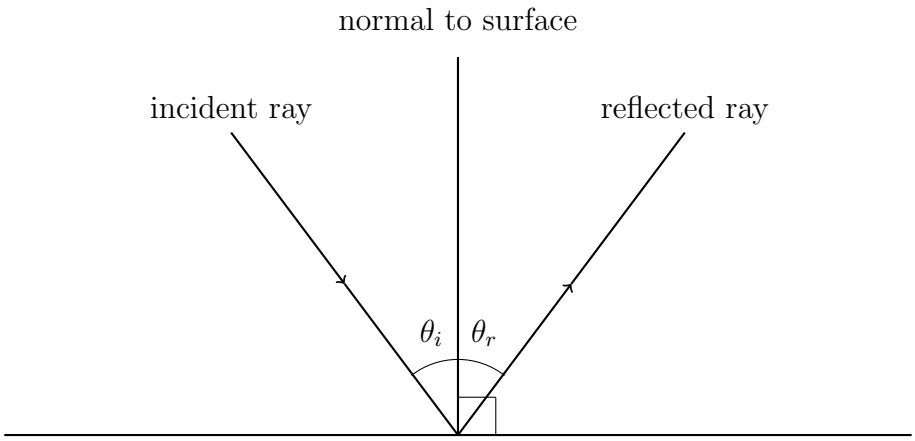

Figure 4.1: Diagram of the Law of Reflection

In §4.1 we present the setup for finding reflected ray directions for scattering by a general smooth convex obstacle. Once the reflected direction at a single point is found, it can be considered with those for neighbouring points, allowing a centre of curvature to also be derived for wavefronts at the point. Two particular examples are considered: we apply the ray tracing techniques to the case of scattering by a circle in §4.1.1, and to the case of scattering by an ellipse in §4.1.2. Scattering by a circle is a good initial case to study due to its symmetric properties and the existance of a known exact solution (presented in §4.2.1). Scattering by an ellipse is a more complex case than that of a circle as there are fewer symmetrical properties. A known solution is presented for completeness in §4.2.2, as well as a numerical reference solution provided by the MFS in §4.2.3. The presence of exact solutions allows us to study the best approximation

achievable through the use of our ray-traced directions and centres of curvature alone. We present two best approximation studies: in §4.3.1 we consider the element-wise best approximation to the scattered field for the case of a circular scatterer. This is done first for the approximation on a single element, and then for all elements in a discretised domain. A second study is presented in §4.3.2, where we consider the best approximation to the total field for both differing sizes of the area of approximation and for different regions around the domain. The best approximation studies give insight into the value ray tracing techniques may have in aiding the choice of basis functions in the UWVF.

4.1 Ray Tracing for Wave Scattering by a Smooth Convex Obstacle

Here we present the outline of a method for finding ray directions for the case of scattering by a general smooth, convex obstacle $\overline{\Omega^+}$, the closure of the bounded convex domain Ω^+. We consider a wave scattering problem in the exterior domain $\Omega := \mathrm{R}^2 \backslash \overline{\Omega^+}$, as per Figure 2.1. We define the boundary of the scatterer by $\Gamma_1 = (R(\theta)\cos(\theta), R(\theta)\sin(\theta))$ where $R(\theta) > 0$ is the radial distance, and $\theta \in [-\pi, \pi)$. Any smooth convex obstacle can be written like this. Without loss of generality we take the incident plane wave to be propagating in the negative x direction, $u^i(\mathbf{x}) = \exp(-\mathrm{i}\kappa x)$, with the unit incident direction vector $\mathbf{d}_i = (-1, 0)$.

We must first consider the regions of the domain in which the incident field can propagate. We call the lit side of the obstacle Γ_{lit} the portion of Γ_1 that the incident field will hit and produce a reflected wave, i.e. the part where $\mathbf{d}_i \cdot \mathbf{n} \leq 0$, where $\mathbf{n}$ is the unit outward normal vector from Γ_1 into Ω. The remainder of the obstacle boundary for which $\mathbf{d}_i \cdot \mathbf{n} > 0$ we call the shadow side Γ_{shadow}, where the incident field is blocked by the obstacle and so can not penetrate. The shadow region Ω_{shadow} is the region extended from this: $\Omega_{shadow} = \{\boldsymbol{\alpha} + t\mathbf{d}_i; t \geq 0, \boldsymbol{\alpha} \in \Gamma_{shadow}\}$. We call the remainder of the domain the lit (also known as illuminated) region $\Omega_{lit} = \Omega \backslash \Omega_{shadow}$. The boundary between the

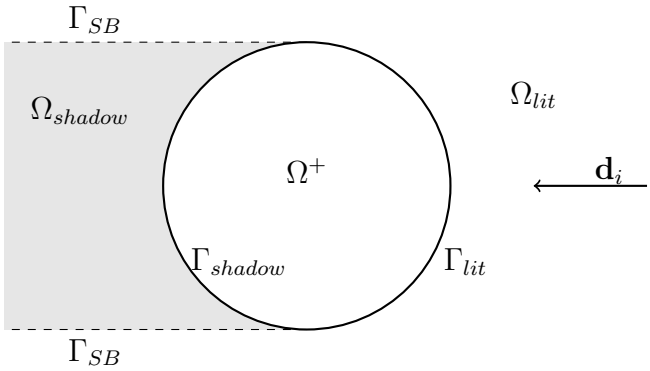

Figure 4.2: The exterior scattering problem

two regions is known as the shadow boundary Γ_{SB}. This set-up is illustrated in Figure 4.2.

As the incident field does not penetrate the shadow region, we need only consider points in Ω_{lit} for the application of ray tracing techniques. To find our ray directions throughout the lit region we first consider the ray setup for a single point. At any point in Ω_{lit} there will be at most two rays: one representing the incident wave direction, and another representing the scattered field (there may be more in the case of a non-convex or non-smooth obstacle). We aim to find for any given point $\mathbf{x} \in \Omega_{lit}$: the direction of the reflected ray, given by the unit vector $\mathbf{d}_r$; the unique point of reflection $\mathbf{z} \in \Gamma_{lit}$ where the incident ray hits the scatterer; and the angle at which it reflects, $\theta = \theta_i = \theta_r$. We define the reflection point $\mathbf{z}$ on the surface of the scatterer by

$$\mathbf{z} = (R(\psi)\cos(\psi), R(\psi)\sin(\psi)) = R(\psi)\cos(\psi)\mathbf{i} + R(\psi)\sin(\psi)\mathbf{j}, \tag{4.1}$$

for an angle ψ to be found. Here $\mathbf{i}$ and $\mathbf{j}$ are, as usual, unit vectors in the x and y directions. Now consider an independent coordinate system $(\mathbf{v}, \mathbf{n})$ as per Figure 4.3, where $\mathbf{n} = \cos(\theta_i)\mathbf{i} + \sin(\theta_i)\mathbf{j}$ is a unit vector in the normal direction, and $\mathbf{v} = -\sin(\theta_i)\mathbf{i} + \cos(\theta_i)\mathbf{j}$ is perpendicular to $\mathbf{n}$. In the new coordinate system we have

$$\mathbf{d}_i = (\mathbf{d}_i \cdot \mathbf{n})\mathbf{n} + (\mathbf{d}_i \cdot \mathbf{v})\mathbf{v}. \tag{4.2}$$

Using the Law of Reflection,

$$\mathbf{d}_r = -(\mathbf{d}_i \cdot \mathbf{n})\mathbf{n} + (\mathbf{d}_i \cdot \mathbf{v})\mathbf{v}. \tag{4.3}$$

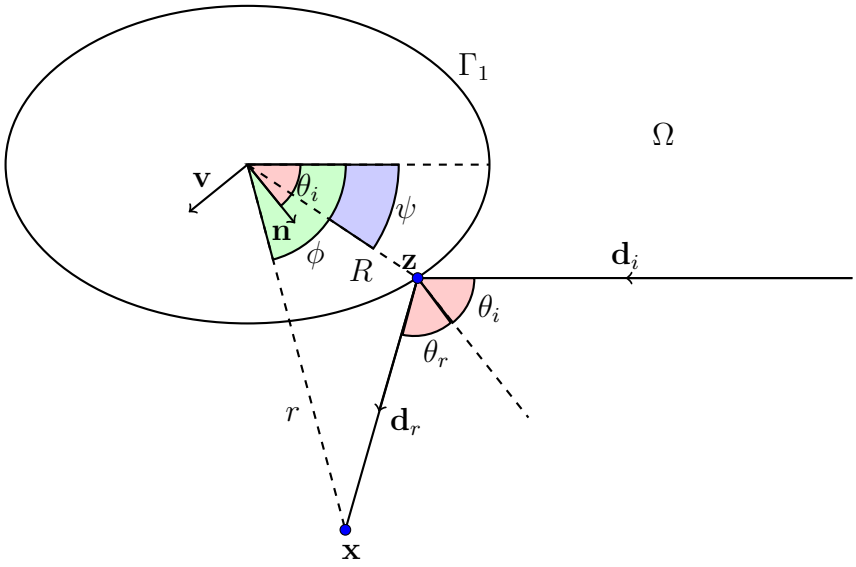

Figure 4.3: The set-up of scattering by a smooth convex obstacle.

As per Figure 4.3, the point $\mathbf{x}$ is on the line $\{\mathbf{z} + t\mathbf{d}_r; t \geq 0\}$ if and only if

$$\mathbf{x} = \mathbf{z} + t\mathbf{d}_r \tag{4.4}$$

for some $t \geq 0$. From (4.4) and (4.3) we have

$$\mathbf{x} = \mathbf{z} + t\left((-\mathbf{d}_i \cdot \mathbf{n})\mathbf{n} + (\mathbf{d}_i \cdot \mathbf{v})\mathbf{v}\right), \tag{4.5}$$

and so it follows by taking the scalar (dot) product with $\mathbf{n}$ and $\mathbf{v}$, that

$$\mathbf{x} \cdot \mathbf{n} = \mathbf{z} \cdot \mathbf{n} - t\mathbf{d}_i \cdot \mathbf{n} \tag{4.6}$$

and

$$\mathbf{x} \cdot \mathbf{v} = \mathbf{z} \cdot \mathbf{v} + t\mathbf{d}_i \cdot \mathbf{v}. \tag{4.7}$$

Writing $\mathbf{x} = x\mathbf{i} + y\mathbf{j}$, we have

$$x\cos(\theta_i) + y\sin(\theta_i) = \mathbf{z} \cdot \mathbf{n} + t\cos(\theta_i) \tag{4.8}$$

and

$$-x\sin(\theta_i) + y\cos(\theta_i) = \mathbf{z} \cdot \mathbf{v} + t\sin(\theta_i). \tag{4.9}$$

Multiplying (4.8) by $\sin(\theta_i)$ and (4.9) by $\cos(\theta_i)$ and taking the difference, we are left with

$$\begin{aligned} x\sin(2\theta_i) - y\cos(2\theta_i) &= \mathbf{z}\cdot(\mathbf{n}\sin(\theta_i) - \mathbf{v}\cos(\theta_i)) \\ &= R(\psi)\sin(2\theta_i - \psi). \end{aligned} \tag{4.10}$$

Now writing $\mathbf{x}$ in polar cordinate form, $\mathbf{x} = (r\cos(\phi), r\sin(\phi))$, where r is the radial distance from the origin and ϕ is the angle measured from the positive x axis (as shown in Figure 4.3), (4.10) can be written as

$$\hat{f}(\theta_i, \psi) := \frac{r}{R(\psi)}\sin(2\theta_i - \phi) - \sin(2\theta_i - \psi) = 0. \tag{4.11}$$

At $\mathbf{z}$, the unit tangent vector is given by

$$\mathbf{s}(\psi) = \lim_{\delta\psi\to 0}\frac{\mathbf{z}(\psi+\delta\psi) - \mathbf{z}(\psi)}{|\mathbf{z}(\psi+\delta\psi) - \mathbf{z}(\psi)|} \tag{4.12}$$

in other words,

$$\mathbf{s}(\psi) = \frac{\mathbf{z}'(\psi)}{|\mathbf{z}'(\psi)|} \tag{4.13}$$

where $\mathbf{z}'(\psi) = (R'(\psi)\cos(\psi) - R(\psi)\sin(\psi), R'(\psi)\sin(\psi) + R(\psi)\cos(\psi))$. We find the unit normal $\mathbf{n} = (n_1, n_2)$ at $\mathbf{z}$ using $\mathbf{s}\cdot\mathbf{n} = 0$, thus taking

$$\mathbf{n} = \frac{(R'(\psi)\sin(\psi) + R(\psi)\cos(\psi), -R'(\psi)\cos(\psi) + R(\psi)\sin(\psi))}{\sqrt{(R'(\psi)\cos(\psi) - R(\psi)\sin(\psi))^2 + (R'(\psi)\sin(\psi) + R(\psi)\cos(\psi))^2}}. \tag{4.14}$$

To find θ_i, the angle between the incident ray and the normal $\mathbf{n}$ at $\mathbf{z}$, we then use the sine rule to obtain

$$\frac{n_2}{\sin(\theta_i)} = \frac{|\mathbf{n}|}{\sin(\pi/2)} = 1. \tag{4.15}$$

Using this to eliminate θ_i in (4.11), we are left with an equation for ψ. Defining

$$f(\psi) := \frac{r}{R(\psi)}\sin(2\arcsin(n_2) - \phi) - \sin(2\arcsin(n_2) - \psi), \tag{4.16}$$

our point of reflection is given by (4.1), i.e. by

$$\mathbf{z} = (R(\psi)\cos(\psi), R(\psi)\sin(\psi)),$$

where $\psi \in (-\pi/2, \pi/2]$ is the value which satisfies

$$f(\psi) = 0. \tag{4.17}$$

We can find solutions to (4.17) using the bisection algorithm. We discuss this method for finding solutions of (4.17) in more detail in §4.1.1.

Once the ray directions have been obtained, we can then use them as an aid to enhance the approximation in our discretised domain. For points inside a single element we would expect the local scattered field to be propagating in the ray direction, but we would also expect there to be some curvature of the wave fronts. We can use the point of reflection $\mathbf{z}$ and angle of reflection θ_i to find the intersection of rays from points which are close to one another, in order to find an originating centre of curvature. Given a point $\mathbf{x}$, let a second point $\mathbf{x_0}$ have a distance from the origin r_0, and angle ϕ_0 between the point and the x axis. Let rays through $\mathbf{x}_0$ be at an angle of reflection θ_0, having reflected off the scatterer at the point $\mathbf{z_0}$. For the two points $\mathbf{x} = (x, y)$ and $\mathbf{x_0} = (x_0, y_0)$, if we extend the rays that travel through these points back through the scatterer Ω^+, they will cross at some point $\mathbf{x_C}$ either within or on the opposite side of the scatterer. This setup is illustrated in Figure 4.4. Using this idea, we can write

$$\mathbf{x_C} = \mathbf{z} + \tilde{\lambda}(\mathbf{x} - \mathbf{z}) \tag{4.18}$$

and

$$\mathbf{x_C} = \mathbf{z_0} + \tilde{\lambda}_0(\mathbf{x_0} - \mathbf{z_0}) \tag{4.19}$$

where $\tilde{\lambda}$ and $\tilde{\lambda}_0$ are to be found. By equating the right hand sides of (4.18) and (4.19) and writing the points $\mathbf{z}$, $\mathbf{z_0}$, $\mathbf{x}$ and $\mathbf{x_0}$ in their polar coordinate form, we are left with two equations,

$$R(\psi)\cos(\psi) + \tilde{\lambda}(r\cos(\phi) - R(\psi)\cos(\psi)) = R(\psi_0)\cos(\psi_0) + \tilde{\lambda_0}(r_0\cos(\phi_0) - R(\psi_0)\cos(\psi_0)) \tag{4.20}$$

and

$$R(\psi)\sin(\psi) + \tilde{\lambda}(r\sin(\phi) - R(\psi)\sin(\psi)) = R(\psi_0)\sin(\psi_0) + \tilde{\lambda_0}(r_0\sin(\phi_0) - R(\psi_0)\sin(\psi_0)). \tag{4.21}$$

Through rearranging and substituting for $\tilde{\lambda}_0$, we obtain the equation for

$$\tilde{\lambda} = \frac{T}{B}. \tag{4.22}$$

where

$$\begin{aligned} T &= (r_0\cos(\phi_0) - R(\psi_0)\cos(\psi_0)) \times (R(\psi_0)\sin(\psi_0) - R(\psi)\sin(\psi)) \\ &\quad +(R(\psi)\cos(\psi) - R(\psi_0)\cos(\psi_0)) \times (r_0\sin(\phi_0) - R(\psi_0)\sin(\psi_0)) \\ &= r_0R(\psi_0)\sin(\psi_0 - \phi_0) + R(\psi)r_0\sin(\phi_0 - \psi) \\ &\quad +R(\psi_0)R(\psi)\sin(\psi - \psi_0) \end{aligned} \tag{4.23}$$

and

$$\begin{aligned} B &= (r_0\cos(\phi_0) - R(\psi_0)\cos(\psi_0)) \times (r\sin(\phi) - R(\psi)\sin(\psi)) \\ &\quad -(r\cos(\phi) - R(\psi)\cos(\psi)) \times (r_0\sin(\phi_0) - R(\psi_0)\sin(\psi_0)) \\ &= r_0r\sin(\phi - \phi_0) + R(\psi)r_0\sin(\phi_0 - \psi) \\ &\quad +R(\psi_0)r\sin(\psi_0 - \phi) + R(\psi)R(\psi_0)\sin(\psi - \psi_0). \end{aligned} \tag{4.24}$$

As we are considering points close to each other, we also consider the limit as $\theta \to \theta_0$, and so it follows that $\phi \to \phi_0$ and $\psi \to \psi_0$. In the current form however an indeterminate form may arise, in which case the use of l'Hôpital's Rule is required. We define

$$\lambda^* := \lim_{\psi\to\psi_0} \tilde{\lambda} = \lim_{\psi\to\psi_0} \frac{\frac{\partial T}{\partial \psi_0}}{\frac{\partial B}{\partial \psi_0}} \tag{4.25}$$

To calculate the centre of curvature for a circular wave (to be used in our UWVF basis) propagating in an element we take the point $\mathbf{x}$ in (4.18) to be the centroid of each element. The limiting value of $\tilde{\lambda}$ in (4.25) with $r = r_0$, is then substituted into (4.18). This is a realistic way of finding the centre of curvature $\mathbf{x_C}$, as the points within each element are close together, so we have $\theta \to \theta_0$ and $r \to r_0$. Thus overall we have

$$\mathbf{x_C} = \mathbf{z} + \lambda^*(\mathbf{x} - \mathbf{z}). \tag{4.26}$$

This is illustrated in Figure 4.4.

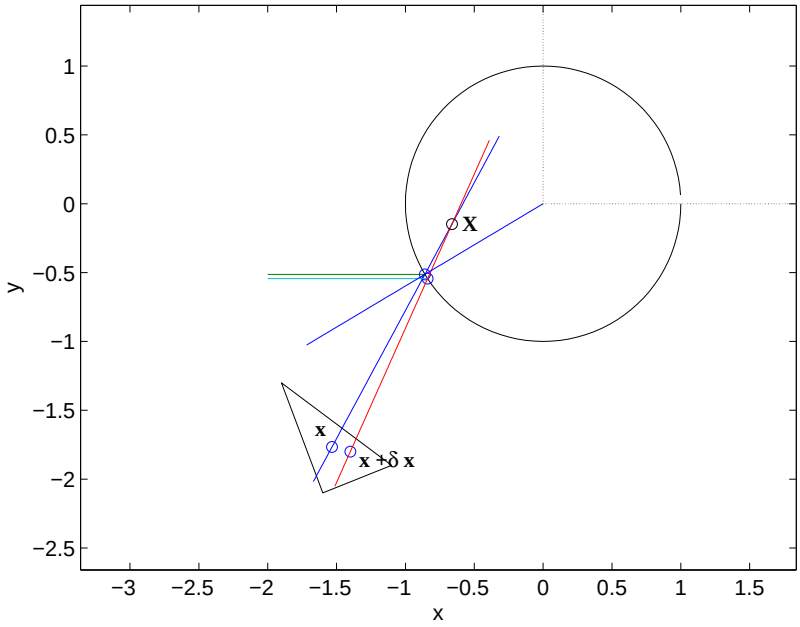

Figure 4.4: Rays through points $\mathbf{x}$ and $\mathbf{x} + \delta\mathbf{x}$ cross at the point $\mathbf{X}$. The centre of curvature of wavefronts at x is $x_C = \lim_{\delta\mathbf{x}\to 0} \mathbf{X}$.

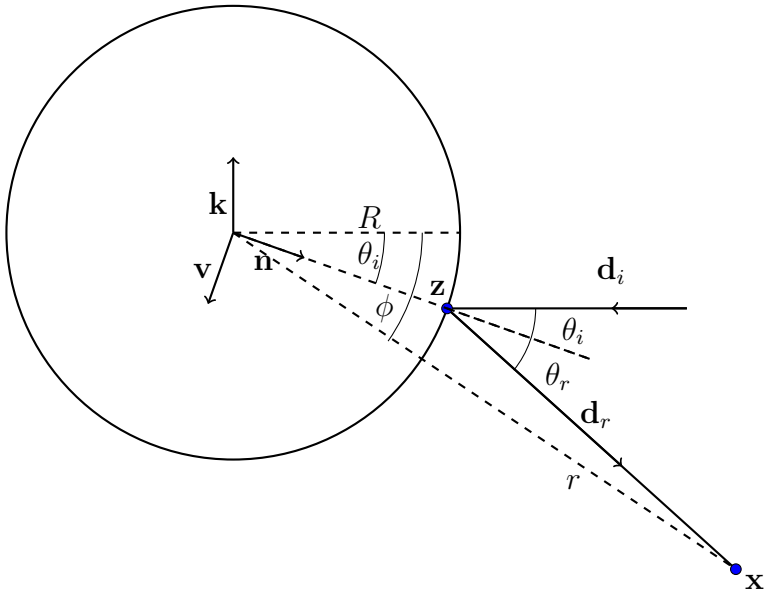

Figure 4.5: The set-up of scattering by a circle.

4.1.1 Ray Tracing for Scattering by a Circle

As an initial study we first consider the simple case of scattering by a circle, $C_R(0,0)$, of radius R centred at the origin. This is a good test case to use as the exact solution is known, allowing calculation of errors to test for improved accuracy. We again do the ray tracing theory for an incident field from the $+\infty$ direction, so $u^i(\mathbf{x}) = \exp(-i\kappa x)$, and maintain the boundary of the circular scatterer $\Gamma_1 = (R\cos(\theta), R\sin(\theta))$ where $R > 0$ is the (now constant) radius of the circle, and $\theta \in [-\pi, \pi)$.

We use the same set up as presented in §4.1, with unit incident and reflected direction vectors $|\mathbf{d}_i| = 1$, $|\mathbf{d}_r| = 1$, and $\mathbf{d}_i = -\mathbf{i}$. We again use the independent coordinate system $(\mathbf{v}, \mathbf{n})$ as per Figure 4.5, where $\mathbf{n} = \cos(\theta_i)\mathbf{i} + \sin(\theta_i)\mathbf{j}$ and $\mathbf{v} = -\sin(\theta_i)\mathbf{i} + \cos(\theta_i)\mathbf{j}$, and equations (4.2–4.4) still hold. However as we are now considering a circular scatterer rather than a general convex obstacle, through a priori knowledge of the geometry of the circle (that the surface normal is in the radial direction), we know that the angle for our point of reflection $\mathbf{z}$ is equal to the angle of reflection, $\psi = \theta_i$. As per Figure 4.5, we have our reflection point on the surface of the scatterer

$$\mathbf{z} = R\mathbf{n}. \tag{4.27}$$

As the circle is a special case with the property $\psi = \theta_i$, we can use the equality to eliminate ψ in (4.11), rather than eliminating θ_i to obtain (4.16). We are left with a simpler equation to solve for θ_i. We define

$$f(\theta_i) := \sin(2\theta_i - \phi) - \upsilon \sin(\theta_i), \tag{4.28}$$

where $\upsilon = R/r \in (0, 1]$. The angle of incidence and reflection is given by θ_i, the value for which

$$f(\theta_i) = 0, \tag{4.29}$$

and our point of reflection between the ray and the circular scatterer is given by $\mathbf{z} = (R\cos(\theta_i), R\sin(\theta_i))$.

An example of (4.28) is shown in Figure 4.6 for a point $\mathbf{x} = (2, 2)$. As can be seen, there are multiple solutions of $\frac{x}{R}\sin(2\theta) - \frac{y}{R}\cos(2\theta) - \sin(\theta) = 0$ ($f(\theta)$ rearranged) for $\theta \in [-\pi, \pi)$. The correct solution corresponds to taking θ_i as the angle of incidence and reflection as measured from the exterior normal (outwards into Ω). The remaining solution corresponds to θ_i being measured from the interior normal (into Ω^+), if the incident ray was interacting with the scatterer on its interior. To find the appropriate solution we use the bisection algorithm, using our knowledge of the physical setup to set an appropriate starting interval. As the total angle between the incident and reflected ray is $\theta_i + \theta_r = 2\theta_i$, we actually require $\theta_i \in [-\pi/2, \pi/2]$. For points $\mathbf{x} = (x, y) = (r\cos(\phi), r\sin(\phi))$ with $x > 0$, we require our solution θ_i to satisfy $|\phi|/2 \leq |\theta_i| \leq |\phi|$ and so we use this for our starting bounds for the bisection algorithm. When $x > 0$ and $y = 0$ we have the solution $\theta_i = 0$. When $x < 0$ we take $\theta_i \in (0, \pi/2]$ for $y > R$ and $\theta_i \in [-\pi/2, 0)$ for $y < R$. In the shadow region Ω_{shadow} (see Figure 4.2) where $x < 0$ and $|y| < R$ there is no solution ($\theta_i = \pi/2$ is included here).

Continuing with the structure of §4.1, we now use the point of reflection $\mathbf{z}$ and angle of reflection θ_i in order to find an originating centre of curvature. We again use equations (4.18) and (4.19), write the points in polar coordinates, rearrange, and substitute for λ_0 (see §4.1 for details). We obtain (4.22) for the circle,

$$\tilde{\lambda} = \frac{R(R\sin(\theta_i - \theta_0) + r_0[\sin(\phi_0 - \theta_i) + \sin(\theta_0 - \phi_0)])}{R^2\sin(\theta_i - \theta_0) + R[r_0\sin(\phi_0 - \theta_i) + r\sin(\theta_0 - \phi)] + rr_0\sin(\phi - \phi_0)}. \tag{4.30}$$

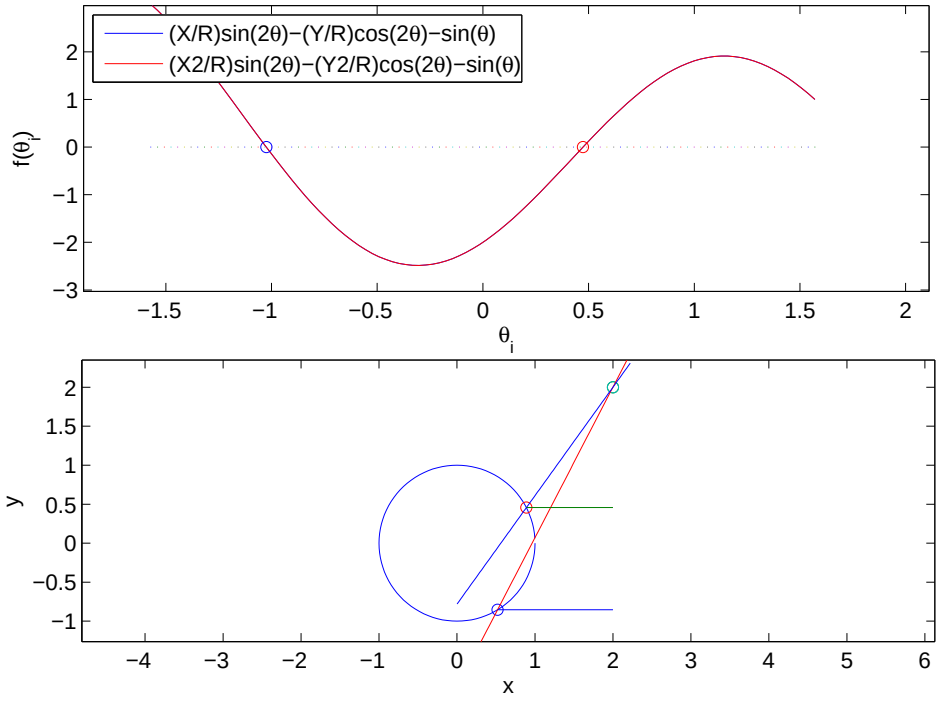

Figure 4.6: Multiple solutions of equation (4.29) for a point $\mathbf{x} = (2, 2)$. The correct solution and reflection point $\mathbf{z}$ shown by the red circles, the incorrect solution and reflection point shown by the blue circles.

As we are considering points close to each other, we also consider (4.25), this time however using the limit as $\theta_i \to \theta_0$, $\phi \to \phi_0$ as for the circle $\theta_i = \psi$. Using l'Hôpital's Rule, we have

$$\lim_{\theta_i \to \theta_0} \tilde{\lambda} = \frac{-R^2 + Rr_0 \cos(\theta_i - \phi)}{-R^2 + (2 - \frac{\nu \cos(\theta_i)}{\cos(2\theta_i - \phi)})(Rr_0 \cos(\phi - \theta_i) - rr_0) + Rr \cos(\theta_i - \phi)} \tag{4.31}$$

Each of these values for $\tilde{\lambda}$ give a fairly good approximation of our intersection point. As illustrated in Figure 4.7, the intersection points calculated using (4.31) in (4.19) get better as $\theta_i \to \theta_0$, and the value of $\tilde{\lambda}$ using (4.30) approaches the limiting value from (4.31), as shown in Figure 4.8.

To calculate a single centre of curvature for a circular wave propagating in an element, we take the point $\mathbf{x}$ in (4.18) to be the centroid of the element. The limiting

value of $\tilde{\lambda}$ in (4.31) with $r = r_0$, is then substituted into (4.18). This is a realistic way of finding the centre of curvature $\mathbf{x_C}$, as the points within each element are close together, so we have $\theta_i \to \theta_0$ and $r \to r_0$. Thus overall we have (4.26),

$$\mathbf{x_C} = \mathbf{z} + \lambda^*(\mathbf{x} - \mathbf{z}),$$

with

$$\lambda^* = \frac{-R^2 + Rr\cos(\theta_i - \phi)}{-R^2 + (2 - \frac{\nu\cos(\theta_i)}{\cos(2\theta_i - \phi)})(Rr\cos(\phi - \theta_i) - r^2) + Rr\cos(\theta_i - \phi)}. \tag{4.32}$$

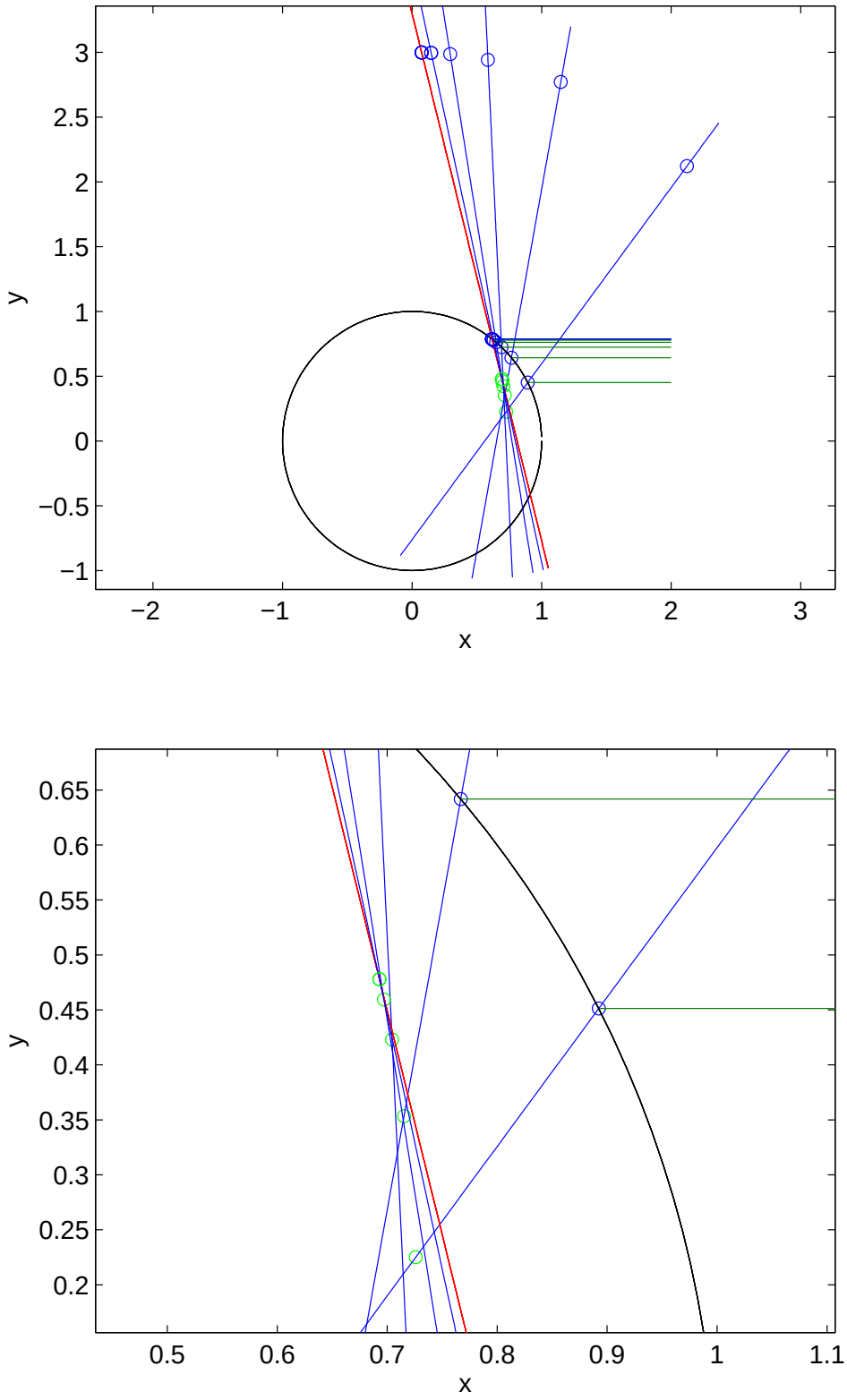

Figure 4.7: Approximations of intersection of the red and blue rays using (4.31), shown by green circle markers. Improving as $\theta_i \to \theta_0$.

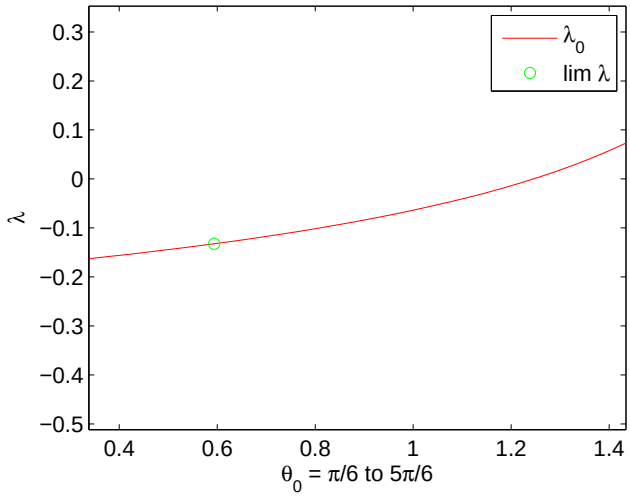

Figure 4.8: $\tilde{\lambda}$ using (4.30) approaches the limiting value from (4.31)

4.1.2 Ray Tracing for Scattering by an Ellipse

We now consider the use of our ray tracing algorithm detailed in §4.1 for the case of scattering by an ellipse. This is a more challenging test case than the circle as there are fewer symmetrical properties. We continue with the ray tracing theory detailed in §4.1, with an incident field $u_i(\mathbf{x}) = \exp(-i\kappa x)$, and then reflect all results in the y-axis in later numerical experiments. Define the boundary of the ellipse scatterer by $\Gamma_1 = (R(\theta)\cos(\theta), R(\theta)\sin(\theta))$ where $\theta \in [-\pi, \pi)$, and $R(\theta) > 0$ is the radius of the ellipse given by

$$R(\theta) = \frac{ab}{\sqrt{b^2\cos^2(\theta) + a^2\sin^2(\theta)}}. \tag{4.33}$$

where a and b are the lengths of the major and minor semi-axis respectively. In parametric form, the boundary can be written as

$$\Gamma_1 = (a\cos(t), b\sin(t)),$$

for $t \in [0, 2\pi)$ [72]. The incident ray interacts with the scatterer at the point given by (4.1),

$$\mathbf{z} = (R(\psi)\cos(\psi), R(\psi)\sin(\psi)), \tag{4.34}$$

and reflects at an angle of reflection θ_i.

The ellipse is a particular case of a smooth convex obstacle, as considered in §4.1. We proceed in the same manner as for the case of scattering by a general convex obstacle. Again we use the independant coordinate system $(\mathbf{v}, \mathbf{n})$ as per Figure 4.3, where $\mathbf{n} = \cos(\theta_i)\mathbf{i} + \sin(\theta_i)\mathbf{j}$ and $\mathbf{v} = -\sin(\theta_i)\mathbf{i} + \cos(\theta_i)\mathbf{j}$. The derivation in equations (4.2)–(4.11) all hold. To eliminate θ_i in (4.11), we use $\mathbf{n}$ as in (4.14) with

$$R'(\psi) = \frac{ab(b^2 - a^2)\sin(\psi)\cos(\psi)}{(b^2\cos^2(\psi) + a^2\sin^2(\psi))^{3/2}}. \tag{4.35}$$

This is then used in (4.15), and so we can solve an equation for ψ. Using definition (4.16),

$$f(\psi) := \frac{r}{R(\psi)}\sin(2\arcsin(n_2) - \phi) - \sin(2\arcsin(n_2) - \psi),$$

the value ψ such that $f(\psi) = 0$ gives our point of reflection between the ray and the circular scatterer, $\mathbf{z} = (R(\psi)\cos(\psi), R(\psi)\sin(\psi))$. We again find solutions to (4.17) using the bisection algorithm.

Continuing with the structure of §4.1, we seek to find a centre of curvature for wave fronts over an element. For two points $\mathbf{x} = (x, y)$ and $\mathbf{x_0} = (x_0, y_0)$ in the domain, and their respective points of reflection $\mathbf{z} = (R(\psi)\cos(\psi), R(\psi)\sin(\psi))$ and $\mathbf{z_0} = (R(\psi_0)\cos(\psi_0), R(\psi_0)\sin(\psi_0))$, we can use these to find the intersection of rays from points which are close to one another. Following the arguments in §4.1, we need to consider (4.18)–(4.19). Equating the right hand sides and writing the points in polar form, we obtain equations (4.20)–(4.21). Through rearranging and substituting for $\tilde{\lambda}_0$, we obtain the equation (4.22),

$$\tilde{\lambda} = \frac{T}{B},$$

where T is given by (4.23),

$$\begin{aligned} T &= r_0 R(\psi_0)\sin(\psi_0 - \phi_0) + R(\psi) r_0 \sin(\phi_0 - \psi) \\ &\quad + R(\psi_0)R(\psi)\sin(\psi - \psi_0) \end{aligned}$$

and B is given by (4.24),

$$\begin{aligned} B &= r_0 r \sin(\phi - \phi_0) + R(\psi) r_0 \sin(\phi_0 - \psi) \\ &\quad + R(\psi_0) r \sin(\psi_0 - \phi) + R(\psi)R(\psi_0)\sin(\psi - \psi_0). \end{aligned}$$

As we are considering points close to each other, we also consider the limit as $\psi \to \psi_0$. Using l'Hôpital's Rule, we have

$$\lim_{\psi \to \psi_0} \tilde{\lambda} = \lim_{\psi \to \psi_0} \frac{\frac{\partial T}{\partial \psi_0}}{\frac{\partial B}{\partial \psi_0}} \tag{4.36}$$

with

$$\begin{aligned} \frac{\partial T}{\partial \psi_0} &= r_0 \big(R'(\psi_0)\sin(\psi_0 - \phi_0) + R(\psi_0)\cos(\psi_0 - \phi_0) \\ &+ \frac{\partial \phi_0}{\partial \psi_0} \left(R(\psi_0)\cos(\psi_0 - \phi_0) + R(\psi)\cos(\phi_0 - \psi) \right) \big) \\ &+ R(\psi)\left(R'(\psi_0)\sin(\psi - \psi_0) - R(\psi_0)\cos(\psi - \psi_0) \right) \end{aligned} \tag{4.37}$$

and

$$\begin{aligned} \frac{\partial B}{\partial \psi_0} &= R(\psi_0)\left(r\cos(\psi_0 - \phi) - R(\psi)\cos(\psi - \psi_0) \right) \\ &+ R'(\psi_0)\left(r\sin(\psi_0 - \phi) + R(\psi)\sin(\psi - \psi_0) \right) \\ &+ \frac{\partial \phi_0}{\partial \psi_0} r_0 \left(R(\psi)\cos(\phi_0 - \psi) - r\cos(\phi - \phi_0) \right), \end{aligned} \tag{4.38}$$

and where

$$\frac{\partial\phi_0}{\partial\psi_0} = \frac{2}{\sqrt{1-n_2^2}} - \frac{R'(\psi_0)\sin(2\arcsin(n_2)-\psi_0) - R(\psi_0)\cos(2\arcsin(n_2)-\psi_0)(\frac{2}{\sqrt{1-n_2^2}}-1)}{r\cos(2\arcsin(n_2)-\phi_0)},$$

obtained by differentiating (4.16) with respect to ψ_0 and rearranging.

To calculate the centre of curvature for a cylindrical wave travelling over an element we take the point $\mathbf{x}$ in (4.18) to be the centroid of each element. The limiting value of $\tilde{\lambda}$ in (4.36) with $r = r_0$, is then substituted into (4.18). This is a realistic way of finding the centre of curvature $\mathbf{x_C}$, as the points within each element are close together, so we have $\theta \to \theta_0$ and $r \to r_0$. Thus overall we have

$$\mathbf{x_C} = \mathbf{z} + \lambda^*(\mathbf{x} - \mathbf{z}) \tag{4.39}$$

with

$$\lambda^* = \frac{r\left(R'(\psi)\sin(\psi-\phi) + R(\psi)\cos(\psi-\phi)(1+2\frac{\partial\phi}{\partial\psi})\right) - R^2(\psi)}{R(\psi)r\cos(\psi-\phi) - R^2(\psi) + R'(\psi)r\sin(\psi-\phi) + \frac{\partial\phi}{\partial\psi}\left(R(\psi)r\cos(\phi-\psi) - r^2\right)}. \tag{4.40}$$

4.2 Exact and Reference Solutions

The ray-traced centres of curvatures computed in §4.1 are to be used to enrich the basis when approximating wave scattering by a smooth convex obstacle using the UWVF. In order to find the level of accuracy achieved for the two cases we explore, the circle and the ellipse, we require a reference solution with which errors can be computed. Here we present the exact solution for the circle in §4.2.1, and for the ellipse in §4.2.2. However, the exact solution for the elliptical case is presented for completeness alone: due to the difficulty in evaluating the Mathieu functions required for the exact solution for the ellipse, we instead used a MFS solution as detailed in §4.2.3 as a reference solution.

4.2.1 The Exact Solution for a Circular Scatterer.

We now present the known exact solution for the problem of acoustic wave scattering by a circle for a plane wave incident field, so that it can be used for measuring the accuracy of our ray-traced centres of curvature and the solutions produced by the UWVF. The exact solution can be represented in the form of an eigenfunction expansion (see [49]). The incident wave when coming from $-\infty$ in the x direction, $u^i = \exp(\mathrm{i}\kappa x)$, can be written in polar coordinates as

$$u^i(r,\theta) = \sum_{m=0}^{\infty} \varepsilon_m \mathrm{i}^m J_m(\kappa r)\cos(m\theta), \tag{4.41}$$

[49, eqn. 2.77], and the outgoing diffracted field can be written as

$$u^d(r,\theta) = \sum_{m=0}^{\infty} a_m \varepsilon_m \mathrm{i}^m H_m^{(1)}(\kappa r)\cos(m\theta), \tag{4.42}$$

[49, eqn. 2.78] where ε_m is the Neumann symbol defined as

$$\varepsilon_m = \begin{cases} 1, & \text{for } m = 0, \\ 2, & \text{for } m \geq 1, \end{cases} \tag{4.43}$$

and $J_m(z)$ is a Bessel function of the first kind of order m centred at z. By applying Dirichlet boundary conditions (the total field $u = 0$) on the boundary of a circular

scatterer $C_R(0,0)$ centred at the origin with radius R, we can obtain the coefficients a_m. Thus the total field u is given by

$$u(r,\theta) = \sum_{m=0}^{\infty} \varepsilon_m \mathrm{i}^m \left(J_m(\kappa r) - \frac{J_m(\kappa R)}{H_m^{(1)}(\kappa R)} H_m^{(1)}(\kappa r) \right) \cos(m\theta) \tag{4.44}$$

and the scattered field u^s is given by

$$u^s(r,\theta) = \sum_{m=0}^{\infty} \varepsilon_m \mathrm{i}^m \frac{-J_m(\kappa R)}{H_m^{(1)}(\kappa R)} H_m^{(1)}(\kappa r) \cos(m\theta). \tag{4.45}$$

In the case of Neumann boundary conditions ($\partial u/\partial n = 0$ on the boundary of the circular scatterer), the scattered field is given by

$$u^s(r,\theta) = \sum_{m=0}^{\infty} \varepsilon_m \mathrm{i}^m \left(\frac{-J_m'(\kappa R)}{H_m^{(1)'}(\kappa R)} H_m^{(1)}(\kappa r) \right) \cos(m\theta). \tag{4.46}$$

In practice, as we cannot evaluate an infinite sum in our numerical computations, we have to truncate the series. If we consider the error in approximating our incident field by a series truncated after N terms,

$$E_N = u^i - u_N^i = \sum_{m=N+1}^{\infty} \varepsilon_m \mathrm{i}^m J_m(\kappa r) \cos(m\theta), \tag{4.47}$$

it follows that

$$|E_N| \;\leq\; 2 \sum_{m=N+1}^{\infty} |J_m(\kappa r)|. \tag{4.48}$$

Using [3, 9.1.62], that for $z \geq 0$ fixed and $m \geq 1/2$,

$$|J_m(z)| \leq \frac{|\frac{1}{2}z|^m}{\Gamma(m+1)} = \frac{|z|^m}{2^m m!},$$

it follows that

$$\begin{aligned}
|E_N| &\leq 2 \sum_{m=N+1}^{\infty} \frac{(\frac{\kappa r}{2})^m}{m!} \\
&= 2 \left(\frac{\kappa r}{2}\right)^{N+1} \frac{1}{(N+1)!} \sum_{m=0}^{\infty} \frac{(\frac{\kappa r}{2})^m (N+1)!}{(N+1+m)!} \\
&\leq 2 \left(\frac{\kappa r}{2}\right)^{N+1} \frac{1}{(N+1)!} \sum_{m=0}^{\infty} \frac{(\frac{\kappa r}{2})^m}{m!} \\
&= 2 \left(\frac{\kappa r}{2}\right)^{N+1} \frac{1}{(N+1)!} \exp(\kappa r/2).
\end{aligned} \tag{4.49}$$

By [3, 6.1.38],

$$(N+1)! \geq \sqrt{2\pi}(N+1)^{N+3/2}\exp(-N-1), \tag{4.50}$$

and so

$$|E_N| \leq \sqrt{\frac{2}{\pi(N+1)}}\exp(\kappa r/2)\left(\frac{\mathrm{e}\kappa r}{2(N+1)}\right)^{N+1}. \tag{4.51}$$

To achieve an error in our truncated series that is less than a set tolerance ϵ, we find the appropriate N to truncate the series at by finding the zero of the function

$$\tilde{f}(\tilde{N}) = \sqrt{\frac{2}{\pi\tilde{N}}}\exp(\kappa r/2)\left(\frac{\mathrm{e}\kappa r}{2\tilde{N}}\right)^{\tilde{N}} - \epsilon. \tag{4.52}$$

It is necessary to start with $N > \frac{\mathrm{e}\kappa r}{2} - 1$, as

$$\left(\frac{\mathrm{e}\kappa r}{2(N+1)}\right)^{N+1} \to 0$$

provided

$$\left(\frac{\mathrm{e}\kappa r}{2(N+1)}\right) < 1,$$

ensuring $\tilde{f}$ will be decreasing. For any N greater than the $\tilde{N}$ for which $\tilde{f} = 0$, the error in the truncation of the series will be less than ϵ. We set $\epsilon = 10^{-8}$ and use the Matlab root finding function fzero to find the appropriate term after which to truncate the series. This requires inputs of a function handle for the function for which the root is required, $\tilde{f}$, and we provide as an initial value $N = \frac{\mathrm{e}\kappa r}{2} - 1$.

4.2.2 The Exact Solution for Scattering by an Ellipse

As is the case for scattering by a circle, there exists a known solution for exterior scattering by an ellipse. It comes in the form of an infinite series of Mathieu functions. In practice this solution is rarely used however, due to the difficulty in computing Mathieu functions [49]. However, we present the solution here for completeness. As detailed in [33], the solution is represented in terms of elliptic coordinates (μ, η), which are related to Cartsesian coordinates (x, y) by

$$x = s\cosh(\mu)\cos(\eta), \tag{4.53}$$

and

$$y = s\sinh(\mu)\sin(\eta), \tag{4.54}$$

where s describes the location of the foci of the ellipse. We set a parameter q to satisfy $\sqrt{q} = \kappa s/2$, and consider the scatterer boundary Γ_1 on which $\mu = \hat{a}$, a constant. Let $ce_r(\eta, q)$ and $se_r(\eta, q)$ denote angular functions that satisfy Mathieu's differential equation

$$\frac{d^2y}{d\eta^2} - (\hat{\lambda} - 2q\cosh(2\eta))y = 0, \tag{4.55}$$

where the seperation constant $\hat{\lambda}$ is denoted by a_r and b_r for ce_r and se_r respectively. Let $Mc_r^{(3)}(\mu, q)$, $r = 0, 1, ...$ and $Ms_r^{(3)}(\mu, q)$, $r = 1, 2, ...$ denote the radial Mathieu-Hankel functions, as given in [3]. These satisfy Mathieu's modified differential equation

$$\frac{d^2y}{d\mu^2} - (\hat{\lambda} - 2q\cosh(2\mu))y = 0, \tag{4.56}$$

where again the seperation constant $\hat{\lambda}$ is denoted by a_r and b_r for $Mc_r^{(3)}$ and $Ms_r^{(3)}$ respectively. The solution of the exterior scattering problem for $\mu \geq \hat{a}$ is given by

$$\begin{aligned} u^E(\mu,\eta) &= \frac{1}{\pi}\sum_{r=0}^{\infty}\frac{Mc_r^{(3)}(\mu,q)}{Mc_r^{(3)}(a,q)}ce_r(\eta,q)\int_0^{2\pi}u^E(a,\eta')ce_r(\eta',q)d\eta' \\ &+ \frac{1}{\pi}\sum_{r=0}^{\infty}\frac{Ms_r^{(3)}(\mu,q)}{Ms_r^{(3)}(a,q)}se_r(\eta,q)\int_0^{2\pi}u^E(a,\eta')se_r(\eta',q)d\eta'. \end{aligned} \tag{4.57}$$

For more information on this exact solution see [33, §4.4]. Due to the difficulty in computing Mathieu functions needed to evalute (4.57), we do not use (4.57) as an exact solution with which to reference our UWVF solutions to. In the following §4.2.3 we present an alternative, the MFS solution, with which we can compare our UWVF results to.

4.2.3 The Method of Fundamental Solutions for Scattering by an Ellipse

Due to the computational difficulty of evaluating the Mathieu function representation of the solution of scattering by an ellipse (see §4.2.2), we instead use the MFS, as detailed

in 2.2.1 and [9], to find a reference solution (which we take as being "exact" for the purpose of computing errors). For the purpose of computing a reference solution, the MFS represents a fast, reliable, and relatively easy to program option. However, the number of degrees of freedom in MFS scales with the wavenumber [9]. We investigate the use of ray-traced basis functions in the UWVF, in the hope that we will have a scheme for which the number of degrees of freedom will grow at a sublinear rate as the wavenumber increases.

We find a solution $u^{(N)}$ in the form of (2.9), a linear combination of N fundamental solutions

$$u(\mathbf{x}) \approx u^{(N)}(\mathbf{x}) = \frac{\mathrm{i}}{4}\sum_{j=1}^{N} \alpha_j H_0^1(k|\mathbf{x}-\mathbf{y}_j|) \qquad \mathbf{y}_j \in \mathbb{R}^2 \backslash \overline{\Omega}.$$

The $\mathbf{y}_j$ are the source points of the fundamental solutions. These are chosen to lie equi-spaced along a smooth closed curve Γ^E on the exterior of the domain, i.e. the interior of the ellipse, such that Γ^E and Γ_1 are distinct, $\mathrm{dist}(\Gamma_1, \Gamma^E) > 0$. The curve Γ^E is taken to be an ellipse with major and minor axis $\epsilon := \lambda/3$ less than the scatterer ellipse Γ_1, so source points are positioned at $\mathbf{y}_j = ((a-\epsilon)\cos(\psi_j), (b-\epsilon)\sin(\psi_j))$ for $\psi_j = 2\pi j/N$, $j = 1, ..., N$. This set-up is illustrated in Figure 4.9.

We look for a solution in the form

$$u(\mathbf{x}) \quad = \quad u^i(\mathbf{x}) + \int_{\Gamma^E} \left(\frac{\partial \Phi(\mathbf{x},\mathbf{y})}{\partial \mathbf{n}(\mathbf{y})} - \mathrm{i}\kappa\Phi(\mathbf{x},\mathbf{y}) \right) \hat{\alpha}(\mathbf{y}) ds(\mathbf{y}). \tag{4.58}$$

Here $\Phi(\mathbf{x},\mathbf{y}) = \frac{\mathrm{i}}{4}H_0^1(\kappa|\mathbf{x}-\mathbf{y}|)$ is the standard fundamental solution of the Helmholtz equation (2.5) and $\hat{\alpha}$ is a function to be determined. The motivation for this comes from [18, Equation (2.70)], where the scattered field is represented using the boundary integral representation

$$u^s(\mathbf{x}) \quad = \quad \int_{\Gamma_1} \left(\frac{\partial \Phi(\mathbf{x},\mathbf{y})}{\partial \mathbf{n}(\mathbf{y})} - \mathrm{i}\kappa\Phi(\mathbf{x},\mathbf{y}) \right) \hat{\alpha}(\mathbf{y}) ds(\mathbf{y}). \tag{4.59}$$

This combined layer potential form provides a unique integral representation of the scattered field [18]. We cannot use this form directly for our MFS representation as the singularities of the fundamental solutions would lie on Γ_1 where we are forcing our boundary condition $u = 0$ to hold. However it is hoped that by instead taking

the integral over the boundary Γ^E we will still get an accurate representation as the two boundaries are taken to be close together. With the form (4.58) we still have that the scattered field satisfies the Sommerfeld Radiation Condition (2.8) and the solution satisfies the Helmholtz equation, the only thing remaining is to enforce the boundary condition $u = 0$ within our MFS. Thus for our MFS approximation we use a representation of (4.58) of the form

$$u^{(N)}(\mathbf{x}) = u^i(\mathbf{x}) + \sum_{j=1}^{N} \alpha_j \left[\mathbf{n}(\mathbf{y}_j) \cdot \nabla_{\mathbf{y}} \Phi(\mathbf{x}, \mathbf{y}_j) - \mathrm{i}\kappa\Phi(\mathbf{x}, \mathbf{y}_j)\right], \qquad \mathbf{x} \in \Omega, \tag{4.60}$$

where the coefficients α_j approximate the unknown function $\hat{\alpha}$. We choose the coefficients α_j to enforce that

$$u(\mathbf{x}_m) \approx 0, \qquad m = 1, ..., M. \tag{4.61}$$

at $M \geq N$ collocation points $\mathbf{x}_m \in \Gamma_1$, applying the boundary condition $u = 0$ for $\mathbf{x} \in \Gamma_1$. This results in a linear system $A\alpha = \mathbf{v}$, in which we force

$$-u^i(\mathbf{x}) \quad = \quad \sum_{j=1}^{N} \alpha_j \left[\mathbf{n}(\mathbf{y}_j) \cdot \nabla_{\mathbf{y}} \Phi(\mathbf{x}, \mathbf{y}) - \mathrm{i}\kappa\Phi(\mathbf{x}, \mathbf{y})\right], \tag{4.62}$$

to hold at $\mathbf{x}_m$, $m = 1, ..., M$. The entries of matrix A are given by

$$A_{m,j} = \mathbf{n}(\mathbf{y}_j) \cdot \nabla_{\mathbf{y}_j} \Phi(\mathbf{x}_m, \mathbf{y}_j) - \mathrm{i}\kappa\Phi(\mathbf{x}_m, \mathbf{y}_j). \tag{4.63}$$

In this equation $\mathbf{n}(\mathbf{y}_j)$ represents the outward normal vector at $\mathbf{y}_j$. The entries of vector $\mathbf{v}$ are given by

$$v_j = -\exp(\mathrm{i}\kappa x^{(m)}). \tag{4.64}$$

We use a standard matrix solver, Matlab's backslash operator, to solve the system $A\alpha = \mathbf{v}$ in order to find the vector α of coefficients α_j. For a matrix A and vector $\mathbf{v}$, using Matlab's backslash operator in $\alpha = A\backslash\mathbf{v}$ provides the least squares solution to $A\alpha = \mathbf{v}$. The coefficients in α can then be used in (4.60) to approximate the solution over the whole domain.

The real part of the MFS solution for $\kappa = 10$ for scattering by an ellipse with $a = 1.2$ and $b = 1$ is shown in Figure 4.10, with the total field on the left and the scattered

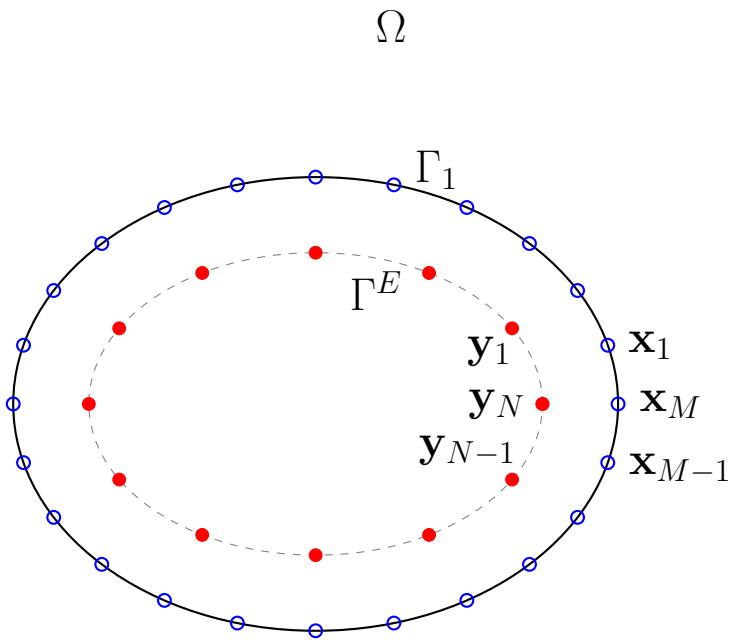

Figure 4.9: The MFS set-up for wave scattering by an ellipse. Source points are represented by red dots, collocation points are represented by blue circles.

field on the right. This approximation was achieved using $N_\lambda = 10$ degrees of freedom per wavelength on the boundary of the ellipse: we take $N = \text{ceil}(L_{\Gamma_1} N_\lambda/\lambda)$ where the function ceil rounds upwards towards positive infinity, and

$$L_{\Gamma_1} \approx \pi(a+b)\left(1 + \frac{3\hat{h}}{10 + \sqrt{4 - 3\hat{h}}}\right),$$

with $\hat{h} = \frac{(a-b)^2}{(a+b)^2}$, gives the approximate circumference of the ellipse [72]. Thus the results shown in Figure 4.10 were achieved using $N = 111$ point sources on Γ^E in the approximation, with $M = 131$ collocation points on Γ_1.

To test the accuracy of the MFS approximation we consider the maximum absolute error on the boundary of our scatterer Γ_1, at points away from the collocation points where we have forced the boundary condition to hold. Figure 4.11 shows the maximum absolute error on Γ_1 against the number of degrees of freedom per wavelength N_λ on the

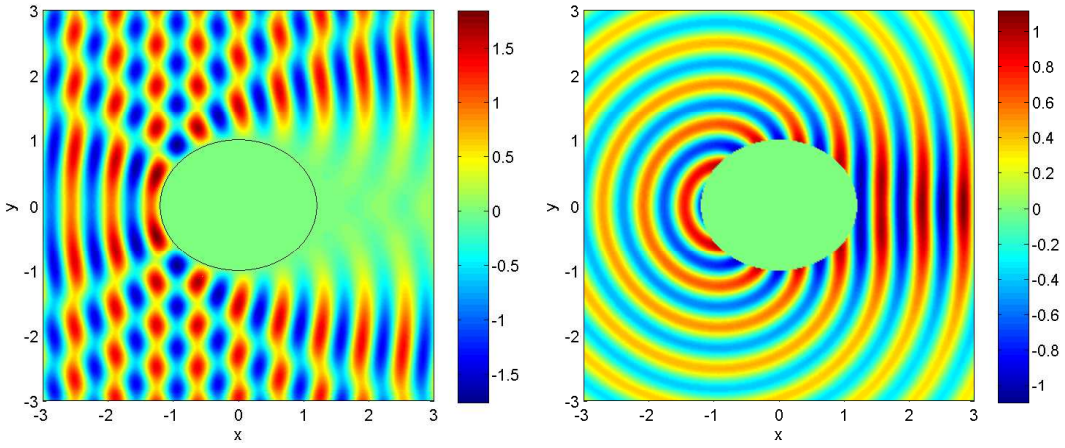

(a) $\operatorname{Re} u$ (b) $\operatorname{Re} u_s$

Figure 4.10: The MFS approximation for $\kappa = 10$, $a = 1.2$, $b = 1$, with $N = 111$ and $M = 131$.

boundary in the computation of the MFS solution. As can be seen we get exponential convergence, i.e. the error $\approx C \exp(-cN_\lambda)$. With this high level of accuracy achieved, we can conclude that the MFS using the representation of the form (4.58) gives an accurate solution for the purpose of comparing with our UWVF solutions.

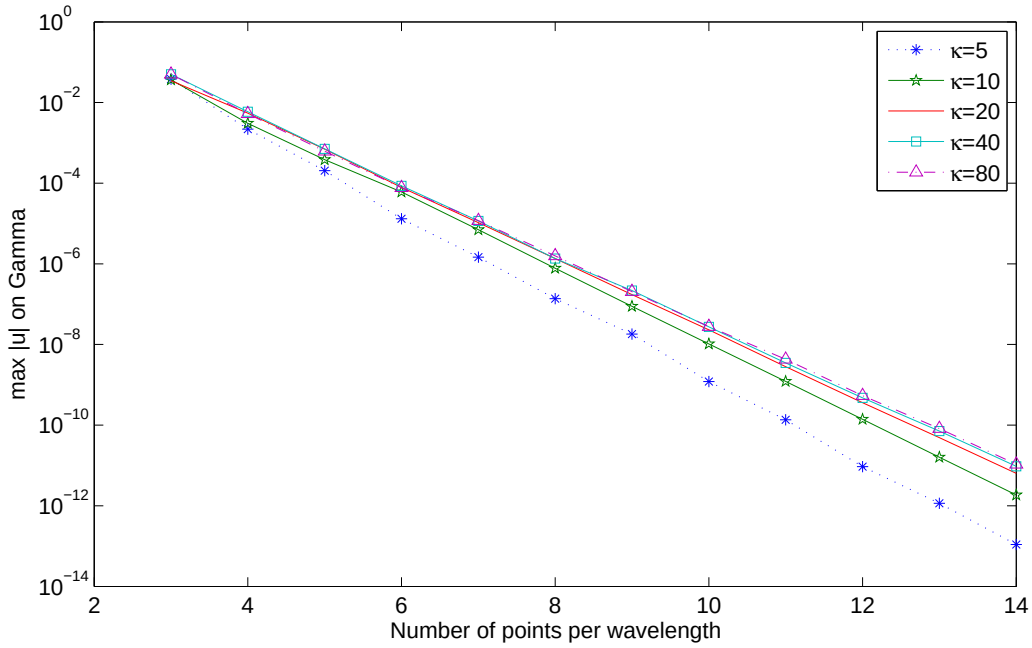

Figure 4.11: Maximum error of MFS on the boundary Γ_1 for various κ.

4.3 Best Approximation Studies

Here we present two initial studies which aim to see how well the ray-traced wave directions and centres of curvatures obtained in §4.1 can be used to approximate wave scattering by a convex obstacle. These studies give insight into the value ray tracing techniques may have as an aid for the enrichment of the UWVF basis. First, in §4.3.1, we consider the element-wise best approximation of the scattered field for the case of a circular scatterer. This is done first for the approximation on a single element, and then for all elements in a discretised domain. The second study is presented in §4.3.2, where we consider the best approximation to the total field for both differing sizes of the area of approximation and for different regions around the domain.

4.3.1 A Preliminary Study: Best Approximation for Wave Scattering by a Circle

Equipped with an exact solution (4.44), we can now investigate the level of accuracy it is possible to achieve by using the ray-traced centres of curvatures of §4.1.1 in our approximation space. Before implementing these centres of curvature in the UWVF basis, we first do an initial study to give an indication as to how well a ray-traced basis may work, for the case of scattering by a unit circle ($R = 1$). As with FEM and the UWVF, we find a solution on a discretised domain of triangular elements. The incident plane wave direction is given and so can easily be approximated, thus for our initial study we only test the scattered field approximation. We consider the best approximation to the scattered field using just one degree of freedom per element, using the ray-traced centres of curvature $\mathbf{x_C}$, given by (4.26) with (4.32), either in the basis or as an initial guess when searching for an optimal centre of curvature (as explained below). However, the exact solution we have is for an incident field $u^i = \exp(\mathrm{i}\kappa x)$ (see §4.2.1), whereas our ray tracing algorithm assumed an incident field $u^i = \exp(-\mathrm{i}\kappa x)$ (see §4.1.1). For all further work we reflect the ray-traced centres of curvature in the y axis (i.e. $\mathbf{x_C} = (x, y)$ becomes $\mathbf{x_C} = (-x, y)$), so that the two methods correspond.

To find a good approximation to the scattered field in each element, we minimise

$$||u^s - u_{opt}||_{L^2(\Omega_k)} \tag{4.65}$$

where u^s is the scattered field given by (4.45), and u_{opt} is an optimal approximation we seek to find. Note that although we use the exact solution here to test how well this method can work, the algorithmic ray tracing approach does not require a priori knowledge of the solution. To minimise the norm (4.65), we used the Matlab function fminsearch, a nonlinear optimisation routine that finds a local minimum of an inputted function of several variables, requiring initial starting estimates. We experiment with various options, the first using

$$u_{opt}(\mathbf{x}) = A\tilde{\Phi}(\mathbf{x}, \hat{\mathbf{z}}), \tag{4.66}$$

where A is a complex amplitude, and $\tilde{\Phi}(\cdot, \hat{\mathbf{z}})$ is a Hankel function circular wave, propagating outwards from a source point $\hat{\mathbf{z}}$, which we seek to find. We use the ray-traced centre of curvature $\mathbf{x_C}$ as an initial guess for $\hat{\mathbf{z}}$ and then optimise over both A and $\hat{\mathbf{z}}$. For the second option we consider the best approximation by a single plane wave basis, taking

$$u_{opt}(\mathbf{x}) = A\exp(i\kappa\mathbf{x}\cdot\mathbf{d}), \tag{4.67}$$

and optimise over both A and $\mathbf{d}$, where we use the ray-traced direction

$$\mathbf{d}_r = (-\cos(2\theta_i), \sin(2\theta_i))$$

(again having reflected in the y axis) as an initial guess. For the final set we again use a Hankel basis, taking

$$u_{opt}(\mathbf{x}) = A\tilde{\Phi}(\mathbf{x}, \mathbf{x_C}), \tag{4.68}$$

optimising over A only and maintaining the centre of curvature as $\mathbf{x_C}$. In all cases for an initial guess for the amplitude, we use

$$\hat{A} = \frac{u^s(\mathbf{x})}{\tilde{\Phi}(\mathbf{x}, \mathbf{x_C})} \tag{4.69}$$

for a point $\mathbf{x}$ close to the centroid of Ω_k.

As discussed in the above paragraph we first find the best approximation to the scattered field using a single Hankel degree of freedom per element by minimising (4.65), with u_{opt} given by (4.66), optimising over the amplitude A and the centre of curvature $\hat{\mathbf{z}}$. For a single element Ω_1 with vertices $(-1.9, 1.6)$, $(-1.4, 2.5)$, $(-2.4, 2.1)$, we use the ray tracing algorithm detailed in §4.1.1 to find the centre of curvature for wavefronts at the centroid of the element, at $(-1.9, 2.066)$. This gave the value of $\mathbf{x_C} = (-0.6403, 0.1098)$. This value of $\mathbf{x_C}$ is used as an intial guess in the optimisation routine, which found the optimal centre of curvature $\hat{\mathbf{z}}_{opt} = (-0.6575, 0.1269)$. The proximity of the obtained optimal and ray-traced centres of curvatures suggests that the use of the ray tracing algorithm for the direction and local curvature of wavefronts is accurate. Numerical results of the best approximation by a single optimal Hankel degree of freedom using (4.66) are shown in Figure 4.12 for $\kappa = 10$ and Figure 4.13 for $\kappa = 80$. In these figures we show the real part of the exact scattered field (given by (4.45)) in $\Omega = [-3, 0] \times [0, 3] \backslash C_R(0, 0)$ and in the element alone in the two upper plots. In the lower left plot we have the real part of the approximation by a single optimal Hankel function, and in the lower right we have the absolute error plotted on a $\log_{10}$ scale. The ray-traced centre of curvature $\mathbf{x_C}$ is shown by the black circle marker, whilst the optimal centre of curvature $\hat{\mathbf{z}}_{opt}$ is shown by the red circle marker. Clearly the solution is most accurate around the centroid of the element, however there is still in both cases high accuracy, of less than 0.01 absolute error over the whole element for $\kappa = 10$ and over the majority of the element for $\kappa = 80$.

This can be compared with conventional FD or low order FEM, where a rule of thumb of $N_\lambda = 10$ degrees of freedom per wavelength is needed for a reliable approximation, of engineering accuracy [18, 44, 47]. In one spatial dimension, the total number of degrees of freedom N_T on a segment of length L is given by

$$N_T = \frac{N_\lambda L}{\lambda} = \frac{N_\lambda L \kappa}{2\pi}.$$

Extending this to two dimensions, to achieve N_λ degrees of freedom per wavelength in each direction in a domain Ω, we need a number of degrees of freedom

$$N_T = \frac{N_\lambda^2 |\Omega| \kappa^2}{4\pi^2} \tag{4.70}$$

where $|\Omega|$ is the area of the region. Thus with standard FD and FEM, to discretise the element shown in Figure 4.12 we would expect to need 89 degrees of freedom for $\kappa = 10$ and 5674 degrees of freedom for $\kappa = 80$ to achieve an accurate representation of the scattered field in the element.

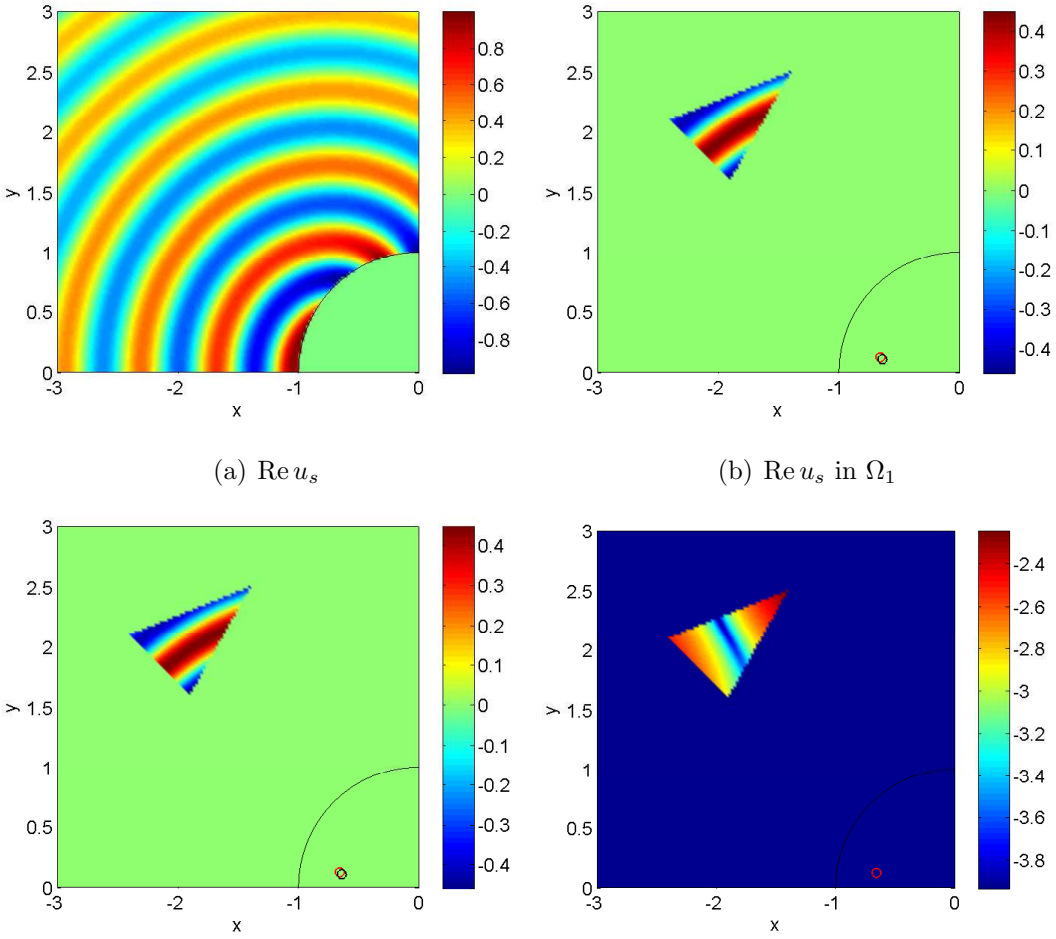

(a) $\mathrm{Re}\, u_s$ (b) $\mathrm{Re}\, u_s$ in Ω_1

(c) $\mathrm{Re}\, u_{\mathrm{opt}}$ in Ω_1 (d) $\log_{10} |u_s - u_{opt}|$ in Ω_1

Figure 4.12: Best approximation by $A\tilde{\Phi}(\cdot, \hat{\mathbf{z}})$ optimising over A and $\hat{\mathbf{z}}$ (as in (4.66)), for $\kappa = 10$. $\mathbf{x_C}$ shown by the black circle marker, $\hat{\mathbf{z}}_{opt}$ shown by the red circle marker.

To see the effectiveness of the new Hankel basis compared to the conventional plane wave basis, we compare these results with those of an approximation by a single optimal plane wave direction using (4.67). In the case of the plane wave we used the ray-traced reflected direction $\mathbf{d}_r$ as an initial guess and then optimised over the amplitude and the direction of the plane wave. Table 4.1 compares the Root Mean Square Error

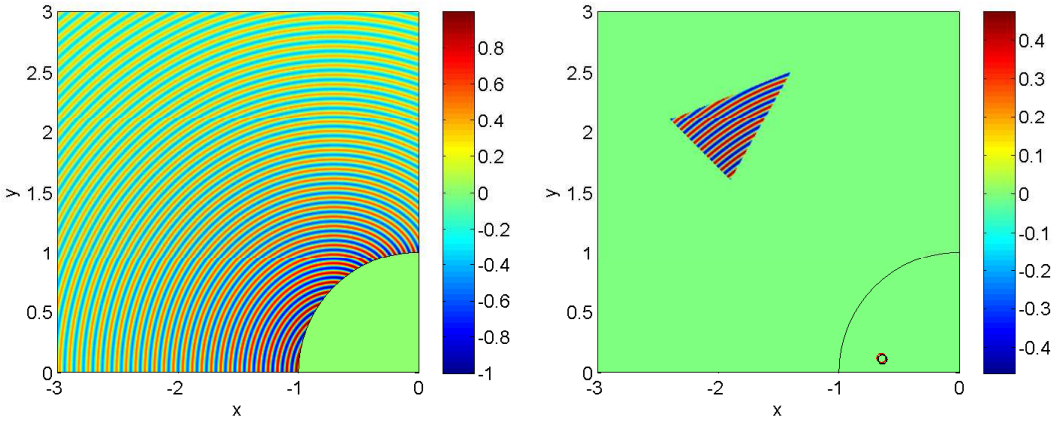

(a) $\mathrm{Re}\, u_s$ (b) $\mathrm{Re}\, u_s$ in Ω_1

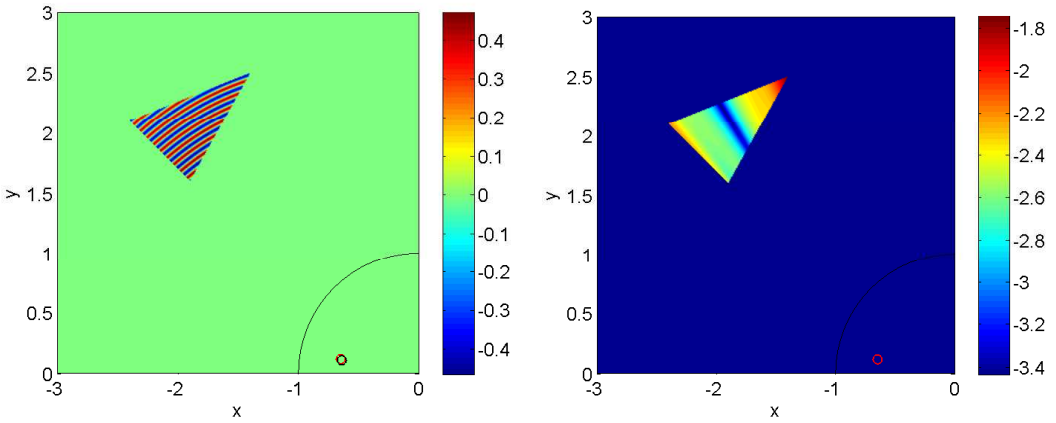

(c) $\mathrm{Re}\, u_{\mathrm{opt}}$ in Ω_1 (d) $\log_{10} |u_s - u_{opt}|$ in Ω_1

Figure 4.13: Best approximation by $A\tilde{\Phi}(\cdot, \hat{\mathbf{z}})$ optimising over A and $\hat{\mathbf{z}}$ (as in (4.66)), for $\kappa = 80$. $\mathbf{x_C}$ shown by the black circle marker, $\hat{\mathbf{z}}_{opt}$ shown by the red circle marker.

(RMSE) and Relative Root Mean Square Error (RRMSE) obtained by approximating the scattered field using a single Hankel circular wave and a single plane wave on the element. Here the RMSE and RRMSE are computed using

$$\text{RMSE}= \sqrt{\frac{\sum_{j=1}^{N_P} |u_s(\mathbf{x}_j) - u_{opt}(\mathbf{x}_j)|^2}{N_P}} \quad \text{RRMSE}= \sqrt{\frac{\sum_{j=1}^{N_P} |u_s(\mathbf{x}_j) - u_{opt}(\mathbf{x}_j)|^2}{\sum_{j=1}^{N_P} |u_s(\mathbf{x}_j)|^2}}$$

where x_j, $j = 1, ..., N_P$, are equi-spaced evaluation points in the element. The number of evaluation points N_P is chosen as $N_P = N_T$ of (4.70) with $N_\lambda = 10$.

Clearly the Hankel basis gives a much better approximation with an RRMSE of less

Table 4.1: Comparison of Hankel Circular Wave (using (4.66)) and Plane Wave (using (4.67)) Approximation Errors in Ω_1 for an Optimal Basis.

	Circular Wave		Plane Wave	
κ	RMSE	RRMSE	RMSE	RRMSE
10	1.8×10^{-3}	4.1×10^{-3}	5.4×10^{-2}	1.2×10^{-1}
20	2.4×10^{-3}	5.5×10^{-3}	1.0×10^{-1}	2.3×10^{-1}
40	2.8×10^{-3}	6.5×10^{-3}	1.9×10^{-1}	4.5×10^{-1}
80	3.4×10^{-3}	7.9×10^{-3}	3.0×10^{-1}	6.9×10^{-1}

than 1% in all cases, compared to those from 12% to 69% for the approximation by a single plane wave. It is also worth noting that, for the Hankel basis, where the wavenumber κ has increased by a factor of eight, the RRMSE has not even doubled.

We now move to the best approximation by a single basis function in elements over an entire domain $\Omega = [-3, 3] \times [-3, 3] \backslash C_R(0, 0)$, rather than a single element. The ray tracing algorithm works in the illuminated region of the domain, the region in which the incident field can penetrate. In the shadow region, where the obstacle blocks the incident field (on the opposite side of the circle from the direction of incidence in this case -see §4.1) the ray tracing theory does not hold. Thus we took elements with centroids with $x_k^C > 0$ and $|y_k^C| \leq R$ to be those in the shadow. For these elements we used as an initial guess for $\hat{\mathbf{z}}$ in (4.66) a point source in the far field in the negative x direction ($x = -600$), to represent the incident field. This is a good starting choice, as where the total field $u^t \approx 0$ in the shadow, it means that the scattered field $u^s \approx -u^i$.

Figure 4.14 shows some example numerical results with (4.66) taken in $K = 184$ elements over the entire domain for $\kappa = 30$. It has three plots: (a) shows the real part of the exact solution u^s with the computational mesh imposed over it; (b) shows the real part of the optimal approximate solution using one Hankel function on each element, optimised over the amplitude and centre of curvature separately in each element; and (c) shows the absolute error plotted on a $\log_{10}$ scale. For the optimal approximation we have not used curved edges for elements adjacent to the scatterer boundary, instead

using triangular elements. This means that part of each triangle adjacent to the circle extends slightly into the circle interior, however all errors are set to zero here (as it is not part of Ω considered). Overall we get a fairly accurate solution in the illuminated region, with errors ranging from 10^{-3} to 10^{-5}. In the region immediately close to the scatterer, in the shadow region, and on the shadow boundary, absolute errors increase to around 10^{-1}.

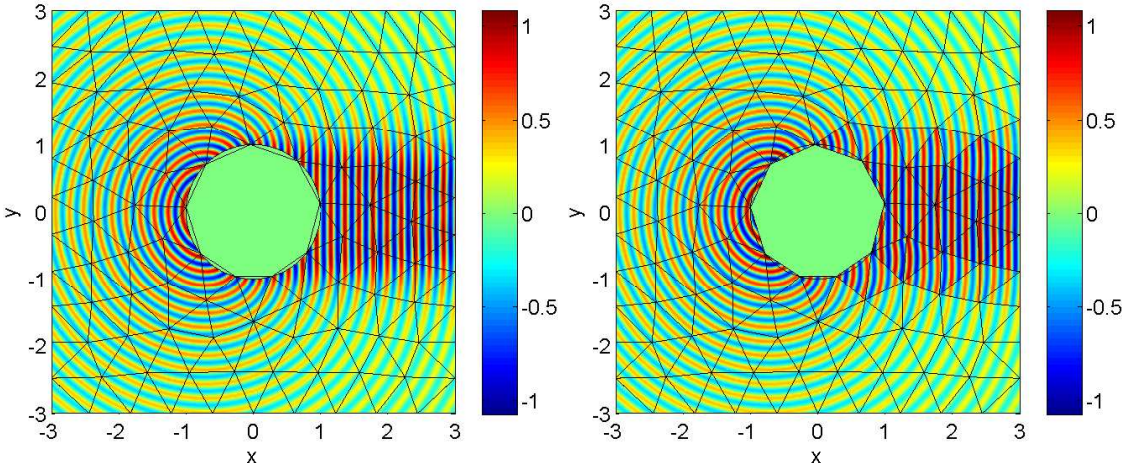

(a) $\operatorname{Re} u_s$

(b) $\operatorname{Re} u_{\text{opt}}$

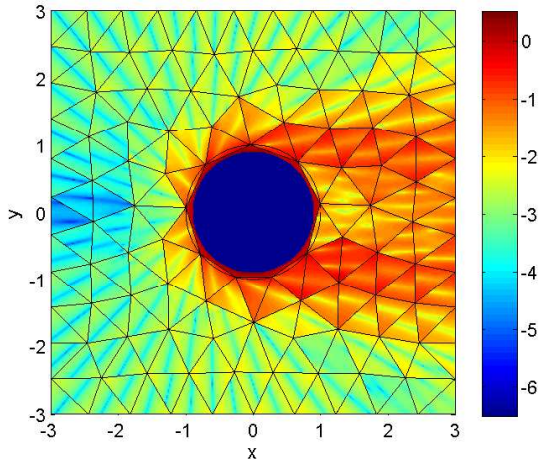

(c) $\log_{10} |u_s - u_{opt}|$

Figure 4.14: Best approximation optimised over A and $\hat{\mathbf{z}}$ by $A\tilde{\Phi}(\cdot, \hat{\mathbf{z}})$ (using (4.66)), for $\kappa = 30$, $K = 184$ elements.

Now we compare this with the best approximation by a conventional plane wave basis, using (4.67), optimising over A and $\mathbf{d}$ in $A\exp(i\kappa\mathbf{x}\cdot\mathbf{d})$. Figure 4.15 shows comparable numerical results, with (4.67) taken on elements of the same mesh of $K = 184$ elements over the entire domain for $\kappa = 30$. Again there are three plots: (a) shows the real part of the exact solution with the computational mesh imposed over it; (b) shows the real part of the optimal approximate solution using one plane wave on each element and optimising over the amplitude and direction; and (c) shows the absolute error plotted on a $\log_{10}$ scale. We use the same colour range for plot (c) as in Figure 4.14 for easier comparison. Clearly here we get much higher errors throughout the domain, suggesting the Hankel basis is preferable in this case. However it is interesting to note that the plane wave approximation is more accurate than the Hankel basis in the shadow region directly behind the scatterer. Theoretically the optimal Hankel basis should be no worse than the optimal plane wave basis (as a Hankel function can replicate a plane wave), suggesting there is some sort of error in the optimisation routine.

The motivation behind finding the ray-traced centres of curvatures is for their eventual use in the basis set for the UWVF. In the approximation of the form (4.68), we use our ray-traced centre of curvature and optimise over the amplitude alone. Optimising over the amplitude alone provides a more realistic comparison with the UWVF: we are testing for a given enriched basis to be be used in the UWVF; amplitude coefficients are solved for separately within the formulation. Figure 4.16 shows some example numerical results with an ansatz (4.68) in each element for $\kappa = 30$. Again there are three plots: (a) shows the real part of the exact solution with the same computational mesh of $K = 184$ elements imposed over it; (b) shows the real part of the optimal approximate solution using one Hankel function on each element and optimising over the amplitude only; and (c) shows the absolute error plotted on a $\log_{10}$ scale. Again the same colour range as in Figure 4.14 is used for plot (c) for easier comparison. Here we get a similar pattern to those using (4.66) in Figure 4.14, with a fairly accurate solution in the illuminated region, and errors increasing in the region immediately close to the scatterer

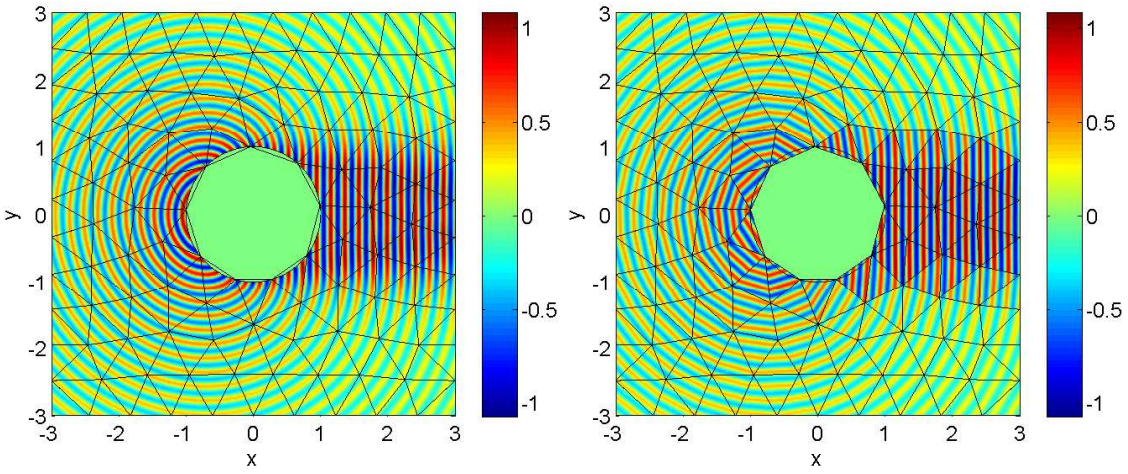

(a) $\operatorname{Re} u_s$ (b) $\operatorname{Re} u_{\text{opt}}$

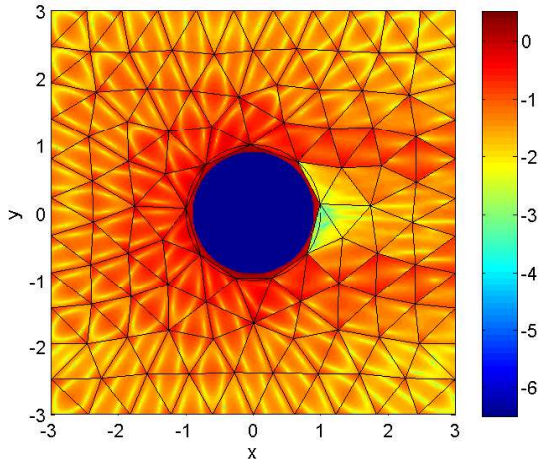

(c) $\log_{10} |u_s - u_{opt}|$

Figure 4.15: Best approximation over A and $\mathbf{d}$ by $A \exp(i\mathbf{x} \cdot \mathbf{d})$ (using (4.67)), for $\kappa = 30$, $K = 184$ elements.

and on the shadow boundary. However the errors are generally slightly higher overall, as we would expect; theoretically the absolute errors in Figure 4.16 must be at least as large as those in Figure 4.14.

By considering the error in each individual element, we can deduce in which region our ray tracing algorithm gives good accuracy, and in which regions we might need to augment the UWVF basis to achieve a better approximation. Figure 4.17 shows for the

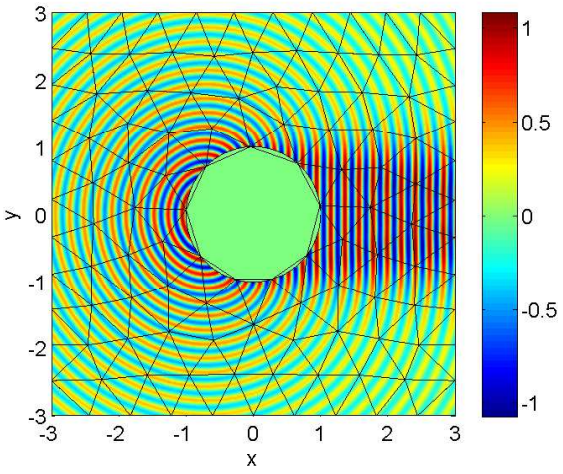

(a) $\operatorname{Re} u_s$

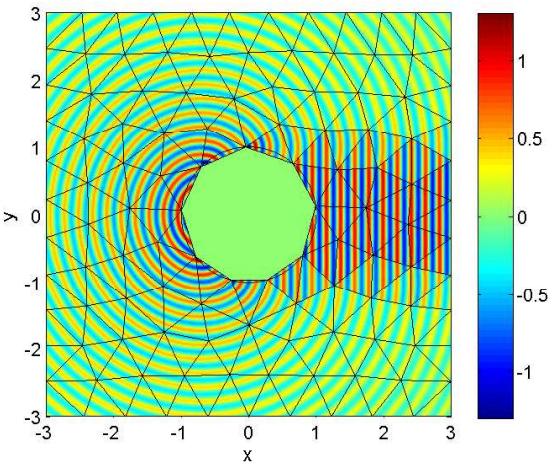

(b) $\operatorname{Re} u_{\text{opt}}$

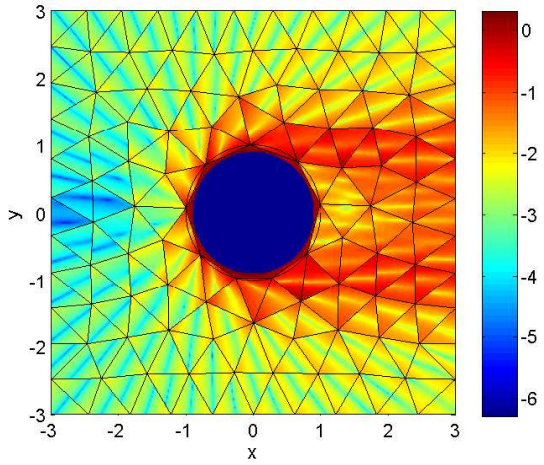

(c) $\log_{10} |u_s - u_{opt}|$

Figure 4.16: Best approximation by $A\tilde{\Phi}(\cdot, \mathbf{x_C})$ optimising over A (using (4.68)), for $\kappa = 30$, $K = 184$ elements.

higher wavenumber $\kappa = 50$, and finer discretisation of $K = 334$ elements, the absolute error around the domain plotted on a $\log_{10}$ scale, as well as a table showing the RMSE and RRMSE for various elements in the domain. The different coloured entries of the table correspond to the different highlighted elements. Here the approximate solution has been found using one Hankel function on each element and optimising over the amplitude alone, using the ray-traced centres of curvature. Again we get some very accurate results, with the highest accuracy in Ω_{lit} and higher errors in the shadow region and on the shadow boundary.

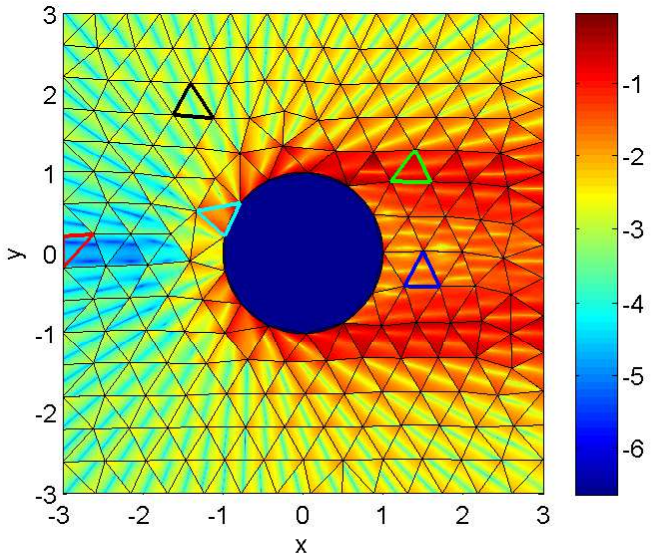

$\log_{10} |u_s - u_{opt}|$

RMSE	RRMSE
2.98×10^{-5}	6.49×10^{-5}
1.60×10^{-3}	3.40×10^{-3}
5.40×10^{-2}	6.04×10^{-2}
3.08×10^{-2}	3.07×10^{-2}
1.85×10^{-2}	2.76×10^{-1}

Figure 4.17: The absolute error in the best approximation using (4.68), on a $\log_{10}$ scale for $\kappa = 50$, $K = 334$. The different coloured entries correspond to the different highlighted elements.

Overall, from this study we found that a single Hankel degree of freedom per element provides a good approximation, particularly in the illuminated region to the forefront of the scatterer. Our initial experiments suggest that in some cases it may be possible to use one degree of freedom to replace 5000 degrees of freedom that may be required in conventional FD and FEM. The main areas of error were near the shadow boundary, near the scatterer, and in the shadow zone generally. Using a single plane wave degree of freedom is much less accurate (for the mesh sizes/wavelengths explored).

4.3.2 Best Approximation Study

We now present a further study into the best approximation by a ray-traced basis. Here we systematically investigate the best approximation achievable by the ray-traced basis in different areas of the domain, and in different sized regions. We now consider the total field, for both a circular and an elliptical scatterer. We seek to find this best approximation in a circle $B_\varepsilon(\mathbf{x}^p)$, centred at a point $\mathbf{x}^p$ with radius ε, for various positions

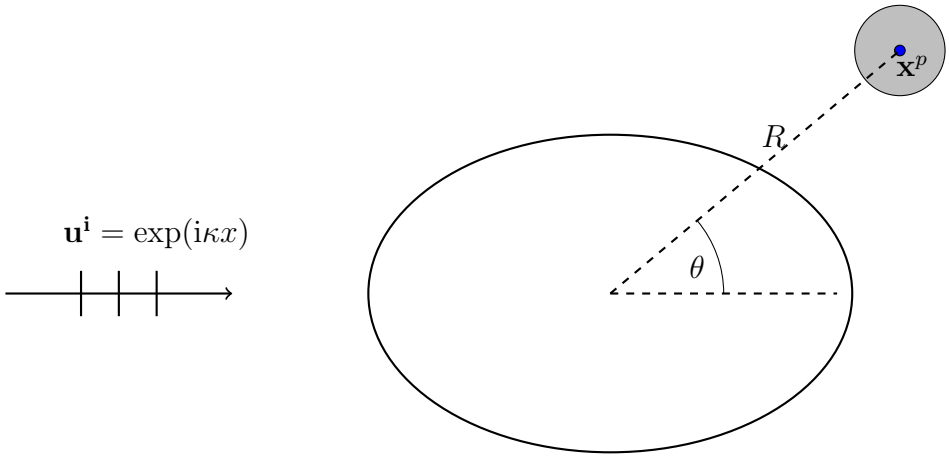

Figure 4.18: Best approximation in $B_\varepsilon(\mathbf{x}^p)$

throughout the domain, for example as per Figure 4.18. We use a representation from the two dimensional subspace

$$V = \{A\exp(\mathrm{i}\kappa x) + BH_0^1(\kappa|\mathbf{x}-\mathbf{x}_C|) : A, B \in \mathbb{C}\} \tag{4.71}$$

where $\mathbf{x}_C$ is the ray-traced centre of curvature. The first term represents a plane wave incident field, and the second term represents the scattered field by just a single Hankel function. We seek to find the appropriate $\xi_N \in V$ that minimises the dimensionless quantity

$$\begin{aligned} E &= \min_{\xi_N \in V} \frac{\|u-\xi_N\|_{L^2(B_\varepsilon(\mathbf{x}^p))}}{\|1\|_{L^2(B_\varepsilon(\mathbf{x}^p))}} \\ &= \min_{\xi_N \in V} \frac{\|u-\xi_N\|_{L^2(B_\varepsilon(\mathbf{x}^p))}}{\sqrt{\pi}\varepsilon}. \end{aligned} \tag{4.72}$$

To find the value of our dimensionless quantity E, we consider it as a classical least squares problem. Linear least squares is a method for best fitting data in an overdetermined linear system of equations by minimising the residuals [8]. We use it to find the best fitting coefficients $\mathbf{c} = (c_1, c_2)$ for our approximation

$$\xi_N(\mathbf{x}) = \sum_{i=1}^{2} a_i c_i = c_1\exp(\mathrm{i}\kappa x) + c_2 H_0^1(\kappa|\mathbf{x}-\mathbf{x}_C|), \tag{4.73}$$

for $\mathbf{x} \in B_\varepsilon(\mathbf{x}^p)$. To do this we consider (4.73) at M points $\mathbf{x}_j \in B_\varepsilon(\mathbf{x}^p)$, and denote $a_{1,j} = \exp(\mathrm{i}\kappa x_j)$ (with $\mathbf{x}_j(=(x_j, y_j))$ and $a_{2,j} = H_0^1(\kappa|\mathbf{x}_j - \mathbf{x}_C|)$ in the matrix $\hat{A} = [a_{i,j}]$.

The continuous ratio E is approximately equal to the corresponding discrete ratio, and so in this way we can write

$$\begin{aligned} E &\approx \frac{1}{\sqrt{\pi}\varepsilon} \min_{\xi_N \in V} \sum_{j=1}^{M} |u(\mathbf{x}_j) - \xi_N(\mathbf{x}_j)|^2 \\ &= \frac{1}{\sqrt{\pi}\varepsilon} \min_{\mathbf{c}\in\mathbb{C}^2} \sum_{j=1}^{M} |u(\mathbf{x}_j) - \sum_{i=1}^{2} a_{i,j} c_i|^2 \\ &= \frac{1}{\sqrt{\pi}\varepsilon} \min_{\mathbf{c}\in\mathbb{C}^2} \sum_{j=1}^{M} |u(\mathbf{x}_j) - (\hat{A}\mathbf{c})_j|^2 \\ &= \frac{1}{\sqrt{\pi}\varepsilon} \min_{\mathbf{c}\in\mathbb{C}^2} \|\mathbf{u} - (\hat{A}\mathbf{c})\|_2^2. \end{aligned} \tag{4.74}$$

Here $\mathbf{u} = (u(\mathbf{x}_j))_{j=1}^M$ is a vector of our exact reference solution evaluated at M points $\mathbf{x}_j \in B_\varepsilon(\mathbf{x}^p))$. For the case of a circular scatterer we use (4.44), and for an ellipse we use the MFS solution obtained by (4.60). The solution $\mathbf{c}$ of (4.74) is then the solution of the normal equations [8, Equation 6.22]

$$\hat{A}^H \hat{A}\mathbf{c} = \hat{A}^H \mathbf{u} \tag{4.75}$$

given by

$$\mathbf{c} = (\hat{A}^H \hat{A})^{-1} \hat{A}^H \mathbf{u}, \tag{4.76}$$

where the H superscript indicates the conjugate transpose of a matrix.

The value of E is computed for various $B_\varepsilon(\mathbf{x}^p)$ centred at $\mathbf{x}^p = \mathbf{x}^p(R \times R(\theta), \theta)$ for $R = 1.5, 2, 3$, $R(\theta)$ as in (4.33), and $\theta \in (0, \pi)$ provided $\mathbf{x}^p$ is in the illuminated region with $|R \times R(\theta)\sin(\theta)| \geq a$ and $R \times R(\theta)\cos(\theta) < 0$. Example points and the corresponding ray-traced centres of curvatures are shown in Figure 4.19 for an ellipse with $a = 1$, $b = 1.2$, $R = 2$. The dimensionless best approximation quantity E for a unit circle is shown in Figures 4.20–4.21, and an ellipse with $a = 1.2$ and $b = 1$ in Figures 4.22–4.23. Results are shown for $\kappa = 10, 80$, in $B_\varepsilon(\mathbf{x}^p)$ with $\varepsilon = 0.5\lambda, 2\lambda$, and $R = 1.5, 2, 3$, $\theta \in (0, \pi]$. Clearly the ray-traced approximation is less accurate in the near field close to the scatterer ($R = 1.5$), and the approximation is more accurate further away, for $R = 2, 3$. It is also more accurate for the circular scatterer than the ellipse. The approximation is least accurate in the region close to the shadow boundary, improving as $\mathbf{x}^p$ enters the region to the forefront of the scatterer. In all cases the

$\kappa = 80$ best approximations are more accurate than the $\kappa = 10$ best approximations. This may be due to ray-traced basis working better at high frequencies as it is a high frequency approximation, or that the area considered $B_\varepsilon(\mathbf{x}^p)$ is much smaller for the higher frequency as we use radii dependant upon the wavelength λ. The levels of accuracy achieved is again promising, suggesting that the ray-traced centres of curvatures do provide a good approximation to the scattered field wavefronts in a limited region around the evaluation point.

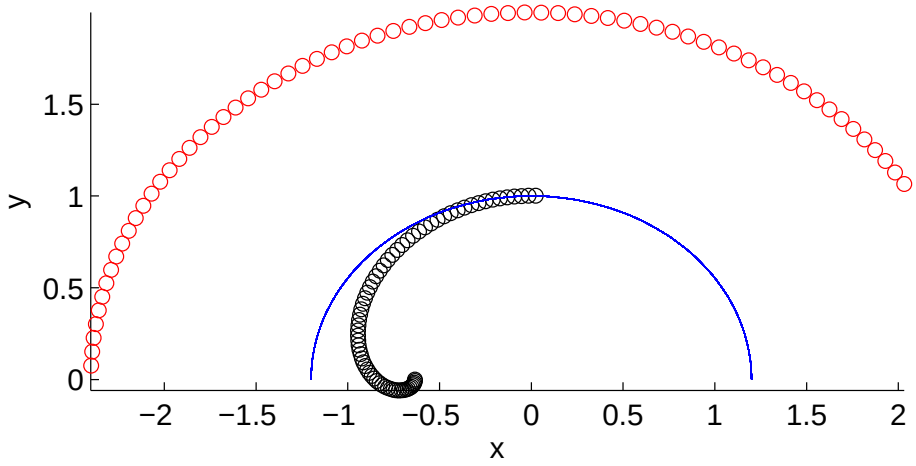

Figure 4.19: $\mathbf{x}^p$ in red markers and the corresponding $\mathbf{x}_C$ in black markers (moving anti-clockwise together) for an ellipse with $a = 1$, $b = 1.2$, $R = 2$. The boundary of the scatterer shown in blue.

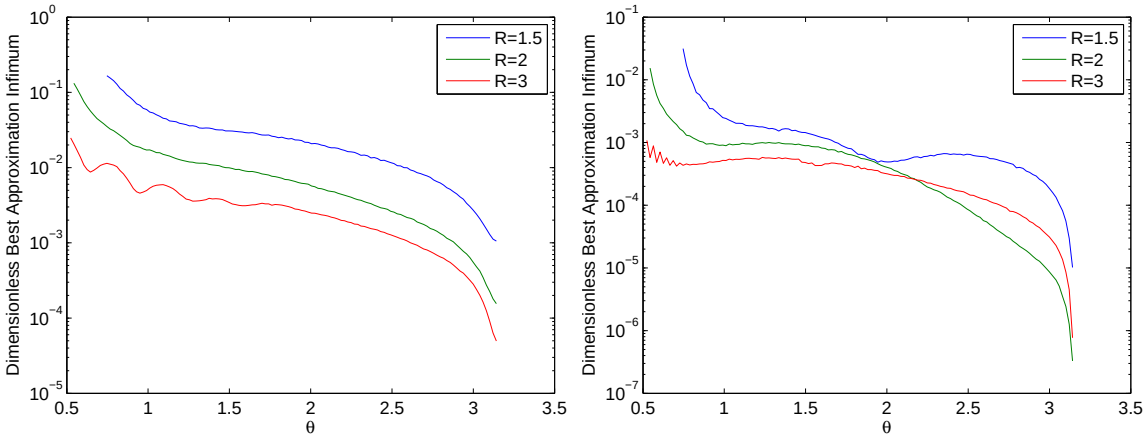

(a) $\kappa = 10$ (b) $\kappa = 80$

Figure 4.20: The dimensionless best approximation quantity E for a unit circle, for $\varepsilon = 0.5\lambda$, $R = 1.5, 2, 3$, $\theta \in (0, \pi]$.

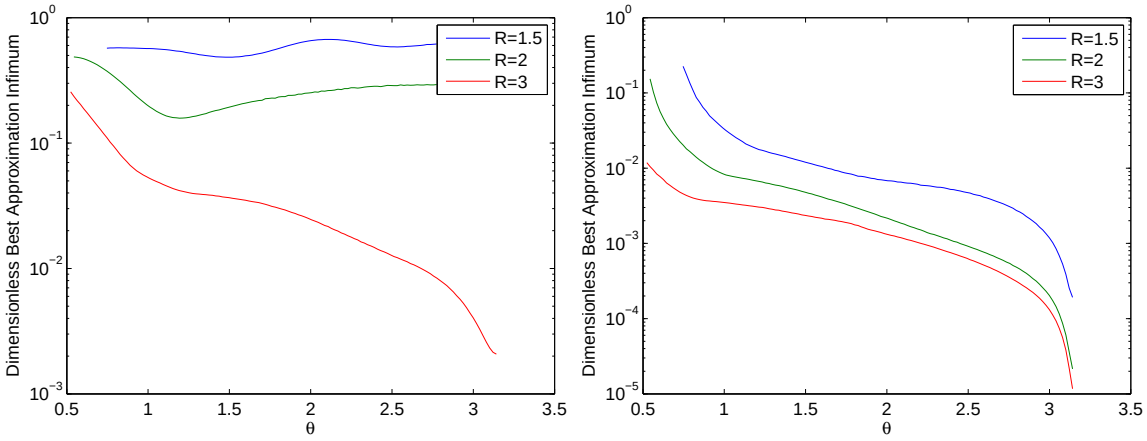

(a) $\kappa = 10$ (b) $\kappa = 80$

Figure 4.21: The dimensionless best approximation quantity E for a unit circle, for $\varepsilon = 2\lambda$, $R = 1.5, 2, 3$, $\theta \in (0, \pi]$.

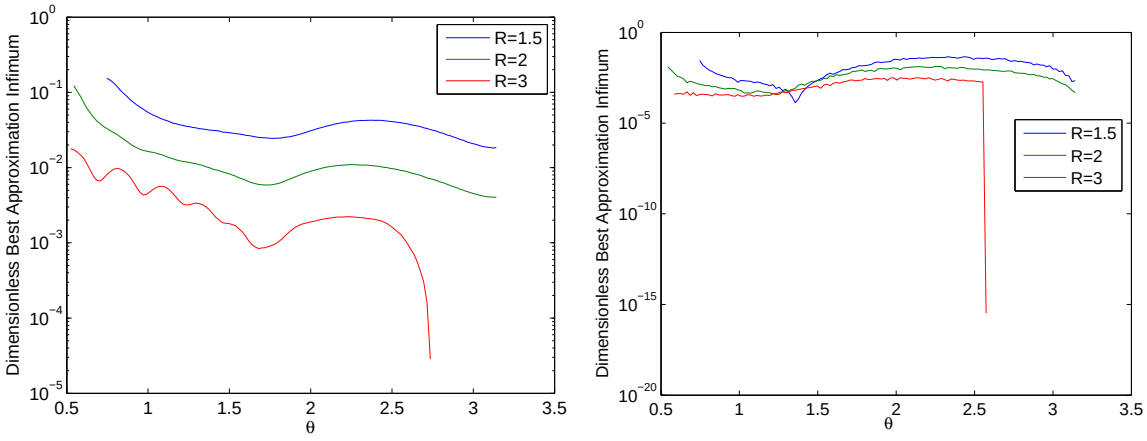

(a) $\kappa = 10$ (b) $\kappa = 80$

Figure 4.22: The dimensionless best approximation quantity E for an ellipse with $a = 1$, $b = 1.2$, for $\varepsilon = 0.5\lambda$, $R = 1.5, 2, 3$, $\theta \in (0, \pi]$.

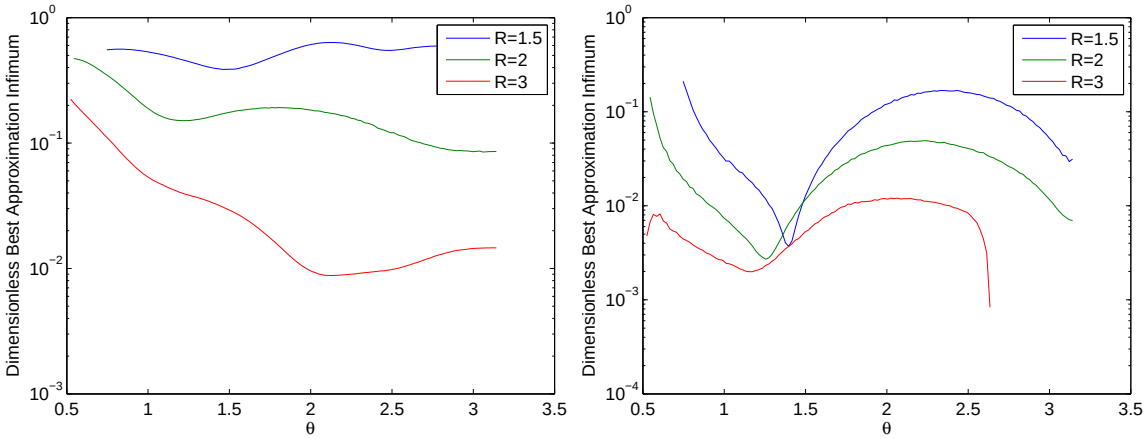

(a) $\kappa = 10$ (b) $\kappa = 80$

Figure 4.23: The dimensionless best approximation quantity E for an ellipse with $a = 1$, $b = 1.2$, for $\varepsilon = 2\lambda$, $R = 1.5, 2, 3$, $\theta \in (0, \pi]$.

4.4 Summary

In this chapter we presented a ray tracing method to be used as an aid for finding a good a priori choice of basis function for the UWVF, which follows in Chapter 5. We considered the case of wave scattering by a smooth convex obstacle in a domain of constant wavespeed, with examples given of circular (§4.1.1) and elliptical (§4.1.2) scatterers. In §4.1, ray tracing techniques were used to develop an algorithm that gives reflected ray directions and the local centre of curvature for reflected wavefronts. In §4.2 exact and reference solutions are presented, with which we conducted best approximation studies to give insight into the value ray tracing techniques may have in aiding the choice of basis functions in the UWVF. Initial studies were presented in §4.3, considering the best approximation by various bases in an individual element, and regions of the domain the ray-traced basis is most accurate. The results were promising, with the wavefield representation by two ray traced basis functions per element achieving high accuracy in large regions of the domain.

Chapter 5

Ray Enrichment of the UWVF basis: High Frequency Scattering by Convex Obstacles

To further progress the UWVF, here we incorporate the ray tracing techniques detailed in Chapter 4 into the method, in order to find a good a-priori choice of basis function. Similar techniques have been trialled in [11]. A strength of the UWVF is the incorporation of the intrinsic wavelength into the method. In a similar fashion we now adapt the method to incorporate details based upon the structure of the domain.

As explained in Chapter 3, the UWVF approximation holds on a domain that has been discretised into triangular finite elements. In this chapter we seek to find a good choice of basis function on each of these elements Ω_k, $k = 1, \dots K$, using ray tracing theory as an aid for finding dominant wave directions and choosing point source positions for a Hankel basis. We consider the case of two dimensional wave scattering by a smooth convex obstacle, in a domain where the wave speed, and thus the wavenumber, is constant. We will consider how similar ideas can be applied to more general domains of non-constant wavespeed in Chapter 6.

In §5.1 aspects of the use of the UWVF for the case of scattering by a circle are ex-

plained, with comparison between the conventional equally-spaced basis (§5.1.1) and a ray tracing augmented basis (§5.1.2) given. The UWVF for an elliptical scatterer is presented in §5.2, again with comparison of the equally-spaced and ray tracing augmented basis given in §5.2.3.

5.1 Approximating Wave Scattering by a Circle with the UWVF

We now progress to the use of the UWVF for approximating our wave scattering problem, first considering the case of scattering by a circle. This is an ideal case to use to test the use of a ray enriched UWVF basis as the exact solution is known, and so we can easily calculate errors and levels of accuracy. To implement this numerically in our UWVF codes, we truncate the unbounded exterior domain to a square of edge length 6 where we are considering scattering by a circle of radius $R = 1$, both centred at the origin: $\Omega = [-3, 3] \times [-3, 3] \backslash C_R(0, 0)$, as illustrated in Figure 5.1. We approximate the total field produced by a plane wave incident field $u^i = \exp(\mathrm{i}\kappa x)$, solving the Helmholtz equation (3.1a) with a zero interior source term $f = 0$ and constant wavenumber κ and density $\rho = 1$ throughout. For the boundary conditions on the surface of the scatterer Γ_1 we use $Q_1 = -1$ in (3.1b) for Dirichlet boundary conditions and take the source term $g_1 = 0$. On the outer boundary Γ_2 we use $Q_2 = 0$ in (3.1b) for impedance boundary conditions, and take source term $g_2 = \frac{\partial u}{\partial n} - \mathrm{i}\kappa u$, where u is obtained from (4.44) truncated at the appropriate N which achieves a zero of $\tilde{f}$ in (4.52). These Q and g terms correspond to those of the boundary condition set-up of the UWVF detailed in §3.1, where we have added the subscript $1, 2$ for the parameters holding on Γ_1 and Γ_2 respectively.

With the aim of improving the accuracy of results, various mesh adaptations are made, suited to the shape of the domain. The mesh is refined in the region close to the scatterer, as recommended by [37, 44]. In all results in this section the geometry is represented exactly through curved elements. Element edges on Γ_1 are given a different

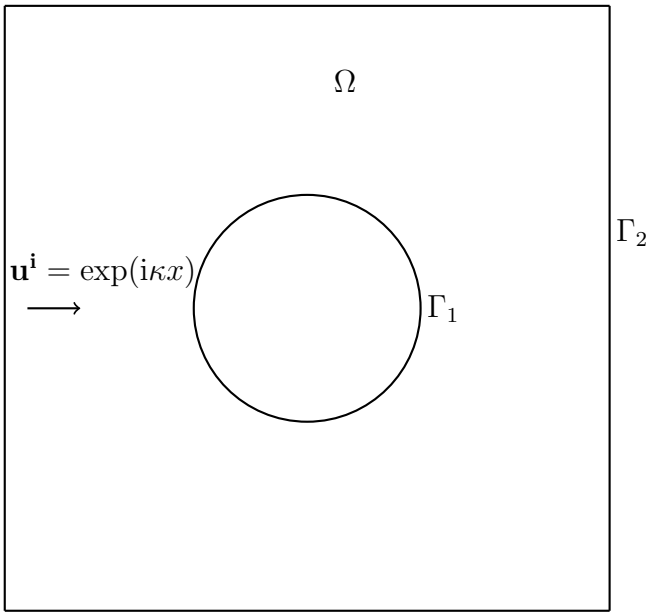

Figure 5.1: The domain set-up for approximating scattering by a circle by the UWVF.

parameterisation, so that integrals in submatrices D (given by (3.45)) and C (given by (3.46)) are evaluated along the curve of the scatterer, rather than along a straight element edge. The representation of the exact geometry in this way negates the need for mesh refinement around the scatterer: it is still possible to use large elements, permitting high numbers of basis functions to hold (recall that as the element size is reduced in comparison to wavelength, problems with ill-conditioning arise -see §3.5).

The numerical results are set into three sections. In §5.1.1 we present results for the UWVF approximation using the conventional angularly equi-spaced basis. In §5.1.2 we then compare these results to those obtained using a basis enriched with ray-traced centres of curvature. Finally in §5.1.3 we consider ways of combining the two approaches, with the aim of reducing the overall number of degrees of freedom required.

5.1.1 Approximation by an Equi-spaced Basis

We first present results using an angularly equi-spaced Hankel basis (3.49), with point sources (3.50) taken in the far field around a circle of radius $R_{PS} = 6000$. This setup

replicates an equi-spaced plane wave basis, as used conventionally in the UWVF. We consider $\kappa = 10, 20, 40$.

Figure 5.2 shows the approximate solution for $\kappa = 10$ using the mesh of $K = 455$ elements shown in Figure 5.3 and using p_k basis functions in element k, for $k = 1, , K$, where the values of p_k are as shown in Figure 5.3. We remind the reader (see §3.5) that our strategy for selecting the values of p_k is to choose a number of degrees of freedom p (in this case $p = 18$) and then in each element to take p_k to be as large as possible subject to the constraints that $p_k \leq p$ and that $\text{cond}(D_k)$, the condition number of the local submatrix D_k, is $\leq 10^{10}$. For a fixed discretisation, the conditioning improves for a larger κ, allowing a higher number of basis functions to be used in an element. For the lower wave number $\kappa = 10$ we get a highly accurate approximation, with the absolute error plotted on a $\log_{10}$ scale shown in Figure 5.4. Although the domain is symmetric in the x axis, here we do not have symmetric errors as the discretisation of the domain and the number of basis functions on each element is not symmetric. However, as the wave number increases so does the absolute error when the same approximation parameters ($K = 455$ and $p = 18$) are used, as can be seen in Figure 5.5 for $\kappa = 20$. Clearly using the same discretisation parameters regardless of frequency results in reduced accuracy as the solution becomes more oscillatory. For the higher wavenumber $\kappa = 40$ there are not enough degrees of freedom per wavelength to well represent the highly oscillatory solution accurately, either because the mesh is not sufficiently refined or more basis functions per element are required to well represent the solution (or both). This is further illustrated in Figure 5.6 where the $L^2(\Omega)$ relative errors against the average degrees of freedom per wavelength N_λ are presented for wavenumbers $\kappa = 10, 20, 40$ for varying p.

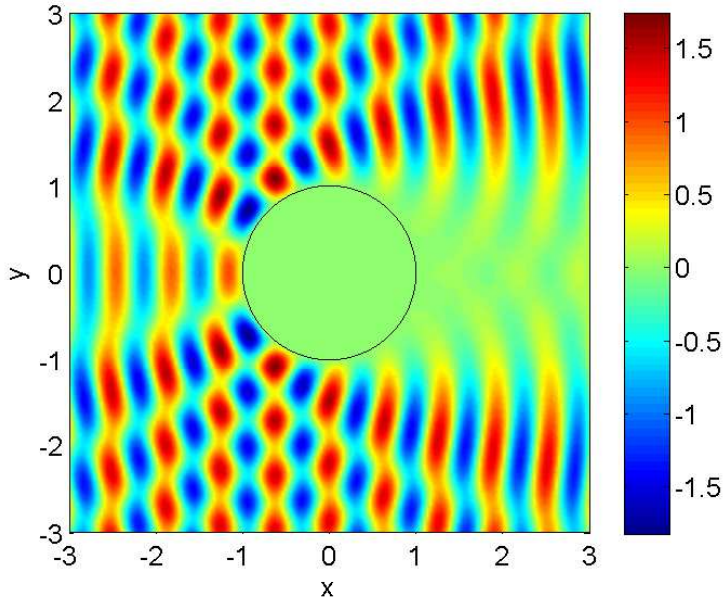

Figure 5.2: Real part of the UWVF approximation using an equi-spaced plane wave basis, $\kappa = 10$, $p = 18$, $K = 455$.

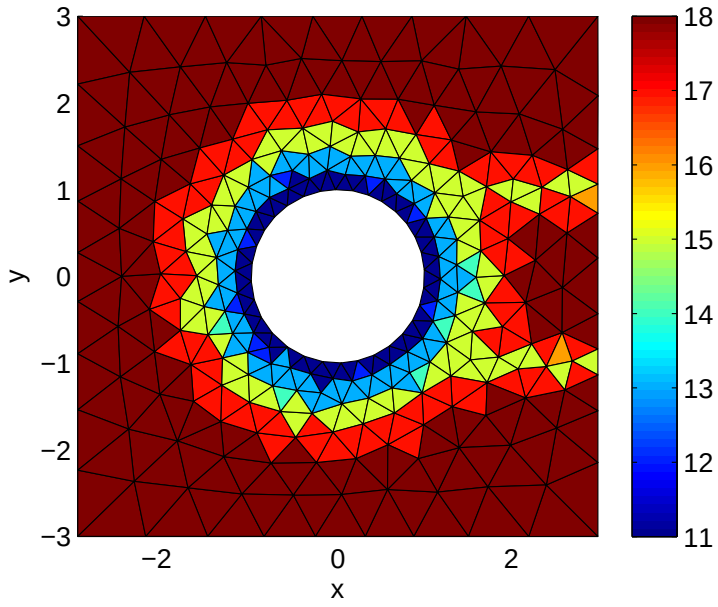

Figure 5.3: Mesh discretisation of domain, with number of basis functions tested upon each element, for approximation with $\kappa = 10$, $K = 455$. A maximum of $p = 18$ degrees of freedom is tested, with p_k reduced depending upon the conditioning of the submatrices D_k (see §3.5).

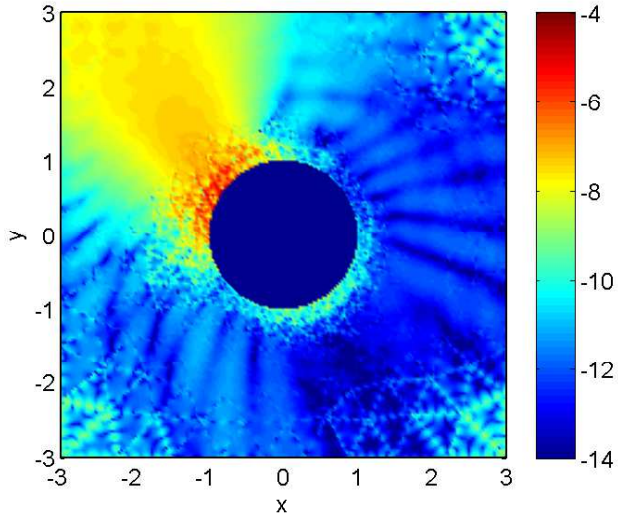

Figure 5.4: Absolute error on a $\log_{10}$ scale for approximation by equi-spaced plane wave basis, $\kappa = 10$, $p = 18$, $K = 455$ (the computational mesh and range of p_k is shown in Figure 5.3). We believe that the lack of symmetry in the error is due to the non symmetry of the underlying triangulation.

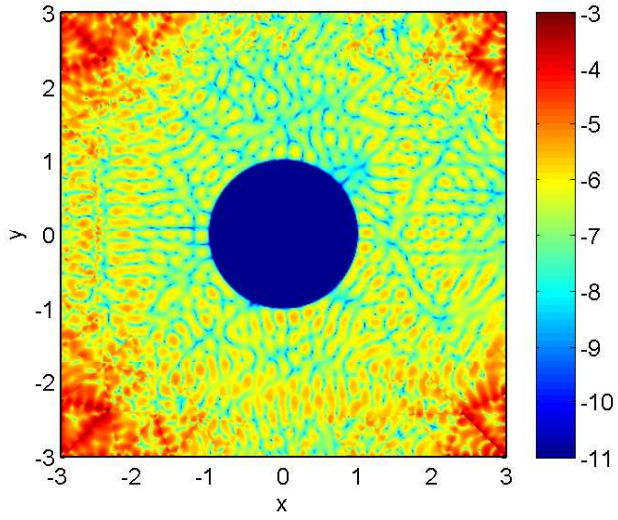

Figure 5.5: Absolute error on a $\log_{10}$ scale for approximation by equi-spaced plane wave basis, $\kappa = 20$, $p_k \in \{17, 18\}$, $K = 455$ (the computational mesh is shown in Figure 5.3).

Here the $L^2(\Omega)$ relative error is approximated by

$$L^2(\Omega) \text{ relative error} \approx \sqrt{\frac{\sum_{j=1}^{N_P} |u(\mathbf{x}_j) - u_N(\mathbf{x}_j)|^2}{\sum_{j=1}^{N_P} |u(\mathbf{x}_j)|^2}}, \tag{5.1}$$

where u is the exact solution given by (4.44), u_N is the UWVF approximation (3.11), and x_j, $j = 1, ..., N_P$, are evaluation points in the element, taken equi-spaced to satisfy $N_\lambda = 10$ (i.e. N_P is computed using $N_P = N_T$ given by (4.70)). The average number of degrees of freedom per wavelength used in the UWVF approximation is computed by inversion of (4.70), giving

$$N_\lambda = \lambda \sqrt{\frac{\sum_{k=1}^{K} p_k}{|\Omega|}}, \tag{5.2}$$

where $|\Omega|$ is the area of the domain. Oscillations can be seen in the $L^2(\Omega)$ relative errors in Figure 5.6, the troughs corresponding to the incident field direction $\mathbf{d}_i$ being included in the basis.

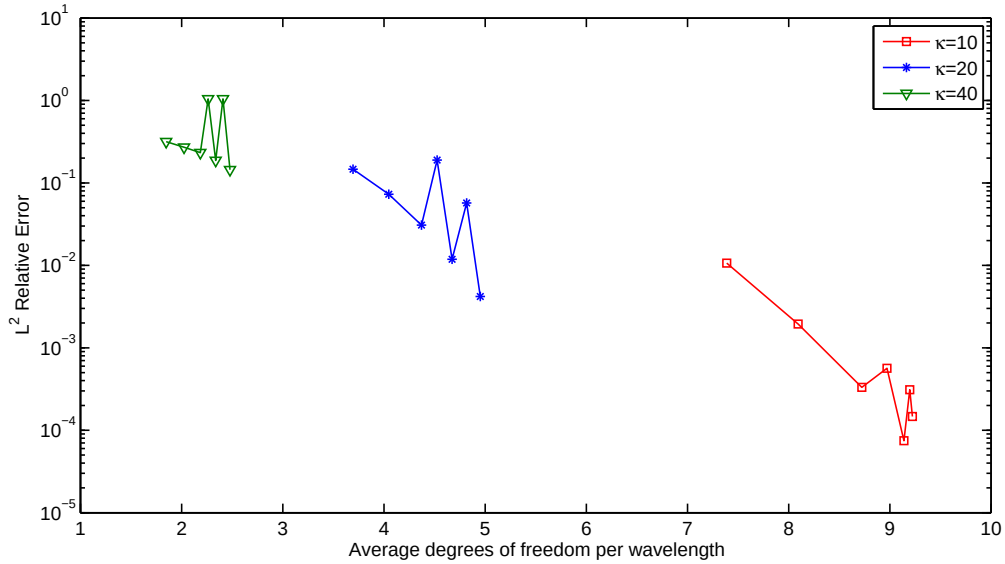

Figure 5.6: L^2 relative errors (5.1) against average degrees of freedom per wavelength (5.2) for the UWVF approximation by an equi-spaced plane wave basis for $\kappa = 10, 20, 40$, $K = 455$.

5.1.2 Incorporating Ray Tracing into the UWVF

The results of the preliminary study detailed in §4.3.1 are very promising, suggesting that the ray tracing algorithm does provide an accurate centre of curvature for the approximation of the scattered field by a single Hankel function on each element. We now go on to enrich the UWVF Hankel basis, incorporating the ray-traced centres of curvature. We intend to see if there is improvement by using the ray-traced basis in terms of achieving a given level of accuracy for a reduced number of degrees of freedom in comparison to the traditional equi-spaced basis. We test on the same case of scattering by a unit circle first of all, and extend this to the case of scattering by an ellipse in Sections 4.1.2 and 5.2. There are several different ways in which the ray-traced basis can be incorporated in the lit region Ω_{lit}:

(A) using only the two ray-traced Hankel basis functions per element: one a single far field source representing the plane wave incident field and another with the point source at the ray-traced centre of curvature $\mathbf{x_C}$, given by (4.26) with (4.32), to represent the scattered field.

(B) using the ray-traced basis as detailed in (A), as well as equi-spaced plane wave directions (represented by far field point sources) on each element.

(C) using only the ray-traced basis as detailed in (A) in a sectioned portion of the domain, and equi-spaced directions together with the ray-traced basis elsewhere.

In the shadow region Ω_{shadow}, basis functions are set to represent equi-spaced plane waves, including the incident wave direction. Again we need to match the incident wave directions used in our ray tracing algorithm and the UWVF approximation. We are using an incident field $u^i = \exp(\mathrm{i}\kappa x)$ (matching our boundary source term to the exact solution in §4.2.1), whereas our ray tracing algorithm assumed an incident field $u^i = \exp(-\mathrm{i}\kappa x)$ (see §4.1.1). Again we reflect the ray-traced centres of curvature in the y axis (i.e. $\mathbf{x_C} = (x, y)$ becomes $\mathbf{x_C} = (-x, y)$), so that the two methods correspond.

For option (A), our numerical results below show that only a limited level of accuracy can be achieved. Table 5.1 shows the RMSE (4.3.1), maximum error, and L^2

relative error (5.1) for the UWVF approximation using method (A), two ray-traced basis functions per element, for a wavenumber $\kappa = 10$. For an increasingly refined mesh (higher number of elements K), there are not significant gains in accuracy, with L^2 relative errors remaining at around 5%. This suggests that there are wave directions present in the exact solution which are not picked up by the ray-traced basis.

Table 5.1: Error in UWVF approximation for $\kappa = 10$ using method (A) of 2 ray-traced basis functions per element.

K	RMSE	Maximum Error	L^2 Relative Error
334	6.23×10^{-2}	3.13×10^{-1}	6.18×10^{-2}
719	5.34×10^{-2}	2.85×10^{-1}	5.31×10^{-2}
1022	5.24×10^{-2}	2.92×10^{-1}	5.20×10^{-2}
1434	5.06×10^{-2}	3.17×10^{-1}	5.02×10^{-2}

We would expect our ray-traced basis to be more effective at higher frequencies, as ray tracing gives the wave directions that are dominant in the high frequency limit. For a high wavenumber $\kappa = 80$, Table 5.2 shows that we can get an L^2 relative error of under 9% using the two ray-traced basis functions alone. Although this is a rather high error, it has been achieved with an average of just 0.4 degrees of freedom per wavelength (as computed by (5.2)), rather than the 10 degrees of freedom per wavelength rule of thumb requirement in standard FD and FEM. This massive computational saving could be useful in applications where a more general idea of the wave reflection is needed rather than high accuracy, perhaps as an initial guess of state. The levels of accuracy achieved by the UWVF with the two ray-traced basis basis functions is lower than one might expect given the high level of accuracy achieved in the preliminary study of §4.3.1 when the ray-traced centres of curvature was used to find a best approximation to the scattered field, optimising over the amplitude alone (using (4.68). This could perhaps be due to the matching of solutions on interelement boundaries (3.21) in the UWVF, meaning that high errors in one element could be carried across to neighbouring elements (whereas in the best approximation study solutions in each element were independent of one another).

Table 5.2: Errors in UWVF approximation for $\kappa = 80$ using method (A) of 2 ray-traced basis functions per element.

K	482
Total Degrees of Freedom	964
RMSE	8.97×10^{-2}
L^2 Relative Error	8.88×10^{-2}
Max Error	8.16×10^{-1}
Average DoF per Wavelength	4.25×10^{-1}

Further UWVF results using two ray-traced basis functions are shown in Figures 5.7 – 5.9. Figure 5.7 shows the computational mesh of $K = 422$ elements; in each element only the two ray-traced basis functions were used, resulting in a total of 844 degrees of freedom. Figure 5.8 has the real part of the approximate solution using this mesh on the left and the absolute error plotted on a $\log_{10}$ scale on the right for $\kappa = 10$. This approximation required an average of 3.18 degrees of freedom per wavelength, to achieve a 7.34% L^2 relative error. For comparison, using the same mesh but with the wavenumber quadrupled, Figure 5.9 has results in the same layout for $\kappa = 40$. Here a 7.94% L^2 relative error has been achieved using an average of 0.80 degrees of freedom per wavelength.

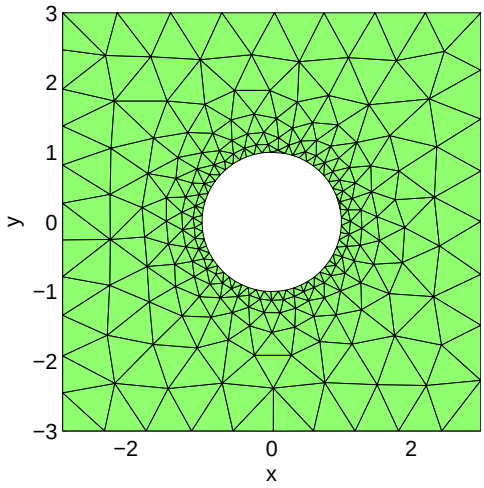

Figure 5.7: Computational Mesh with $K = 422$ elements.

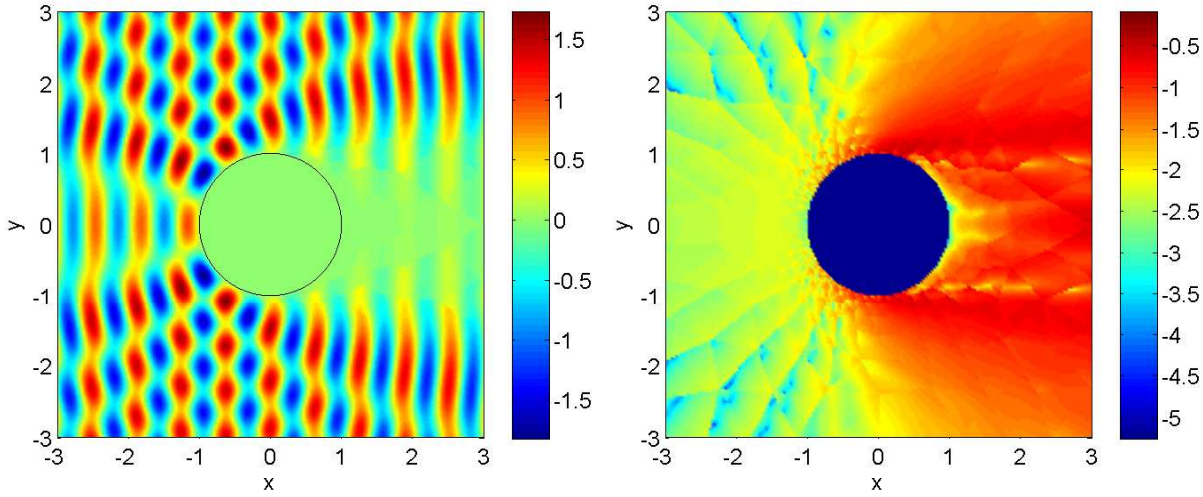

(a) $\operatorname{Re} u_N$ (b) $\log_{10} |u - u_N|$

Figure 5.8: The real part of the total field in (a) and the absolute error plotted on a $\log_{10}$ scale in (b) for $\kappa = 10$, by $p = 2$ ray-traced basis functions (method (A)) and $K = 422$ elements (mesh shown in Figure 5.7).

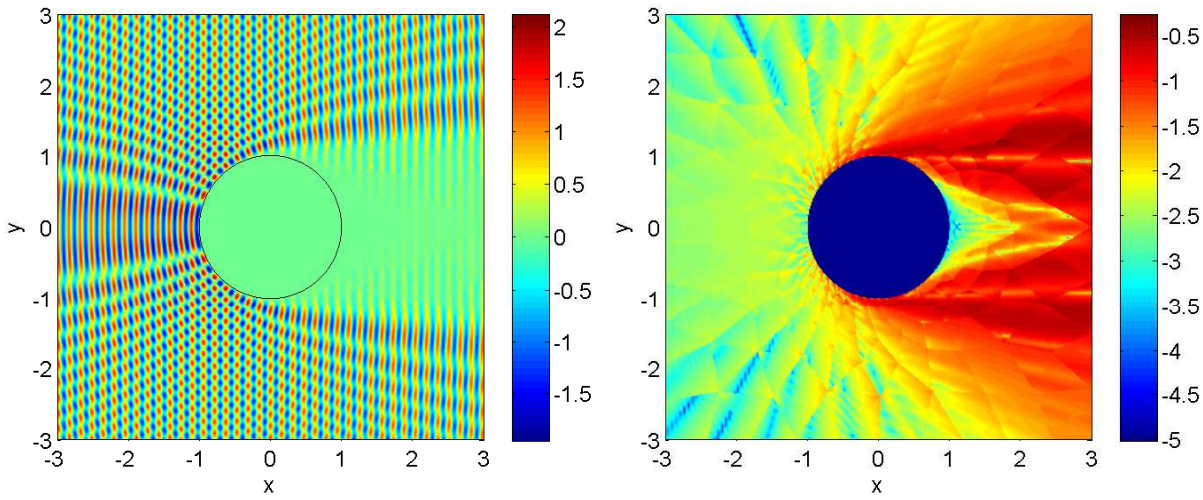

(a) $\operatorname{Re} u_N$ (b) $\log_{10} |u - u_N|$

Figure 5.9: The real part of the total field in (a) and the absolute error plotted on a $\log_{10}$ scale in (b) for $\kappa = 40$, by $p = 2$ ray-traced basis functions (method (A)) and $K = 422$ elements (mesh shown in Figure 5.7).

We now investigate whether we can achieve higher accuracy with method (B) or (C). For the second option (B) of using the ray-traced basis as well as equi-spaced plane wave directions on each element, care had to be taken to avoid basis functions becoming close to linearly dependant. The equi-spaced basis functions are taken around a circle of radius $R_{PS} = 6000$. To include the ray-traced basis representing the incident field (as in §5.1.1, from $-\infty$ in the x direction: $\mathbf{d}_i = (1, 0)$) we take the set to always include this direction and then the remainder are equi-spaced around this. Thus the equi-spaced basis functions in the kth element Ω_k are given by (3.49) with the point source locations given by

$$\mathbf{y}_{k,l} = \left(x_k^C + R_{PS} \cos\left(\frac{2\pi l}{p_k - 1} - \pi \right), y_k^C + R_{PS} \sin\left(\frac{2\pi l}{p_k - 1} - \pi \right) \right), \qquad l = 1, ..., p_k - 1. \tag{5.3}$$

For the final basis function we use as the point source location the centre of curvature $\mathbf{x_C}$, (4.26) with (4.32), given by our ray tracing algorithm. Figures 5.10–5.12 show the L^2 relative error achieved using an equi-spaced plane wave basis (represented by the Hankel basis (3.49) with sources given by (3.50)) as done in §5.1.1 and existing literature, and those achieved by method (B), combining the ray tracing and an equi-spaced plane wave basis, for $\kappa = 10, 20, 40$ respectively. For these approximations we again use the mesh of $K = 455$ elements, as shown in Figure 5.3, and take $p = 10, 12, 14, 15, 16, 17, 18$ for the equi-spaced approximation and $p = 2, 10, 12, 14, 15, 16, 17, 18$ for the equi-spaced and ray-traced approximation ($p = 2$ corresponds to option (A), the ray-traced direction basis only). As can be seen, in all cases a given level of accuracy is achieved using fewer degrees of freedom when the ray-traced centres of curvature are used within the basis as well. The oscillations in the equi-spaced basis results correspond to the case where the incident field is (the troughs) or is not (the peaks) included in the basis. In all cases, the approximations using the 2 ray traced basis functions combined with n equi-spaced wave directions leads to better results than using the traditional equi-spaced basis in $n + 2$ directions. These results suggest that the ray-traced basis is more effective at increasing the accuracy of the solution as the wave frequency increases.

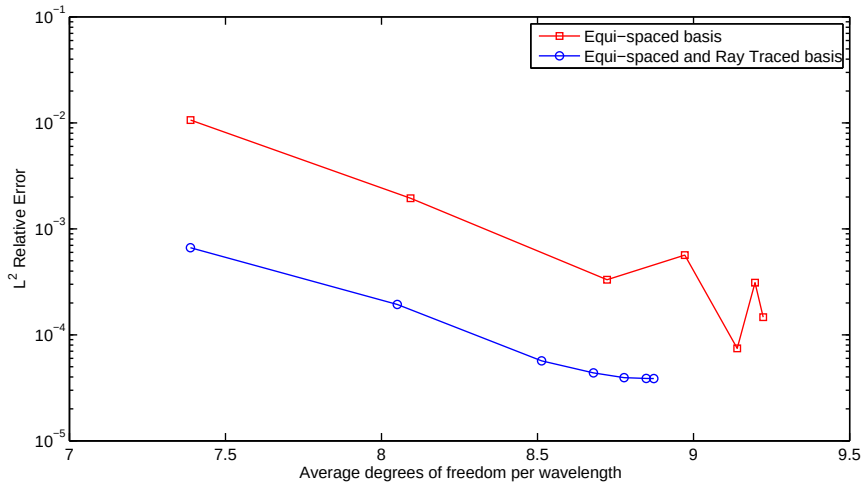

Figure 5.10: L^2 Relative Error against average degrees of freedom per wavelength for an equi-spaced basis ($p = [10, 12, 14, 15, 16, 17, 18]$) and an equi-spaced basis combined with ray tracing ($p = [10, 12, 14, 15, 16, 17, 18]$), $\kappa = 10$, $K = 455$.

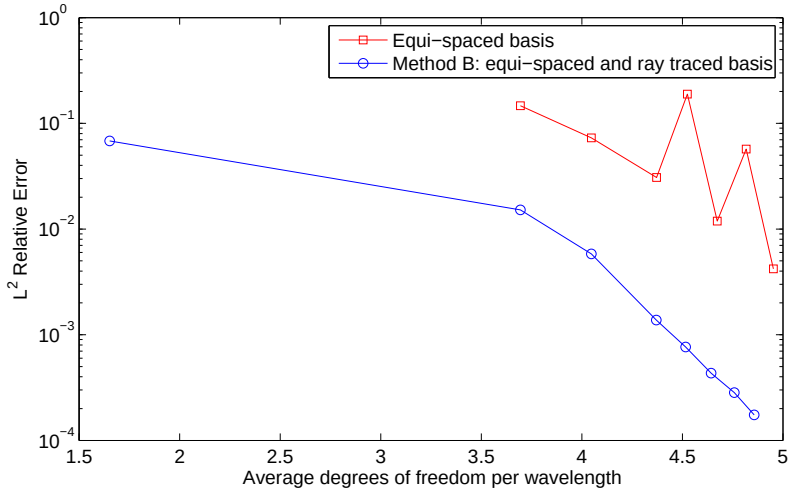

Figure 5.11: L^2 Relative Error against average degrees of freedom per wavelength for an equi-spaced basis ($p = [10, 12, 14, 15, 16, 17, 18]$) and an equi-spaced basis combined with ray tracing ($p = [2, 10, 12, 14, 15, 16, 17, 18]$), $\kappa = 20$, $K = 455$.

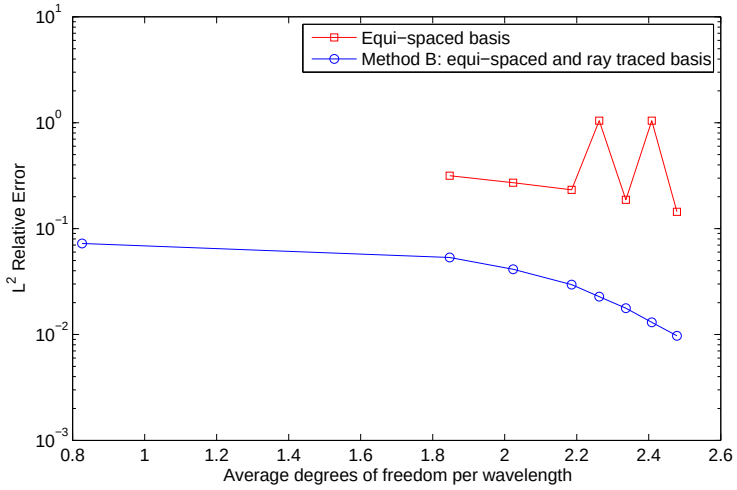

Figure 5.12: L^2 Relative Error against average degrees of freedom per wavelength for an equi-spaced basis ($p = [10, 12, 14, 15, 16, 17, 18]$) and an equi-spaced basis combined with ray tracing ($p = [2, 10, 12, 14, 15, 16, 17, 18]$), $\kappa = 40$, $K = 455$.

5.1.3 Sectioning of the Domain

The UWVF results in Figures 5.8(b) and 5.9(b) show that there are areas of the domain where errors are consistently higher when the ray-traced basis is used alone (method (A)). As the initial study in §4.3.1 suggested, the highest errors were around the surface of the scatterer, and towards the shadow region. We now consider method (C), a way of using the ray-traced basis selectively: we wish to maintain a low number of degrees of freedom in elements where the ray tracing is most effective, and use a higher number in elements where errors have shown to be higher. We separate areas of the domain into regions in which a higher or lower number of basis functions is used in each element. This region $\Omega_{p+} \subset \Omega$ is defined by taking the intersection of Ω, a circle of radius $H > 0$ centred at the origin and a region $\{(x, y) : x \geq (1 + H) + R\cos\eta; |y| \leq R\sin\eta\}$, for $R > 0$ and some $\eta \in [-\pi/2, \pi/2]$. For elements whose centroids are contained in Ω_{p+}, a higher number of basis functions per element is used. For the elements whose centroids lie outside this region, i.e. in $\Omega \backslash \Omega_{p+}$, we use the two ray-traced basis functions per element of the form (3.49), one with point source at $(-6000, y_k^C)$ to approximate the

incident field, and the other using the ray-traced centre of curvature. An example of the mesh used and number of basis functions per element is shown in Figure 5.13 for $H = 0.2$ and $\eta = \pi/4$. Here, as just described, the two ray-traced degrees of freedom have been used in part of the lit region, and a higher number of degrees of freedom used on elements in the remainder of the domain, again with a reduced number used in some smaller elements to maintain $\text{cond}(D_k) \leq 10^{10}$ (see §3.5 for more detail).

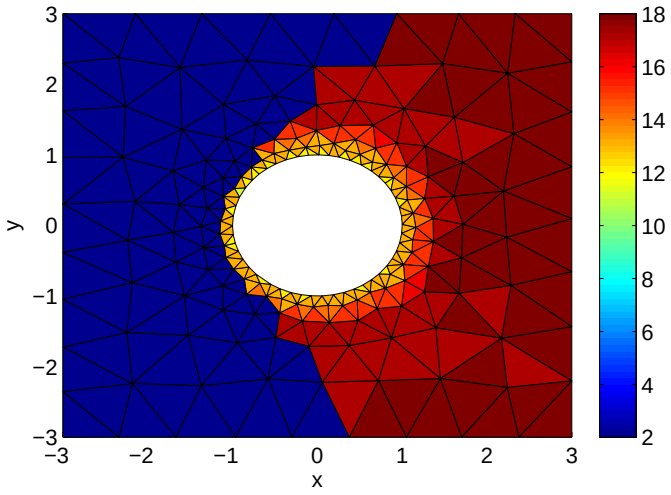

Figure 5.13: Example mesh discretisation of domain, with number of basis functions tested upon each element, for $K = 338$, $\kappa = 10$, $H = 0.2$ and $\eta = \pi/4$. For $\Omega_k \subset \Omega \backslash \Omega_{p+}$ $p = 2$, whilst for $\Omega_k \subset \Omega_{p+}$ $p_k \in [10, 18]$.

A variety of sectionings of the number of basis functions on each element was tried. Figure 5.14 shows the L^2 errors over the domain for $H = 0.2$ and $\eta = \pi$, $\eta = \pi/2$, $\eta = \pi/4$, $\eta = \pi/6$, and a comparison with the original formulation of §5.1 using equi-spaced plane wave basis functions with no ray tracing over the whole domain. In the results of the original formulation and those of the $\eta = \pi$ sectioning (corresponding to using $p = 2$ ray-traced basis functions in elements with the centroid $\mathbf{x}_k^C = (x_k^C, y_k^C)$ with $x_k^C \leq -H = -0.2$ and a larger p for elements with $x_k^C \geq -H = -0.2$), the accuracy is increased by using an increased number of basis functions. For the remaining paritionings of the domain the L^2 errors start off decreasing but soon plateau, at fairly low levels of accuracy. One explanation for this is that only limited accuracy can be

achieved by the ray-traced basis, and so higher errors in the elements where only two basis functions per elements were used may be carried over into elements where a large number of basis functions were used, by the transmission conditions (3.21) matching the solutions on the interelement edges.

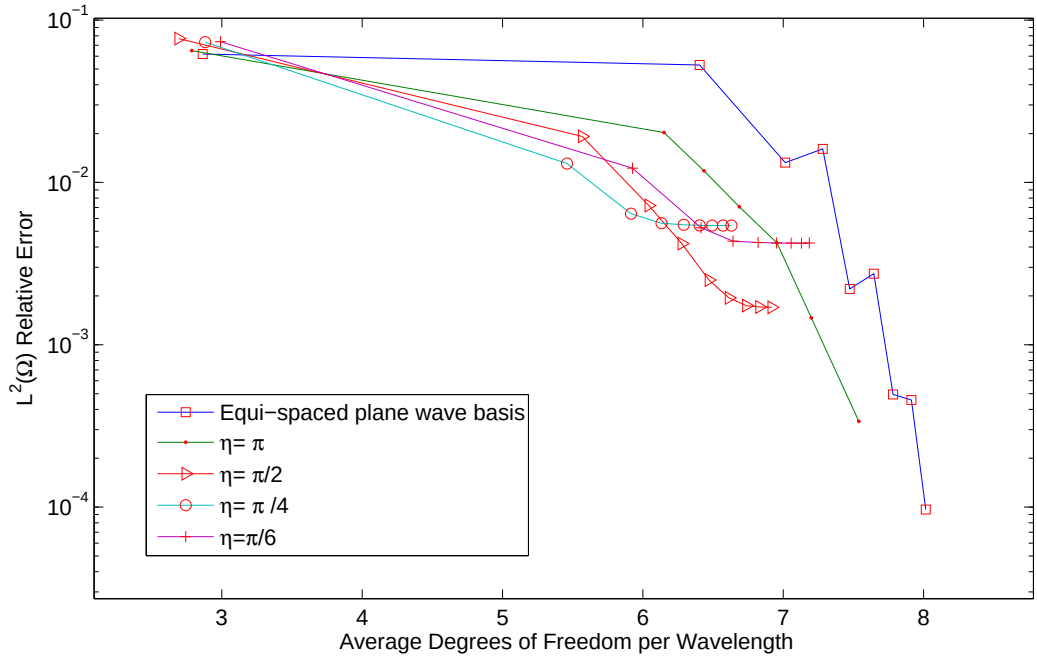

Figure 5.14: L^2 Relative Error over the domain against average degrees of freedom per wavelength, for an equi-spaced basis and an equi-spaced basis combined with ray tracing in various sections of the domain. Here $K = 364$, and $p = [2, 10, 12, 13, 14, 15, 16, 17, 18]$.

5.2 The UWVF for Scattering by an Ellipse

We now progress to the second of our convex obstacles considered, the case of the ellipse. The ellipse is a more complex case for approximating wave scattering, as there are fewer symmetrical properties of the domain and the curvature of the scatterer is no longer constant. We again present first of all the UWVF approximation using an an angularly equi-spaced basis, replicating the plane wave basis conventionally used in the literature, in §5.2.1. We then compare this in §5.2.2 with a the results of the UWVF approximation using a ray enriched basis, where the centres of curvatures computed in §4.1.2 are incorporated.

We approximate the total field produced by a plane wave incident field $u^i = \exp(\mathrm{i}\kappa x)$, solving the Helmholtz equation (3.1a) with constant density $\rho = 1$ and a zero interior source term $f = 0$. To implement the case of scattering by an ellipse numerically in the UWVF codes, we use a simillar domain set up to that in §5.1, truncating the domain in a square of edge length 6, centred at the origin. For the boundary conditions on the surface of the scatterer Γ_1 we use $Q_1 = -1$ in (3.1b) for Dirichlet boundary conditions and take the source term $g_1 = 0$. On the outer boundary Γ_2 we use $Q_2 = 0$ for impedance boundary conditions, and take source term $g_2 = \frac{\partial u}{\partial n} - \mathrm{i}\kappa u$, where u is our MFS reference solution (2.9) with representation (4.60).

In order to obtain high accuracy of results, we again refine the mesh around the scatterer, to have a closer representation of the smooth, curved edge. To further improve this, element edges on Γ_1 were given a different parameterisation, so that integrals in submatrices D and C are evaluated along the curve of the scatterer rather than a straight element edge. This means that the elements with edges on Γ_1 are curvilinear triangles, whereas those in the remainder of the domain have three straight edges.

5.2.1 Approximation with an Equi-Spaced Basis

We first present results using an angularly equi-spaced Hankel basis (3.49), with point sources given by (3.50) taken in the far field around a circle of radius $R_{PS} = 6000$,

replicating the conventional equi-spaced plane wave basis. We use the same computational mesh for all experiments, with $K = 250$, as shown in Figure 5.15. Accuracy is then improved by increasing the number of basis functions on each element, subject to bounds on the condition number of the corresponding matrices D_k. The L^2 relative error for wavenumbers $\kappa = 10, 20, 40$ is shown in Figure 5.16. As can be seen, these approximation parameters well represent the solution for the lower wavenumber of $\kappa = 10$, with the L^2 relative error converging to zero. For the higher wavenumbers $\kappa = 20, 40$ the L^2 relative error is decreasing but is still at a high level. The trend suggests that by further increasing the average number of basis functions (either by increasing the number of basis functions in each element or using a finer discretisation or both) a higher accuracy can be achieved.

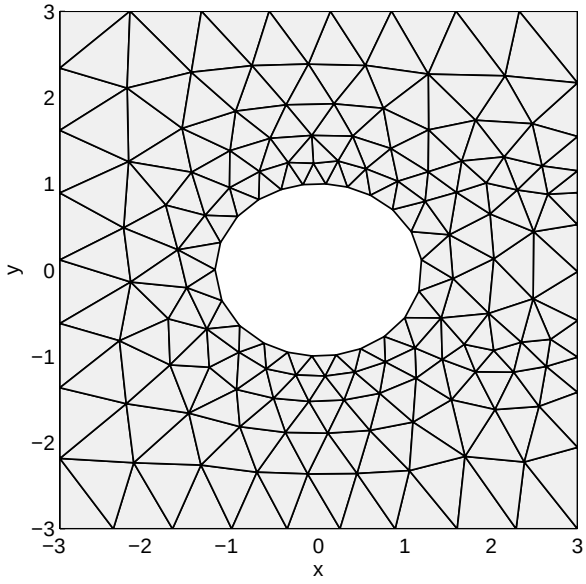

Figure 5.15: Mesh discretisation of domain, for $a = 1.2$, $b = 1$, $K = 250$.

5.2.2 Incorporating Ray Tracing

We now present results of the UWVF extended to incorporate the ray-traced centres of curvature into the Hankel basis. We intend to see if, as with the circular scatterer, the use of ray tracing techniques can achieve a given level of accuracy for a reduced number

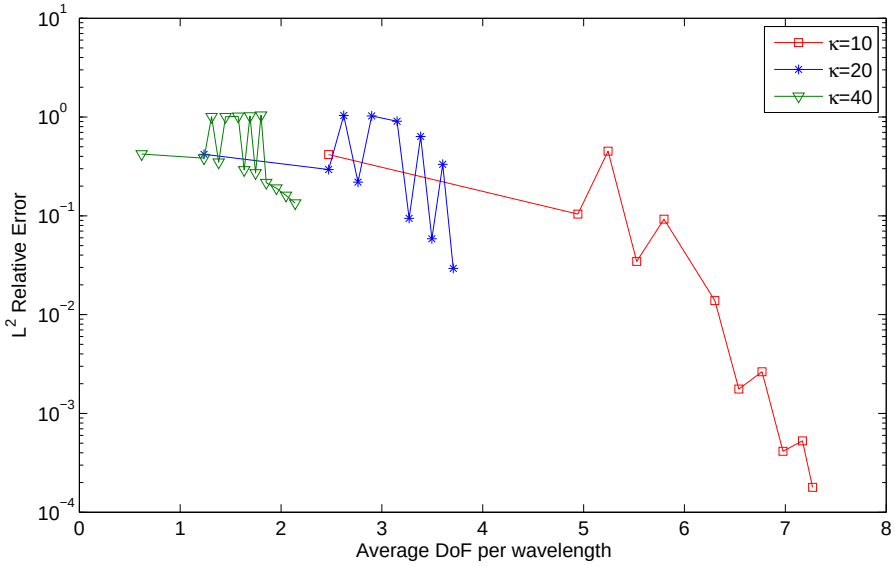

Figure 5.16: L^2 relative errors for approximation by equi-spaced plane wave basis for $\kappa = 10, 20, 40$, $K = 250$. For $\kappa = 10, 20$, $p = [2, 8, 9, 10, 11, 13, 14, 15, 16, 17, 18]$ and for $\kappa = 40$, $p = [2, 8, 9, 10, 11, 13, 14, 15, 16, 17, 18, 20, 22, 24]$.

of degrees of freedom compared to the conventional equi-spaced basis. We consider two options for incorporating the ray-traced basis in Ω_{lit}:

(A) Use only the two ray-traced Hankel basis functions per element, one with a far field source representing the plane wave incident field and another with the point source at the ray-traced centre of curvature $\mathbf{x_C}$, given by (4.39) with (4.40), to represent the scattered field.

(B) Use the ray-traced basis as detailed above, as well as equi-spaced directions on each element.

In Ω_{shadow} basis functions are set to represent equi-spaced plane waves, including the incident wave direction.

For the first option, (A), of using just the two ray-traced basis functions per element, we can get a fair representation of the total and scattered wave field, as shown in Figure 5.17. However, although the phase and directions are essentially correct, the amplitudes

are not smoothly varying and only a limited level of accuracy can be achieved. Table 5.3 contains the root mean square error (RMSE), maximum error, and L^2 relative error for the UWVF approximation by two ray-traced basis functions per element for a wavenumber $\kappa = 10$. For an increasingly refined mesh (higher number of elements K), there are no significant gains in accuracy. This can be compared with Table 5.1: clearly the ray-traced basis is less effective for the elliptical scatterer, as the L^2 relative errors now remain at around 10%.

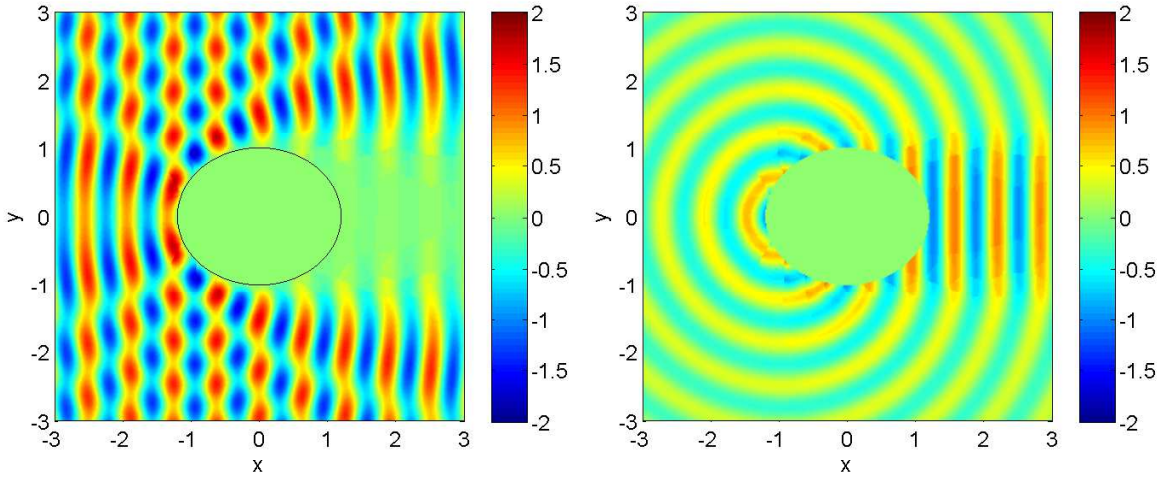

(a) $\operatorname{Re} u_N$ (b) $\operatorname{Re} u_N^s$

Figure 5.17: UWVF approximation for scattering by an ellipse, $\kappa = 10$ by option (A), $p = 2$ ray-traced basis functions per element, for $a = 1.2$, $b = 1$, $K = 250$. The real part of the total field shown in (a), and the real part of the scattered field shown in (b).

For the second option, (B), of using the ray-traced basis as well as equi-spaced plane wave directions on each element, we use the same positionings (5.3) as those for the scattering by a circle: $p_k - 1$ are equi-spaced around a circle of radius $R_{PS} = 6000$, including the incident field direction. For the final point source we use the centre of curvature given by our ray tracing algorithm.

Figure 5.18 shows numerical results for the same ellipse with $a = 1.2$, $b = 1$, achieved by $p = 18$ basis functions per element on the computational mesh as in Figure 5.15

K	RMSE	Maximum Error	L^2 Relative Error
89	1.090×10^{-1}	5.09×10^{-1}	1.08×10^{-1}
182	9.93×10^{-2}	6.07×10^{-1}	9.81×10^{-2}
250	9.78×10^{-2}	5.48×10^{-1}	9.66×10^{-2}
452	1.04×10^{-1}	5.89×10^{-1}	1.02×10^{-1}
728	9.29×10^{-2}	5.14×10^{-1}	9.18×10^{-2}

Table 5.3: Error in UWVF approximation for $\kappa = 10$ using 2 ray-traced basis functions per element.

with $k = 250$ elements. This approximation has taken a much higher 4468 total degrees of freedom, increasing the average degrees of freedom per wavelength to 3.69. This is still much less than the standard 10 degrees of freedom per wavelength required in conventional methods, and has achieved an L^2 relative error of 8.93×10^{-4}.

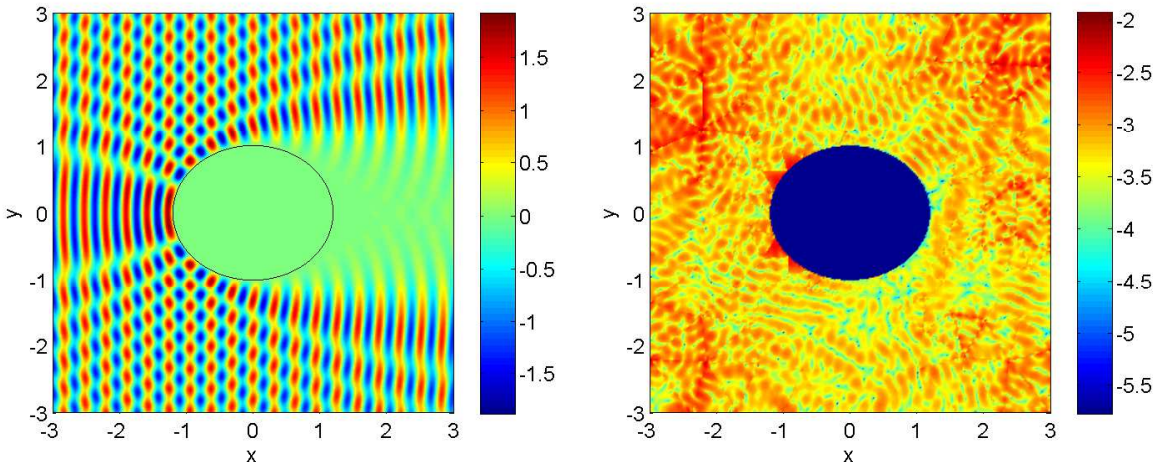

(a) $\mathrm{Re}\, u_N$ (b) $log_{10}|u - u_N|$

Figure 5.18: The real part of the total field in (a) and the absolute error plotted on a $\log_{10}$ scale in (b) for $\kappa = 20$, by option (B), $p = 18$ ray-traced basis functions and $K = 250$ elements.

5.2.3 Conventional and Ray-Traced Basis Comparison

Figures 5.19-5.21 show the L^2 relative error achieved using an equi-spaced plane wave basis as done in existing literature, and those achieved by combining the ray tracing and an equi-spaced plane wave basis, for $\kappa = 10, 20, 40$. Again the peaks in the equi-spaced basis results correspond to the case where the incident field is not included in the basis, and the to troughs where it is. As with the case of the circular scatterer, the approximations using the 2 ray traced basis functions combined with n equi-spaced wave directions leads to better results than using the traditional equi-spaced basis in $n + 2$ directions. Overall a given level of accuracy is achieved using fewer degrees of freedom when a ray tracing augmented basis is used, compared to the traditional equi-spaced direction UWVF basis.

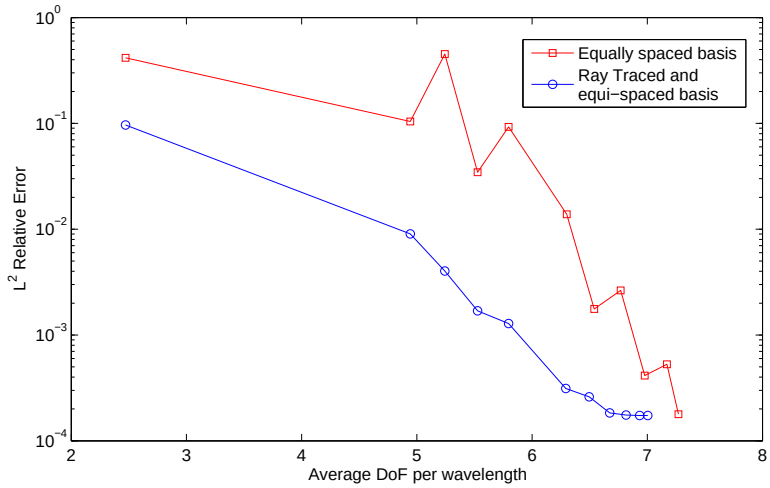

Figure 5.19: Comparison of equispaced and ray-traced with equispaced point source basis sets in UWVF approximation of total field for $\kappa = 10$ for an elliptical scatterer with $a = 1.2$, $b = 1$, $K = 250$, $p = [2, 8, 9, 10, 11, 13, 14, 15, 16, 17, 18]$. L^2 relative error against average degrees of freedom per wavelength.

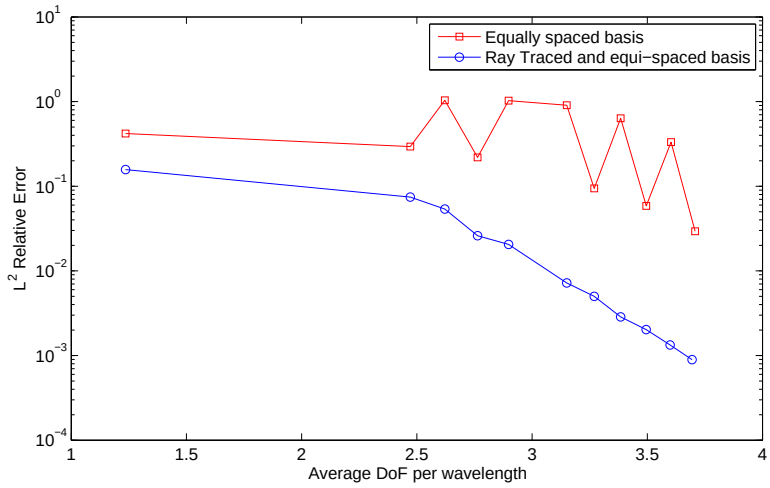

Figure 5.20: Comparison of equispaced and ray-traced with equispaced point source basis sets in UWVF approximation of total field for $\kappa = 20$ for an elliptical scatterer with $a = 1.2$, $b = 1$, $K = 250$, $p = [2, 8, 9, 10, 11, 13, 14, 15, 16, 17, 18]$. L^2 relative error against average degrees of freedom per wavelength.

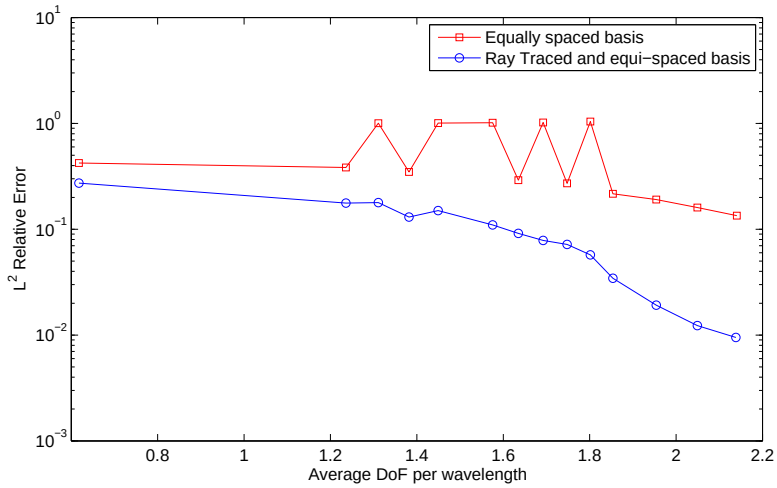

Figure 5.21: Comparison of equispaced and ray-traced with equispaced point source basis sets in UWVF approximation of total field for $\kappa = 40$ for an elliptical scatterer with $a = 1.2$, $b = 1$, $K = 250$, $p = [2, 8, 9, 10, 11, 13, 14, 15, 16, 17, 18, 20, 22, 24]$. L^2 relative error against average degrees of freedom per wavelength.

5.3 Summary

This chapter is the first in which we investigate the enrichment of the UWVF basis using ray tracing techniques. We considered the case of wave scattering by a smooth convex obstacle in a domain of constant wavespeed, and use the ray tracing algorithm developed in §4.1 to provide the local centre of curvature for the reflected wavefronts. The use of the UWVF for approximating wave scattering by a circle was presented in §5.1 , and by an ellipse in §5.2. Accurate results were achieved in both cases with the conventional angularly equi-spaced basis, as used in existing literature. The UWVF basis was then enriched with the ray-traced wave directions and centres of curvature computed in §4.1. Results of the UWVF approximations show a reduction in the number of degrees of freedom required for a given level of accuracy when using the ray enriched basis compared to the original equi-spaced basis. In all cases, the approximations using the 2 ray traced basis functions combined with n equi-spaced wave directions leads to better results than using the traditional equi-spaced basis in $n + 2$ directions.

Chapter 6

Ray Tracing for Enriching the UWVF Basis, with Seismic Imaging Applications.

6.1 Introduction

In this chapter we now turn to the approximation of acoustic wave propagation in a representative geophysical model: large domain of varying wavespeeds thoughout, where the medium is layered horizontally and may include seismic faults. The sound speed profile we use is the Marmousi model [46, 54, 71], a commonly used test case in geophysics. In order to use the UWVF for seismic imaging applications, we must take into consideration the representation of the sound speed profile by a finite element mesh where the wave number is constant in each element. In seismics, acoustic waves are typically at low frequencies. However as the wavelength $\lambda = 2\pi/\kappa$ is very small compared to the size of the domain and the structures within, there are many wavelengths across the domain and so it can be considered as a high frequency problem. Extending the work in Chapter 5, we seek to augment the UWVF by using the ideas of ray tracing to find a good a priori choice of basis function. The use of ray tracing techniques to augment numerical methods has been demonstrated in much literature, for example [2, 11].

We implement two types of ray tracing techniques, using the method of characteristics [14,32] and the Fast Marching Method (FMM) [13,67] to solve the eikonal equation (2.19). These methods are used to provide a high frequency asymptotic approximation to the direction of wave propagation from a point source in our seismic model. We use a point source in order to replicate a single explosive sound source, as used in seismic data aquistition (see §2.3 for more details). We compare the ray paths obtained by both methods with a reference solution achieved using the UWVF. Throughout this chapter we use the notation $\mathbf{x} = (x, z)$, where x is the horizontal distance and z is the vertical depth.

The structure of the chapter is as follows. In §6.2 we present the synthetic seismic sound speed profile that we will be using for our numerical simulations, the Marmousi model. The method of characteristics technique for ray tracing is detailed in §6.3, with numerical results presented in §6.3.1 and compared with a reference solution obtained by the UWVF in §6.3.2. In §6.4 we present an alternative method for finding ray directions, using Fast Marching Methods. In §6.5 we then incorporate these ray directions into the UWVF, with numerical results given comparing an equally spaced basis and the ray enhanced basis. Although there is some improvement in accuracy for a low number of degrees of freedom when using the ray enriched basis, as the number of degrees of freedom increases and the UWVF solutions converge to a fixed state, the difference between the solutions achieved by the two bases are minimal.

6.2 The Marmousi Model

The original Marmousi model, shown in the upper plot of Figure 6.1, is a complex 2D synthetic acoustic velocity model based upon a composite of some typical geological structures. The model was created in 1988 by the Institut Français du Petrole (IFP), based upon the geology in the Kwanza Basin of Angola [46]. It is one of the most widely published geophysical data sets, and has been used by researchers throughout the world as a test case for seismic migration and calibration of travel time and velocity

analysis [54].

The data was originally provided in metres per second for a domain of length 9.216 km and 3 km in depth; for work done here we have scaled the data to be in terms of kilometres per second. It includes a 32 metre layer of water (the sea), under which the different velocities are presented in clear layers, with faults and tilted blocks representative of the different substructures seen in the subsurface of the earth. These layers correspond to different materials, such as sand, water, shale, and salt [54].

As detailed in [71], the computation of rays requires smoothness in the model, to avoid inaccuracies in the numerical approximation of the derivatives of sharply varying medium parameters. A smooth model also avoids the need for computing reflection and transmission coefficients at interfaces for multiple reflections. The asymptotic derivation of the eikonal equation relies upon both a high frequency and the velocity to be smoothly varying, rather than having sharp discontinuities as in the original Marmousi model. Accordingly, a smoothed Marmousi data set of the same data dimensions is instead used for further work here, shown in the lower plot of Figure 6.1. The smoothing was using an isotropic Gaussian smoother [1] on the true velocity model, so the original Marmousi model is convolved pointwise with a Gaussian smoother with a 100 metre smoothing length. Unfortunately the requirement of smoothness results in a loss of detail in some of the structures in the model.

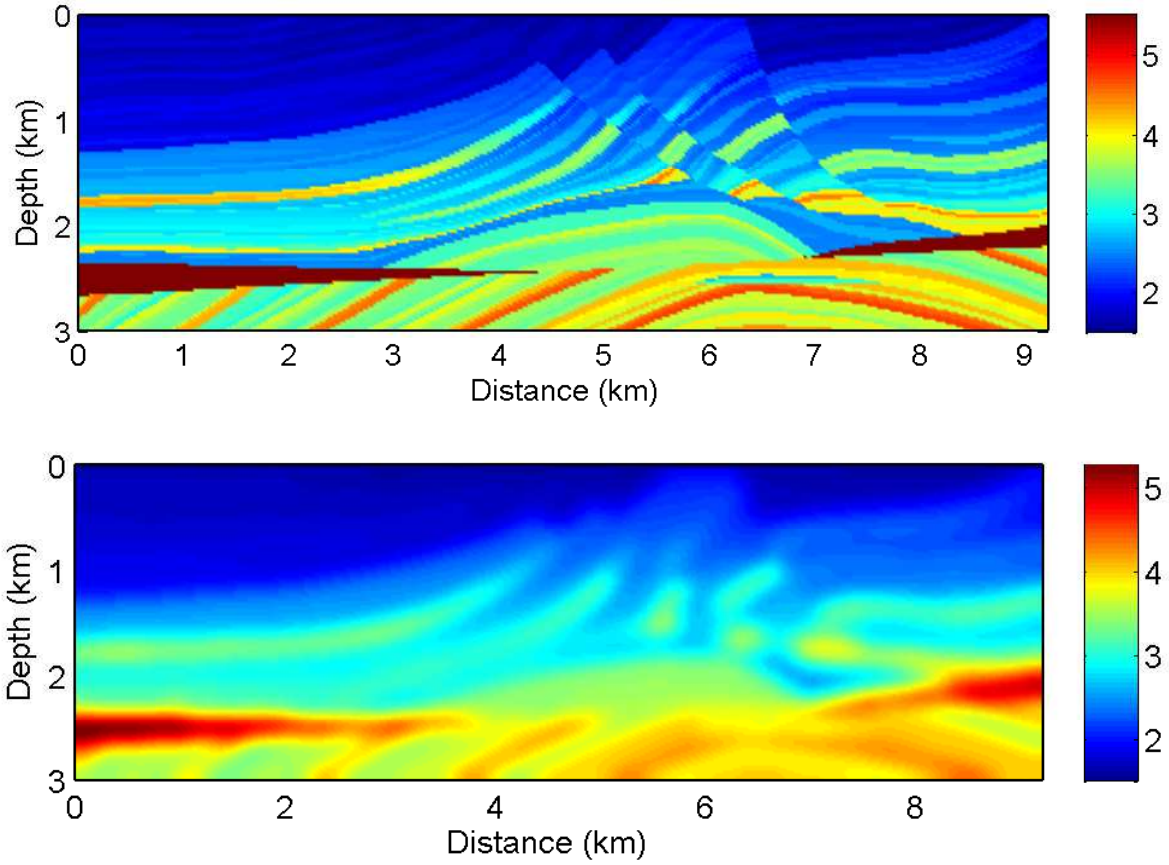

Figure 6.1: The Marmousi model shown in the upper plot, and the smoothed Marmousi model shown in the lower plot: sound speed shown in kilometres per second.

6.3 The Method of Characteristics for Ray Tracing

As detailed in Chapter 2, we consider ray tracing techniques which require the solving of the eikonal equation (2.19). We first of all solve the eikonal equation using the method of characteristics; later in §6.4 we use an alternative method, the FMM.

We use the method of characteristics to obtain the characteristic curves: these are the geometric trajectories of the rays travelling through the domain [12, 14]. This method provides multiple ray paths from an original starting point, so giving the direction of propagation of wavefronts propagating outwards from a point source. It allows rays to cross, permitting multi-valued solutions at these points, rather than just providing the path of quickest return to the surface for a point. The multi-valued solution corresponds to the wavefront folding, due to reflections in different directions [14]. However, this method provides directions only for points through which the rays pass, and not for every point in the domain. Details of the amplitude are also given by the rays: regions which are densely populated by rays are those in which the wave field has a higher amplitude than those in which rays are sparse [14, §5.1].

We write the eikonal equation (2.19) in the form of a Hamilton-Jacobi equation,

$$H(\mathbf{x}, \mathbf{s}) = 0 \qquad \text{with } s_i = \frac{\partial \tau}{\partial x_i}. \tag{6.1}$$

Here $\tau = \tau(x_i)$ is the generating function to be determined (the eikonal) and s_i are the generalised momenta (the slowness in each direction), with $i = 1, 2$, representing the two spatial dimensions (so $x_1 := x$ and $x_2 := z$). The Hamilton-Jacobi equation (6.1) is solved along characteristics which satisfy the canonical equations:

$$\frac{dx_i}{d\nu} = \frac{\partial H}{\partial s_i}, \qquad \frac{ds_i}{d\nu} = -\frac{\partial H}{\partial x_i}, \qquad \frac{d\tau}{d\nu} = \sum_i s_i \frac{\partial H}{\partial s_i}, \qquad i = 1, 2 \tag{6.2}$$

[14, Equation (3.31)], where ν is a flow parameter. Along these curves the eikonal equation is satisfied and the generating function τ can be computed. These characteristic curves are the seismic rays.

Note: these equations ensure that the Hamiltonian H= constant as

$$\frac{dH}{d\nu} = \frac{\partial H}{\partial x}\frac{\partial x}{\partial \nu} + \frac{\partial H}{\partial s}\frac{\partial s}{\partial \nu} \tag{6.3}$$

$$= -\frac{\partial s}{\partial \nu}\frac{\partial x}{\partial \nu} + \frac{\partial x}{\partial \nu}\frac{\partial s}{\partial \nu} \tag{6.4}$$

$$= 0 \tag{6.5}$$

thus $H = \hat{c}$ for some constant $\hat{c}$.

In isotropic structures, the eikonal equation is of the form (2.21),

$$\sum s_i(\mathbf{x})^2 = \frac{1}{c^2}. \tag{6.6}$$

Taking our eikonal equation in Hamilton-Jacobi form

$$H(\mathbf{x}, \mathbf{s}) = \sum s_i(\mathbf{x})^2 - \frac{1}{c^2} \tag{6.7}$$

and applying the canonical equations (6.2), we obtain the system

$$\frac{\partial}{\partial \nu}\begin{pmatrix} x_1 \\ x_2 \\ s_1 \\ s_2 \\ \tau \end{pmatrix} = \begin{pmatrix} \frac{\partial H}{\partial s_1} \\ \frac{\partial H}{\partial s_2} \\ -\frac{\partial H}{\partial x_1} \\ -\frac{\partial H}{\partial x_2} \\ \mathbf{s}\cdot\frac{\partial H}{\partial \mathbf{s}} \end{pmatrix} = \begin{pmatrix} 2s_1 \\ 2s_2 \\ -2c^{-3}\frac{\partial c}{\partial x_1} \\ -2c^{-3}\frac{\partial c}{\partial x_2} \\ 2\left\|\mathbf{s}\right\|_2^2 \end{pmatrix}. \tag{6.8}$$

We chose an initial starting point $\mathbf{x}$ (where $\tau = 0$) and initial direction for the trajectory, and compute the slowness in that initial direction. By solving system (6.8) we get updates for the travel times τ, the geometric trajectories (the updated point $\mathbf{x}$), and the slowness vector for points along the trajectory $\mathbf{s}$.

The Hamilton-Jacobi system (6.8) is of the form

$$\frac{\partial}{\partial \nu}(\mathbf{X}) = F(\mathbf{X})$$

and so can be solved numerically using a Runge-Kutta scheme, integrating for updates of the vector $\mathbf{X}$. We use the ode45 routine inbuilt in Matlab, which is an explicit Runge-Kutta formula for fourth and fifth order accurate solutions. The inputs required for the ode45 routine are: the functional form F, a time interval over which to integrate, and

an initial state vector $\mathbf{X}$. The output produced is the updates of the state vector $\mathbf{X}$ over the time period, which gives the updates for our ray path $\mathbf{x}$, the slowness $\mathbf{s}$ in each direction at the points on the ray, and the eikonal along the ray. Options for ode45 are set to assert that the initial point source is within the domain, and to stop the method when rays travel out of the domain. For the spatial derivatives in (6.8) we use a central derivative approximation of the form

$$\frac{\partial c}{\partial x} = \frac{c_{i+1,j} - c_{i-1,j}}{2\Delta x} \tag{6.9}$$

$$\frac{\partial c}{\partial z} = \frac{c_{i,j+1} - c_{i,j-1}}{2\Delta z} \tag{6.10}$$

where Δx and Δz are the spatial step lengths in the x and z directions respectively. Care must be taken at edges of the domain to not use points outside of the domain, using the approximations

$$\frac{\partial c}{\partial x} = \frac{c_{2,j} - c_{1,j}}{\Delta x} \tag{6.11}$$

on the left-hand boundary and

$$\frac{\partial c}{\partial z} = \frac{c_{i,2} - c_{i,1}}{\Delta z} \tag{6.12}$$

on the upper boundary, and similar approximations for the right and lower boundaries. As the rays pass through points which are not grid points of our discretisation, we then used 2D cubic interpolation to find the sound speed c and spatial derivatives for points along the ray.

6.3.1 Example Numerical Results for Ray Tracing on Smoothed Marmousi Data

Here we present example results of rays sent out at angles $\theta \in (0, \pi)$ from a point source close to the surface, at the point $(4.692, 0.02)$ in Figure 6.2. Results are shown for 50 starting rays in equispaced directions in the upper plot, for 200 rays in the centre plot, and for 400 rays in the lower plot. Clearly by using more initial starting rays we can glean more information about the direction of wave propagation in the domain. The rays travel through the domain, turning more in regions where there is a

sharper increase in velocity of the model. We would predict higher amplitudes of waves propagating through areas in which rays accumulate. In areas where rays are sparse, ray theory predicts there to be lower amplitudes [14, §5.1].

The method of characteristics technique for ray tracing is widely used in the geophysics community, as the dominant ray directions can be found by considering multiple ray paths from a source [2, 14]. However, for the use of implementing an initial guess of wave directions in an enriched UWVF basis, this type of ray tracing method is not optimal. The areas in which the rays are dense or crossing would have many possible direction choices, whereas in the regions where rays are sparse the choice may be limited. An initial guess of directions could be taken by interpolating directions from the closest rays to a point, however could potentially be erroneous as the velocity profile may be highly varying in the region between neighbouring rays.

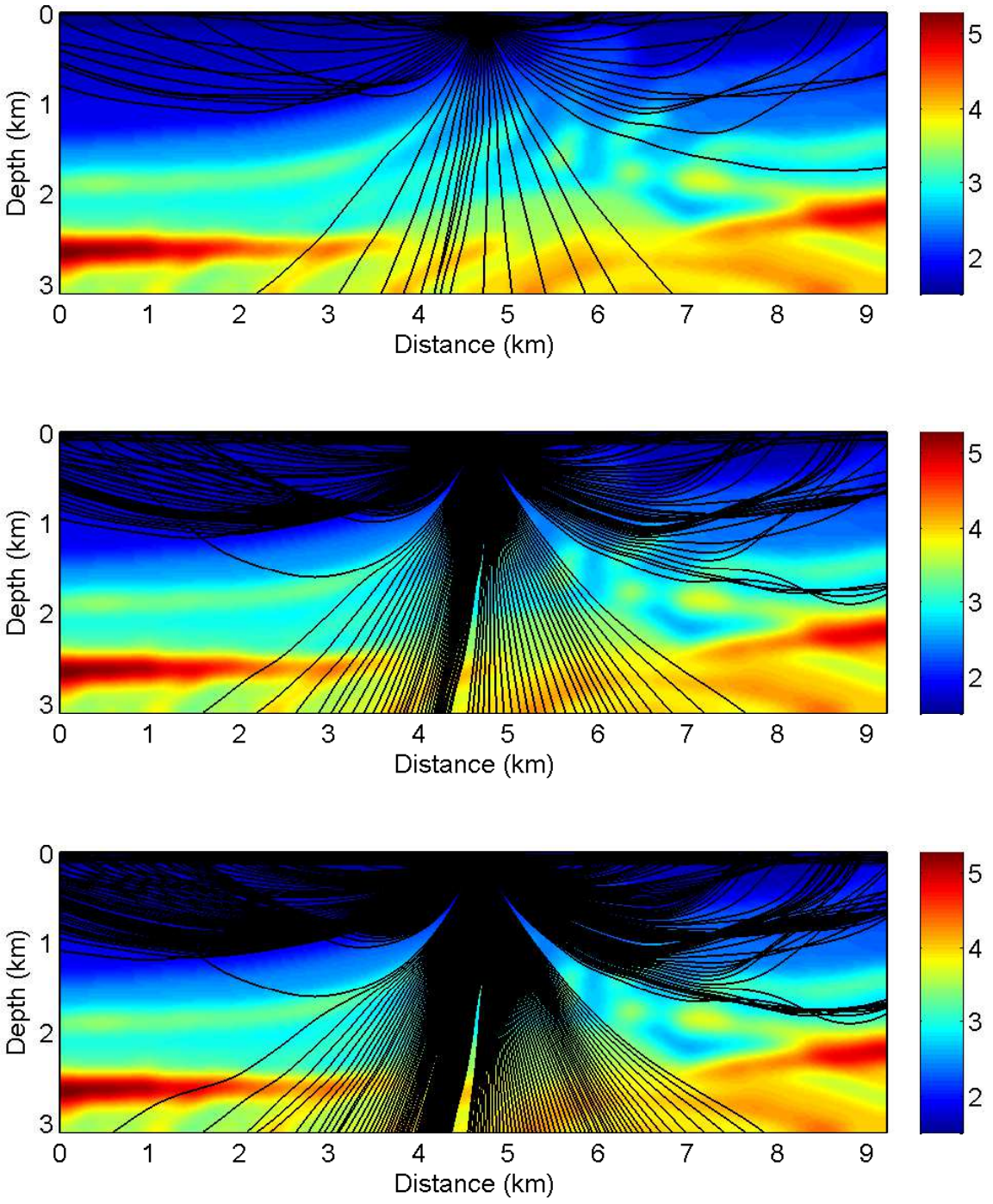

Figure 6.2: Example of the method of characteristics for ray tracing on the smoothed Marmousi model (km/s), from a source at $(4.692, 0.02)$. Shown in the upper plot are the trajectories of 50 equi-spaced ray directions, in the centre plot are the trajectories of 200 equi-spaced ray directions, and in the lower plot are those of 400 equi-spaced ray directions.

6.3.2 Comparison of Ray Directions with Wave Propagation Solution by the Ultra Weak Variational Formulation

We now use the UWVF to find an approximation of wave propagation through our geophysical domain, and compare these results with the ray directions given by the method of characteristics. The Marmousi model is a highly complex domain, representative of the complexities of the subsurface of the Earth. As such, we do not have an exact solution with which to compare our UWVF results to. Thus the ray tracing results supply us with an alternative measure with which to compare our results. As the UWVF is highly computationally expensive to run on a fine mesh, we instead use a section of the smoothed Marmousi model for our domain Ω, rather than the entire model. This allows us to maintain more of the detail of the variation in the velocity profile for a given number of elements when the domain is discretised. We now take for our domain the section $\Omega = [3.5131, 7.0022] \times [0, 2.0565]$ km of the Marmousi model, as shown in Figure 6.3. To obtain a piecewise-constant wavenumber, for each $\Omega_k \in \mathcal{T}^E$, $\kappa|_{\Omega_k} = \kappa_k$ is taken to be the average of the wavenumber of the smoothed Marmousi model at the three vertices of the element. Examples of the resultant wavenumber discretisation are shown in Figure 6.5.

As we only have the sound speed profile from the Marmousi data set, we use a constant density $\rho \equiv 1$ throughout. The UWVF has difficulty representing a point source on the interior of the domain (see Chapter 7). To avoid this difficulty, we use an exterior point source and so solve the homogeneous Helmholtz equation (3.1a) with $f = 0$. Specifically, we solve

$$\nabla^2 u + \kappa^2 u = 0, \qquad \text{in } \Omega. \tag{6.13}$$

We use impedance boundary conditions with $Q = 0$ in (3.1b) giving

$$\frac{\partial u}{\partial n} - \mathrm{i}\sigma u = g \qquad \text{on } \Gamma. \tag{6.14}$$

We use the radiating solution from an external source to impose g on Γ. For the sound source we use a point source incident field $u^i = H_0^1(\kappa_{sea}|\mathbf{x}-\mathbf{x}_s|)$ imposed only on the top

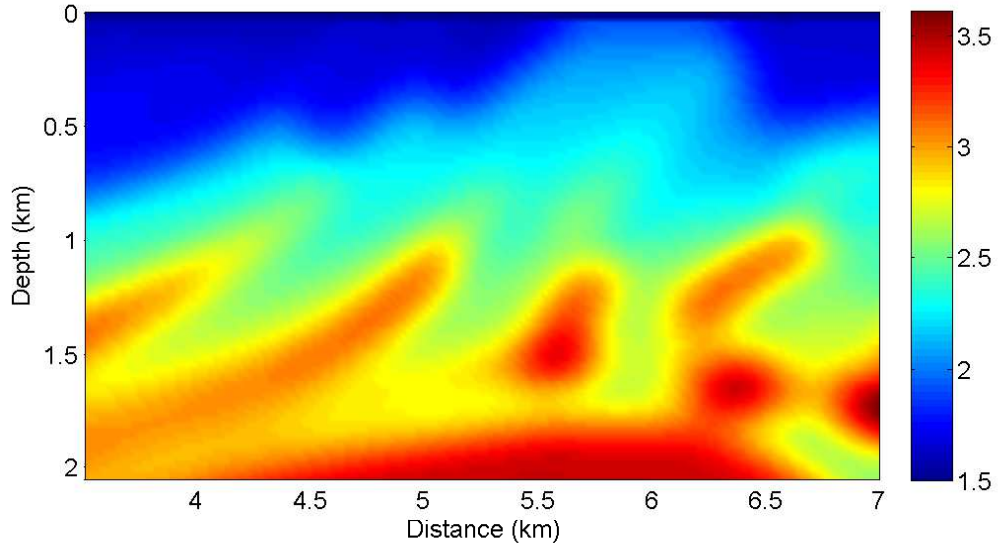

Figure 6.3: Section of Smoothed Marmousi Velocity Model

boundary $\Gamma_{surface}$ for which $z = 0$. We take the point source $\mathbf{x}_s \notin \Omega$ as a point exterior to the domain on the $z < 0$ side. We use the value κ_{sea} in our incident field equal to the wavenumber corresponding to the sound speed in the upper two rows of the discrete Marmousi data set, representing water. This simulates the sea being extended and the incident field originating at a point within this extended sea, which should minimise any reflections when the incident field reaches the domain. Thus for the source term in (6.14) we take $g = \frac{\partial u^i}{\partial n} - \mathrm{i}\sigma u^i$, resulting in

$$g = \begin{cases} \nabla H_0^1(\kappa_{sea}|\mathbf{x} - \mathbf{x}_s|) \cdot \mathbf{n} - \mathrm{i}\sigma H_0^1(\kappa_{sea}|\mathbf{x} - \mathbf{x}_s|) & \text{on } \Gamma_{surface} \\ 0 & \text{in } \Gamma/\Gamma_{surface}. \end{cases} \tag{6.15}$$

The impedance boundary condition (6.14) ensures that the incident field is out going from the domain, however we are unable to force this to hold for the scattered field, as it is unknown. A more accurate method would be to use a Perfectly Matched Layer around the domain, which adds exponential decay to waves leaving the domain ensuring any reflections are negligible [27, 41]. Here we use the conventional equi-spaced plane wave basis, by using (3.49) with point sources (3.50) in the far field ($R_{PS} = 600$). An initial maximum of $p = 20$ directions per element is set, and then reduced if $\mathrm{cond}(D_k) \geq 10^{10}$, following the method of [44] detailed in §3.5.

The method of characteristics requires the initial starting point source for rays to be on the interior of the domain, whereas for our UWVF implementation we require an exterior source (difficulties in the implementation of an interior source in the UWVF will be discussed in the following Chapter 7). For the ray tracing algorithm it was therefore necessary to use an artificially extended domain, Ω^+, so that the point source is on the interior $\mathbf{x}_s \in \Omega^+ \backslash \Omega$. For Ω^+ we deepen the region of the sea, corresponding to the first two rows of data of the discrete Marmousi model. This was done by adding rows of data with the same velocity of the former upper rows. The extended smoothed Marmousi model in Ω^+ is shown in Figure 6.4, as well as 50 equi-spaced (in the half-plane) rays generated by the method of characteristics from a point source at $\mathbf{x}_s = (4.69, -0.10)$. For the UWVF we consider the solution only in the original domain Ω, but with the point source exterior, in the same location $\mathbf{x}_s$ as for the ray tracing. As the velocity is a constant in the extended region, rays are straight lines and so it is permissable to match up with the UWVF solution of the original grid lower down. This is also acceptable practically, as in real world implementation the signal may come from a seismic source on the surface of the sea, being towed by a boat. Some rays reflect back upon entering Ω, this represents wave energy being reflected back off the sea bed.

Following are the numerical results for the point source at $\mathbf{x}_s = (4.69, -0.10)$. For the UWVF approximation we test two frequencies, $f_r = 5, 10$ Hz. Three levels of discretisation are compared: the first with $K = 85$ elements, the second with $K = 367$ elements, and the finest discretisation with $K = 1569$ elements. The discretisations and wavenumber per element are shown in Figure 6.5 for $f_r = 5$ Hz; for $f_r = 10$ Hz the pattern is the same but with the wavenumbers doubled throughout. For $f_r = 5$ Hz: in Figure 6.6 the number of basis functions on each element (reduced depending upon $\text{cond}(D_k)$) is shown for the three discretisations; in Figure 6.7 the UWVF approximation is shown; in Figure 6.8 the UWVF approximation is shown with the ray traced directions superimposed, for comparison of directions. Similarly for $f_r = 10$ Hz: in Figure 6.9 we have the number of basis functions on each element for the two finer discretisations (for $K = 85$ and $p_k = 20$ throughout); in Figure 6.10 is the UWVF approximation; in Figure 6.11 we have the UWVF approximation and ray traced directions superimposed.

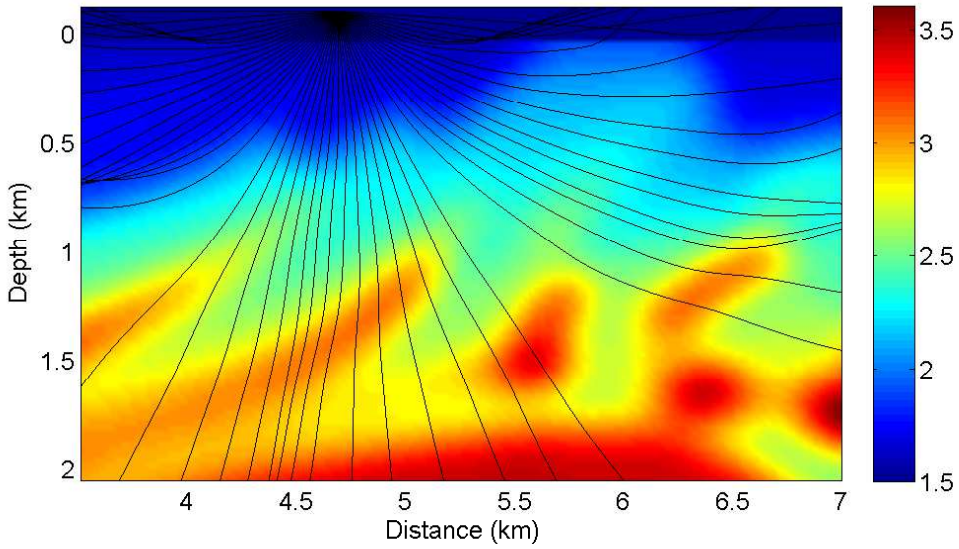

Figure 6.4: The extended smoothed Marmousi sound speed profile (km/s) in Ω^+, with 50 ray paths from $\mathbf{x}_s = (4.69, -0.10)$ obtained by the method of characteristics.

When comparing the UWVF approximations in Figures 6.7 and 6.10 there are similarities but also clear differences in the approximations provided by the different discretisations. However we do not have an exact or comparison solution with which to gauge the accuracy of the UWVF solution. If we consider the representation of the velocity profile by the discretised domain, shown in Figure 6.5, the coarsest discretisation loses much of the detail, whilst the finest discretisation keeps a good representation of the background velocity profile (here colours are inverse to the smoothed Marmousi model, due to the inverse relationship between frequency and wavenumber). However, we must question the accuracy that can be achieved using such a fine discretisation: as the element size becomes smaller, fewer basis functions can be used in each element (as can be seen in Figures 6.6 and 6.9) before we have problems with ill-conditioning, and so the resultant directions in the basis may not be sufficient to represent the directions of the solution. For the frequency $f_r = 5$ Hz it could be concluded that the central discretisation with $K = 367$ elements might be the most accurate representation, as there is still the detail of the velocity profile, the element size and variation in wavenumber in comparison to the wavelength is sufficiently small, and there is still a moderate number

of directions being tested throughout the domain. For the higher frequency $f_r = 10$ Hz, as the wavelength is shorter the conditioning improves, and so the finer discretisation of $K = 1569$ elements does still permit a moderate number of directions per element. In this case the variation in the profile is small compared to the element size, and so much of the detail of the smoothed Marmousi model is maintained. However, the literature [31] suggests to improve accuracy through increasing the number of basis function per element rather than through mesh refinement, subject to the mesh size being 'sufficiently small' -of order of the wavelength. The central discretisation with $K = 367$ does still provide a fairly small element size compared to the wavelength, and a much higher number of basis functions per element can be used. By comparing with the ray traced directions in Figure 6.11 it is still ambiguous as to which may be the more accurate solution. Nevertheless, the ray directions and the UWVF solutions do coincide well: rays travel perpendicular to wavefronts, are sparse in the areas of low amplitude, and are dense in the areas of higher amplitudes.

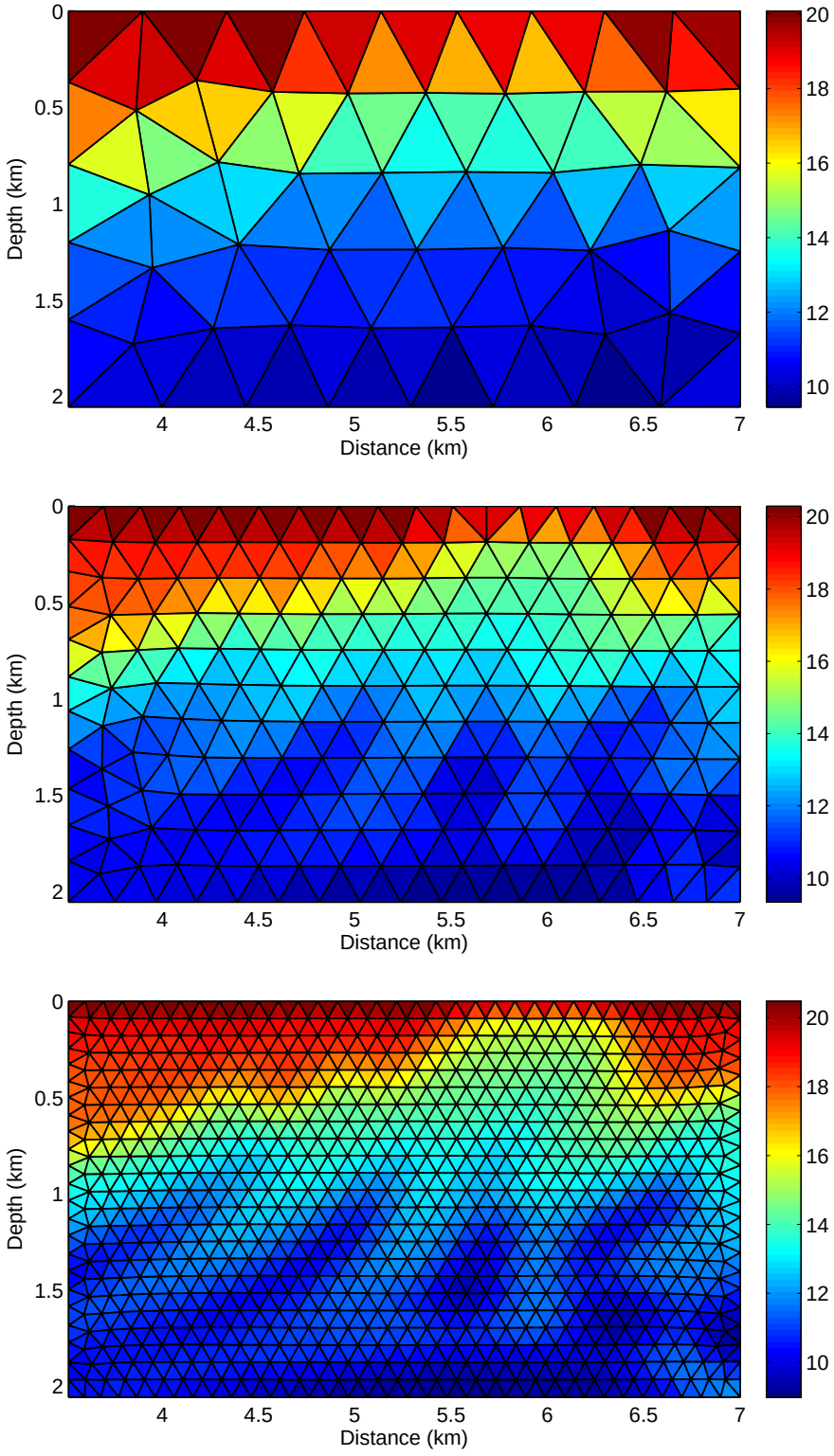

Figure 6.5: Wavenumber in a discretised section of the Smoothed Marmousi model, for $f_r = 5$ Hz, with $K = 85$ elements in the upper plot, $K = 367$ in the center, and $K = 1569$ in the lower plot.

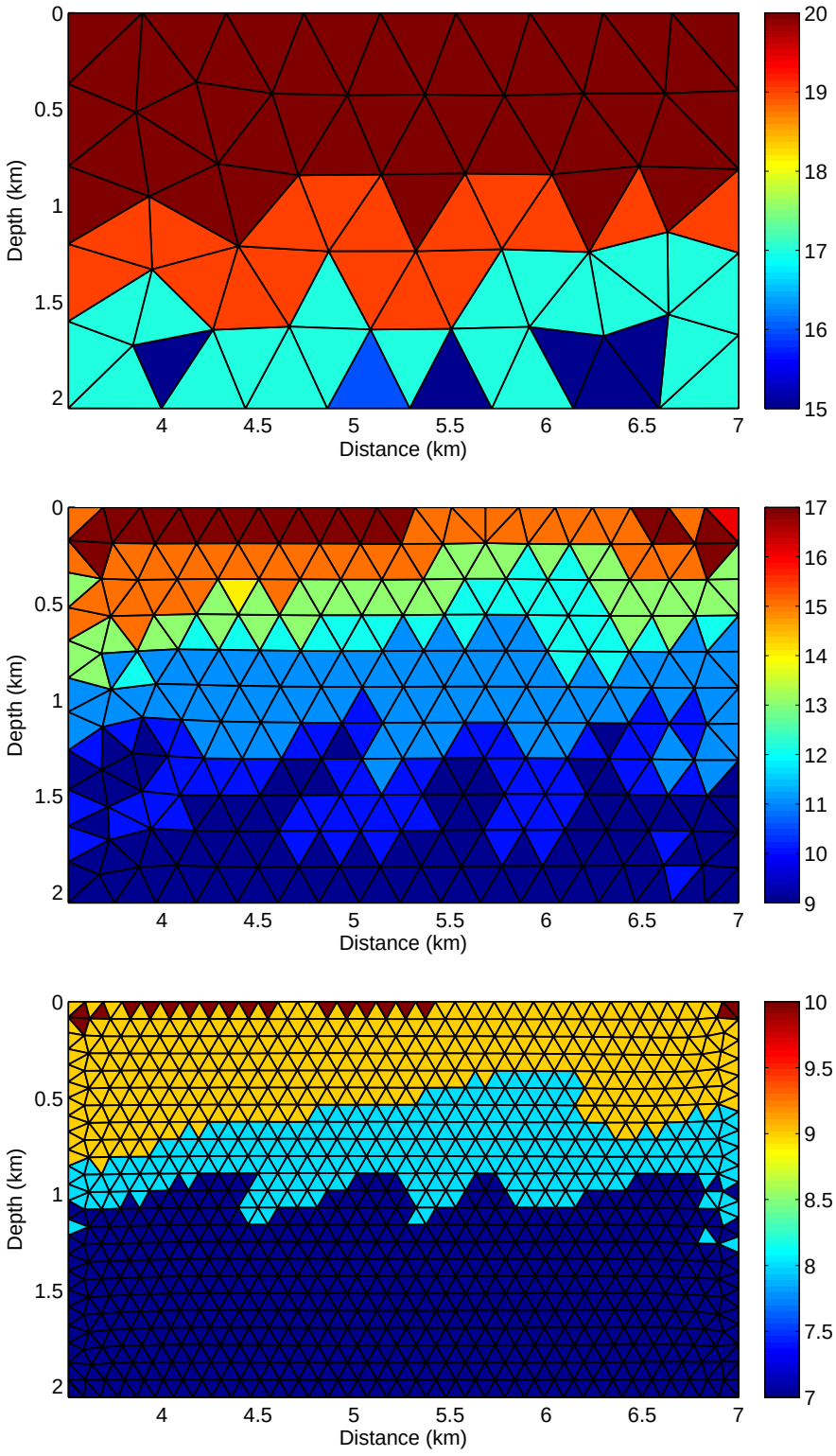

Figure 6.6: Number of basis functions per element in UWVF approximation of wave propagation in a section of the Smoothed Marmousi model, for $f_r = 5$ Hz, with $K = 85$ elements in the upper plot, $K = 367$ in the center, and $K = 1569$ in the lower plot.

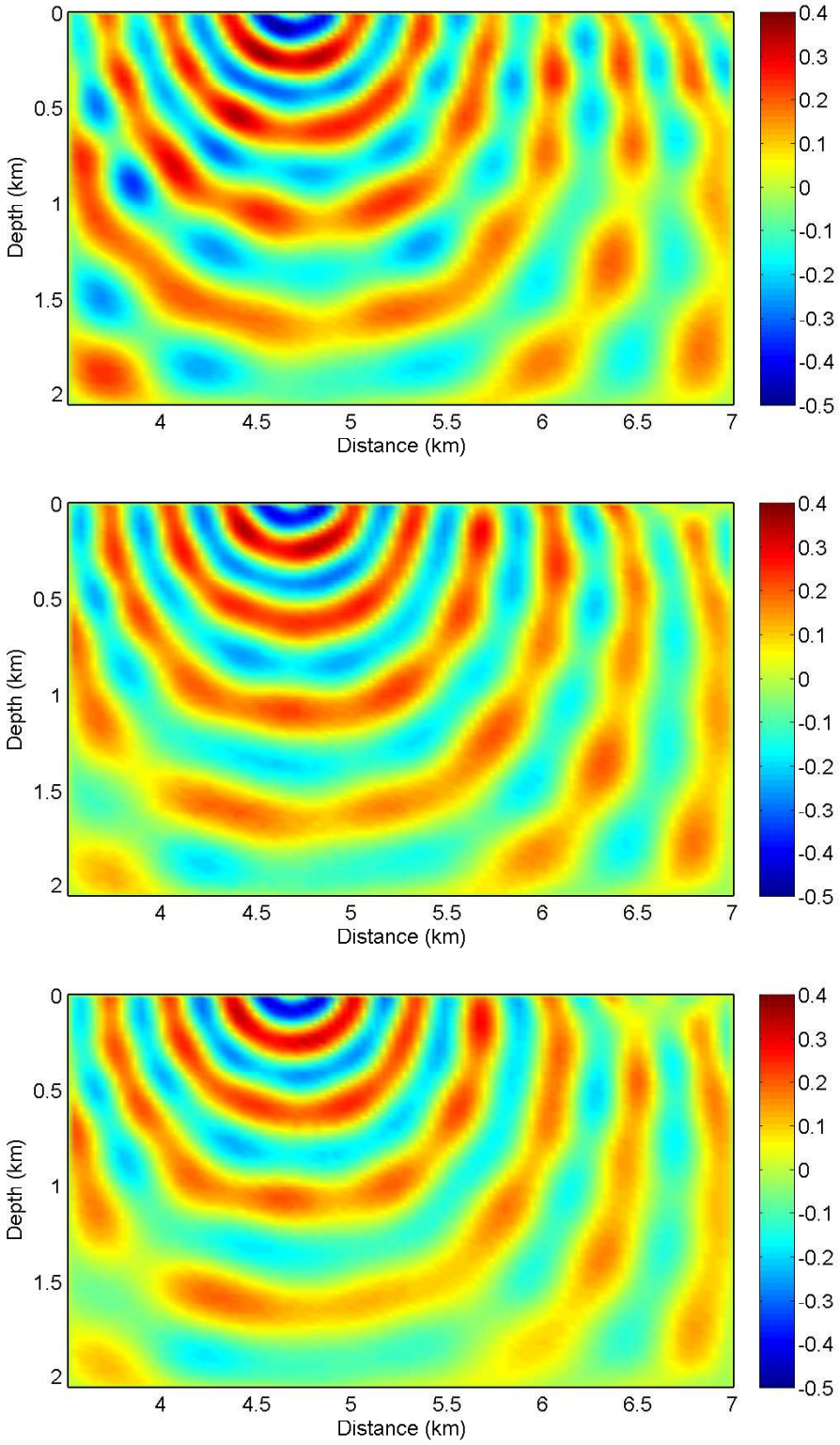

Figure 6.7: Real part of UWVF approximation of wave propagation in a section of the Smoothed Marmousi model, for $f_r = 5$ Hz, with $K = 85$ elements and $\max_k(p_k) = 20$ in the upper plot, $K = 367$ and $\max_k(p_k) = 17$ in the center, and $K = 1569$ and $\max_k(p_k) = 10$ in the lower plot.

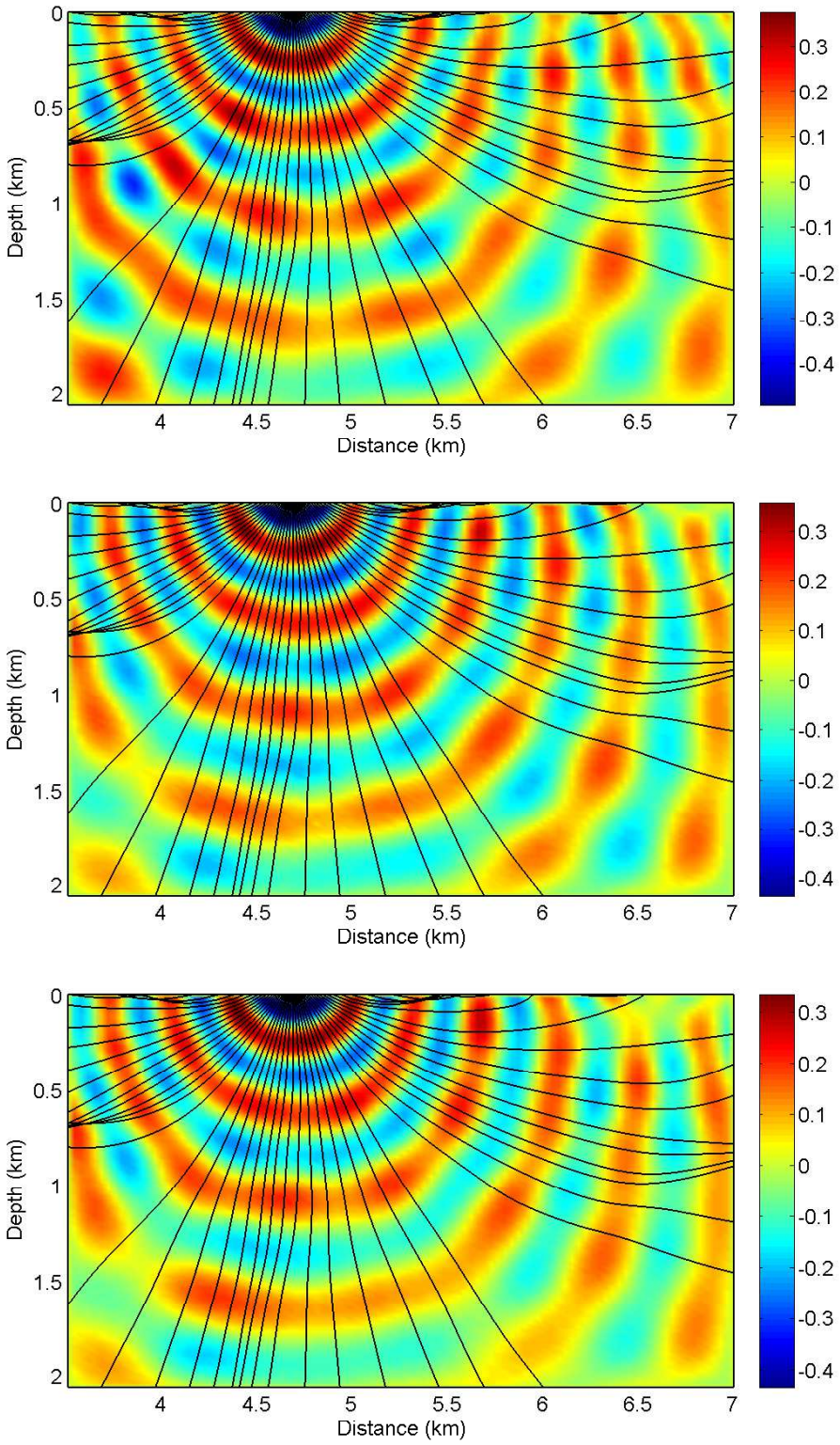

Figure 6.8: Real part of UWVF approximation of wave propagation and ray tracing in a section of the Smoothed Marmousi model, for $f_r = 5$ Hz, with $K = 85$ elements and $\max_k(p_k) = 20$ in the upper plot, $K = 367$ and $\max_k(p_k) = 17$ in the center, and $K = 1569$ and $\max_k(p_k) = 10$ in the lower plot.

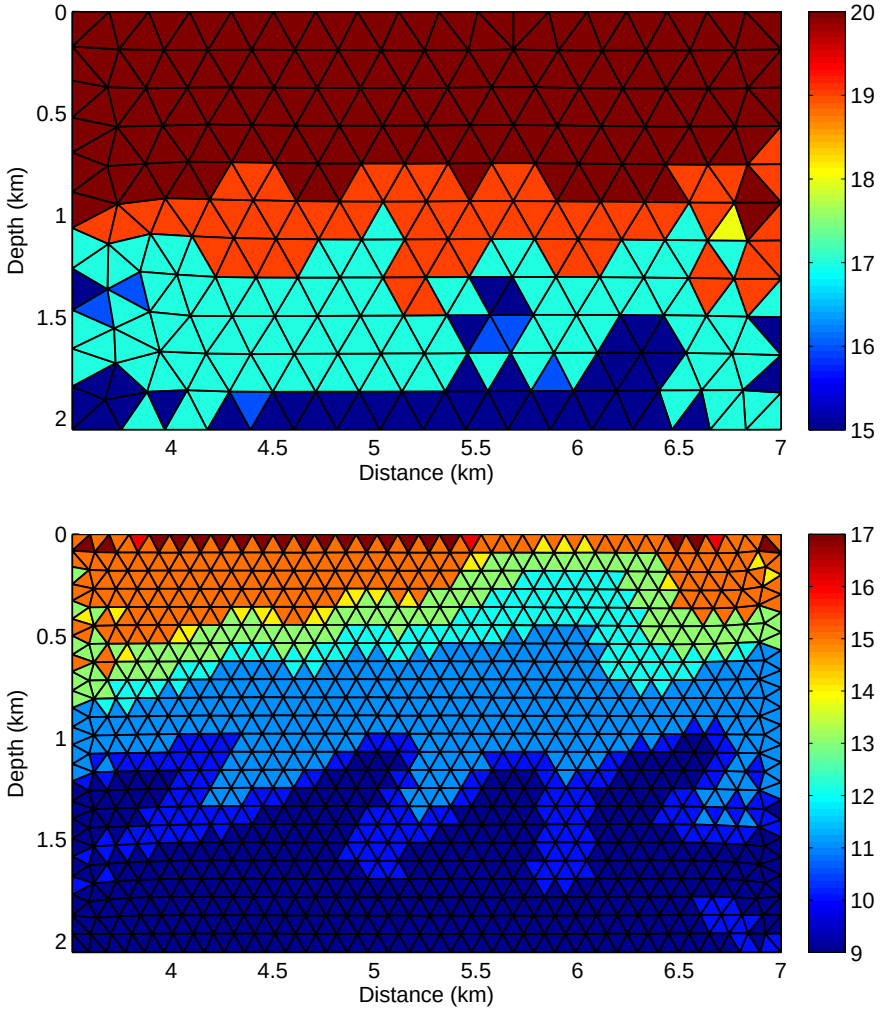

Figure 6.9: Number of basis functions per element in UWVF approximation of wave propagation in a section of the Smoothed Marmousi model, for $f_r = 10$ Hz, with $K = 367$ elements in the upper plot, and $K = 1569$ in the lower plot.

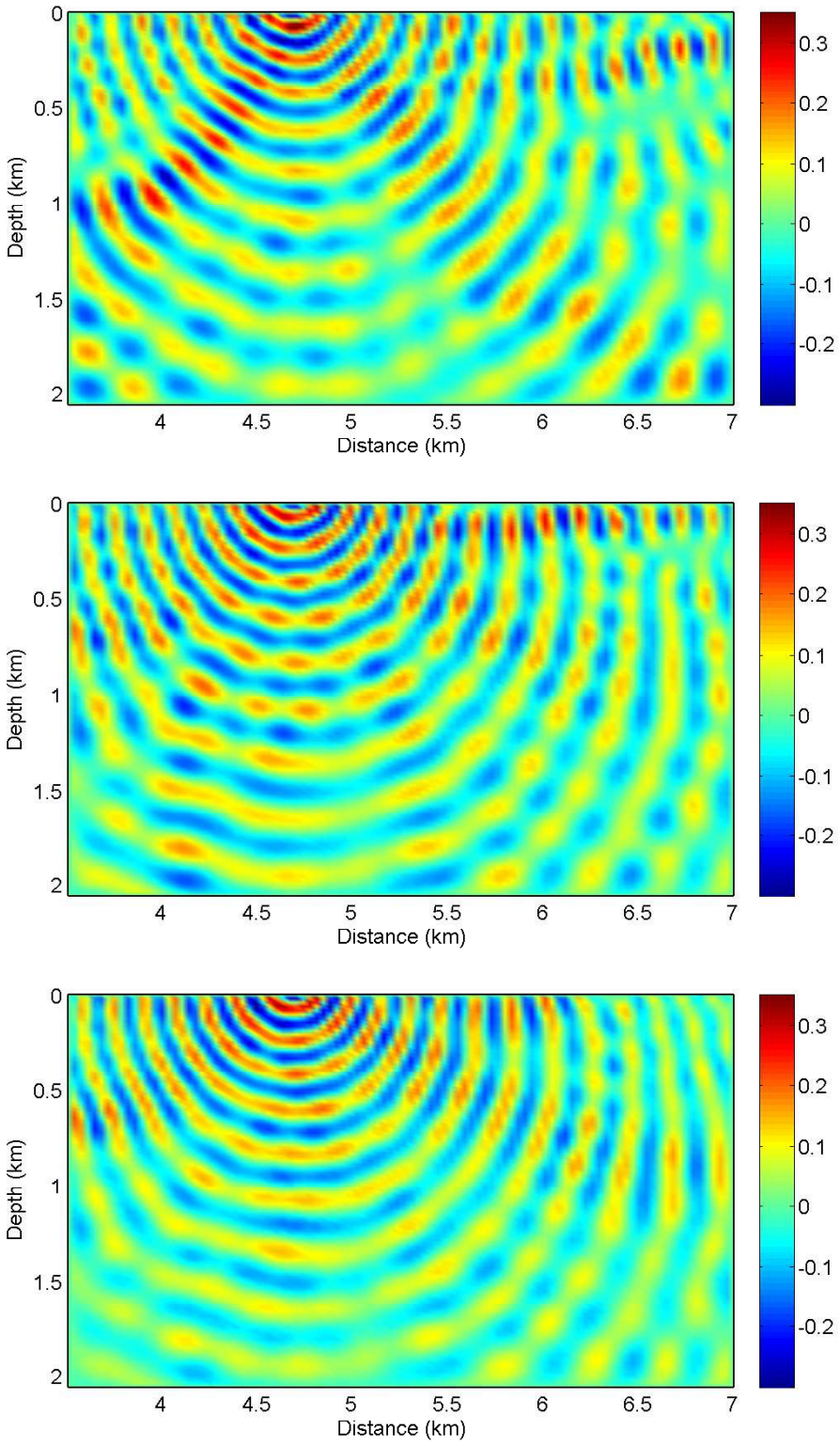

Figure 6.10: Real part of UWVF approximation of wave propagation in a section of the Smoothed Marmousi model, for $f_r = 10$ Hz, with $K = 85$ elements and $\max_k(p_k) = 20$ in the upper plot, $K = 367$ and $\max_k(p_k) = 20$ in the center, and $K = 1569$ and $\max_k(p_k) = 17$ in the lower plot.

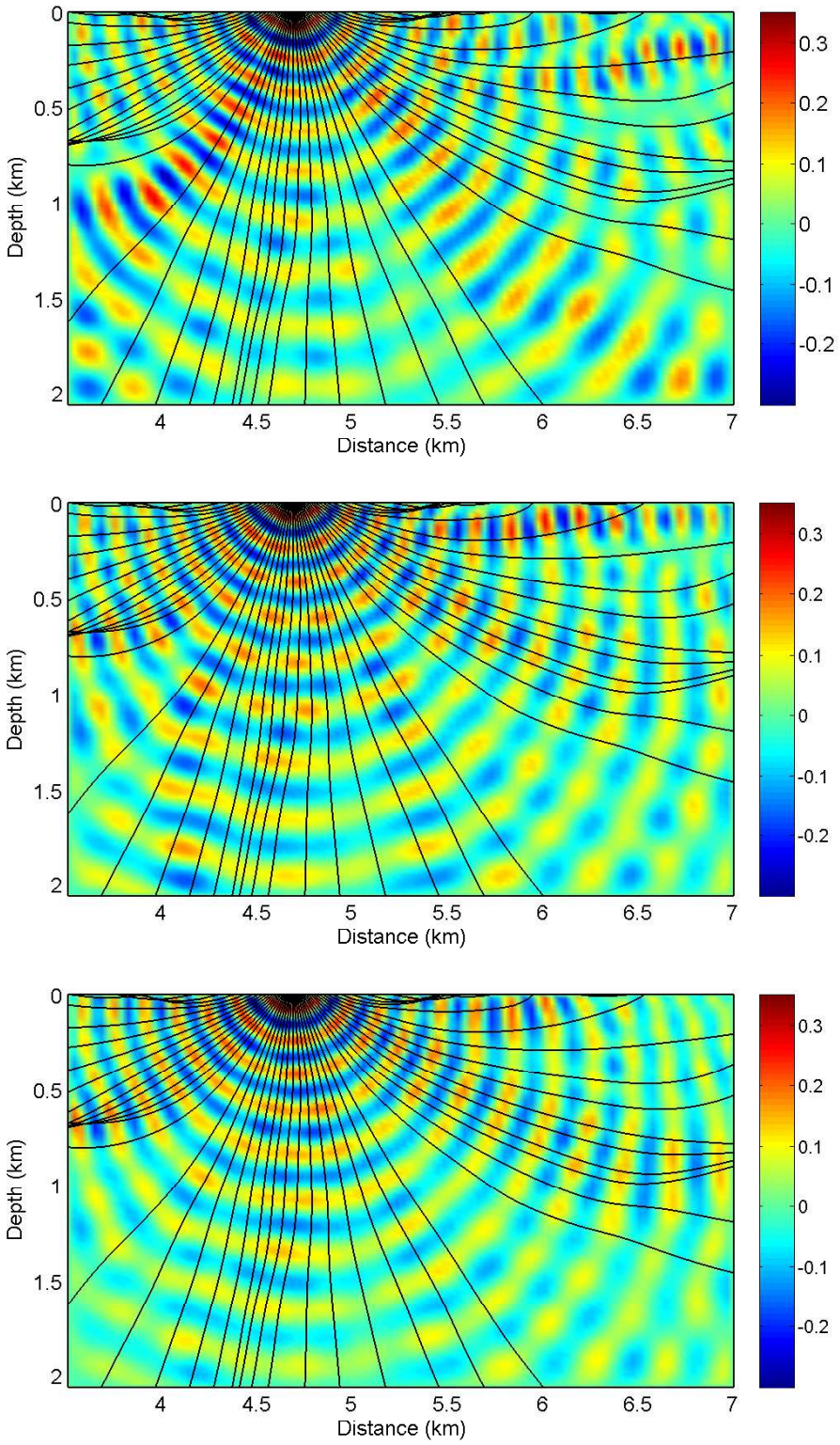

Figure 6.11: Real part of UWVF approximation of wave propagation and ray tracing in a section of the Smoothed Marmousi model, for $f_r = 10$ Hz, with $K = 85$ elements and $\max_k(p_k) = 20$ in the upper plot, $K = 367$ and $\max_k(p_k) = 20$ in the center, and $K = 1569$ and $\max_k(p_k) = 17$ in the lower plot.

6.4 Ray Tracing using Fast Marching Methods

As we have promising ray tracing results using the method of characteristics that support our UWVF solutions, we now seek to augment the UWVF basis with the ray traced directions, similar to the techniques used in Chapter 5. By enriching the basis of the UWVF with these directions, we aim to converge to a solution requiring fewer degrees of freedom than using the standard equi-spaced basis. The ray directions provided by the method of characteristics are dense in the regions where amplitudes are highest, and so here can provide valuable information. However, there are also large regions in the domain in which the rays generated are sparse. Due to this disparity, ray directions obtained by the method of characteristics are not sufficient to be practically implemented in a ray enriched basis for the UWVF. In this section we now use an alternative method for solving the eikonal equation, the FMM [13, 67]. This method gives ray directions for the path of quickest return at any point in the domain, rather than multi travel timed crossing rays as provided by the method of characteristics (see §6.3).

The FMM is a direct grid based method for solving the eikonal equation (2.19)

$$|\nabla\tau(\mathbf{x})|c(\mathbf{x}) = 1 \qquad \text{in } \Omega$$

with

$$\tau = g_{FMM}(\mathbf{x}) \qquad \text{on } \Gamma_{FMM} \tag{6.16}$$

for the travel time function τ given a positive speed function c. The method computes the evolution of an expanding wavefront from an initial boundary Γ_{FMM}. The initial data is given by the function g_{FMM} on Γ_{FMM}, from where the curve propagates outwards. The speed function c first must be defined on a Cartesian grid. Using upwind finite difference operators, travel times τ to reach the neighbouring grid points are calculated given the velocity profile. The path of shortest travel time is then selected for the expanding wavefront. As the arrival time must be uniquely determined, the method can only compute uniformly expanding wavefronts [13], and not those that contract. The FMM is considered similar to Dijkstra's method for computing the shortest path

on a network [67], in that for any given time and wavefront position, the method computes the shortest time to reach the next point, and then the wavefront moves forward to include this point. The process is then continually repeated, the wavefront moving forward at the quickest rate possible given the speed profile of the domain.

As the FMM is a widely used method there are many resources available online. For work in this thesis we use the Toolbox Fast Marching on Matlab Central File Exchange, written by G. Peyre [63]. To use this Toolbox the inputs required are: the starting points that make up Γ_{FMM}, and the velocity profile c of our domain, given on a Cartesian grid. The output produced is the results of the FMM: the travel time τ for all points on the cartesian grid (x_i, z_j), $i = 1, \ldots, N_x$, $j = 1, \ldots, N_z$. These values of τ are the shortest time taken for a wavefront to reach each point given the starting points and velocity profile of the domain. Wavefronts are given by the curves for which τ is constant. However we require the direction of propagation of the waves, given by rays perpendicular to the wavefront. Thus to find the ray directions for the points in our domain, we take a FD approximation of the partial derivatives of τ in the x and z direction:

$$\frac{\partial \tau}{\partial x} = \frac{\tau_{i+1,j} - \tau_{i-1,j}}{2\Delta x} \tag{6.17}$$

$$\frac{\partial \tau}{\partial z} = \frac{\tau_{i,j+1} - \tau_{i,j-1}}{2\Delta z}, \tag{6.18}$$

where $\tau_{i,j}$ is defined as the value of τ at the point (x_i, z_j) in the discretsation of the domain. Care is taken around the edges of the domain to approximate the derivatives using values inside the domain, so for example we instead take

$$\frac{\partial \tau}{\partial x} = \frac{\tau_{1,j} - \tau_{2,j}}{\Delta x} \tag{6.19}$$

to calculate values on the left hand edge of the domain, and similar for the remaining edges.

6.5 Ray Directions in the UWVF

Work in current literature for the UWVF finds an approximate solution using equally spaced plane wave basis functions [16, 17, 31, 36, 41, 44]. When the form of the solution is unknown this is an appropriate method for finding accurate solutions. However, when more information is known about the form of the solution, by incorporating these details into our numerical method it may be possible to save computational time and expense. We aim to use ray directions gained from the FMM to enrich the basis for the UWVF.

We use the Hankel basis in the UWVF, which still allows a plane wave representation by taking the point sources in the far field. To enrich the basis by ray directions gained from the FMM, we take the ray direction as $\mathbf{d}_{ray} = \nabla\tau$ at the centroid of each element $\mathbf{x}_k^C$. However, as we have the travel times on the cartesian grid, it was neccessary to use cubic interpolation of $\nabla\tau$ to find the direction at the centroid. We take for the first of the basis functions of each element the centre of curvature to be

$$y_{k,1} = \mathbf{x}_C - R_{PS}\mathbf{d}_{ray} \tag{6.20}$$

with $R_{PS} = 6000$. For the remaining basis functions, we take the centres of curvature as equally spaced around a circle of radius R_{PS} centred at the centroid of the element, starting from the ray traced direction. This replicates an equi-spaced plane wave basis, but with the ray traced direction included in the set.

We use the same set up for the UWVF as in §6.3.2, with impedance boundary conditions (6.14), constant density $\rho \equiv 1$, and an exterior point source to solve the homogeneous form of the Helmholtz equation (6.13). For our source term g we again apply the boundary condition to an incident wave $u^i = H_0^1(\kappa(\mathbf{x} - \mathbf{x}_s))$ propagating outwards from a point source at $\mathbf{x}_s \notin \Omega$, resulting in the form (6.15).

Results were gathered for the frequencies $f_r = 5, 20$ Hz of wave propagation from a point source at $\mathbf{x}_s = (6.0157, -0.024194)$. We use one of the same discretisations used in §6.3.2, that of $K = 367$ elements; the discretisation and the wavenumber in each element is shown in the central plot of Figure 6.5 for $f_r = 5$ Hz, with wavenumbers

quadrupled for $f_r = 20$ Hz. The background wavespeed profile and FMM ray directions $\mathbf{d}_{ray}$ at the centroid of each element are shown in Figure 6.12. Sample UWVF solutions for $K = 367$ with the ray enhanced basis are shown in Figure 6.13 for $f_r = 5$ Hz, and Figure 6.14 for $f_r = 20$ Hz.

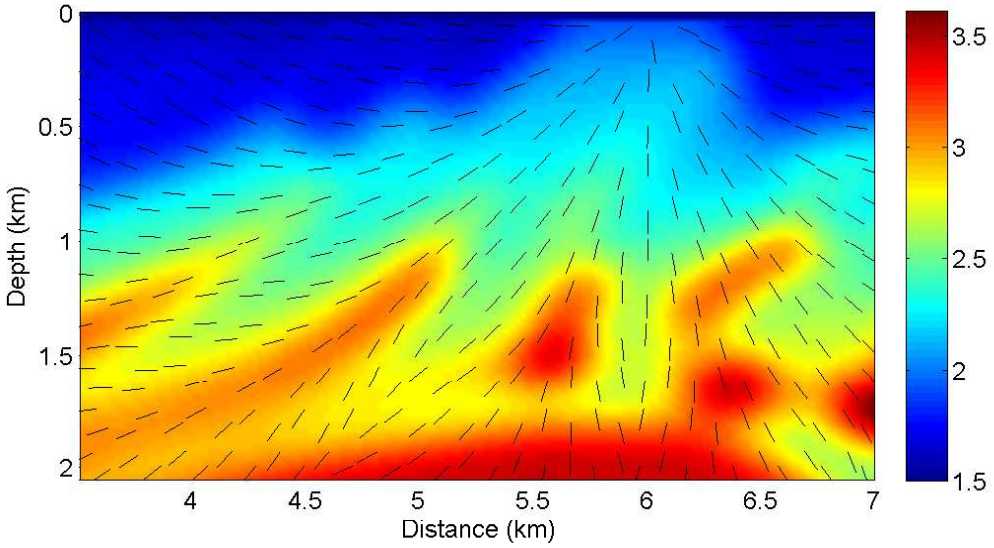

Figure 6.12: FMM ray directions from a source at $\mathbf{x}_s = (6.0157, -0.024194)$ for wave propagation in a section of the smoothed Marmousi model.

As we do not have an exact solution or reference solutions for this model to compare the results to, we instead take as an reference solution the solution produced using the highest number of degrees of freedom tested for each frequency, and so we can see the rate of convergence to a final estimation state. We now consider the rate of convergence of the relative L^2 error (5.1), produced comparing approximations using an increasing number of degrees of freedom (an increased maximum number of basis functions tested per element) to this reference solution. For $f_r = 5$ Hz we use $p = 6, 8, 10, 12, 14, 16$, and use the solution with $p = 16$ as the reference solution. For $f_r = 20$ Hz we use $p = 6, 8, 10, 12, 14, 16, 18, 20, 22, 24$, and use the solution with $p = 24$ as the reference solution. Figure 6.15 shows that for the low frequency wave using the ray directions in the basis does not make a significant amount of difference to the convergence of the solution. For the higher frequency, where we would expect our solution to behave more

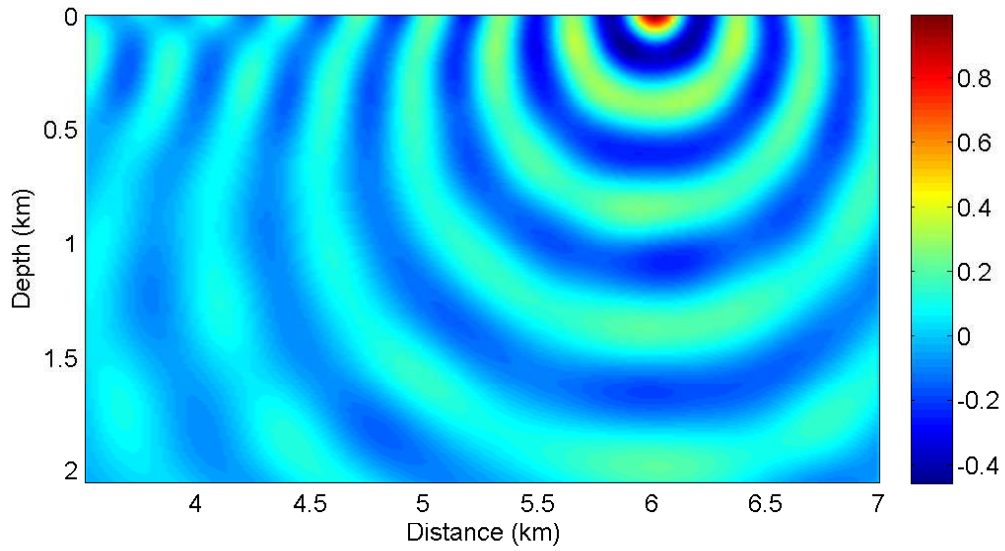

Figure 6.13: Real part of approximate solution for wave propagation from a point source at $(6.0157, -0.024194)$ with $f_r = 5$ Hz through a section of the Marmousi model.

like the ray model, the use of the ray directions does bring the relative L^2 norm of the error towards its final convergant state quicker than the equally spaced basis, as shown in Figure 6.16, however only marginally and these gains are lost as we reach the final state.

It may be that the ray directions provided by the FMM are not the optimal directions to use in the UWVF either. The directions provided are those for the fastest expanding wavefront, which does not necessarily mean that they are the dominant direction or that reflections are included. An equi-spaced basis may not be the best here either: perhaps ray directions that are a slight modification of $\mathbf{d}_{ray}$ could be used. However, for this set-up consideration would need to be given to keeping the basis functions in each element sufficiently distinct, to avoid the issues of ill-conditioning that arise when the basis is close to linear dependance.

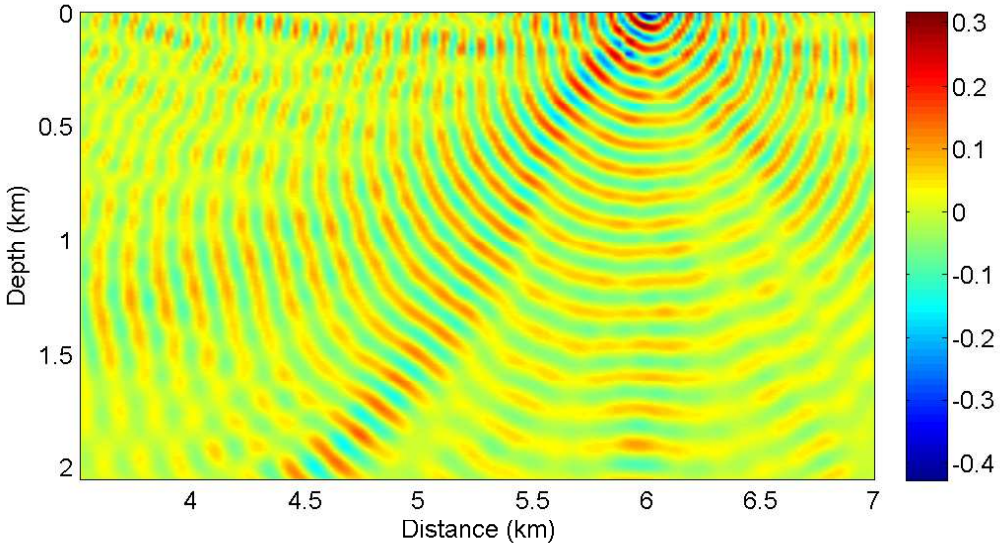

Figure 6.14: Real part of approximate solution for wave propagation from a point source at $(6.0157, -0.024194)$ with $f_r = 20$ Hz through a section of the Marmousi model.

6.6 Summary

In this chapter we have tested the use of the UWVF for forward seismic imaging, by simulating wave propagation in a synthetic sound speed profile, the Marmousi model. In order to implement the UWVF, the domain requires discretisation into finite elements, and a constant wave number taken within each element. For a highly variable sound speed profile, this has meant that the domain must be finely discretised in order to maintain the details of the internal structures. However, as the element sizes get smaller in comparison to the wavelength, a reduced number of basis functions can be used in each element before problems of ill conditioning arise. When using an equi-spaced basis, this could mean that key wave directions are excluded. Therefore consideration must be given as to how much detail it is necessary to represent in the domain at the cost of the wave directions being well represented in the basis.

We have also considered two types of ray tracing techniques, the method of characteristics and using the Fast Marching Method, to provide ray directions for wave propagation from a point source through the seismic domain. Results of the UWVF

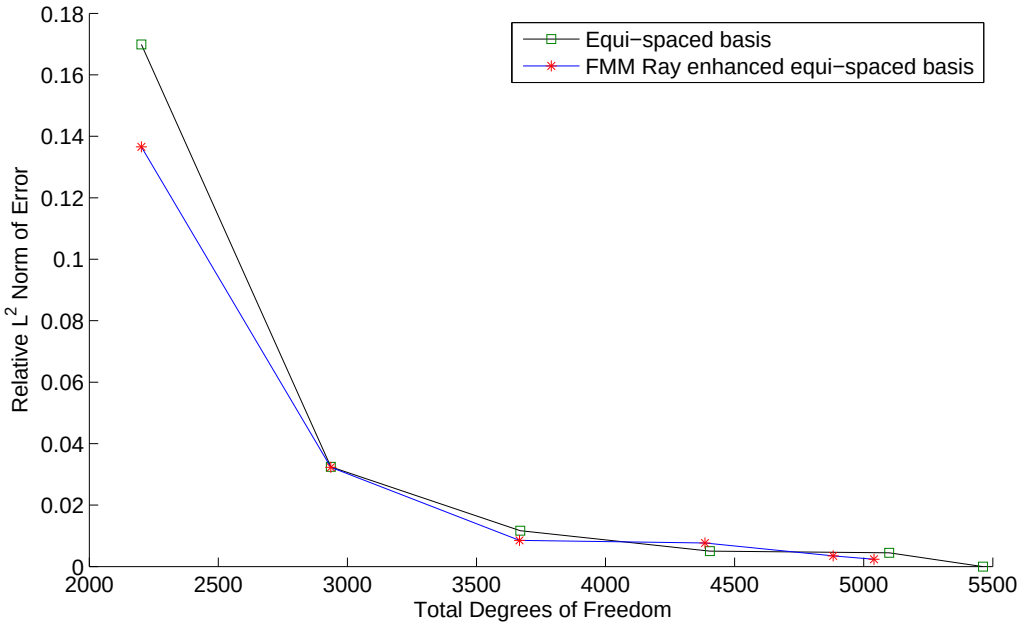

Figure 6.15: L^2 norm of relative error of solutions with and without ray directions in the UWVF basis, for $f_r = 5$ Hz, $K = 367$.

concur with the ray directions obtained by the method of characteristics. We have included ray directions obtained by the FMM in a ray enhanced basis for the UWVF. However when compared with the standard equi-spaced basis, although there is initially some improvement in accuracy in representing the solution for a given number of degrees of freedom, these gains are lost as the solution converges to a final fixed state.

The initial results are promising however, as including the ray traced solution in the approximation space has made some improvement when compared to the standard equi-spaced basis without ray directions. This suggests that further work is required: here we have only tried one strategy for finding ray directions. The question arises: could one find a better strategy to improve the results more significantly? Perhaps instead ray directions obtained by the method of characteristics in the regions available, or through a combination of the two methods as done in [2], would be more effective.

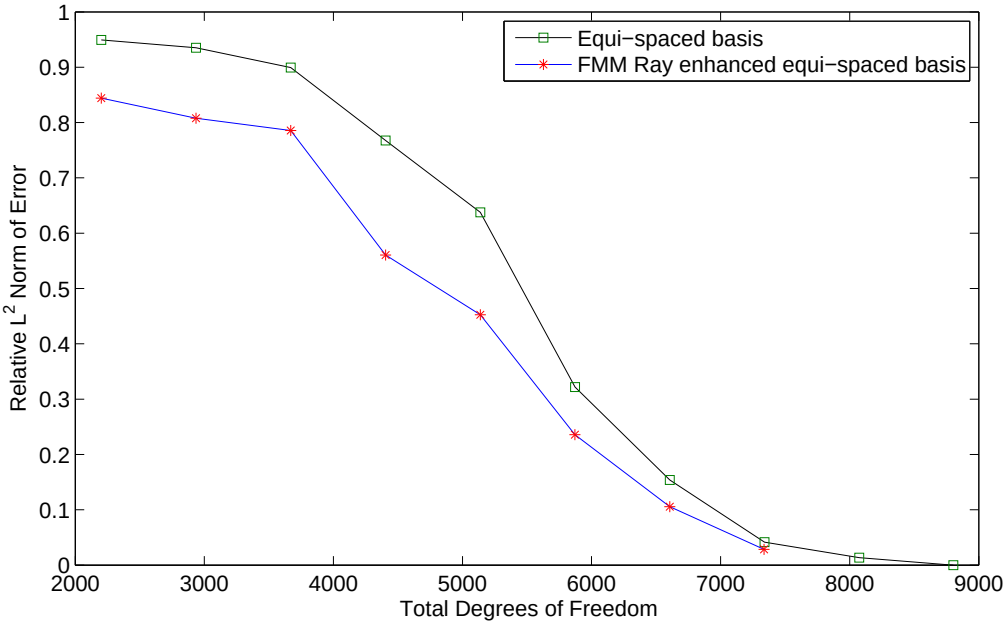

Figure 6.16: L^2 norm of relative error of solutions with and without ray directions in the UWVF basis, for $f_r = 20$ Hz, $K = 367$.

Chapter 7

An Extension of the Ultra Weak Variational Formulation for Modelling an Interior Point Source

So far in this thesis the use of UWVF has only been considered for the solution of the homogeneous form of the Helmholtz equation. We now progress to the use of the UWVF to simulate 2D acoustic wave propagation from an interior point source, as modelled by the inhomogeneous Helmholtz equation. As explained in §3.1, the use of Trefftz type basis functions incorporates the known wave-like behaviour of the solution allowing large reductions in the required number of degrees of freedom for a given level of accuracy when compared to standard FEM. However, when solving the inhomogeneous form of the Helmholtz equation, the UWVF is not well disposed to the accurate approximation of sources on the interior of the domain of approximation. This is because the UWVF approximation takes the form of a linear combination of solutions of the homogeneous Helmholtz equation, and as such cannot well represent the inhomogeneity. The use of interior sources is indispensable in many problem set-ups in the seismic industry, as we saw in Chapter 6, and so this handicap will need to be overcome if the UWVF is to be useful for widespread seismic imaging applications.

Here, we investigate the applicability of the UWVF to seismic imaging by considering

the typical situation of an interior point source. We present a simple yet accurate method to augment the UWVF in the case of a localised non-zero source term f, which we call the Source Extraction UWVF. Although we are primarily concerned with seismic imaging, the technique is applicable to other problem types the UWVF may be used for. In this approach, the domain Ω is split into two regions: an inner region Ω^S containing the source, and an outer region Ω^E which is the remainder of the domain, i.e. $\Omega^E = \Omega \backslash \Omega^S$. In the inner region, a particular radiating solution of the inhomogeneous Helmholtz equation with source f is subtracted from the field, so that the remainder of the wavefield is amenable to a Trefftz approximation in the interior (this remainder is the wavefield which is back-scattered from the outer region into the inner region). In the outer region we solve for the total field. The solutions in the two regions are matched by prescribing the jumps of the impedance and the conjugate-impedance traces. We consider a point source (a Dirac delta) and subtract a fundamental solution in the source region, however the augmentation can be easily generalised to other forms of sources and related analytic solutions, such as a dipole source. We first consider a domain of constant wave speed, and then extend our investigations to the simulation of wave propagation through a layered velocity profile. This work has been published seperately in [38]. A related approach based on splitting of outgoing and back-scattered fields is used in [6, 59] for finite difference methods in time domain. A similar approach for the UWVF has been derived separately by Gabard in [29, §5.1] for a system of linear hyperbolic equations, applied with accurate results to the linearised Euler equations.

Details of the UWVF are given in §7.1, with explanation given as to why solving the inhomogeneous form of the Helmholtz equation poses challenges for the numerical method. In §7.2 we present the new adjustment of the UWVF for the representation of an interior point source. Accurate results for a domain with constant wavenumber are presented in §7.3, followed by results for a domain with a smoothly varying sound speed profile. The sound speed profile for the later case is taken from a synthetic 2D acoustic model often used as a test case in seismic inversion, the Marmousi model (see Chapter 6 or [2, 54] for example).

7.1 The Ultra Weak Variational Formulation of the Inhomogeneous Helmholtz Problem

In seismic wave simulation, the use of point sources (monopoles or dipoles) in the interior of the domain is typically required, representing the case of an explosive sound source. To model this situation requires solving the inhomogeneous Helmholtz equation (3.1a) for a non-zero and singular source term f, for example a Dirac delta function. The use of the UWVF to solve the inhomogeneous form of the Helmholtz equation is an area that has not received a great deal of attention. In much of the literature, sources in the exterior of the domain are used, allowing the homogeneous form of the Helmholtz equation ((3.1a) with $f = 0$) to be solved, where the superior approximation properties of Trefftz methods can be exploited at their best.

In [16, 17, 31], the UWVF with non-zero source term f has been investigated, both a priori analysis and numerical experiments are presented. In [50], Loeser and Witzigmann use the UWVF to solve the Helmholtz equation (3.1a) with source term $f = 1$ in Ω^S and $f = 0$ elsewhere, for an active region $\Omega^S \subset \Omega$. However, the use of the UWVF on regions where the equation is inhomogeneous is avoided. The UWVF solution is found in the source free region $\Omega \setminus \Omega^S$ only, after which, in an additional post-processing step, a standard FEM is used in the active region where f is non-zero. Little detail is given in [50] on how the solutions and flow were matched on the inter-element edges of the active and source free regions. Loeser and Witzigmann suggest that in practice the FEM mesh size in the active region should be no larger than $\lambda/30$, where λ is the problem wavelength, leading to a potentially computationally expensive scheme. This high computational expense is minimised by the fact that the active region is small, in their case, only one element of the UWVF mesh. One of the main benefits of the UWVF is the ability to find accurate solutions on a fairly coarse mesh; to use a $\lambda/30$ mesh size for a FEM simulation in the domain of a larger element used in the UWVF solution could still potentially be computationally expensive, especially in the case of high frequencies.

When solving the homogeneous Helmholtz equation, all of the integrals in the UWVF weak form (3.7) are defined on the element boundaries (as $f \equiv 0$ the only volume integral in (3.7) vanishes). In the general case the right-hand side of (3.7) includes an integral over all the elements where the source term f is non zero (or point evaluations if f is a linear combination of point sources).

A standard choice of the Trefftz basis functions $\phi_{k,l}$, i.e. equispaced plane waves (3.13) or circular waves (3.49), allows high orders of approximation in the elements where $f = 0$; see [58]. On the contrary, when $f \neq 0$ inside Ω_k, Trefftz functions lose their approximation properties, as they are complementary rather than particular solutions. Numerical results in [17, 31] suggest that the use of plane waves in the inhomogeneous case can provide the same approximation of u as piecewise-linear polynomials only; moderately high orders of convergence were achieved for the approximation of u on the skeleton of the mesh but only linear order in the meshsize h for the volume error measured in the $L^2(\Omega)$-norm, see [17, Tables 3.3 and 3.4] and [31, Section 5].

These two reasons, the desire to integrate only on the mesh skeleton without the need for volume integrals, and the desire to achieve higher orders of approximation, motivated the investigation of the UWVF in the homogeneous case, while not much effort has been devoted to the source case. If the UWVF is to be used in more general problems that may practically arise in seismic imaging, this situation needs to be tackled. In the next section we propose a modified formulation to extend the advantages of the UWVF to the special case of point sources.

7.2 The Source Extraction UWVF

We wish to solve the inhomogeneous Helmholtz BVP (3.1) in the domain Ω, when the source term f is a point source:

$$f(\mathbf{x}) = -\delta(\mathbf{x} - \mathbf{x}_0), \qquad \mathbf{x} \in \Omega, \tag{7.1}$$

where δ is the Dirac delta function and $\mathbf{x}_0 \in \Omega$. In this case, the right-hand side of the UWVF formulation (3.7) becomes $\int_{\Omega_k} f\overline{v_k}\,\mathrm{d}V = -\overline{v_k}(\mathbf{x}_0)$; $f \notin L^2(\Omega)$ and $u \notin H^1(\Omega)$.

As it might be expected, numerical tests using the formulation (3.7) proved extremely inaccurate at representing the source, with high errors in the element containing $\mathbf{x}_0$; numerical experiments for this case are provided in §7.3.1.

In order to introduce a modified formulation, we now fix some notation. We split the domain in two open regions Ω^S and Ω^E, $\Omega = \Omega^S \cup \Omega^E \cup \Gamma^S$ where $\Gamma^S = \partial\Omega^S$ (as illustrated in Figure 7.1) such that the two regions correspond to a partition of the mesh: $\mathcal{T} = \mathcal{T}^S \cup \mathcal{T}^E$ with $\Omega_k \in \mathcal{T}^S$ if $\Omega_k \subset \Omega^S$ and $\Omega_{k'} \in \mathcal{T}_E$ if $\Omega_{k'} \subset \Omega^E$. On Γ_S, we denote by $\mathbf{n}_S$ the unit normal vector pointing outward from Ω^S, and set $\mathbf{n}_E = -\mathbf{n}_S$. Moreover, we require: $\mathbf{x}_0 \in \Omega_k$ for some $\Omega_k \in \mathcal{T}^S$ (thus the source is located in Ω^S and it does not lie on the mesh skeleton); the physical parameters to be constant in Ω^S, i.e. $\rho_k(\mathbf{x}) = \rho^S$ and $\kappa(\mathbf{x}) = \kappa^S$ for all $\mathbf{x} \in \Omega^S$; and $\overline{\Omega^S}$ to lie in the interior of Ω, i.e. $\Gamma^S \cap \Gamma = \varnothing$.

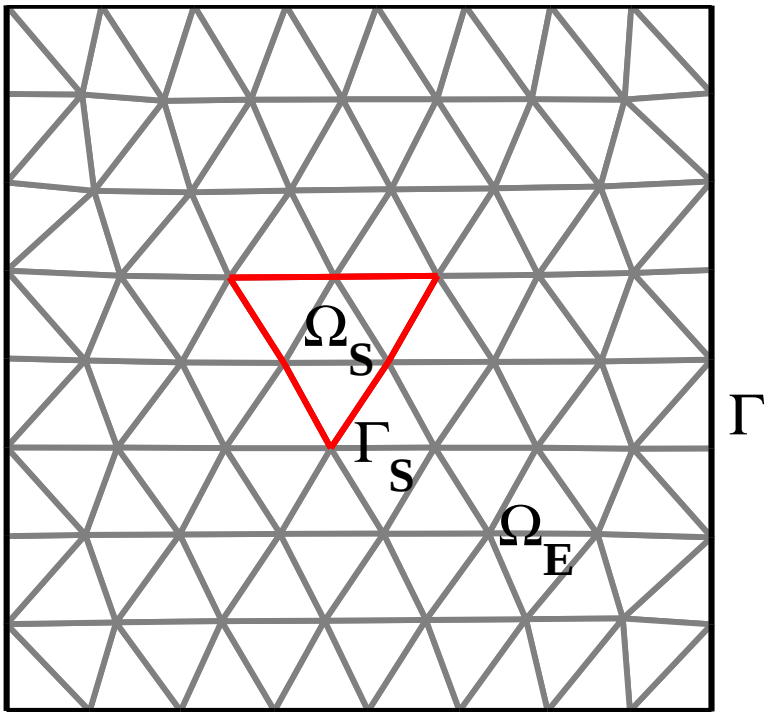

Figure 7.1: Subdivision of the domain and the mesh. Γ^S is in bold red.

In Ω^S, we write the field u as the sum of the known field u^I generated by the source

term in free space (i.e., with constant parameters ρ^S and κ^S in the whole plane and without any boundary conditions) and the unknown remainder u^S, i.e.

$$u = u^I + u^S \qquad \text{in } \Omega^S, \qquad \text{where} \qquad u^I(\mathbf{x}) := \rho^S \frac{\mathrm{i}}{4} H_0^1(\kappa^S |\mathbf{x} - \mathbf{x}_0|).$$

By separating out the total field u into the sum of the unknown field and the known local particular solution of the inhomogeneous Helmholtz equation, we can remove the known part, and so are left with the homogeneous form of the equation. We can then use the UWVF to approximate u^S alone, and add in the known u^I in a post-processing step. In the remainder of the domain Ω^E we approximate the total field, which we now denote u^E for clarity.

Since u^I is solution of

$$\nabla \cdot \left(\frac{1}{\rho} \nabla u^I \right) + \frac{\kappa^2}{\rho} u^I = f \qquad \text{in } \Omega^S,$$

and the traces of $(u^S + u^I)$ and u^E agree on Γ^S, we are left with two homogeneous Helmholtz equations for u^S and u^E, posed in Ω^S and Ω^E respectively, coupled via the impedance traces of u^I:

$$\begin{aligned}
\nabla \cdot \left(\frac{1}{\rho} \nabla u^S \right) + \frac{\kappa^2}{\rho} u^S &= 0 && \text{in } \Omega^S, \\
\nabla \cdot \left(\frac{1}{\rho} \nabla u^E \right) + \frac{\kappa^2}{\rho} u^E &= 0 && \text{in } \Omega^E, \\
(1+Q) \frac{1}{\rho} \frac{\partial u}{\partial n} - (1-Q) \mathrm{i}\sigma u &= g && \text{on } \Gamma, \\
\left(\frac{1}{\rho^S} \frac{\partial}{\partial n_S} - \mathrm{i}\sigma \right) u^S &= \left(-\frac{1}{\rho^E} \frac{\partial}{\partial n_E} - \mathrm{i}\sigma \right) u^E - \left(\frac{1}{\rho^S} \frac{\partial}{\partial n_S} - \mathrm{i}\sigma \right) u^I && \text{on } \Gamma^S, \\
\left(\frac{1}{\rho^E} \frac{\partial}{\partial n_E} - \mathrm{i}\sigma \right) u^E &= \left(-\frac{1}{\rho^S} \frac{\partial}{\partial n_S} - \mathrm{i}\sigma \right) u^S + \left(-\frac{1}{\rho^S} \frac{\partial}{\partial n_S} - \mathrm{i}\sigma \right) u^I && \text{on } \Gamma^S,
\end{aligned} \tag{7.2}$$

where ρ^E is the trace of ρ on Γ^S taken from Ω^E (which does not need to be constant along Γ^S, differently from ρ^S). Recall that on Γ^S we defined $\mathbf{n}_E = -\mathbf{n}_S$, thus the last two conditions in (7.2) correspond to the continuity of u and $\rho^{-1}\nabla u$ across Γ^S.

The benefit of using the UWVF to approximate u^S alone in Ω^S is threefold: *(i)* the fields to be approximated are much smoother than the solution of the original problem; *(ii)* they are solutions of the homogeneous Helmholtz equation, thus the approximation

by Trefftz functions can deliver great accuracy; and *(iii)* all the terms that will appear at the right-hand side of the UWVF are integrals on some part of the mesh skeleton (see equation (7.4) below).

In the case of a domain of constant wavenumber it would be possible to approximate u^S only on the whole domain (i.e., to choose $\Omega^S = \Omega$, $\Omega^E = \varnothing$, and solve a BVP whose trace source g is modified by subtracting a trace of u^I). However, if the wavenumber is varying in the domain, it is unlikely that a special solution u^I would be known in the whole of Ω.

As in Chapter 3, if we follow the proof of [17, Theorem 1.3] and insert the last two conditions of (7.2) in (3.20), we obtain the ultra weak variational formulation of the BVP (7.2) as

$$\text{seek } u^* \in H \text{ such that} \qquad d(u^*, w) - c(u^*, w) = \hat{\beta}(w) \qquad \forall w \in H, \tag{7.3}$$

where u^* stands for u^S and u^E in Ω^S and Ω^E respectively. The Trefftz space H is as defined in §3.1 by $H := \prod_{k=1}^K H_k$, where H_k is given by (3.4). The sesquilinear forms $d(\cdot,\cdot)$ and $c(\cdot,\cdot)$ were defined in (3.5) and the antilinear functional $\hat{\beta} : H \to \mathbb{C}$ is defined as

$$\begin{aligned}\hat{\beta}(w) := &\sum_{k=1}^{K} \int_{\Gamma_k} \frac{g}{\sigma} \overline{\left(\frac{1}{\rho_k}\frac{\partial}{\partial n_k} - \mathrm{i}\sigma\right) w_k}\,\mathrm{d}S \\ &- \sum_{\Omega_K \in \mathcal{T}^S} \int_{\partial\Omega_k \cap \Gamma^S} \frac{1}{\sigma}\left(\frac{1}{\rho_S}\frac{\partial}{\partial n_S} - \mathrm{i}\sigma\right) u^I \overline{\left(\frac{1}{\rho_S}\frac{\partial}{\partial n_S} - \mathrm{i}\sigma\right) w_k}\,\mathrm{d}S \\ &+ \sum_{\Omega_K \in \mathcal{T}^E} \int_{\partial\Omega_k \cap \Gamma^S} \frac{1}{\sigma}\left(-\frac{1}{\rho_S}\frac{\partial}{\partial n_S} - \mathrm{i}\sigma\right) u^I \overline{\left(\frac{1}{\rho_E}\frac{\partial}{\partial n_E} - \mathrm{i}\sigma\right) w_k}\,\mathrm{d}S \qquad \forall w \in H.\end{aligned} \tag{7.4}$$

The new augmented discrete version of the UWVF reads as follows: given a finite dimensional subspace $H_h \subset H$,

$$\text{seek } u_h^* \in H_h \text{ s.t.} \qquad d(u_h^*, w_h) - c(u_h^*, w_h) = \hat{\beta}(w_h) \qquad \forall w_h \in H_h. \tag{7.5}$$

The corresponding linear system of equations reads $(D - C)X = \hat{b}$, where X is the coefficient vector of u_h^* in a given basis of H_h. As the extra terms of the impedance traces of u^I are known, the resulting extra integrals in the formulation can be brought

to the right hand side, so that the matrices D and C of (3.43) remain the same as in the standard formulation (3.7), and the only changes are in the vector $\hat{b}$. Entries for b are now given by

$$\begin{aligned} b_k^l &= \int_{\Gamma_k} \frac{g}{\sigma} \overline{\left(\frac{1}{\rho_k}\frac{\partial \phi_{k,l}}{\partial n} - \mathrm{i}\sigma\phi_{k,l}\right)} \\ &- \int_{\Sigma_{k,j}\cap\Gamma^S\cap\Omega^S} \frac{1}{\sigma}\left(\frac{1}{\rho_k}\frac{\partial}{\partial n_k} - \mathrm{i}\sigma\right)\frac{i}{4}H_0^1(\kappa_k|\mathbf{x}-\mathbf{x}_0|)\overline{\left(\frac{1}{\rho_m}\frac{\partial \phi_{k,l}}{\partial n_k} - \mathrm{i}\sigma\phi_{k,l}\right)} \\ &+ \int_{\Sigma_{j,k}\cap\Gamma^S\cap\Omega^E} \frac{1}{\sigma}\left(-\frac{1}{\rho_j}\frac{\partial}{\partial n_j} - \mathrm{i}\sigma\right)\frac{\mathrm{i}}{4}H_0^1(\kappa_j|\mathbf{x}-\mathbf{x}_0|)\overline{\left(\frac{1}{\rho_k}\frac{\partial \phi_{k,l}}{\partial n_m} - \mathrm{i}\sigma\phi_{k,l}\right)} \end{aligned} \tag{7.6}$$

for $k = 1, ..., K$, $l = 1, ..., p_k$. We solve the linear system (3.43) to find the unknown weights X and use this to approximate the solution u over the whole domain as in (3.11), using

$$u = \sum_{l=1}^{p_k} \chi_{k,l}\phi_{k,l} \qquad \text{in } \Omega_k \cap \Omega^E \tag{7.7}$$

for elements in Ω^E, and

$$u = \sum_{l=1}^{p_k} \chi_{k,l}\phi_{k,l} + \rho^S \frac{\mathrm{i}}{4}H_0^1(\kappa|\mathbf{x}-\mathbf{x}_0|) \qquad \text{in } \Omega_k \cap \Omega^S. \tag{7.8}$$

7.2.1 Well-posedness and coercivity of the Source Extraction UWVF

We define the trace space $V := \prod_{k\in K} L^2(\partial\Omega_k)$, equipped with the norm

$$\|\mathcal{X}\|_X^2 := \sum_{k=1}^{K} \int_{\partial\Omega_k} \frac{1}{\sigma}|\mathcal{X}_k|^2 \,\mathrm{d}S \qquad \forall \mathcal{X} = (\mathcal{X}_1, \ldots \mathcal{X}_K) \in V.$$

In the space X we define the impedance and the "adjoint impedance" trace operators

$$\mathcal{I} : H \to V, \qquad F : \mathcal{I}(H) \to V$$

as

$$\mathcal{I}(v) := \big(\mathcal{I}_1(v), \ldots, \mathcal{I}_K(v)\big), \qquad \mathcal{I}_k(v) := -\frac{1}{\rho_k}\frac{\partial v_k}{\partial n} - i\sigma v_k \quad \text{and}$$

$$F\big(\mathcal{I}(v)\big) := \Big(F_1\big(\mathcal{I}_1(v)\big), \ldots, F_K\big(\mathcal{I}_K(v)\big)\Big), \qquad F_k\big(\mathcal{I}_k(v)\big) := \frac{1}{\rho_k}\frac{\partial v_k}{\partial n} - i\sigma v_k.$$

Then the UWVF sesquilinear form may immediately be rewritten as

$$d(u,v) - c(u,v) = \sum_{k=1}^{K} \Bigg[\int_{\partial\Omega_k} \frac{1}{\sigma} \mathcal{I}_k(u) \overline{\mathcal{I}_k(v)} \,\mathrm{d}S - \sum_{\substack{j=1 \\ j\neq k}}^{K} \int_{\Sigma_{j,k}} \frac{1}{\sigma} \mathcal{I}_j(u) \overline{F_k\big(\mathcal{I}_k(v)\big)} \,\mathrm{d}S - \int_{\Gamma_k} \frac{Q}{\sigma} \mathcal{I}_k(u) \overline{F_k\big(\mathcal{I}_k(v)\big)} \,\mathrm{d}S \Bigg].$$

Buffa and Monk defined in [15, (2.16)] the sesquilinear form $a : V \times V \to \mathbb{C}$

$$a(\mathcal{X}, \mathcal{Y}) := \frac{1}{2}\big(d(u,v) - c(u,v)\big) \qquad \text{for } u, v \in H \text{ such that } \mathcal{I}(u) = \mathcal{X},\ \mathcal{I}(v) = \mathcal{Y}$$

in the case $Q = 0$. The form $a(\cdot,\cdot)$ is well-defined, as there exists a unique $u \in H$ satisfying $\mathcal{I}(u) = \mathcal{X} \in V$ by the well-posedness of the corresponding Helmholtz impedance BVPs posed in the mesh elements. In other words $\mathcal{I} : H \to V$ is invertible. Note that in [15] κ is taken constant, $\rho = 1$, σ corresponds to η and the relationship between $\mathcal{X}$ and u (and similarly between $\mathcal{Y}$ and v) follows a different sign convention as a consequence of a different impedance boundary condition.

Lemma 3.4 of [15] provides the coercivity of $a(\cdot,\cdot)$ when $Q = 0$. This can be verified by defining $\mathbf{v} := (-\mathrm{i}\rho)^{-1}\nabla u$, $\mathcal{X}_k := (-\mathrm{i}\sigma u_k + \mathrm{i}\mathbf{v}_k \cdot \mathbf{n}_k) \in L^2(\partial\Omega_k)$ and repeating exactly the same proofs of [15] with a different sign convention; the discontinuous coefficients do not affect this result. From this, both the continuous and the discrete problems (7.3) and (7.5) are well-posed. The following error bound for the discretisation of the UWVF was proved in [15, Theorem 3.5]:

$$\begin{aligned} &\sum_{j,k=1}^{K} \int_{\Sigma_{j,k}} \left(\frac{\sigma}{2} \big| [\![u^* - u_h^*]\!] \big|^2 + \frac{1}{2\sigma} \left| \left[\!\!\left[\frac{1}{\rho} \nabla u^* - \nabla u_h^* \right]\!\!\right] \cdot \mathbf{n} \right|^2 \right) \mathrm{d}S \\ &+ \sum_{k} \int_{\Gamma_k} \frac{1}{2\sigma} \Big(\Big| F_k\big(\mathcal{I}_k(u^*)\big) - F_k\big(\mathcal{I}_k(u_h^*)\big) \Big|^2 + \Big| \mathcal{I}_k(u^*) - \mathcal{I}_k(u_h^*) \Big|^2 \Big) \,\mathrm{d}S \\ &\leq 4 \inf_{v_h \in H_h} \| \mathcal{I}(u^*) - \mathcal{I}(v_h) \|_V^2 , \end{aligned} \tag{7.9}$$

where $[\![\cdot]\!]$ denotes the jumps across the mesh faces.

This bound allows us to control the traces of the error on the mesh skeleton only. Theorem 4.1 of [15] gives an error estimate in the volume, i.e. in $L^2(\Omega)$-norm, but holds for UWVF solutions with $H^2(\Omega)$-regularity only: since Ω^E is non-convex and here we

consider discontinuous coefficients, it is not directly applicable in our case. In order to obtain estimates in $L^2(\Omega)$, a new duality result similar to Lemma 4.4 of [37] (which improves on [15, Theorem 4.1] in requiring weaker regularity than $H^2(\Omega)$) would be required.

Given a particular discrete Trefftz space, in order to obtain orders of convergence from the quasi-optimality bound (7.9), only best-approximation estimates are needed. In the case of plane wave or Fourier–Bessel (i.e. circular waves) basis, these approximation bounds are proved and discussed in [58].

7.3 Numerical examples

We now present two numerical examples of the Source Extraction UWVF described in §7.2 for solving the inhomogeneous Helmholtz equation (3.1a). In the first we consider the approximation of a point source in a domain of constant wave speed, and compare the accuracy with that of the original formulation. In the second example we consider the suitability of the Source Extraction UWVF for seismic imaging applications, testing on a wave speed profile given by a synthetic seismic model.

We solve the inhomogeneous Helmholtz problem (3.1) with a point source as in (7.1). In both examples we use a constant density $\rho = 1$ over the domain, while we take the wavenumber κ to be constant in the first example and discontinuous in the second one. We fix $Q = 0$ in the impedance boundary condition (3.1b). The source region Ω^S is defined to comprise four triangular elements: that containing the point source and its three neighbours (see Figure 7.1). The region Ω^S was extended to be larger than just the single element containing the point source in order to reduce numerical errors in imposing the impedance traces of u^I on Γ^S; close to the centre of the point source the gradient of the source field will be steep. By moving the boundary Γ^S away from the source the impedance traces will have to pass less steep changes in the particular solution into and out of the different subdomains.

The Trefftz basis functions $\phi_{k,l} \in H_k$ used are circular wave functions, as defined

by (3.49) with their equispaced sources given by (3.50), located externally to their respective elements. In each simulation, an initial maximum number $p = \max_k(p_k)$ of basis functions per element is set, and then p_k reduced if the condition number of the submatrix D_k is above a set tolerance level of 10^{10}; the scheme for reducing p_k first introduced in [44] and detailed in §3.5.

7.3.1 Interior point source in a domain with constant parameters

For the first example we consider a square domain $\Omega = (0,3) \times (0,3)$ in which the wavenumber is constant throughout. In order to focus just on the accuracy of the Source Extraction UWVF, the boundary condition (3.1b) (with $Q = 0$) was set to impose as exact solution of the BVP the fundamental solution of the Helmholtz equation,

$$u(\mathbf{x}) = \frac{\mathrm{i}}{4} H_0^1(\kappa|\mathbf{x} - \mathbf{x}_0|), \tag{7.10}$$

with $\mathbf{x}_0 = (1.40, 1.60) \in \Omega$. Thus the boundary source term is given by

$$g = \left(\frac{1}{\rho} \frac{\partial u}{\partial n} - \mathrm{i}\sigma u \right).$$

We approximate this solution using both the classical UWVF (3.7) and the Source Extraction UWVF described in §7.2.

An example solution of the Source Extraction UWVF is shown in Figure 7.2 for $\kappa = 10$, along with the computational mesh of $K = 116$ elements; this approximation was achieved using $p = 15$ basis functions on each element. Table 7.1 shows the relative error, measured in the $L^2(\Omega)$-norm, for the two methods, together with the average number N_λ of degrees of freedom per wavelength in each direction, computed as

$$N_\lambda = \lambda \sqrt{\frac{\sum_{k=1}^{K} p_k}{|\Omega|}},$$

where $|\Omega|$ is the area of the domain. The Source Extraction UWVF provides much higher accuracy than the classical formulation for the same approximation parameters

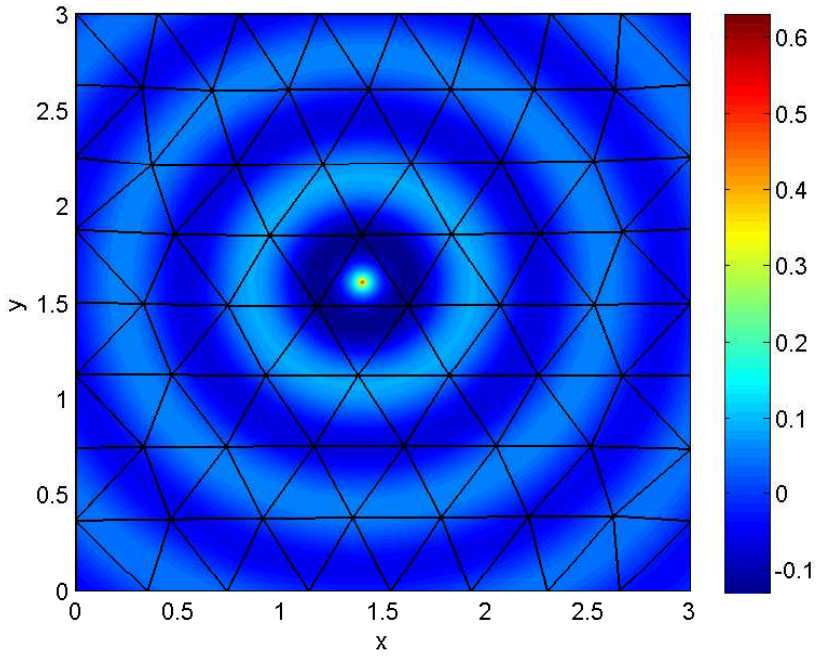

Figure 7.2: The real part of the inhomogeneous Helmholtz problem with constant coefficients for $\kappa = 10$, approximated using the Source Extraction UWVF on $K = 116$ elements by $p = 15$ basis functions per element. The computational mesh is superimposed.

K and p. In all cases it was not necessary to reduce p_k to maintain the condition number bound, so $p_k = p$ for $k = 1, ..., K$.

The accuracy obtained by the Source Extraction UWVF for this BVP is comparable to that achieved by the classical formulation of the UWVF when solving the homogeneous Helmholtz equation ($f = 0$) for a BVP whose exact solution is a fundamental solution centred outside the domain Ω (i.e. u as in (7.10) with $\mathbf{x}_0 \notin \Omega$); see Table 7.2 for the UWVF error in this setting.

p	$L^2(\Omega)$ relative error, classical UWVF	$L^2(\Omega)$ relative error, Source Extraction UWVF	N_λ
9	4.6148×10^{-1}	9.8941×10^{-3}	6.7672
10	4.6138×10^{-1}	5.2901×10^{-3}	7.1332
11	4.6087×10^{-1}	1.5578×10^{-3}	7.4814
12	4.6159×10^{-1}	8.2696×10^{-4}	7.8140
13	4.6154×10^{-1}	3.3895×10^{-4}	8.1331
14	4.6151×10^{-1}	2.2961×10^{-4}	8.4401
15	4.6145×10^{-1}	8.5399×10^{-5}	8.7364
16	4.6145×10^{-1}	6.5757×10^{-5}	9.0229

Table 7.1: Errors of the classical and the Source Extraction UWVF measured in $L^2(\Omega)$-norm for a point source in the interior of a homogeneous domain. Approximation by p equally spaced point sources per element, $K = 116$, $\kappa = 10$, $\Omega = (0, 3) \times (0, 3)$.

p	$L^2(\Omega)$ relative error, classical UWVF	N_λ
10	5.6961×10^{-3}	7.1332
11	1.1964×10^{-3}	7.4814
12	8.6834×10^{-4}	7.8140
13	1.7065×10^{-4}	8.1331
14	9.6792×10^{-5}	8.4401
15	1.8955×10^{-5}	8.7364

Table 7.2: Errors of the classical formulation measured in $L^2(\Omega)$-norm for the homogeneous Helmholtz equation: the exact solution is a fundamental solution centred at $(-0.5, 1.5)$, exterior to the domain. Approximation by p equally spaced point sources per element, $K = 116$, $\kappa = 10$, $\Omega = (0, 3) \times (0, 3)$.

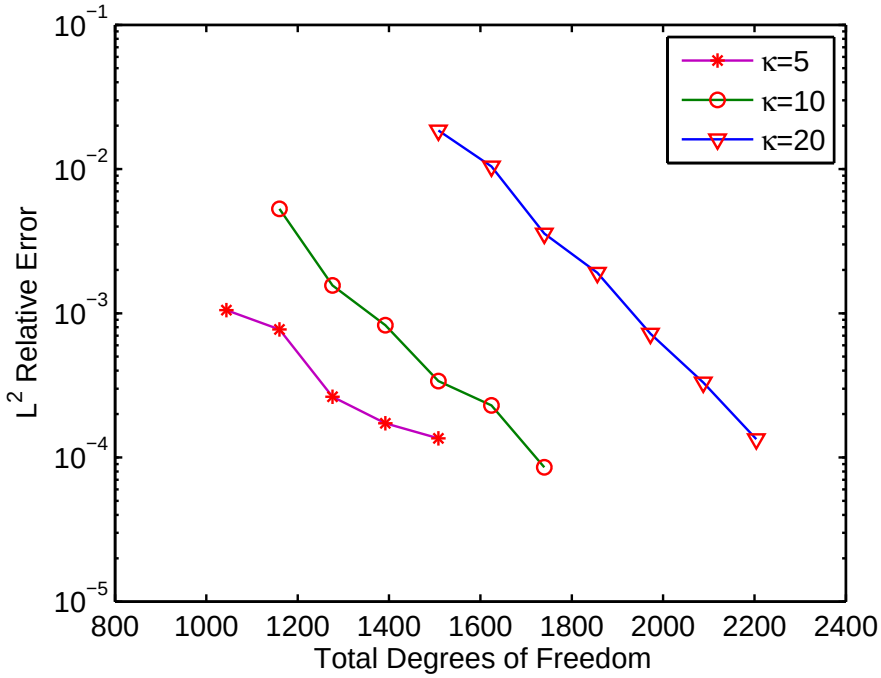

Figure 7.3: Relative $L^2(\Omega)$ errors against total number of degrees of freedom for the inhomogeneous Helmholtz problem with constant coefficients, approximated using the Source Extraction UWVF on $K = 116$ elements in $\Omega = (0,3) \times (0,3)$. For $\kappa = 5$ we use $p = 9, \ldots, 13$, for $\kappa = 10$ we use $p = 10, \ldots, 15$, and for $\kappa = 20$ we use $p = 13, \ldots, 19$.

The plot in Figure 7.3 shows that accurate results can be achieved for various wavenumbers using the Source Extraction UWVF for approximating an interior point source problem. In separate computations where a Hankel function centred at $\mathbf{x}_0$ was used as one of the basis functions, results were accurate to machine precision, as expected, even when using elements several wavelengths in size.

7.3.2 Interior point source in a section of a smoothed Marmousi model

As the results of the Source Extraction UWVF approximation of an interior point source in the constant wavenumber case were highly accurate compared to those of the original formulation, we now progress to testing the method on a domain more relevant

to seismic imaging, where the sound speed is a non-constant representation of typical geophysical structures in the subsurface of the Earth. We use the same sound speed profile as first introduced in §6.3.2: the domain Ω is taken as a section of a smoothed Marmousi model, that of $x \in [3.5131, 7.0022]$ km, $z \in [0, 2.0565]$ km, as shown in the upper plot of Figure 7.4. As we use a constant density $\rho = 1$ throughout, the only discontinuous parameter in the discretisation of the domain is the wavenumber κ.

For the Source Extraction UWVF approximation, two levels of mesh refinements are used, resulting in $K = 485$ and $K = 771$ triangular elements. The point source is located in $\mathbf{x}_0 = (6.018, 0.5768)$ and lies in the interior of an element, thus we avoid the case of the solution singularity coinciding with element edges or vertices. In order to explore just the accuracy associated with source extraction, a simple homogeneous impedance condition is imposed on the boundary (3.1b with $Q = 0$ and $g = 0$).

To obtain a piecewise-constant wavenumber, for each $\Omega_k \in \mathcal{T}^E$, $\kappa|_{\Omega_k} = \kappa_k$ is taken to be the average of the wavenumber of the smoothed Marmousi model at the three vertices of the element. In Ω^S the wavenumber is constant, taken as the average of values interpolated at the centre of each $\Omega_k \in \mathcal{T}^S$. The centre and lower plots of Figure 7.4 show the two meshes used, the discretised (piecewise constant) wavenumber for a frequency of 5 Hz and the position of the point source. The same discretisations are used for the frequency 10 Hz, resulting in the wavenumber in each element being doubled. Note that these figures are very similar to those in Figure 6.5 in Chapter 6.

The angularly equi-spaced basis (3.49) is used, with $R_{PS} = 100$ in (3.50) to replicate the conventional plane wave basis. An initial maximum number $p = 15$ of basis functions per element is set, and then p_k reduced if the condition number of the submatrix D_k is above the tolerance level of 10^{10}. The range of values taken by p_k across the mesh and the total number of degrees of freedom obtained for the frequencies 5 and 10 Hz and for the two meshes is summarised in Table 7.3.

The upper and centre plots of Figure 7.5 show the real part of the Source Extraction UWVF solution for the frequency $f_r = 5$ Hz and for the discretisations with $K = 485$ and $K = 771$ elements, respectively. The lower plot shows the real part of a reference

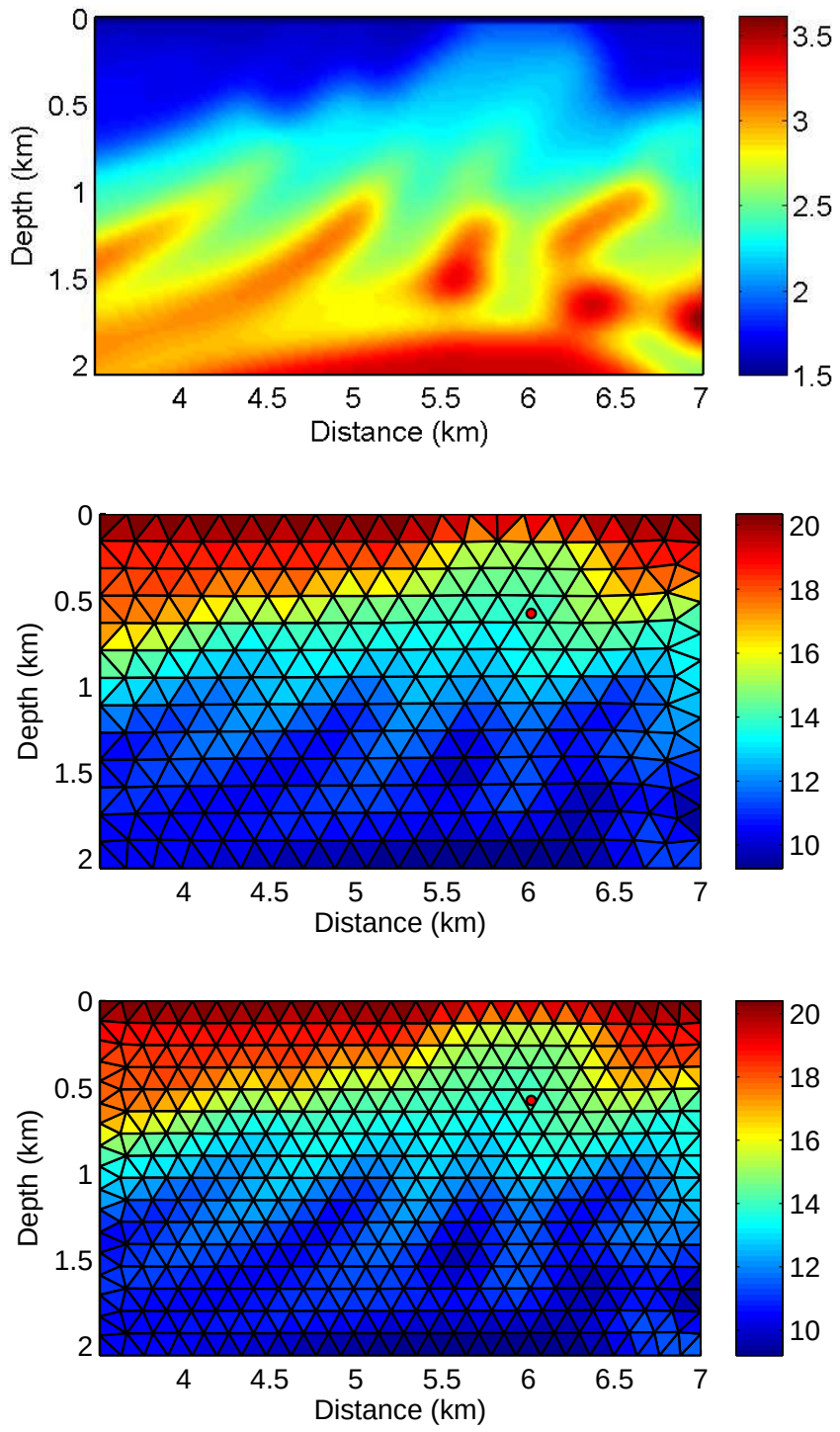

Figure 7.4: Upper plot: the wave speed (km/s) in a section of the smoothed Marmousi model. Centre and lower plots: for the frequency $f_r = 5$ Hz, the wavenumber κ_k in each element of the discretisation of the above velocity profile, using $K = 485$ elements (centre plot) and $K = 771$ elements (lower plot). The point source is marked by a red dot.

Frequency	K	Range of p_K	Total number of degrees of freedom
5 Hz	485	[8,...,15]	5,162
5 Hz	771	[8,...,13]	6,636
10 Hz	485	[11,...,15]	7,417
10 Hz	771	[10,...,15]	9,749

Table 7.3: The range of the values taken by the local number of degrees of freedom p_k and the total number of degrees of freedom $\sum_{k=1}^{K} p_k$ obtained with the adaptive procedure for the frequencies $f_r = 5$ and $f_r = 10$ Hz and for the two meshes with 485 and 771 triangles shown in Figure 7.4.

solution provided by Dr Paul Childs of Schlumberger Gould Research, computed with a FD scheme, for comparison. This was obtained on a regular structured grid with 180 points per wavelength using the method described in [35]. Figure 7.6 shows results in the same setup for the frequency $f_r = 10$ Hz. In both cases, the general pattern and areas of heightened or dampened amplitudes do coincide.

7.4 Summary

In this chapter we present work that has been published seperately in [38]. We have considered the use of the UWVF for the solving of the inhomogeneous Helmholtz equation. The UWVF typically has problems when the Trefftz basis functions do not well represent the inhomogeneity of the equation, such as the singularity of a point source. To avoid the use of alternative numerical methods in the region of inhomogeneity, we propose an augmentation of the UWVF equations called the Source Extraction UWVF. This technique requires only a homogeneous equation to be solved, with inhomogeneity introduced in a post-processing step, thus it better exploits the Trefftz property of the discrete space. For an incident point source, we approximate the unknown back-scattered field in a region surrounding the source, and match this to the total field approximated in the remainder of the domain. We use a monopole Hankel point source, however the augmentation of the method can be easily generalised to other

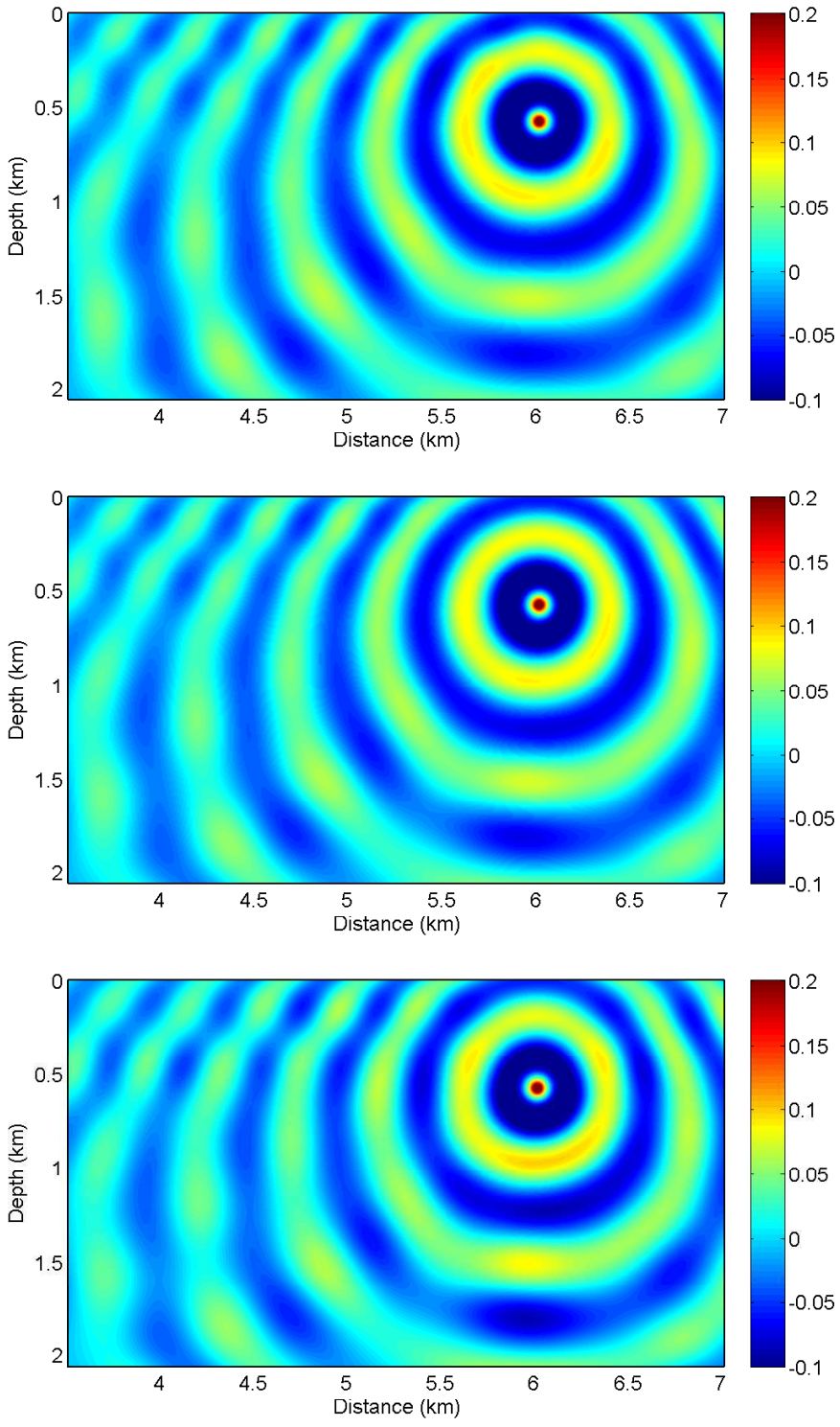

Figure 7.5: Real part of the total field approximation in the smoothed Marmousi section with frequency 5 Hz: UWVF solution with $K = 485$ and $p = 15$ (upper plot), UWVF solution with $K = 771$ and $p = 13$ (centre plot), finite difference solution (lower plot).

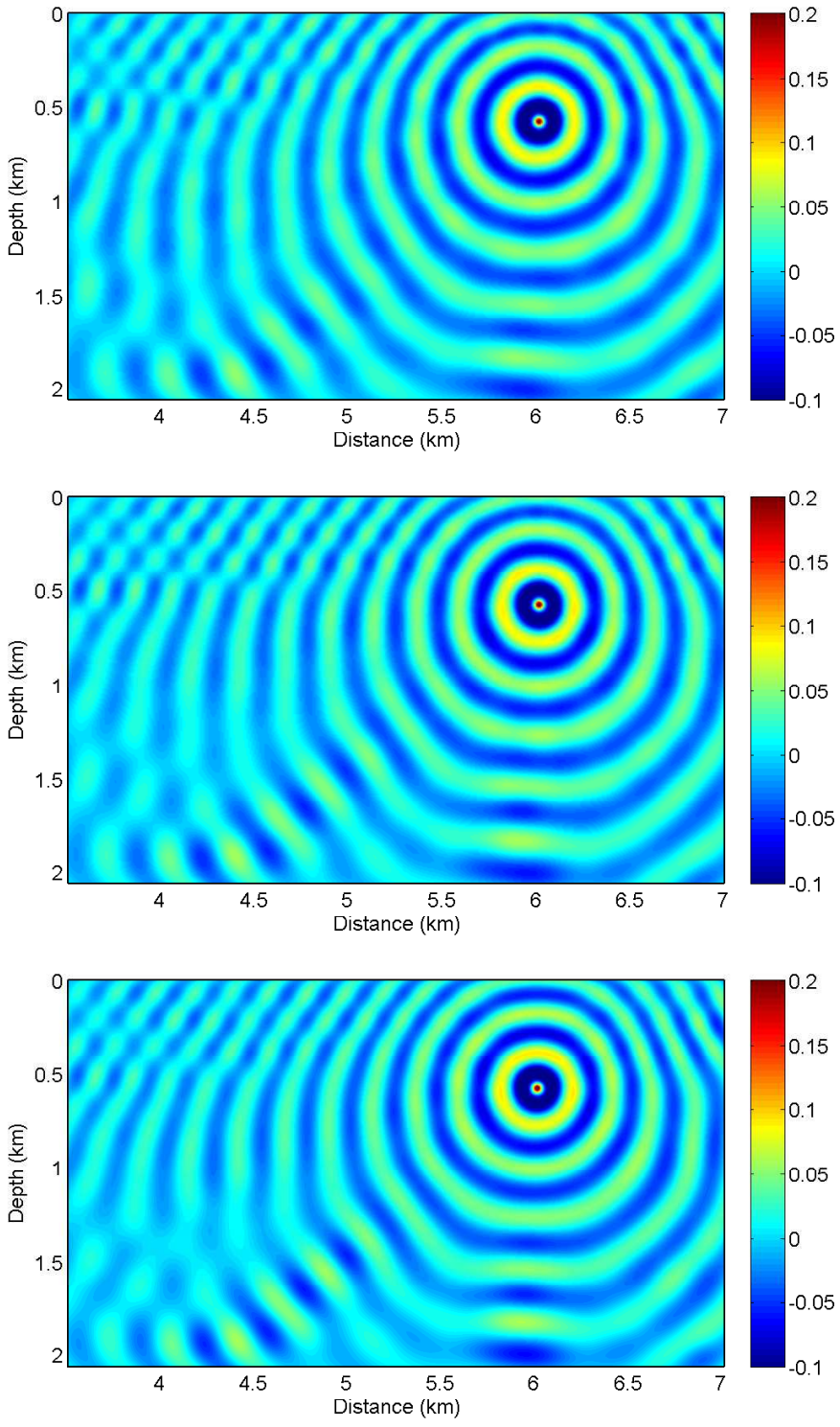

Figure 7.6: Real part of the total field approximation in the smoothed Marmousi section with frequency 10 Hz: UWVF solution with $K = 485$ and $p = 15$ (upper plot), UWVF solution with $K = 771$ and $p = 13$ (centre plot), finite difference solution (lower plot).

forms of source function, such as dipoles. Following on from work in [15], we show that the Source Extraction UWVF is well-posed and satisfies the error bound (7.9) on the mesh skeleton in the case of impedance boundary conditions and sufficiently smooth solution. Numerical simulation has shown that the Source Extraction UWVF is a much more accurate method than the classical UWVF for the approximation of interior point sources. The method is also used to provide simulation of wave scattering in a sound speed profile typical of seismic imaging applications. Results presented concur with those of a high resolution finite difference method.

Chapter 8

Conclusions

We now summarise this thesis, present the conclusions found, and give suggestions for further expansion of the work.

8.1 Summary

In Chapter 2 we provided the context for the research in the subsequent chapters. We gave some background of acoustic wave propagation in two dimensions, and introduced the equation governing time harmonic wave motion, the Helmholtz equation. Explanation was given of factors that need to be taken into consideration for the accurate numerical simulation of acoustic wave propagation, such as boundary conditions, computational time, and storage costs. Details of two methods for understanding wave propagation were given: the Method of Fundamental Solutions (MFS), and ray tracing. The motivation for this research from the seismic industry was explained, as well as background about the numerical methods currently used and the practicalities of real world seismic data aquisition.

The main numerical method used in this thesis, the Ultra Weak Variational Formulation (UWVF), was introduced in Chapter 3. The specific problem set up for the Helmholtz equation and the UWVF approximation form was given, as well as the

derivation of the UWVF in the original variational and the more recently shown Discontinuous Galerkin framework. Key theoretical results of the UWVF from the literature were explained, as well as computational aspects such as the linear system of equations, ill-conditioning issues that arise, and the difficulties in approximating the inhomogeneous form of the governing equation. A new Hankel basis was introduced, allowing more flexibility in the set than the traditional plane wave basis.

In Chapter 4 we considered the case of high frequency wave scattering by a smooth convex obstacle, with examples given of circular and elliptical scatterers. We considered a domain of constant wavespeed, and used ray tracing techniques to develop an algorithm that gives the wave direction and local centre of curvature for the reflected wavefronts. Initial studies were presented considering the best approximation by various bases in an individual element, and regions of the domain in which the ray traced basis is most accurate. The results were promising, with the wavefield representation by two ray traced basis functions per element achieving high accuracy in large regions of the domain.

Chapter 5 was the first in which we investigated ways of enriching the UWVF basis for specific problem types. The UWVF approximations for both scattering by a circle and by an ellipse were presented, initially using the traditional equi-spaced basis, followed by the those achieved by a basis including the ray traced centres of curvature derived in Chapter 4. Results show a reduction in the number of degrees of freedom required for a given level of accuracy when using the ray traced augmented basis.

The use of the UWVF for seismic imaging was then applied in Chapter 6, testing on the smoothed Marmousi sound speed profile, a synthetic model of the subsurface of the Earth widely used as a test case in the seismic industry. The idea of using ray tracing to enhance the UWVF basis was then extended, with two ray tracing methods presented. Ray directions obtained via the Fast Marching Method were implemented into the UWVF basis, and compared with results of the standard equi-spaced plane wave basis. In this case numerical results suggest that an alternative method of implementing ray directions may be more effective. With the directions obtained by the FMM, although

accuracy is improved by using the ray traced basis when using a low number of degrees of freedom, these initial gains are lost as the solution converges to a fixed final state.

In Chapter 7 another problem highly relevant to seismic imaging was considered, that of wave propagation from a point source on the interior of the domain. This set-up is common place in the seismic industry, representative of an explosive sound source positioned in a well at a significant depth below ground level. Due to the Trefftz basis, the UWVF is not well disposed to solving the inhomogenous Helmholtz equation. An augmentation to the UWVF called the Source Extraction UWVF was presented, in which the inhomogeneity of the equation was effectively removed, allowing the superior approximation properties of the Trefftz basis to be maintained. Accurate results were presented for a domain of constant sound speed. Results for differing discretisations and frequencies were also presented for wave propagation in a section of a smoothed Marmousi velocity profile, which concur with those using a high order FD approximation.

8.2 Conclusions

In this thesis we considered the use of the UWVF for forward seismic imaging, by simulating wave propagation in a synthetic sound speed profile, the Marmousi model. Due to the requirement of the UWVF of a constant wave number in each element, the domain had to be finely discretised in order to maintain the details of the seismic structures. However, as the element sizes get smaller in comparison to the wavelength, a reduced number of basis functions can be used in each element before problems of ill conditioning arise. When using an equi-spaced basis, this could mean that key wave directions are excluded. Therefore consideration must be given as to how much detail it is necessary to represent in the domain at the cost of the wave directions being well represented in the basis. In [31,36] it is recommended that accuracy is improved in the UWVF not through mesh refinement but through using an increased number of basis functions in each element. For the frequencies and length scales applicable in seismic

imaging, this limitation on element size may well affect the level of accuracy achievable. However that said, numerical results of the UWVF in this thesis do concur with those of alternate methods already used by the seismic community.

We also considered ways of enriching the UWVF basis, in the hope of reducing the number of degrees of freedom required for a given level of accuracy. For a domain of constant wave speed, ray tracing techniques were able to provide a good representation of wave directions, and when incorporated into the UWVF basis gave accurate results. Using less than one degree of freedom per wavelength an L^2 relative error of less than 10% was achievable for the high frequency scattering by a unit circle solution for wavenumber $\kappa = 80$. Thus the ray tracing techniques are highly valuable in terms of low computational cost if a general representation of state is needed. For higher levels of accuracy, numerical results shown here found that the ray enhanced basis did provide a reduction in the number of degrees of freedom required. Attempts to further reduce the computational cost by using the ray traced basis alone in sections of the domain found that limited levels of accuracy could be achieved. Overall, a ray enhanced basis in the case of a domain of constant sound speed was highly effective, and could be used for further work in similar set-ups. For wave propagation in the non-constant sound speed profile, the inclusion of ray directions in the basis found some minimal effects. This suggests that there is some influence of the ray enhanced basis: further investigation may find it to be more effective to either implement FMM ray directions through a different strategy, or use ray directions obtained via alternative ray tracing techniques.

Finally, we also considered the use of the UWVF for the solving of the inhomogeneous Helmholtz equation, proposing an augmentation of the UWVF equations called the Source Extraction UWVF. This work has been published seperately in [38]. We used an incident point source on the interior of the domain, which is a highly relevant scenario in seismic imaging, representing an explosive sound source in a well. However the augmentation of the method can be easily generalised to other forms of source function used in alternative situations the UWVF may be used in. As the matrices

of the formulation are unchanged in the Source Extraction UWVF, some theoretical results from the original UWVF still hold and can be generalised. Numerical results in a domain of constant wavenumber proved to be of much higher accuracy than the standard formulation, and those of a varying sound speed profile concured with a high order FD solution.

8.3 Future Work

For the work on the domain of constant wavenumber, there are various extensions and improvements that can be made. Although the ray traced basis did work well in the illuminated region, the basis did not make any consideration for the creeping waves generated at the shadow boundary, caused by diffraction of waves that hit tangent to the obstacle boundary. One could extend the basis to include wavefronts which better represent these creeping waves. Here we only consider a smooth obstacle for the scatterer, one could extend the use of ray directions to the case of non-smooth obstacles such as polygons. In this case there would also be diffracted waves off corners to be considered. At shadow boundaries the amplitude of the solution is highly varying, which the UWVF basis of constant wave height did not cope with well. One could investigate alternative basis functions which may be better suited, such as wavelets.

In this work for the seismic imaging applications we have used a smoothed sound speed profile in order to meet the requirements for the ray tracing to be applicable. As a futher test of the suitability of the UWVF for seimic imaging, one could use a non-smoothed profile, such as the original Marmousi model, where the layers and faults are kept distinct. However in order to maintain the detail of the domain it would require a much more careful meshing, where element edges are lined up with the faults and layers in the domain. This could possibly lead to highly obtuse triangular elements, which in turn may cause issues with the conditioning of the system. In this case it may be preferable to use other polygonal elements as investigated in [52]. Further experimentation could also be done for the suitability of the Hankel basis for seismic

imaging applications, incorporating not just the wave direction but also a higher level of curvature of wavefronts suited to the domain shape, in a similar fashion to the techniques used in Chapters 4 and 5.

The current version of the UWVF requires the wavenumber to be constant in each element, requiring the wavenumber throughout the domain to be discretised into piecewise constants. A significant development would be to extend the UWVF formulation to the case where the wavespeed is varying within each element. For a linear variation in the wavespeed in each element, a plane wave basis could possibly be replaced by an Airy function basis. The derivation of the UWVF would need to be reconsidered, as with this type of basis there may be extra domain based integrals arising in the formulation. A development of this nature would be highly advantageous for seismic imaging and other applications, as it may permit more detail of the variation in the wavenumber to be maintained. Work on similar techniques has been done for the Discontinuous Enrichment Method (DEM): in [69] a basis combining plane waves and Airy functions approximates solutions of the Helmholtz equation obtained by successive Taylor series expansions of the wavenumber around a reference point. An alternative method is detailed in [60], where the values of the local wavenumber are interpolated in the standard nodal-based-FEM manner, while the oscillatory behaviour of the solution is treated by a polynomial modulated plane wave basis.

Bibliography

[1] Gaussian filter.
http://reference.wolfram.com/mathematica/ref/GaussianFilter.html [Online; accessed 2-January-2014].

[2] R. Abgrall and J. Benamou. Big ray-tracing and eikonal solver on unstructured grids: Application to the computation of a multivalued traveltime field in the Marmousi model. *GEOPHYSICS*, 64(1):230–239, 1999.

[3] M. Abramowitz and I. Stegun. *A Handbook of Mathematical Functions*. National Bureau of Standards, 1968.

[4] M. Ainsworth. Dispersive and dissipative behaviour of high order discontinuous Galerkin finite element methods. *Journal of Computational Physics*, 198(1):106 – 130, 2004.

[5] K. Aki and P. Richards. *Quantitative Seismology*. W.H. Freeman and Company, USA, 1980.

[6] Z. Alterman and F. Karal. Propagation of elastic waves in layered media by finite difference methods. *Bulletin of the Seismological Society of America*, 58(1):367–398, 1968.

[7] I. Babuska and S. Sauter. Is the pollution effect of the FEM avoidable for the Helmholtz equation considering high wave numbers? *SIAM Review*, 42(3):451–484, 2000.

[8] R. Barlow. *Statistics: A Guide to the Use of Statistical Methods in the Physical Sciences*. John Wiley & Sons, Ltd., 1989.

[9] A. Barnett and T. Betcke. Stability and convergence of the method of fundamental solutions for Helmholtz problems on analytic domains. *Journal of Computational Physics*, 227:7003–7026, 2008.

[10] C. Bernardi and R. Verfürth. Adaptive finite element methods for elliptic equations with non-smooth coefficients. *Numerische Mathematik*, 85(4):579–608, 2000.

[11] T. Betcke and J. Phillips. Approximation by dominant wave directions in plane wave methods. awaiting publication 2013.

[12] N. Bleistein. *Mathematical Methods for Wave Phenomena*. Academic Press, Inc., 1984.

[13] J. Brentzen. On the implementation of fast marching methods for 3D lattices. Technical report, Informatics and Mathematical Modelling, Technical University of Denmark, 2001.

[14] J. Brokešová. *Asymptotic Ray Method in Seismology: A Tutorial*. Publication No. 168, Matfyzpress,, 2006.

[15] A. Buffa and P. Monk. Error estimates for the ultra weak variational formulation of the Helmholtz equation. *ESAIM: Mathematical Modelling and Numerical Analysis*, 42:925–940, 2008.

[16] O. Cessenat. *Application d'une Nouvelle Formulation Variationnelle aux Équations d'ondes Harmoniques. Problèmes de Helmholtz* $2D$ *et de Maxwell* $3D$. PhD thesis, Paris IX Dauphine, 1996.

[17] O. Cessenat and B. Després. Application of an ultra-weak variational formulation of elliptic PDE's to the two-dimensional Helmholtz problem. *SIAM Journal of Numerical Analysis*, 35(1):255–299, 1998.

[18] S. Chandler-Wilde, I. Graham, S. Langdon, and E. Spence. Numerical-asymptotic boundary integral methods in high-frequency acoustic scattering. *Acta Numerica*, 21:89–305, 2012.

[19] S. Chandler-Wilde and S. Langdon. Boundary element method for acoustics. Technical report, University of Reading, 2007.

[20] S. Chandler-Wilde and S. Langdon. Finite element methods for acoustic scattering. Technical report, University of Reading, 2007.

[21] S. Chandler-Wilde and S. Langdon. A Galerkin boundary element method for high frequency scattering by convex polygons. *SIAM Journal of Numerical Analysis*, 45:610–640, 2007.

[22] C. Chapman. *Fundamentals of Seismic Wave Propagation*. Cambridge University Press, Cambridge, 2004.

[23] D. Colton, H. Haddar, and M. Piana. The linear sampling method in inverse electromagnetic scattering theory. *Inverse Problems*, 19(6):S105, 2003.

[24] E. Darrigrand. Ultra-weak variational formulation and efficient integral representation in electromagnetism: a thorough study of the algorithm complexity. *ESAIM: Proc.*, 22:190–197, 2008.

[25] E. Darrigrand and P. Monk. Coupling of the ultra-weak variational formulation and an integral representation using a fast multipole method in electromagnetism. *Journal of Computational and Applied Mathematics*, 204(2):400 – 407, 2007.

[26] J. De Basabe and M. Sen. New developments in the finite-element method for seismic modeling. *The Leading Edge (May)*, 28(5):562–567, 2009.

[27] L. Ding, T. Van Renterghem, and D. Botteldooren. Estimating the effect of semi-transparent low-height road traffic noise barriers with ultra weak variational formulation. *Acta Acustica united with Acustica*, 97(3):391–402, 2011.

[28] H. Doyle. *Seismology*. John Wiley & Sons Ltd, UK, 1995.

[29] G. Gabard. Discontinuous Galerkin methods with plane waves for time-harmonic problems. *Journal of Computational Physics*, 225(2):1961 – 1984, 2007.

[30] G. Gabard1, P. Gamallo, and T. Huttunen. A comparison of wave-based discontinuous Galerkin, ultra-weak and least-square methods for wave problems. *International Journal For Numerical Methods in Engineering*, 85:380–402, 2011.

[31] C. J. Gittelson, R. Hiptmair, and I. Perugia. Plane wave discontinuous Galerkin methods: Analysis of the h-version. *ESAIM: Mathematical Modelling and Numerical Analysis*, 43:297–331, 2009.

[32] V. Grechka. *Ray Tracing: notes for 'Advanced Seismology' class*, 2001.

[33] M. J. Grote and J. B. Keller. On nonreflecting boundary conditions. *Journal of Computational Physics*, 122:231–243, 1995.

[34] S. Groth, D. Hewett, and S. Langdon. Hybrid numericalasymptotic approximation for high-frequency scattering by penetrable convex polygons. *IMA Journal of Applied Mathematics*, 2013.

[35] I. Harari and E. Turkel. Accurate finite difference methods for time-harmonic wave propagation. *J. Comp. Phys.*, 119:252–270, 1995.

[36] R. Hiptmair, A. Moiola, and I. Perugia. Plane wave discontinuous Galerkin methods for the 2D Helmholtz equation: Analysis of the p-version. *SIAM Journal of Numerical Analysis*, 49:264–284, 2011.

[37] R. Hiptmair, A. Moiola, and I. Perugia. Trefftz discontinuous Galerkin methods for acoustic scattering on locally refined meshes. *Applied Numerical Mathematics*, 2013.

[38] C. Howarth, P. Childs, and A. Moiola. Implementation of an interior point source in the ultra weak variational formulation through source extraction. In Mathematics Preprint Series. http://www.reading.ac.uk/maths-and-stats/research/maths-preprints.aspx. Submitted to Journal of Computational and Applied Mathematics., 2013.

[39] T. Huttunen, P. Gamallo, and R. Astley. Comparison of two wave element methods for the Helmholtz problem. *Communications in Numerical Methods in Engineering*, 25(1):35–52, 2009.

[40] T. Huttunen, J. Kaipio, and P. Monk. An ultra-weak method for acoustic fluid–solid interaction. *Journal of Computational and Applied Mathematics*, 213(1):166 – 185, 2008.

[41] T. Huttunen, J. P. Kaipio, and P. Monk. The perfectly matched layer for the ultra weak variational formulation of the 3D Helmholtz equation. *International Journal for Numerical Methods in Engineering*, 61(7):1072–1092, 2004.

[42] T. Huttunen, M. Malinen, and P. Monk. Solving Maxwell's equations using the ultra weak variational formulation. *Journal of Computational Physics*, 223(2):731 –758, 2007.

[43] T. Huttunen, P. Monk, F. Collino, and J. Kaipio. The ultra-weak variational formulation for elastic wave problems. *SIAM Journal of Scientific Computation*, 25(5):1717 –1742, 2004.

[44] T. Huttunen, P. Monk, and J. P. Kaipio. Computational aspects of the ultra-weak variational formulation. *Journal of Computational Physics*, 182:27–46, 2002.

[45] F. Ihlenburg. *Finite Element Analysis of Acoustic Scattering*. Applied Mathematical Sciences, Springer-Verlag, 1998.

[46] T. Irons. Marmousi model. http://reproducibility.org/RSF/book/data/marmousi/ paper.pdf [Online; accessed 18-July-2013].

[47] O. Laghrouche, P. Bettess, E. Perrey-Debain, and J. Trevelyan. Wave interpolation finite elements for Helmholtz problems with jumps in the wave speed. *Computer Methods in Applied Mechanics and Engineering*, 194(2-5):367 – 381, 2005.

[48] O. Laghrouche and M. Mohamed. Locally enriched finite elements for the Helmholtz equation in two dimensions. *Computers & Structures*, 88(23-24):1469 –1473, 2010.

[49] C. Linton and P. McIver. *Handbook of Mathematical Techniques for Wave/Structure Interactions*. Chapman & Hall/ CRC Press, 2001.

[50] M. Loeser and B. Witzigmann. The ultra weak variational formulation applied to radiation problems with macroscopic sources in inhomogeneous domains. *IEEE Journal of Selected Topics in Quantum Electronics*, 15(4):1144–1155, 2009.

[51] T. Luostari, T. Huttunen, and P. Monk. The ultra weak variational formulation for 3D elastic wave problems. In *Proceedings of 20th International Congress on Acoustics, ICA*, pages 23–27, 2010.

[52] T. Luostari, T. Huttunen, and P. Monk. The ultra weak variational formulation using Bessel basis functions. *Communications in Computational Physics*, 11(2):400–414, 2012.

[53] T. Luostari, T. Huttunen, and P. Monk. Improvements for the ultra weak variational formulation. *International Journal for Numerical Methods in Engineering*, 94(6):598–624, 2013.

[54] G. Martin, R. Wiley, and K. Marfurt. Marmousi2: An elastic upgrade for Marmousi. *The Leading Edge*, 25(2):156–166, 2006.

[55] J. Melenk, A. Parsania, and S. Sauter. Generalized DG-methods for highly indefinite Helmholtz problems based on the ultra-weak variational formulation. Technical report, ASC report, 2012.

[56] J. Melenk and S. Sauter. Wavenumber explicit convergence analysis for Galerkin discretizations of the Helmholtz equation. *SIAM Journal on Numerical Analysis*, 49(3):1210–1243, 2011.

[57] A. Moiola. *Trefftz Discontinuous Galerkin Methods for Time-Harmonic Wave Problems*. PhD thesis, ETH Zurich, 2011.

[58] A. Moiola, R. Hiptmair, and I. Perugia. Plane wave approximation of homogeneous Helmholtz solutions. *Z. Angew. Math. Phys.*, 62:809–837, 2011.

[59] I. Opršal, C. Matyska, and K. Irikura. A general boundary condition in 3D hybrid wave injection modeling based on Alterman and Karal (1968) method. *Proc. 14 World Conf. Earthq. Eng.*, 2008. paper no. $03 - 01 - 0035$.

[60] P. Ortiz. Finite elements using a plane-wave basis for scattering of surface water waves. *Philosophical Transactions of the Royal Society of London. Series A: Mathematical, Physical and Engineering Sciences*, 362(1816):525–540, 2004.

[61] P.-O. Persson. Distmesh - a simple mesh generator in matlab. http://persson.berkeley.edu/distmesh/ [Online; accessed 3-March-2010].

[62] P.-O. Persson and G. Strang. A simple mesh generator in Matlab. *SIAM Review*, 46:329–345, 2004.

[63] G. Peyre. Toolbox fast marching, Matlab Central File Exchange. http://www.mathworks.com/matlabcentral/fileexchange/6110-toolbox-fast-marching [Online; accessed 1-October-2012].

[64] R. Piltner. Trefftz method. http://math.georgiasouthern.edu/ rpiltner/sub_piltner/piltner_Trefftz_method.html [Online; accessed 2-December-2013].

[65] R. Potthast. A point-source method for inverse acoustic and electromagnetic obstacle scattering problems. *IMA Journal of Applied Mathematics*, 61:119–140, 1998.

[66] G. Roach. *Green's Functions: Introductory Theory with Applications*. Van Nostrand Reinhold Company, 1970.

[67] J. Sethian and A. Vladimirsky. Fast methods for the eikonal and related Hamilton-Jacobi equations on unstructured meshes. *Proceedings of the National Academy of Sciences USA*, 97:5699–5703, 2000.

[68] N. Sleep and K. Fujita. *Principles of Geophysics*. Blackwell Science Inc, USA, 1997.

[69] R. Tezaur, I. Kalashnikova, and C. Farhat. The discontinuous enrichment method for medium-frequency Helmholtz problems with a spatially variable wavenumber. *Computer Methods in Applied Mechanics and Engineering*, 268:126–140, 2014.

[70] J. Virieux, S. Operto, H. Ben-Hadj-Ali, R. Brossier, V. Etienne, F. Sourbier, L. Giraud, and A. Haidar. Seismic wave modeling for seismic imaging. *The Leading Edge (May)*, 28(5):538–544, 2009.

[71] K. Žáček. Smoothing the Marmousi model. *Pure and Applied Geophysics*, 159:1507–1526, 2002.

[72] E. W. Weisstein. Ellipse. From Mathworld–a Wolfram web resource. http://mathworld.wolfram.com/Ellipse.html [Online; accessed 2-December-2013].